

## **NIAC Phase I Final Report**

# **Optimal Fragmentation and Dispersion of Hazardous Near-Earth Objects**

**September 25, 2012**

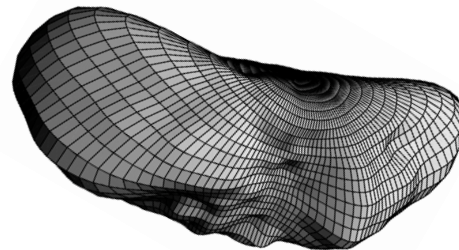
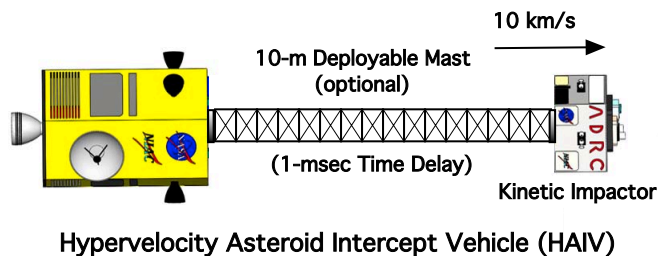
**Prof. Bong Wie (2011 NIAC Phase I Fellow)**

**Graduate Research Assistants:**

**Alan Pitz, Brian Kaplinger, Matt Hawkins, Sam Wagner,  
George Vardaxis, Tim Winkler, and Joshua Lyzhoft**

**Asteroid Deflection Research Center  
Department of Aerospace Engineering  
Iowa State University  
Ames, IA 50011**

**NASA Innovative Advanced Concepts (NIAC) Phase I Study  
Grant Number: NNX11AR43G  
Project Period: 9/16/11 - 9/15/12**



# Contents

<b>1</b>	<b>Executive Summary</b>	<b>11</b>
1.1	Introduction and Summary	11
1.2	Summary of Phase I Study Results	13
1.2.1	Task 1 Study Result Summary	13
1.2.2	Task 2 Study Result Summary	15
1.3	An Overview of Phase II Study	18
1.3.1	Task 1 (9/10/12 - 9/9/14): Detailed Design Evaluation of a Hypervelocity Asteroid Intercept Vehicle (HAIV) and its Mission Architecture	19
1.3.2	Task 2 (9/10/12 - 9/9/14): High-Fidelity 3-D Computational Validation of Optimal Fragmentation and Dispersion of NEOs	22
1.3.3	Task 3 (Year 2): Development and Design of a HAIV Flight Validation Mission Architecture (Development of a Phase III program)	24
1.3.4	Task 4 (10/15/12 - 10/19/12): Five-Day IDC Study at NASA GSFC in Support of Tasks 1 and 3	26
1.3.5	Phase II Deliverables	28
1.3.6	Study Team, Work Plan, and Project Management	29
1.4	Acknowledgments	30
1.5	References	30
<b>2</b>	<b>Conceptual Design of a Hypervelocity Asteroid Intercept Vehicle (HAIV)</b>	<b>32</b>
2.1	Introduction	32
2.2	Nuclear Disruption Mission Requirements	33
2.3	State-of-the-Art Interceptor Technology	35
2.3.1	NASA's Deep Impact Mission	35
2.3.2	ESA's Don Quijote Mission Concept	36
2.4	Design and Analysis of a Baseline HAIV Architecture	36
2.4.1	A Baseline HAIV Mission Architecture	36
2.4.2	Nuclear Fuzing Mechanisms	38
2.4.3	Terminal Guidance Sensors/Instruments	39
2.4.4	Thermal Protection and Shield	39
2.4.5	Optional HAIV Configuration Employing Deployable Mast	44
2.4.6	Shock Prevention Systems	45
2.4.7	Attitude Determination and Control System (ADCS)	46
2.4.8	Power System	47
2.4.9	Mass Budget Summary	48
2.5	Conclusion	49
2.6	References	50

<b>3</b>	<b>Modeling and Simulation of Hypervelocity Kinetic Impact and Nuclear Explosions</b>	<b>52</b>
3.1	Introduction . . . . .	52
3.2	Simulation Model . . . . .	53
3.2.1	HAIV System Targets . . . . .	53
3.2.2	Hydrodynamic Equations . . . . .	55
3.2.3	Tensor Damage Model . . . . .	56
3.2.4	Neighbor Finding Implementation . . . . .	57
3.3	Disruption Mission Profiles . . . . .	58
3.3.1	Subsurface Explosion Setup . . . . .	58
3.3.2	Surface Penetrator Model . . . . .	58
3.3.3	Standoff Energy Deposition . . . . .	59
3.3.4	HAIV Concept . . . . .	59
3.4	Orbit Propagation . . . . .	63
3.4.1	Impacting Orbit Solver . . . . .	67
3.4.2	Fragmented System Estimation . . . . .	68
3.4.3	Uncertainty Analysis . . . . .	68
3.5	Computational Approach . . . . .	70
3.6	Results . . . . .	71
3.6.1	Computational Optimization . . . . .	72
3.6.2	Optimal Mission Results . . . . .	74
3.6.3	Performance . . . . .	75
3.7	Conclusion . . . . .	76
3.8	References . . . . .	79
<b>4</b>	<b>Terminal Intercept Guidance and Control</b>	<b>81</b>
4.1	Introduction . . . . .	81
4.2	Mathematical Modeling . . . . .	81
4.3	Classical Feedback Guidance Laws . . . . .	83
4.3.1	PN-based Feedback Guidance Laws . . . . .	83
4.3.2	Predictive Feedback Guidance Laws . . . . .	86
4.4	Optimal Feedback Guidance Algorithms . . . . .	89
4.4.1	Constrained-Terminal-Velocity Guidance (CTVG) . . . . .	90
4.4.2	Free-Terminal-Velocity Guidance (FTVG) . . . . .	91
4.4.3	Intercept-Angle-Control Guidance (IACG) . . . . .	92
4.4.4	Relationship Between PNG and Optimal Feedback Guidance . . . . .	92
4.4.5	Calculation of Time-To-Go . . . . .	93
4.4.6	ZEM/ZEV Feedback Guidance . . . . .	94
4.4.7	Estimation of the ZEM and ZEV . . . . .	94
4.5	Simulation Results . . . . .	95
4.5.1	Classical Feedback Guidance Laws . . . . .	95
4.5.2	Optimal Feedback Guidance Algorithms . . . . .	96
4.5.3	High-Fidelity Simulation Using CLEON Software . . . . .	96
4.6	Conclusion . . . . .	104
4.7	References . . . . .	104
<b>5</b>	<b>HAIV Flight Validation Mission Design</b>	<b>105</b>
5.1	Introduction . . . . .	105
5.2	Overview of Existing Mission Design Tools . . . . .	105
5.2.1	Integrated HAIV/OTV Design Tool . . . . .	105
5.2.2	An On-line Tool by The Aerospace Corporation . . . . .	107

5.2.3	NASA's Mission Design Software Tools . . . . .	107
5.2.4	NASA's General Mission Analysis Tool . . . . .	108
5.2.5	Mission Design Program Comparisons . . . . .	108
5.3	Asteroid Mission Design Software Tool (AMiDST) . . . . .	108
5.4	Reference Target Asteroids . . . . .	111
5.5	Applications of the AMiDST . . . . .	111
5.5.1	Target List Mission Design . . . . .	111
5.6	Examples of PDT Demonstration Mission Design . . . . .	112
5.7	AMiDST Applications . . . . .	115
5.7.1	Custom Mission Parameter Block . . . . .	115
5.7.2	Spacecraft and Mission Type Block . . . . .	118
5.7.3	Trajectory Block . . . . .	118
5.7.4	Mission Analysis Block . . . . .	120
5.7.5	Perturbed Orbit Trajectory Block . . . . .	120
5.8	Asteroid 2011 AG5 Mission Design Examples . . . . .	122
5.8.1	Rendezvous Mission Design . . . . .	122
5.8.2	HAIV Disruption Mission Design . . . . .	124
5.9	Conclusion . . . . .	126
5.10	References . . . . .	127
<b>6</b>	<b>Target Selection for a HAIV Flight Validation Mission</b>	<b>128</b>
6.1	Introduction . . . . .	128
6.1.1	Previous NEO Missions and Proposals . . . . .	128
6.2	Optimal Target Selection Process . . . . .	130
6.2.1	Launch Options . . . . .	131
6.2.2	Target List . . . . .	132
6.2.3	Target Mission Examples . . . . .	138
6.3	Advanced Mission Design . . . . .	142
6.3.1	Problem Formulation . . . . .	142
6.3.2	Problem Constraints . . . . .	145
6.3.3	Type 1 Mission Results . . . . .	146
6.3.4	Type 2 Mission Results . . . . .	146
6.3.5	Type 3 Mission Results . . . . .	149
6.3.6	Advanced Mission Design Summary . . . . .	149
6.4	Future Work . . . . .	149
6.5	Conclusion . . . . .	149
6.6	References . . . . .	151
<b>7</b>	<b>Fuel-Efficient Proximity Operations Around an Irregular-Shaped Asteroid</b>	<b>152</b>
7.1	Introduction . . . . .	152
7.2	Problem Description . . . . .	153
7.2.1	Coordinate Systems and Dynamic Equations . . . . .	153
7.2.2	Polyhedron Gravitation . . . . .	154
7.2.3	Spherical Harmonics . . . . .	155
7.3	Fuel-Efficient Orbit Control . . . . .	156
7.3.1	PD Control . . . . .	156
7.3.2	Disturbance-Accommodating Control . . . . .	158
7.4	ZEM/ZEV Feedback Guidance . . . . .	159
7.4.1	Generalized ZEM/ZEV Feedback Guidance Algorithm . . . . .	159
7.4.2	ZEM/ZEV Guidance for Orbital Transfer . . . . .	160



7.4.3	ZEM/ZEV Guidance for Soft Landing on an Irregular-Shaped Asteroid . . . . .	162
7.5	Simulation Results . . . . .	163
7.5.1	Low-Thrust Orbital Transfer . . . . .	163
7.5.2	Fuel-Efficient Orbit Control . . . . .	163
7.5.3	Soft Landing on an Irregular-Shaped Asteroid . . . . .	165
7.6	Conclusion . . . . .	171
7.7	References . . . . .	171

# List of Figures

1.1	A hypervelocity asteroid intercept vehicle (HAIV) system/mission concept [3]. . . . .	12
1.2	HAIV configuration options (Task 1). . . . .	13
1.3	A baseline HAIV and its terminal-phase operational concept (Task 1). . . . .	14
1.4	Simplified 2-D computational modeling and simulation of a penetrated, 70-kt nuclear explosion for a 70-m asymmetric reference target body (Task 2). . . . .	16
1.5	Orbital dispersion modeling and Earth-impact simulation of NEO fragments (Task 2). . . . .	17
1.6	A summary of orbital dispersion analysis and Earth-impact simulation of NEO fragments (Task 2). Courtesy of Dr. David Dearborn at Lawrence Livermore National Laboratory. . . . .	18
1.7	Phase II project schedule (to be properly coordinated with a NEO exploration research project of the Asteroid Deflection Research Center). . . . .	19
1.8	NASA's Nuclear Spectroscopic Telescope Array (NuSTAR) scientific satellite, employing ATK's 10-m deployable mast, successfully launched in June 2012. Image courtesy of NASA/JPL. . . . .	20
1.9	A realistic NEO target model for the 3-D computational validation of optimal fragmentation and dispersion (Task 2 of Phase II). Image courtesy of NASA for a reference shape model of asteroid Eros. . . . .	23
1.10	A HAIV flight validation mission trajectory. A HAIV flight validation mission concept that doesn't employ an actual nuclear explosive payload will be developed for Task 3 of Phase II. . . . .	27
1.11	GSFC's IDC (Integrated Design Center) study scheduling, capabilities, tools, and products. . . . .	28
2.1	Equivalent yield factors for total coupled energy and ground-shock coupled energy normalized to a contact burst [5]. . . . .	34
2.2	Conceptual illustration of the baseline HAIV mission architecture. . . . .	37
2.3	Primary two-body HAIV configuration during the terminal phase. . . . .	38
2.4	Secondary HAIV configuration by connection of a deployable boom. . . . .	38
2.5	Preliminary illustrative results for the hypervelocity penetrated subsurface nuclear explosion option. . . . .	40
2.6	Estimated penetration depth of a flat plate and conical cone based on 3 consecutive hits at the same location. . . . .	41
2.7	Estimated penetration depth of a spherical cap and ogive nose cone based on 3 consecutive hits at the same location. . . . .	41
2.8	Peak payload specific energy for flat shield design. . . . .	43
2.9	Example acceleration measurements for flat shield design. . . . .	44
2.10	Illustrations of a deployable boom option that can be employed for the HAIV. . . . .	45
2.11	A baseline two-body HAIV configured for launch. . . . .	49
3.1	Asymmetric target asteroid model for 3D penetrated explosion simulation. . . . .	54
3.2	Description of sorted neighbor kernel process. . . . .	58
3.3	Neighbor search cost. . . . .	59
3.4	Subsurface explosion and resulting fragment velocities. . . . .	60
3.5	Radial energy deposition and total deposition region. . . . .	61

3.6	SPH nodes and resulting ablation for standoff model. . . . .	62
3.7	Radial dispersion velocity histogram for HAIV concept. . . . .	63
3.8	Asymmetric shock behavior. . . . .	64
3.9	Example damage localization for tensor fracture model. . . . .	65
3.10	Final disruption of NEO target. . . . .	65
3.11	Location of slowest moving debris. . . . .	66
3.12	Radial dispersion velocity histogram for contact burst. . . . .	66
3.13	Histograms of known NEO population. . . . .	67
3.14	Cumulative density functions for disrupted asteroid. . . . .	69
3.15	Rotating local-vertical-local-horizontal (LVLH) frame. . . . .	70
3.16	Qualitative GPU memory model. . . . .	72
3.17	Relative performance for surface impactor. . . . .	73
3.18	Impacting mass for subsurface explosion on orbits with varying inclination. . . . .	74
3.19	Impacting mass comparison for subsurface and dynamic surface cases. . . . .	75
3.20	Mean ejecta velocity for single and double impactor cases. . . . .	76
3.21	Comparison of single-node performance on CPU and GPU. . . . .	77
3.22	Cost function contours for sample mission approach asymptotes. . . . .	78
4.1	Coordinate system definition. . . . .	82
4.2	Scmitt trigger on-off logic. . . . .	86
4.3	Trajectories, line-of-sight angle, commanded acceleration, and applied acceleration for PN guidance. . . . .	97
4.4	Closing velocity, line-of-sight rate, $\Delta v$ used, and position difference for PN guidance. . . . .	97
4.5	Trajectories, line-of-sight angle, line-of-sight rate, and detailed view of rate for PI guidance. . . . .	98
4.6	Closing velocity, commanded acceleration, $\Delta v$ used, and position difference for PI guidance. . . . .	98
4.7	FTVG guidance algorithms for asteroid intercept. . . . .	99
4.8	Performance of the FTVG guidance algorithm. . . . .	99
4.9	IACG guidance algorithms for asteroid intercept. . . . .	100
4.10	GMV's CLEON software functional illustration [2,3]. . . . .	101
4.11	ZEM cumulative distribution function, $\Delta v$ cumulative distribution function, impact points on target, and impact radius evolution for PN guidance. . . . .	103
4.12	ZEM cumulative distribution function, $\Delta v$ cumulative distribution function, impact points on target, and impact radius evolution for PI guidance . . . . .	103
5.1	Flowchart illustration of the pre-mission design process. . . . .	106
5.2	Flowchart illustration of the AMiDST. . . . .	109
5.3	Typical Orbits of Apollo, Aten, and Apollo Asteroids. . . . .	111
5.4	Delta II launch vehicle configurations [8]. . . . .	113
5.5	Delta IV (left) and Atlas V (right) launch vehicles [9,10]. . . . .	113
5.6	Block partition depiction of the AMiDST. . . . .	116
5.7	Illustration of the orbit of asteroid 1999 RQ36 in reference to the inner planets [12]. . . . .	117
5.8	Illustration of the orbit of asteroid 2011 AG5 in reference to Earth's and Mars' orbits. . . . .	118
5.9	Selection of launch date and mission duration for 1999 RQ36 disruption mission. . . . .	119
5.10	Left: Orbit diagram of transfer trajectory from Earth to 1999 RQ36. Right: Speeds and angle between spacecraft and 1999 RQ36 at impact. . . . .	120
5.11	Relative error plot of GMAT, STK, and the ADRC's N-body code versus JPL's Sentry. . . . .	122
5.12	Selection of launch date and mission duration for 2011 AG5 rendezvous mission. . . . .	123
5.13	Left: Orbit diagram of transfer trajectory from Earth to 2011 AG5. Right: Speeds and angle between spacecraft and 2011 AG5 at arrival. . . . .	123
5.14	Selection of launch date and mission duration for 2011 AG5 disruption mission. . . . .	125

5.15	Left: Orbit diagram of transfer trajectory from Earth to 2011 AG5. Right: Speeds and angle between spacecraft and 2011 AG5 at impact. . . . .	125
6.1	Illustration of typical orbits of Atira, Apollo, Aten and Amor asteroids. . . . .	130
6.2	Velocity vector diagrams and impact approach angles for the Deep Impact and Don Quijote missions. . . . .	131
6.3	Total $\Delta V$ (km/s) contour plot for 1989 ML. . . . .	132
6.4	Minimum $\Delta V$ required versus launch date for 2003 GA. . . . .	134
6.5	Minimum $\Delta V$ required versus launch date for 2006 SJ198. . . . .	135
6.6	Minimum $\Delta V$ required versus launch date for 2003 QC. . . . .	135
6.7	Minimum $\Delta V$ required versus launch date for 1989 ML. . . . .	136
6.8	Minimum $\Delta V$ plot for 2003 GA using the universal variables method. . . . .	136
6.9	Mission trajectory to 1998 SB15 for the 5/5/2017 launch date. . . . .	139
6.10	Mission trajectory to 2006 SJ198 for the 3/17/2015 launch date. . . . .	140
6.11	Mission trajectory to 1989 ML for the 11/17/2018 launch date. . . . .	141
7.1	Comparisons of stable, escaping, and impacting orbits around 433 Eros. The coordinate system is an inertial frame fixed at Eros' center of mass with the positive Z-axis along the north pole spin axis. Eros is shown at initial conditions. . . . .	153
7.2	Illustration of the facet normal and edge-normal vectors. . . . .	155
7.3	Illustration of the spherical coordinate system with respect to the body-fixed frame. . . . .	156
7.4	Transfer orbit trajectories. . . . .	164
7.5	Transfer orbit acceleration histories. . . . .	164
7.6	Performance index comparison. . . . .	165
7.7	A 35-km prograde orbit in the XY-plane with PD control (top) and disturbance-accommodating control (bottom). . . . .	166
7.8	35-km prograde orbit control acceleration histories with simple PD control. Polyhedron model on the left and the harmonics model on the right. . . . .	167
7.9	FFT plots of the PD control inputs for a 35-km prograde orbit. Polyhedron model on the left and the harmonics model on the right. . . . .	168
7.10	35-km prograde orbit control acceleration histories with disturbance accommodating control. Polyhedron model on the left and the harmonics model on the right. . . . .	169
7.11	FFT plots of the disturbance accommodating control inputs for a 35-km prograde orbit. Polyhedron model on the left and the harmonics model on the right. . . . .	170
7.12	A 35-km prograde orbit in the XY-plane with PD control (top) and disturbance-accommodating control (bottom). . . . .	171
7.13	Inclined orbit control acceleration histories with PD control. . . . .	172
7.14	FFT plots of the PD control inputs for the inclined orbit. . . . .	173
7.15	Inclined orbit control acceleration histories with disturbance-accommodating control. . . . .	174
7.16	FFT plots of the disturbance-accommodating control inputs for the inclined orbits. . . . .	175
7.17	Trajectory and acceleration history, ZEM/ZEV-z. . . . .	175
7.18	Trajectory and acceleration history, ZEM/ZEV-g. . . . .	176
7.19	Trajectory and acceleration history, ZEM/ZEV-p. . . . .	176
7.20	Performance index comparison. . . . .	177

# List of Tables

1.1	Orbital and physical characteristics of target asteroids for a HAIV flight validation mission (to be further investigated for Task 3 of Phase II).	26
2.1	HAIV Imaging sensor package properties.	40
2.2	List of materials and their properties considered for a thermal shield.	42
2.3	DOB based on thickness parameter and shield geometry.	45
2.4	Peak power budget of each subsystem of the HAIV in various operational modes.	47
2.5	Mass breakdown for a baseline primary HAIV using Delta IV M+ launch vehicle class.	48
3.1	Parameters for Tillotson equation of state in core material.	56
3.2	Hardware description for benchmark comparisons	71
4.1	Initial conditions.	95
4.2	Performance comparison of classical feedback guidance laws.	96
5.1	List of NEOs selected for planetary defense technology demonstration missions [8].	110
5.2	List of pre-determined asteroids available for study in the AMiDST [3].	112
5.3	Preferred launch vehicles to be used for PDT demonstration missions and estimated mission costs for 300 kg NED/1000 kg NED/1500 kg NED HAIV spacecraft.	114
5.4	Orbital elements at Epoch 2456000.5 (March 14, 2012) of asteroid 1999 RQ36 [9].	115
5.5	Orbital elements at Epoch 2456200.5 (Sept. 20, 2012) of asteroid 2011 AG5 [9].	117
5.6	Spacecraft and mission types for asteroids 1999 RQ36 and 2011 AG5.	119
5.7	Mission design parameters for intercept with Asteroid 1999 RQ36.	121
5.8	Mission design parameters for rendezvous with Asteroid 2011 AG5.	124
5.9	Mission design parameters for intercept with Asteroid 2011 AG5 [17].	126
6.1	Target selection criteria for the Don Quijote mission.	129
6.2	Properties of candidate targets considered for the Don Quijote mission.	129
6.3	Target selection criteria.	131
6.4	Estimated performance capabilities for various mission configurations.	132
6.5	Optimal targets with corresponding minimum total $\Delta V$ , launch date, and mission duration.	133
6.6	Orbital and physical characteristics of target asteroids.	133
6.7	Early launch windows.	137
6.8	Late launch windows.	137
6.9	Categorization of target asteroids based on launch vehicle capabilities and target size.	138
6.10	Orbital parameters of transfer trajectories and burn magnitudes.	139
6.11	Computer Information for the Workstations Used to Run Programs.	141
6.12	List of mission requirements.	142
6.13	Break down of mission critical elements for the 3 mission types.	143
6.14	Top 10 Asteroids for Type 1 missions.	147
6.15	Top 10 asteroids for type 2 missions.	148

6.16 Top 10 asteroids for Type 3 Missions . . . . .	150
6.17 Top 10 asteroids sorted by required spacecraft $\Delta V$ . . . . .	151

# Chapter 1

## Executive Summary

### 1.1 Introduction and Summary

The complex problem of protecting the Earth from the possibility of a catastrophic impact by a hazardous near-Earth object (NEO) has been recently reassessed in [1]. In a letter on NEOs from the White House Office of Science and Technology Policy (OSTP) to the U.S. Senate and Congress in 2010, the White House OSTP strongly recommended that NASA take the lead in conducting research activities for NEO detection, characterization, and deflection technologies. Furthermore, President Obama's new National Space Policy specifically directs NASA to "pursue capabilities, in cooperation with other departments, agencies, and commercial partners, to detect, track, catalog, and characterize NEOs to reduce the risk of harm to humans from an unexpected impact on our planet." The Planetary Defense Task Force of the NASA Advisory Council also recommended that the NASA Office of the Chief Technologist (OCT) begin efforts to investigate asteroid deflection techniques.

*With national interest growing in the United States, the NEO threat detection and mitigation problem was recently identified as one of NASA's Space Technology Grand Challenges. An innovative solution to NASA's NEO Impact Threat Mitigation Grand Challenge problem was developed through a NIAC Phase I study (9/16/11 - 9/15/12), and it will be further investigated for a NIAC Phase II study (9/10/12 - 9/9/14).*

Various NEO deflection technologies, including nuclear explosions, kinetic impactors, and slow-pull gravity tractors, have been proposed and examined during the past two decades [1]. Still, there is no consensus on how to reliably deflect or disrupt hazardous NEOs in a timely manner. It is expected that the most probable mission scenarios will have a mission lead time much shorter than 10 years, so the use of nuclear explosives becomes the most feasible method for planetary defense [1]. Direct intercept missions with a short warning time will result in arrival closing velocities of 10-30 km/s with respect to the target asteroid. Given such a large arrival  $\Delta V$  requirement, a rendezvous mission to the target asteroid is infeasible with existing launch vehicles. Furthermore, state-of-the-art penetrating subsurface nuclear explosion technology limits the penetrator's impact velocity to less than approximately 300 m/s because higher impact velocities prematurely destroy the nuclear fuzing mechanisms [2]. Therefore, significant advances in hypervelocity nuclear interceptor/penetrator technology must be achieved to enable a last-minute nuclear disruption mission with intercept velocities as high as 30 km/s. Consequently, a HAIV mission architecture (Figure 1.1), which blends a hypervelocity kinetic impactor with a subsurface nuclear explosion for optimal fragmentation and dispersion of hazardous NEOs, has been developed through a Phase I study, and it will be further developed and validated through a Phase II study.

Despite the uncertainties inherent to the nuclear disruption approach, disruption can become an effective strategy if most fragments disperse at speeds in excess of the escape velocity of an asteroid, so that a very small number of fragments impacts the Earth. Thus, the proposed HAIV system will become essential for reliably mitigating the most probable impact threat: NEOs with warning times shorter than 10 years. It offers a potential breakthrough or great leap in mission capabilities for mitigating the impact threat from 1-km

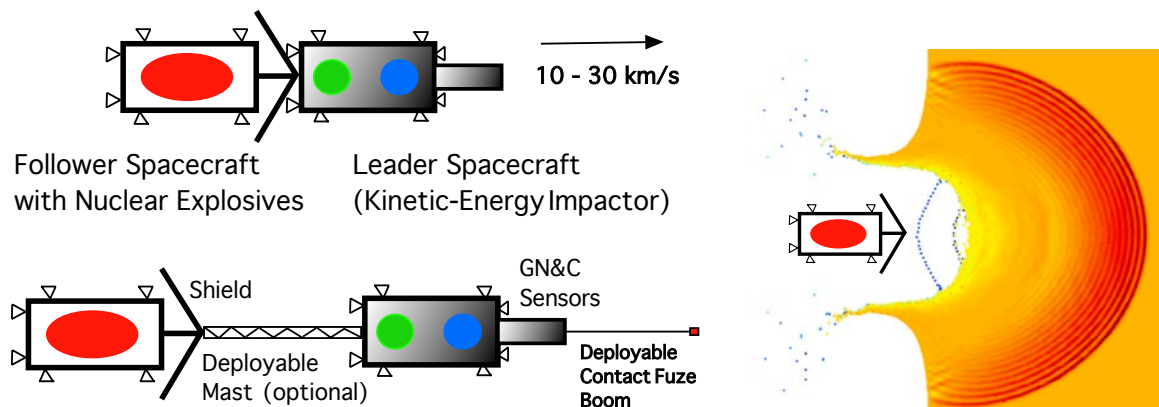


Figure 1.1: A hypervelocity asteroid intercept vehicle (HAIV) system/mission concept [3].

(diameter) class NEOs by using an existing launch vehicle. *Through a Phase II study, we will further develop the HAIV mission architecture, explore its flight validation mission option, and explore its potential infusion options within NASA and beyond.*

As illustrated in Figure 1.1, the proposed HAIV system consists of a fore body (a leader spacecraft) to provide proper kinetic-energy impact crater conditions for an aft body (a follower spacecraft) carrying a nuclear explosive device (NED). The proposed concept exploits the inherent effectiveness of a subsurface nuclear explosion for NEO disruption (fragmentation and dispersion). It is known that a generic 300-kt nuclear explosion at 3-m depth of burst has the ground-shock-coupling enhancement factor of approximately 20, which is equivalent to a contact burst of approximately 6-Mt [2]. However, the proposed system's complexity and reliability versus its major benefit of being 20 times more effective than a simpler and more robust contact burst needs to be further investigated in a Phase II study. *Thus, the primary objective of the Phase II study is to further explore major feasibility issues associated with performance robustness/sensitivity, mission reliability, system/mission complexity vs. benefits, development time and cost, and infusion options within NASA of the proposed innovative yet technically credible solution to NASA's NEO Impact Threat Mitigation Grand Challenge.*

A unique approach in our Phase II study is to collaborate with the IDC (Integrated Design Center) of NASA Goddard Space Flight Center (GSFC). The IDC is a unique facility at GSFC that brings engineers and customers together to conduct rapid space flight system and mission concept design studies. Though established to support GSFC's new business development, IDC customers have also included teams of scientists, engineers and managers from other NASA Centers and Headquarters, other U.S. government agencies and foreign entities, academic institutions, and commercial companies. The IDC at NASA GSFC will rigorously evaluate the technical feasibility and practical effectiveness of the HAIV system/mission concept. Expanding on IDC's technical assessment of the proposed HAIV concept, our Phase II study team will continue to develop, evaluate, and refine the HAIV-based mission architecture and the associated flight validation mission planning.

It is emphasized that NASA's Deep Impact mission, successfully accomplished in 2005, has validated some basic capabilities of a kinetic impactor for a large, 5-km target body at an impact speed of 10 km/s in very favorable lighting conditions. Precision impact targeting of a smaller, 100-300 m target with an impact speed of 30 km/s in worst-case circumstances is a technically challenging problem.

*The goals of the Phase II study are to improve the HAIV technology from TRL 1-2 to TRL 3, to identify the key enabling technologies required for the HAIV system, and to provide NASA with a 10-year technology roadmap for NASA's NEO Impact Threat Mitigation Grand Challenge. The roadmap will include a near-term flight demonstration mission architecture and a cost estimate for flight-validating the HAIV-based planetary defense technology (but without carrying actual nuclear explosives). Thus, the Phase II study will enable the HAIV technology as the most efficient, cost effective, and reliable option for mitigating the most probable*



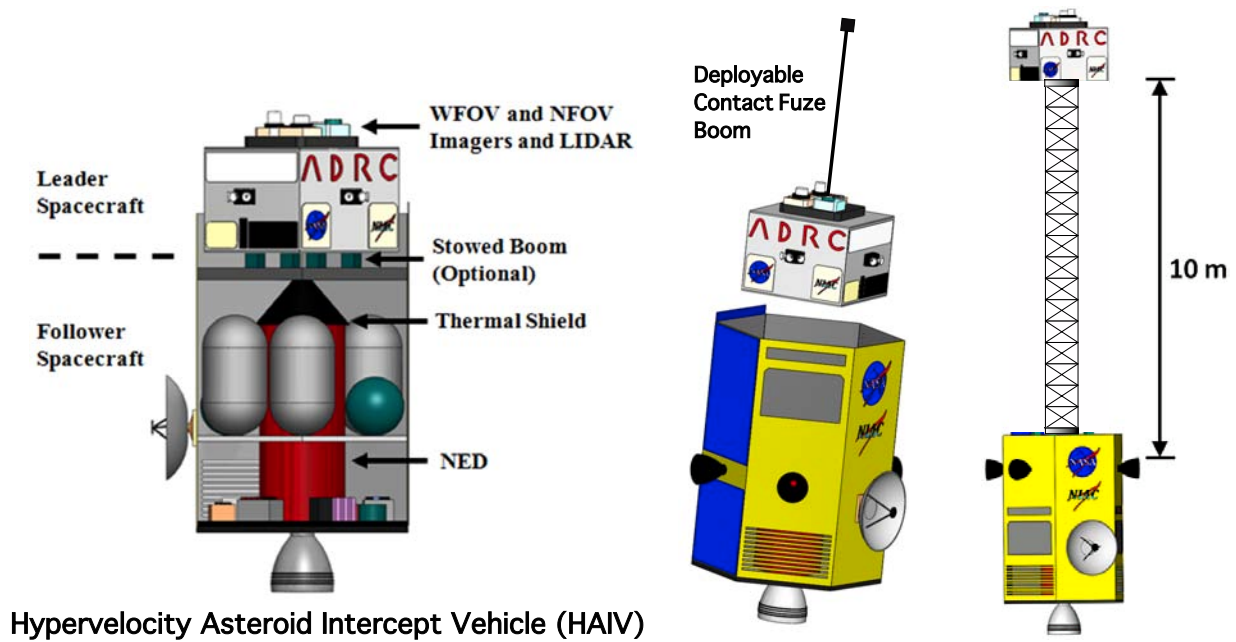


Figure 1.2: HAIV configuration options (Task 1).

*impact threat of a hazardous NEO with a short warning time. Practical implementation of the proposed HAIV technology will require at least 10 years of further analysis, design, space flight validation testing, and refinement. Now is the time to initiate such preparation.*

## 1.2 Summary of Phase I Study Results

The Phase I study consisted of two main tasks:

- Task 1: Conceptual design of a baseline HAIV system and mission architecture
- Task 2: Computational validation of the HAIV concept for optimal fragmentation and dispersion

Both tasks have been successfully completed, and the Phase I study results are summarized in Figures 1.2 through 1.6. Three technical papers on the proposed HAIV technology concept have been accepted for publication in peer-reviewed journals [3-5]. Several technical papers on the proposed HAIV technology and mission concepts were presented at the following conferences [6-11]:

- AAS/AIAA *Space Flight Mechanics Meeting*, Charleston, SC, January 2012.
- IAF/AIAA *Global Space Exploration Conference*, Washington, D.C., May 2012.
- AIAA/AAS *Astrodynamics Specialist Conference*, Minneapolis, MN, August 2012.

### 1.2.1 Task 1 Study Result Summary

A baseline HAIV system and mission concept, illustrated in Figures 1.1-1.3, have been successfully developed for Task 1 of the Phase I study, as evidenced in [3-11].

A nuclear deflection/disruption mission employs nuclear explosive devices (NEDs) in three different ways. A nuclear standoff explosion is a burst from predetermined height and is often considered as the least disruptive approach among the nuclear options. A second nuclear option exploits a contact burst on the NEO's surface. The most efficient nuclear option involves a subsurface explosion. The subsurface explosion,

## Hypervelocity Asteroid Intercept Vehicle (HAIV) Mission Architecture

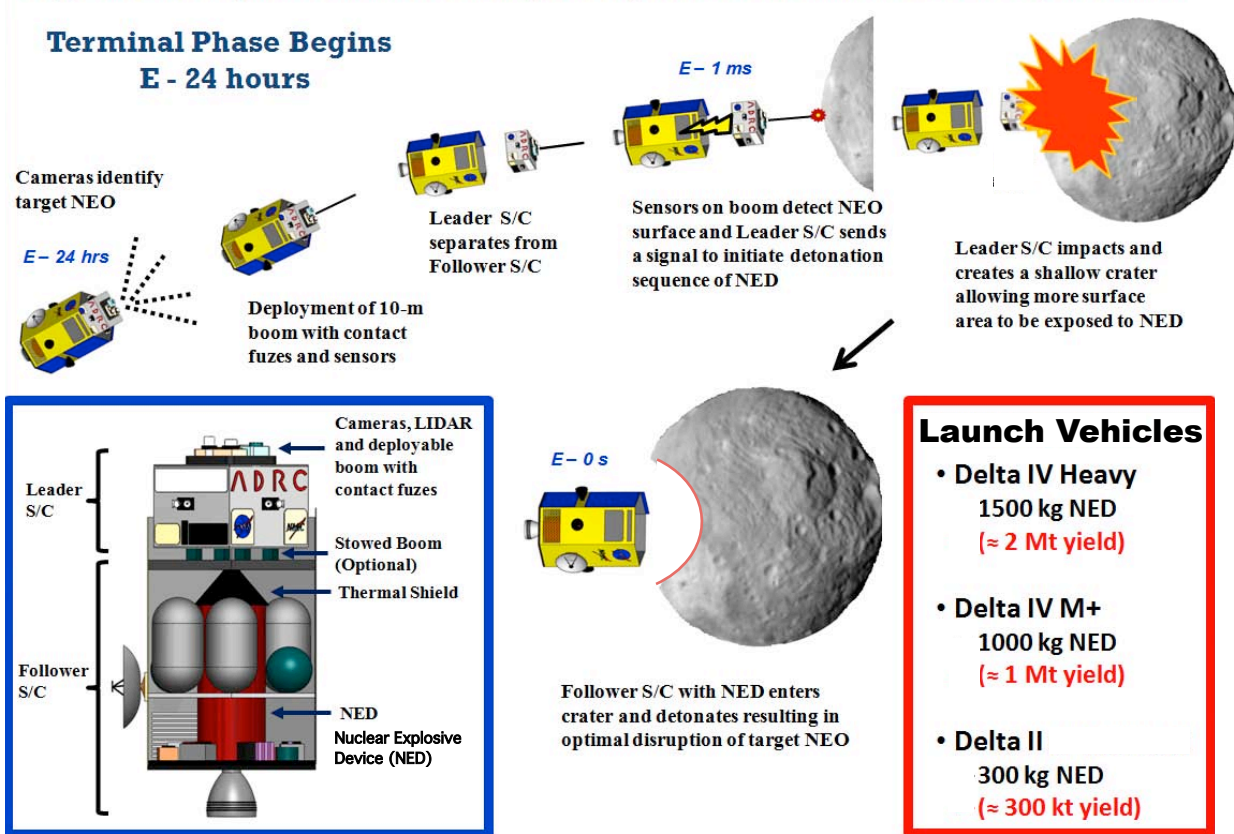


Figure 1.3: A baseline HAIV and its terminal-phase operational concept (Task 1).

even with a shallow burial ( $< 5$  m), delivers a large amount of energy that can totally destroy the target NEO, and is known to be at least 20 times more disruptive than the contact burst.

The NED payloads are categorized into three classes as:

- a 300-kg NED with an approximate yield of 300 kt
- a 1,000-kg NED with an approximate yield of 1 Mt
- a 1,500-kg NED with an approximate yield of 2 Mt

For Task 1 of the Phase I study, a baseline HAIV system has been developed to accommodate the technically challenging problem of a penetrating subsurface nuclear explosion approach. A baseline HAIV consists of a leader spacecraft (kinetic impactor) and a follower spacecraft carrying an NED for the most effective disruption of a target NEO. The leader spacecraft impacts first and creates a shallow crater in the NEO. Then the follower spacecraft enters the crater and detonates the NED. This baseline HAIV mission concept is illustrated in Figure 1.3. The terminal phase starts 24 hours before the impact event. Instruments located on the leader spacecraft detect the target NEO and the subsystems on-board the HAIV become active. Separation occurs between the leader spacecraft and the follower spacecraft and communication is established between the two. Measurements continue through optical cameras and laser radars located on the leader spacecraft and an intercept location is identified on the asteroid body. The high-resolution optical cameras provide successive images of the NEO to each flight computer for precision guidance and navigation. The computer then uses these calculations to compute the necessary adjustments and instructs a guidance and control system to execute a few trajectory correction maneuvers (TCMs). As the distance between the follower spacecraft and NEO becomes smaller, the fuzing system starts, arming the NED payload.

The nuclear fuzing mechanism is initiated by the instruments and the guidance parameters provided by

the leader spacecraft (time-to-go, range distance, and range rate). For the subsurface disruption technique, the timing fuze and proximity or radar fuze need to be properly armed prior to the final detonation. The NED is armed prior to the last few seconds of the impact event. A shallow crater is then created as the leader spacecraft impacts the target NEO. Hot ejecta and debris particles result as the leader spacecraft is destroyed during the hypervelocity impact. The follower spacecraft is equipped with a thermally resistant debris shield that protects the NED and the triggering system. The shield deforms and melts as it passes through the hot plasma ejecta and the NED detonates before striking the bottom of the shallow crater. In the case that the NED does not detonate as planned, back-up fuzes are used to detonate the NED payload. The accuracy and measurement rates of the instruments, flight computer, and fuzing system are key to a successful disruption mission.

Partitioning options between the leader and follower spacecraft to ensure the follower spacecraft enters the crater opening safely were also considered for Task 1. The primary option uses no mechanical connection between the two spacecraft. This separated/fractionated configuration depends on the accuracy and measurement rates of the instruments, communication, flight computer, and guidance and tracking algorithms to carry out the terminal phase. Another option includes the use of a deployable mast between the two spacecraft. Figure 1.2 shows these optional configurations. As the mast is deployed and separation distance increases, the center of mass moves from the center towards the front of the follower spacecraft. This new configuration is still treated as a single body but achieves a two-body arrangement. Divert thrusters are pre-positioned at the expected new center of mass location to control the new system as a single body. These large divert thrusters can be gimballed to achieve the desirable thrust directions. This configuration reduces mission complexity and operations, but is limited to the length of the boom, and further detailed tradeoffs are needed in the proposed Phase II study.

The HAIV concept results in large thermal and structural loads on the NED before detonation. The NED and the triggering system needs to be protected to effectively execute the subsurface explosion. Using an in-house hydrodynamics code, simulations of the NED are performed and the thermal and structural loads are found. Based on the results of the simulations, a protection system is chosen and configured. Detailed technical descriptions of the Task 1 study results are presented in Chapter 2. More detailed studies on thermal protection of NEDs are to be conducted in the Phase II study.

## **1.2.2 Task 2 Study Result Summary**

While Task 1 was concerned with the systems engineering aspects of the HAIV system and mission design, Task 2 was concerned mainly with the computational validation of the innovative concept of blending a hypervelocity kinetic impactor with a subsurface nuclear explosion for optimal fragmentation and dispersion of NEOs.

Figure 1.4 shows some preliminary results for simplified 2-D modeling and simulation of a hypervelocity kinetic impact followed by a subsurface nuclear explosion for an asymmetric target body. An example of an asymmetric target body considered in Task 2 of the Phase I study consists of a contact binary system with a rubble pile exterior. With binary systems comprising about 16% of the known NEO population, a kinetic impactor mission faces an approximately 1 in 6 chance that the target will be a binary system. This is a characteristic that will be unable to be predicted ahead of time without radar observation, in the case of systems with close secondaries. It has been suggested that many irregularly shaped asteroids with unusual spin states could be contact binary (or multiple) systems. These types of systems would exhibit some of the same characteristics as monolithic rocks and as rubble piles. Further, those asteroids identified as rubble piles could have large solid components beneath their regolith.

The two cores of a reference model shown in Figure 1.4 are elliptical, with major and minor axes of 50 and 30 meters, respectively. These cores are given material properties similar to granite using a linear elastic-plastic strength model, and are canted by 45 degrees relative to the horizontal. There is a vertical line of symmetry, so the cores are mirror images of one another. A rubble regolith extends 2 meters in depth

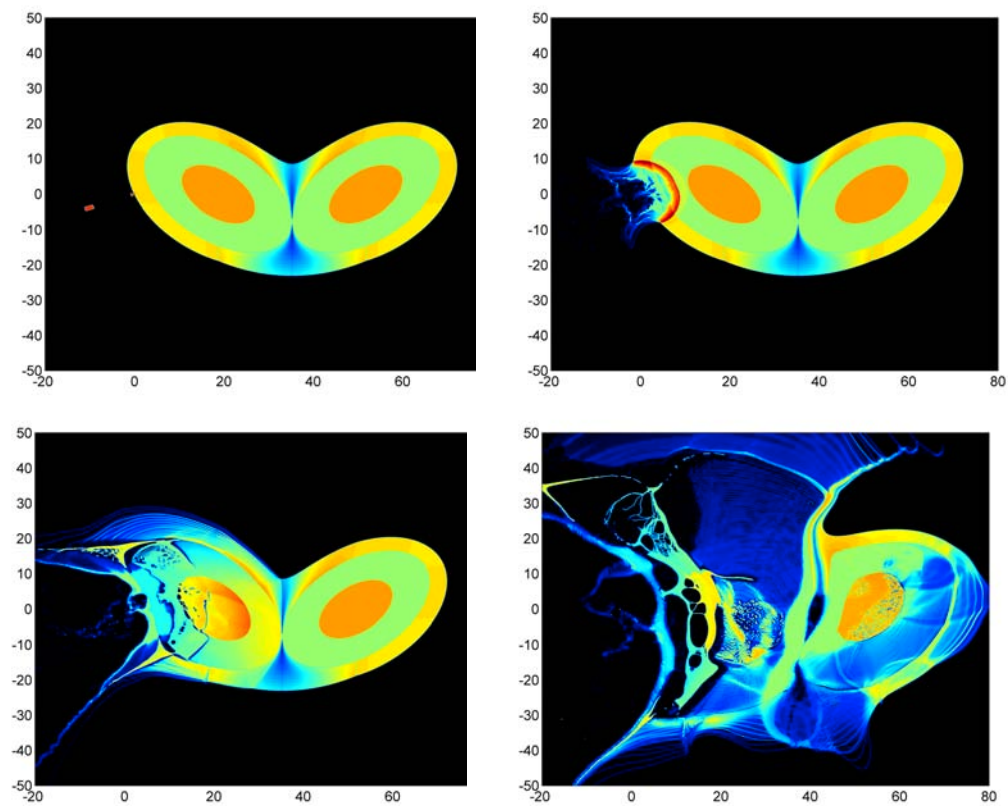
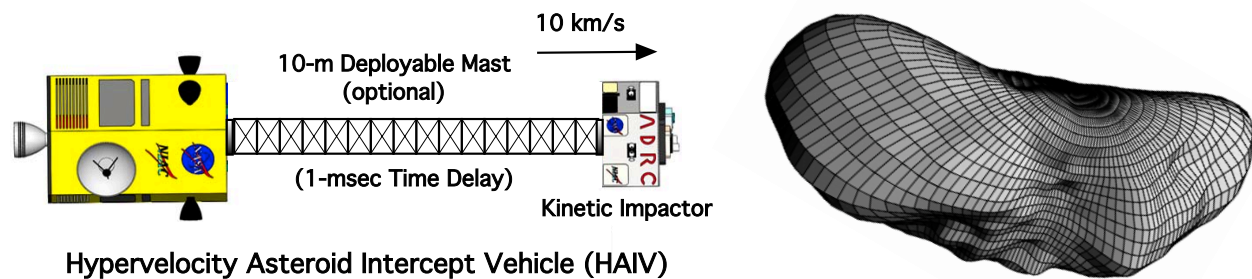


Figure 1.4: Simplified 2-D computational modeling and simulation of a penetrated, 70-kt nuclear explosion for a 70-m asymmetric reference target body (Task 2).

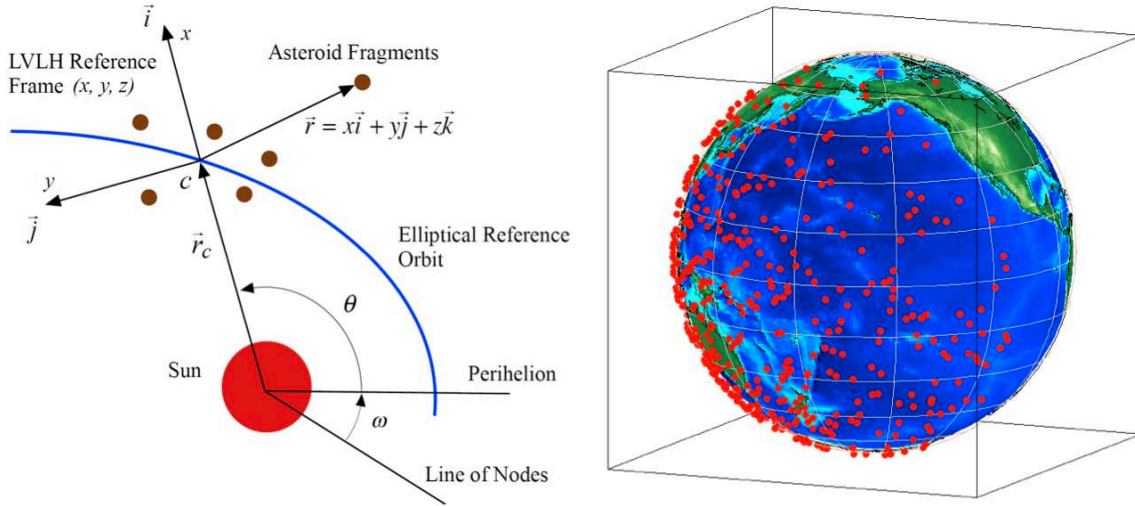


Figure 1.5: Orbital dispersion modeling and Earth-impact simulation of NEO fragments (Task 2).

vertically above each core, and is packed along lines of constant potential around the body, resulting in a maximum regolith depth of 14 meters. These properties result in exterior dimensions of the target being approximately  $76 \times 42$  meters. The inner half of each core has an initial bulk density of  $2630 \text{ kg/m}^3$ , while the outer portion of the core is more porous material with an average bulk density of  $1910 \text{ kg/m}^3$ . Both sections use values for yield strength between 7-203 MPa and shear modulus between 8-22 MPa. For the impactor portion of the mission, the Tillotson equation of state is used.

In our Smoothed Particle Hydrodynamic (SPH) model for brittle materials, the behavior of the core material under high stress is governed by the activation of implicit flaws. These flaws are seeded in the representation particles using a Weibull distribution with a coefficient of around  $4.2 \times 10^{23}$  and an exponent between 6.2-9.5. Using a range of distribution exponents and strength properties allows us to examine the behavior of the core material with varying brittleness and material cohesion. This turns out to be very important for this contact binary system, as strong core material absorbs energy from the disruption shock and can result in large remaining chunks of material. Smoothing lengths are chosen to allow for resolution of between 1 cm and 5 cm, which results in a hydrodynamic system of between 800,000 and 6,000,000 nodes. This system is scaled to be an ideal size for the GPU (Graphic Processing Unit) simulation programs developed at the Iowa State Asteroid Deflection Research Center, maximizing computational efficiency and minimizing simulation turnaround time. For a test case (Figure 1.4), we modeled a kinetic impactor of the two-body HAIV as an aluminum wedge 1 m in base diameter and 1.5 m in length. The nuclear payload follows, depositing 70 kilotons of energy upon reaching the initial impact site of the lead body. Most of this energy is absorbed in the crater region formed by the initial impact, though deeper absorption is allowed due to the fact that much of the material in this region has already been vaporized and superheated into a plasma state. The resulting shock wave has a peak compression of more than 2 times the initial density, and quickly overtakes the initial shock of the lead body impact, which is much weaker. This shock compresses much of one core far beyond the fracture strength of even the worst-case material, rebounding off the nearer side. This asymmetric behavior dissipates some energy due to interactions with the rebounding shock front. In the center area of deeper regolith, the seeding process naturally results in a much more porous material, absorbing energy from the shock. Upon reaching the second core at the far side, some large chunks escape the disruption process in some cases (even with lower material strengths).

*There remains a high risk for this target of single largest chunks on the order of tens of meters. However, this material is highly stressed due to velocity gradients, and may be ripped apart in further time. Further-*



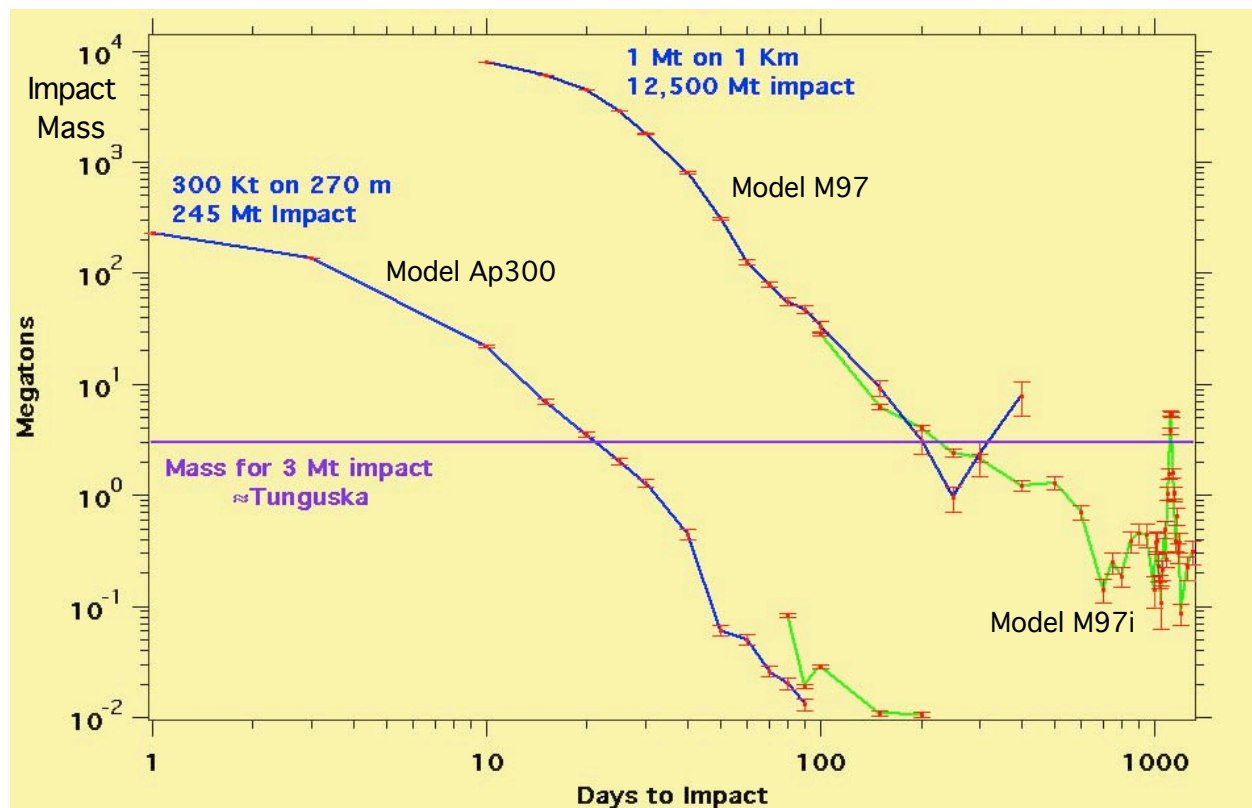


Figure 1.6: A summary of orbital dispersion analysis and Earth-impact simulation of NEO fragments (Task 2). Courtesy of Dr. David Dearborn at Lawrence Livermore National Laboratory.

more, these large chunks still have substantial velocities, of approximately 10-20 m/s, imparted from the blast, and have sufficient energy to disperse from the nominal impacting trajectory over tens of days.

A NEO approximately the size of the asteroid Apophis was also considered as a reference target asteroid for Task 2 of the Phase I study. The model asteroid has a total mass of  $2.058 \times 10^{13}$  kg with a diameter of 270 meters. An ideal nuclear subsurface explosion of this model has been simulated in a cylindrical region below the surface of the body by sourcing in energy corresponding to 300 kt. As illustrated in Figure 1.5, orbital dispersion and Earth-impact simulation studies of NEO fragments have been also conducted for Task 2 of the Phase I study. As can be noticed in Figure 1.6, the preliminary results for a 270-m model with 15 days before Earth-impact indicate that only 3% of the initial mass impacts the Earth even for such a very short time after intercept. The impact mass can be further reduced to 0.2% if the intercept direction is aligned along the inward or outward direction of the orbit, i.e., perpendicular to NEO's orbital flight direction. Such a sideways push is known to be optimal when a target NEO is in the last orbit before the impact. *Figure 1.6 also indicates that a large 1-km target will require a 1-Mt subsurface nuclear explosion with at least one-year mission lead time for sufficient orbital dispersion of its fragments.*

### 1.3 An Overview of Phase II Study

The proposed Phase II study (9/10/12 - 9/9/14) consists of four main tasks, as follows:

- Task 1: Detailed design evaluation of a baseline HAIV and its mission architecture
- Task 2: High-fidelity 3-D computational validation of optimal fragmentation and dispersion of NEOs

NIAC Phase II Tasks	Year 1 (9/10/12 - 9/9/13)	Year 2 (9/10/13 - 9/9/14)
Task 1: Detailed HAIV Design Evaluation	Task 1A	Task 1B
Task 2: 3-D Computational Validation	Task 2A	Task 2B
Task 3: Flight Demo Mission Design		Task 3
Task 4: HAIV Evaluation by IDC at GSFC	10/15/12 -10/19/12 (5-Day IDC Study at GSFC)	

Robotic and Human NEO Exploration Research Project Funded by NASA's Iowa Space Grant Consortium	Year 2 (5/16/12 - 5/15/13)	Year 3 (5/16/13 - 5/15/14)
	NEO Exploration Mission Architecture Design & Development	NEO Exploration/Mitigation Flight Demo Mission Design

Figure 1.7: Phase II project schedule (to be properly coordinated with a NEO exploration research project of the Asteroid Deflection Research Center).

- Task 3: Development and design of a HAIV flight validation mission architecture (in preparation for a Phase III program)
- Task 4: Five-Day IDC Study at NASA GSFC in support of Tasks 1 and 3

The overall schedule of these four tasks is illustrated in Figure 1.7.

### 1.3.1 Task 1 (9/10/12 - 9/9/14): Detailed Design Evaluation of a Hypervelocity Asteroid Intercept Vehicle (HAIV) and its Mission Architecture

As shown in Figure 1.7, Task 1 consists of two subtasks, as follows:

- Task 1A (Year 1): Detailed design evaluation of a baseline HAIV and its real mission concept
- Task 1B (Year 2): Design of a modified HAIV in support of Task 3 (flight demo mission design)

Task 1 of the Phase II study is to further investigate the major feasibility issues associated with performance robustness/sensitivity, mission reliability, system/mission complexity vs. benefits, development time and cost, and infusion path within NASA of the proposed innovative, yet technically credible, solution to NASA's NEO Impact Threat Mitigation Grand Challenge. Expanding on IDC's technical evaluation (Task 4) of the baseline HAIV system of the Phase I study, we will further develop and refine the HAIV system, focusing on the key enabling technologies as described below.

**Two-Body HAIV Configuration Design Tradeoffs.** The leader and the follower can be separated and connected by a deployable mast to ensure that the follower spacecraft, carrying an NED payload, follows the leader spacecraft safely and reliably. The deployable mast must be sufficiently rigid to avoid oscillatory motion of the two bodies. A deployable mechanism is preferable compared to a fixed structure due to volume constraints in the launch vehicle fairing.

A 10-m deployable mast to be employed by NASA's Nuclear Spectroscopic Telescope Array (NuSTAR) scientific satellite shown in Figure 1.8 will be evaluated in detail for the HAIV system. Essential to the NuSTAR satellite, successfully launched in June 2012 is a deployable mast which extends to 10 meters after

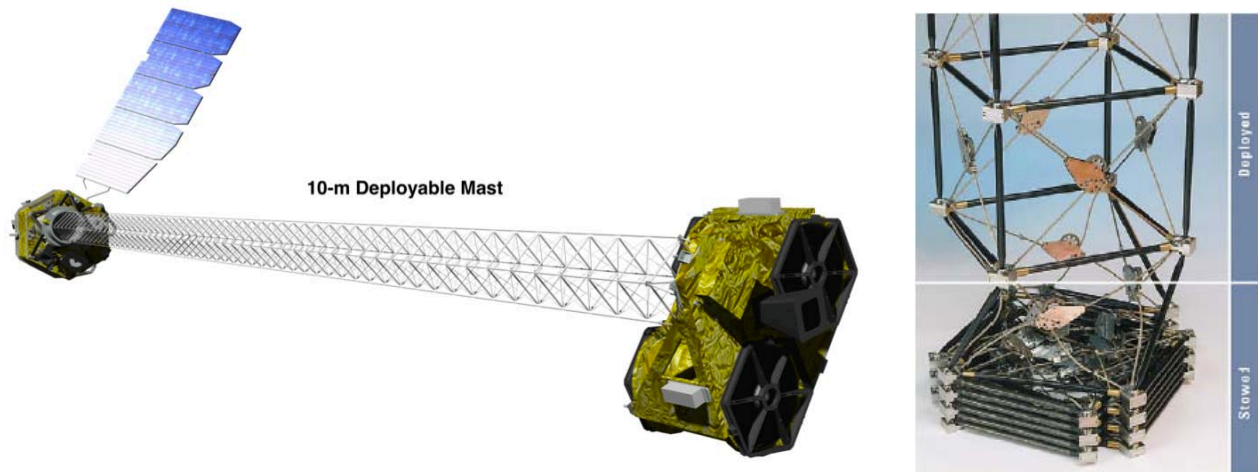


Figure 1.8: NASA's Nuclear Spectroscopic Telescope Array (NuSTAR) scientific satellite, employing ATK's 10-m deployable mast, successfully launched in June 2012. Image courtesy of NASA/JPL.

launch. This mast will separate the NuSTAR X-ray optics from the detectors, necessary to achieve the long focal length required by the optics design. The articulated mast, built by ATK-Goleta, is low-risk, low-weight, compact, and has significant flight heritage. It provides a stiff, stable, and reliable structure on which the optics are mounted. It is based on a design used to establish a 60-meter separation between the two antennae of the the Shuttle Radar Topography Mission (SRTM), which flew on the Space Shuttle Endeavor in February 2000 and made high-resolution elevation (topographic) maps of most of our planet. A hinged deployable mast consists of a hinged truss structure that is collapsible in storage and, when deployed, locks into place and is held firm. ATK, the manufacturer of such trusses, reports 12.4 m and 6.2 m length trusses, both with bending stiffness of  $1.5 \times 10^6 \text{ N}\cdot\text{m}^2$ , although mechanical properties are dependent on component materials. Depending on the materials of the components for the system, the mass cost of such a system could be high. Most such trusses are planned to be retractable which adds a level of complexity that is unnecessary for the HAIV application. ATK has manufactured many systems that have been tailored to specific mission requirements, and provides a favorable flight history.

*For Task 1, we will conduct detailed design tradeoffs of two-body HAIV configuration options (i.e., a precision formation flying, fractionated configuration vs. a separated configuration connected by a deployable mast) to determine the most reliable way of providing a proper separation distance or a proper time delay (e.g., approximately 1-2 milliseconds) between the leader spacecraft and the follower spacecraft.*

**Terminal-Phase Guidance Sensors/Algorithms.** *One of the key enabling technologies required for the HAIV-based mission architecture is terminal-phase guidance, navigation, and control (GNC) technology. NASA's Deep Impact mission, successfully accomplished in 2005, has validated some basic capabilities of a terminal-phase GNC system for a large, 5-km target body at an impact speed of 10 km/s in very favorable lighting conditions. Precision impact targeting of a smaller, 100-300 m target with an impact speed of 30 km/s in worst-case circumstances is a technically challenging problem, which must be further investigated in the proposed Phase II study.*

A baseline terminal-phase GNC system to be further developed and refined in the Phase II study is briefly described here. A baseline HAIV system requires optical cameras, radar altimeters, and Light Detection and Ranging (LIDAR) on the leader spacecraft to accurately identify and track the target NEO and initiate fuzing for the NED. The leader spacecraft uses a Medium Resolution Instrument (MRI) or Wide Field of View (WFOV) Imager as used on the Deep Impact flyby spacecraft. The WFOV Imager is used to locate the target NEO at the start of the terminal phase. It is a small telescope with a diameter of 12 cm which takes



images at a scale of 10 m/pixel in a spectrum of approximately 700 nm. The field of view of the WFOV Imager is approximately 10 deg x 10 deg which allows it to observe more stars and serve as a better navigator for the HAIV during its coasting phase. As soon as possible after acquisition of the target NEO, the WFOV Imager passes information to the High Resolution Instrument (HRI) or Narrow Field of View (NFOV) Imager, which has a field of view of 2.3 deg x 2.3 deg. It is comprised of a 30-cm diameter telescope that delivers light to both an infrared spectrometer and a multispectral camera. The camera has the ability to image the NEO with a scale less than 2 m/pixel when the spacecraft is approximately 700 km away. The Imagers are located on the leading front of the impactor spacecraft. These Imagers are similar to the instruments used on the Deep Impact Mission Flyby and Impactor spacecraft. LIDAR or laser radar measures back-scattered light from a high intensity, short duration output pulse transmitted at the target NEO. It is used in the closing minutes of the terminal phase to calculate the range to the NEO. This information is shared with the fuzing device for detonation of the NED. The LIDAR requires sufficient power to operate over a range equivalent to approximately the last minutes of the terminal phase. It would be similar to the ones used on the NEAR and Clementine missions. The LIDAR has a mass of 20 kg and an estimated power consumption of 50 W. Radar altimeters using radio waves are used in conjunction with LIDAR.

*All of these critical GNC system hardware issues as well as terminal-phase guidance algorithms for achieving a precision targeting accuracy of 10-30 m ( $3\sigma$ ), which is an order of magnitude better than the 300-m ( $3\sigma$ ) targeting accuracy of NASA's Deep Impact mission, will be further studied for Task 1 of the Phase II study.*

**Thermal Protection and Shield of the Follower Spacecraft Carrying an NED.** An in-house hydrodynamics code, which is being developed at the Asteroid Deflection Research Center to accurately study the effects of nuclear disruption missions, is used to estimate the thermal and structural limits experienced by the two-body HAIV. The hydrodynamic code helps to establish a shield design and configuration on the follower spacecraft. Several different geometries include a flat cylindrical plate, conical shape, spherical cap, and an ogive nose cone.

Due to long simulation turnaround times inherent to the use of any hydrocode for testing different shield designs and material properties, a single simulation of the impact event can be used. The simulation starts with a spherical leader spacecraft impacting an asteroid modeled with the strength properties of granite. The leader spacecraft, traveling at approximately 10 km/s, is vaporized at impact. Approximately 1 millisecond later, the follower spacecraft impacts the same location as the leader. The energy experienced by the follower spacecraft is recorded and the simulation is saved. The simulation variables are then used in a MATLAB simulation code to observe energy interactions for given shield geometries. Once the MATLAB shield test concludes specific geometries, the hydrocode simulation tests shield geometry, material properties, and shield thickness. Dissipating energy from the shield is not considered at this time but will be included in the Phase II study.

Based on this initial study, a few conclusions can be drawn for the design of the NED payload thermal shield. First, the primary variables in achievable depth-of-burst (DOB) are the shape, mass, and timing of the leader spacecraft. Additional analysis must be done to optimize this portion of the mission. Second, given a particular environment, a discontinuous shock to the payload presents challenges in determining how far to allow penetration before detonation. The payload cannot survive a direct impact at this speed, so it must be triggered using a combination of sensor and optical data at an appropriate data rate. Third, the geometry of the shield seems to present a greater influence on DOB than any other variable. Adding thickness to the thermal shield in excess of the minimums presented does not result in further penetration, since both shields experience high structural loads at the maximum DOB. Finally, these results appear to be independent of the materials tested, as the limiting factor is the acceptable structural loads on the payload. However, significant mass can be saved by utilizing lighter alloys or materials for the thermal shield, which needs a further detailed study.

**Nuclear Fuzing Mechanisms.** *Although the proposed study considers the nuclear explosive device (NED) simply as a black-box payload to be delivered safely and reliably to a target asteroid, the NED triggering system is an integral part of the HAIV system and is one of the key enabling technologies required for the HAIV. In general, a standard fuzing mechanism ensures optimum NED effectiveness by detecting that the desired conditions for its detonation have been met, and providing an appropriate command signal to the firing set to initiate nuclear detonation. Fuzing generally involves devices to detect the location of the NED with respect to the target, signal processing and logic, and an output circuit to initiate firing. Without the proper selection of a reliable triggering or fuzing mechanism, there is a high risk that the mission can be unsuccessful. Current terrestrial triggering systems such as salvage fuzes, timing, contact, and radar (proximity) fuzes will be further examined for the HAIV. These fuzes act on the instantaneous time scale of approximately 1 milliseconds.*

The salvage fuze acts as a contingency fuze which is employed as a failsafe detonation. The fuze “salvages” the NED and explodes when all other fuzes fail. The salvage fuze serves as a countermeasure to a terminal defense interceptor system and initiates after a detected collision possibility. The NED then explodes as soon as a target comes within a certain range of the NED. Sometimes radar and contact fuzes operate as the failsafe triggers and must function after withstanding extreme deceleration forces and delivery vehicle deformation. In an asteroid intercept scenario, the salvage fuze comprised of several contact and radar fuzes becomes activated. The contact and radar fuzes provide one option for arming and detonating the NED.

Another option for triggering the NED is a timing fuze. The timing fuze operates by using time-to-go, estimated intercept distance, and the rate of the intercept distance. This information is provided to the triggering mechanism by the GNC instruments and flight computer. The computer activates the timing fuze once the guidance parameters meet specific conditions. The timing fuze is the most appropriate as the entire terminal-phase GNC process will be autonomous. However, if the timing fuze proves to be inaccurate, the salvage fuzes (contact and radar fuzes) can restore the arming mechanism of the NED. A salvage fuze is always present to resume the arming of the NED in any such triggering problems.

Proper fuzing systems and operations need to be further investigated in the Phase II study. For a standoff burst disruption mission, radar acts as part of the primary fuzing system. For the subsurface or contact burst option, timing and radar fuzes may represent part of the primary detonation system, and contact fuzes are used as a failsafe detonation. The selection and sequencing of these fuzing options are chosen autonomously and are not dependent on additional hardware or configurations. Contact and radar fuzes can be located on top (front) of the follower spacecraft and in the thermal shield. However, the timing fuze and NED remain protected by the thermal shield.

*It is important to note that such nuclear fuzing mechanisms have never been designed and tested to be used in space. Thus, Task 1 of the Phase II study will establish a solid foundation of the technology development roadmap for such a critical enabling technology. One of the key enabling technologies is to flight validate sensors and electronics for fuzing mechanisms capable of handling a 10-30 km/s intercept.*

### **1.3.2 Task 2 (9/10/12 - 9/9/14): High-Fidelity 3-D Computational Validation of Optimal Fragmentation and Dispersion of NEOs**

As shown in Figure 1.7, Task 2 consists of two subtasks, as follows:

- Task 2A (Year 1): 3-D modeling & simulation for optimal fragmentation and dispersion of NEOs
- Task 2B (Year 2): Computational study in support of Task 3 (flight demo mission design)

Task 2 is mainly concerned with advanced physical modeling and simulation of NEO fragmentation and orbital dispersion, in support of HAIV system development and design. The HAIV’s fore body impacts the asteroid surface first, creating a large crater, followed by the aft body carrying nuclear explosives, which penetrates to a depth of several meters. Task 2 will refine the “static” nuclear blast models used in [4-5] to assess the overall mission robustness in employing such impulsive, high-energy nuclear subsurface explosions in the face of various physical modeling uncertainties, especially those caused by the initial kinetic-energy

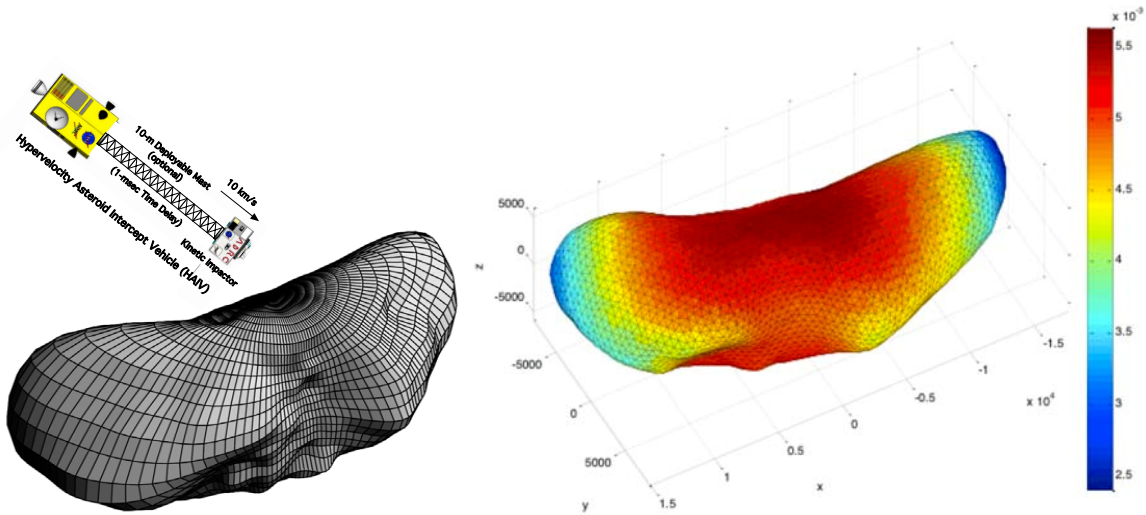


Figure 1.9: A realistic NEO target model for the 3-D computational validation of optimal fragmentation and dispersion (Task 2 of Phase II). Image courtesy of NASA for a reference shape model of asteroid Eros.

impact crater conditions created by the fore body kinetic impactor. *Modeling and simulation of this type of complex multi-phase physics problem has never been discussed in the open literature. The objective of Task 2 is to computationally validate the overall effectiveness and robustness of the proposed two-body HAIV system.*

**3-D Modeling and Simulation.** Initial simulations in [4-5] used a spherical axisymmetric NEO model, with the key limitations being the size of the target and a lack of a range of source energy input. With a new computational approach to the hydrodynamic simulations, we efficiently compute results for a 3D shape of the target asteroid (Figure 1.9). This will allow us to address much larger targets with increased resolution and a faster turnaround time, so the influence of more parameters can be investigated. A nonlinear orbit solver calculates an impacting trajectory given boundaries of the (a, e, i) sampling space. This approach increases our understanding of what components of the interplanetary environment affect the likelihood of a NEO being on a collision path with the Earth. Dispersion along these orbits is computed to determine mission effectiveness for a variety of possible cases. New high-throughput neighbor-finding methods are suggested for the particle representation of disrupted NEOs. This approach becomes more effective using the GPU acceleration technology of the current simulation toolkit. In contrast to the Weibull distribution used to seed implicit flaws in brittle materials [4-5], the current simulation set develops a tensor relationship for material characteristics and orientation. This allows for more realistic size and shape generation for NEO fragments by treating damage as a local quantity (cracks) rather than a distributed state variable. One of the key limitations is that most proposed neighbor-finding methods for interpolation rely on complex logic and lists not suitable for efficient GPU implementation. Therefore, the addition of the third dimension makes this problem far more complex. A new approach for efficiently computing unions and intersections of integer sets on the GPU will be used for Task 2, allowing for neighbor-finding as an update process from previously computed relative relationships. We hope to maintain superlinear scaling of the neighbor computation with problem size, while adapting to fit the limitations of the computational architecture. GPU acceleration of this model is up to 400x on a single workstation, continuing a trend of increasing computational complexity while also increasing efficiency. This approach allows us to compute a range of values rather than monolithic single simulations, and is incredibly important for orbital analysis. Sensitivity to the orbital parameters is a true unknown, since large impacting NEOs have yet to be observed, so computation for a range of these values is a necessity. Previous work [4-5] showed that a large amount of data can be processed using GPU simulation. Initial work was focused mostly on prediction of relative impacting mass, but disruption at different times along a given orbit can have a large effect on the resulting shape of debris. The proposed approach looks

at the fragmentation model to better address how uncertainty in the NEO breakup affects orbital prediction, particularly in the case of variable time-to-impact. This allows for a more clear set of objectives for mission design. Another new result is the availability of representative 3D fragment distributions for non-spherical bodies. This will improve the trajectory of the desired hypervelocity intercept mission by allowing full degrees of freedom in choosing the approach asymptote.

*For Task 2, we will further develop and refine high-fidelity nuclear fragmentation models including the dynamical effect of hypervelocity impact crater condition uncertainties, caused by the fore body kinetic impactor, on the dispersal velocity distribution and the size of each fragment, to develop optimal intercept/impact strategies for robust fragmentation and dispersion.*

**Parametric Characterization of Modeling Uncertainties.** Space missions to deflect or disrupt a hazardous NEO will require accurate prediction of its orbital trajectory, both before and after a deflection/disruption event. Understanding the inherent sensitivity of mission success to *the uncertainties in the orbital elements and material properties of a target NEO* will lead to a more robust mission design, in addition to identifying the required precision for observation, tracking, and characterization of a target NEO. The unique technical challenges posed by NEO deflection/disruption dictate the level of precision needed in the physical modeling of hazardous NEOs and the identification of relevant parameters through computational/analytical/experimental studies, remote observation, and/or characterization missions. Consequently, uncertainty modeling and parametric characterization are of current interest to the planetary defense community. The current study at the ADRC also focuses on the parametric characterization of various physical modeling uncertainties, especially for nuclear deflection/disruption missions. Because the required degree of physical modeling accuracy strongly depends on the specific mitigation mission type, the current study at the ADRC emphasizes parametric characterization of physical modeling uncertainties and their resulting orbital perturbation effects on the outcome of various nuclear deflection/disruption options, such as high- or low-altitude standoff, surface contact burst, and penetrated subsurface nuclear explosions. *The effectiveness and robustness of each option in the presence of significant physical modeling uncertainties needs to be further examined through Task 2 of the Phase II study.*

Space missions requiring nuclear deflection/disruption of NEOs are in general concerned with: i) robust predictability of the sufficient miss distance for a successfully deflected NEO; ii) robust predictability of the fragments impacting the surface of the Earth (for a worst-case situation with a very short warning time); iii) a reliable assessment of reduced impact damages due to a last minute disruption mission; and iv) an accurate modeling of  $\Delta\vec{V}$  (magnitude and direction of velocity change) within desired error bounds. Uncertainties in mass, density, porosity, material strength, and other physical parameters can substantially influence the outcome of any nuclear deflection/disruption attempt. Therefore, a detailed study is needed to characterize these uncertain parameters, especially for robust nuclear deflection/disruption mission design.

Also, we need to characterize, computationally and/or analytically, the modeling uncertainties and the resulting orbit perturbation effects in terms of effective  $\Delta\vec{V}$  uncertainties and/or uncertain perturbations in orbital elements ( $\Delta a$ ,  $\Delta e$ ,  $\Delta i$ ,  $\Delta\Omega$ ,  $\Delta\omega$ ,  $\Delta M_0$ ), as well as fragment velocity dispersion. In particular, the uncertainty associated with the initial dispersal velocity and mass distribution of fragments needs to be rigorously modeled and characterized for robust disruption mission design. Mutual gravitational interactions amongst the fragments also needs to be included in the high-fidelity dispersion modeling and simulation.

*The outcome of Task 2 will help construct the necessary reliable computational models in the face of significant physical modeling uncertainties as well as the practical mission constraints.*

### **1.3.3 Task 3 (Year 2): Development and Design of a HAIIV Flight Validation Mission Architecture (Development of a Phase III program)**

In preparation for a Phase III program, Task 3 explores potential infusion options within NASA and beyond by developing a 10-year technology roadmap for NASA's NEO Impact Threat Mitigation Grand Challenge.

The roadmap will include a near-term flight demonstration mission architecture and a cost estimate for flight-validating the HAIV technology. A HAIV flight validation mission architecture that doesn't employ an actual nuclear explosive payload will be developed for Task 3. A preliminary list of target asteroids to be further explored for this Task 3 is provided in Table 1.1. A sample flight validation mission trajectories is also shown in Figure 1.10. A current research project at the Iowa State ADRC, funded by NASA Iowa Space Grant Consortium, is also concerned with the conceptual design and development of a precursor robotic NEO exploration mission. Expanding on current studies at the ADRC, we will further develop a HAIV flight validation mission architecture through Task 3 of the Phase II study to create a Phase III program.

**NEO Spacecraft Mission Heritage.** At present there have been no flight validation missions for planetary defense technologies. However, between 1986 and 2011, a total of eleven science spacecraft have performed flybys of six comets and seven asteroids, and rendezvoused with two asteroids. The first of these were the Vega 1, Vega 2, and Giotto spacecraft, all of which performed flybys of comet 1P/Halley in 1986. The Galileo spacecraft closely approached two asteroids: 951 Gaspra in 1991 and 243 Ida in 1993. Meanwhile, Giotto performed a flyby of comet 26P/GriggSkjellerup in 1992. In 1997, the NEAR-Shoemaker spacecraft flew past the asteroid 253 Mathilde on the way to the asteroid 433 Eros, where the spacecraft entered a captured orbit and performed an extended scientific survey. During the same time frame, the Deep Space 1 spacecraft performed a flyby of asteroid 9969 Braille in 1999 and comet 19P/Borrelly in 2001. Following this, the Stardust spacecraft flew by asteroid 5535 Annefrank in 2002 and comet 81P/Wild in 2004. With the exception of NEAR-Shoemaker, all of these missions only flew past the asteroids or comets at distances of several hundred to several thousand kilometers. This changed in 2005 when the Deep Impact spacecraft successfully deployed an impactor to collide with comet 9P/Tempel. During the same year, the Hayabusa/MUSES-C spacecraft rendezvoused with asteroid 25143 Itokawa and eventually returned tiny grains of asteroid material to Earth. The Rosetta spacecraft subsequently flew past the asteroids 2867 Steins in 2008 and 21 Lutetia in 2010 on its way to a 2014 rendezvous with comet 67P/ChuryumovGerasimenko. After flying past comet 9P/Tempel in 2005, The Deep Impact spacecraft continued operating in an extended mission and was directed to perform a flyby of comet 103P/Hartley in 2010. The Dawn mission is currently in orbit around 4 Vesta, the largest known main belt asteroid, and will proceed to rendezvous with the dwarf planet Ceres, also located in the main asteroid belt, during the year 2015. NASA is currently developing the OSIRIS-REx mission, which will launch in the year 2016 to rendezvous with asteroid 1999 RQ36 and return samples of the asteroid material to Earth in 2023. The Japanese space program is also currently considering an asteroid sample return mission known as Hayabusa 2, which would launch in 2014 with the goal of returning samples from the NEA known as 1999 JU3.

**The Need for a HAIV Flight Validation Mission.** Each of the aforementioned science missions required at least several years, in some cases 5 to 6 years or more, for mission concept development and spacecraft construction prior to launch. It is also important to note that quite a few of these missions originally targeted different asteroids or comets than those that were actually visited. This is because the mission development schedules slipped and launch windows for particular asteroids or comets were missed. Additionally, several of these missions experienced hardware or software failures or glitches that compromised the completion of mission objectives. None of those things would be tolerable for a planetary defense mission aimed at deflecting or disrupting an incoming NEO, especially with relatively little advance warning. *Thus, while the impressive scientific missions that have been sent to asteroids and comets thus far have certainly provided future planetary defense missions with good heritage on which to build, we are clearly not ready to respond reliably to a threatening NEO scenario.*

Finally, it is also important to note that most of these missions visited asteroids or comets that range in size from several kilometers to several tens of kilometers. Furthermore, the flyby distances ranged from several tens of kilometers to several thousand kilometers. The sole exception to this is the Deep Impact mission, which succeeded in delivering an impactor to the target. However, the mission was aided by the fact that

Table 1.1: Orbital and physical characteristics of target asteroids for a HAIV flight validation mission (to be further investigated for Task 3 of Phase II).

Asteroid	Semi-Major Axis (AU)	Eccentricity	Inclination (deg)	Absolute Magnitude	Diameter (m)	Mass (kg)
2003 GA	1.28	0.191	3.84	21.08	300	2.94E11
2006 SJ198	2.09	0.456	2.43	17.95	1200	1.88E13
2009 TB3	1.32	0.219	12.22	21.09	300	2.94E11
2007 FS35	1.92	0.390	0.32	19.56	620	2.59E12
2003 QC	2.57	0.532	7.85	20.54	400	6.96E11
2004 GY	1.45	0.218	23.44	20.11	480	1.20E12
2001 SX269	1.88	0.346	4.03	21.29	280	2.39E11
1998 SB15	1.27	0.161	15.63	20.9	330	3.91E11
2004 KE1	1.30	0.181	2.88	21.63	240	1.50E11
2011 BX10	2.83	0.639	9.69	18.46	1000	1.09E13

comet 9P/Tempel, is  $7.6 \times 4.9$  km in size and therefore provided a relatively large target to track and intercept. Consequently, the Deep Impact mission was not intended to be a planetary defense flight validation mission. For planetary defense missions requiring NEO intercept, the requirements will be far more stringent: NEO targets with diameters as small as several hundred meters will have to be reliably tracked and intercepted at hypervelocity, with impact occurring within mere meters of the targeted point on the NEOs surface. This will require significant evolution of the autonomous GNC technology currently available for spacecraft missions to NEOs. *Furthermore, none of the potential planetary defense mission payloads to deflect or disrupt a NEO have ever been tested on NEOs in the space environment. Significant work is therefore required to appropriately characterize the capabilities of those payloads, particularly the ways in which they physically couple with a NEO to transfer energy or alter momentum, and ensure robust operations during an actual emergency scenario.*

When a hazardous NEO on a collision course with Earth is discovered we will not have the luxury of selecting a NEO target suitable for our mission design purposes or changing our choice of target if our development schedule slips. Instead, nature will have selected the target for us, along with whatever challenges are posed by its orbit and physical characteristics. *Making preparations now (Task 3) is essential because we will only have one chance to deploy an effective and reliable defense.*

#### 1.3.4 Task 4 (10/15/12 - 10/19/12): Five-Day IDC Study at NASA GSFC in Support of Tasks 1 and 3

A unique approach in our Phase II study is to collaborate with the IDC (Integrated Design Center) of NASA Goddard Space Flight Center (GSFC). The IDC at NASA GSFC will rigorously examine the technical feasibility and practical effectiveness of the HAIV concept and its flight validation mission concept via Task 4. Expanding on the IDC's technical evaluation of the proposed HAIV concept, our Phase II study team will continue to develop and refine the HAIV concept and its flight validation mission architecture concept. Study scheduling, capabilities, tools, and products of GSFC's IDC are illustrated in Figure 1.11.

The IDC is a unique facility at NASA GSFC that brings engineers and customers together to conduct rapid space flight instrument and mission concept design studies. Though established to support GSFC's new business development, IDC customers have also included teams of scientists, engineers and managers from other NASA Centers and Headquarters, other U.S. government agencies and foreign entities, academic institutions, and commercial companies. The IDC performs these studies in two dedicated Labs, the Instrument Design Lab (IDL) and the Mission Design Lab (MDL), where a unique, collaborative design environment has

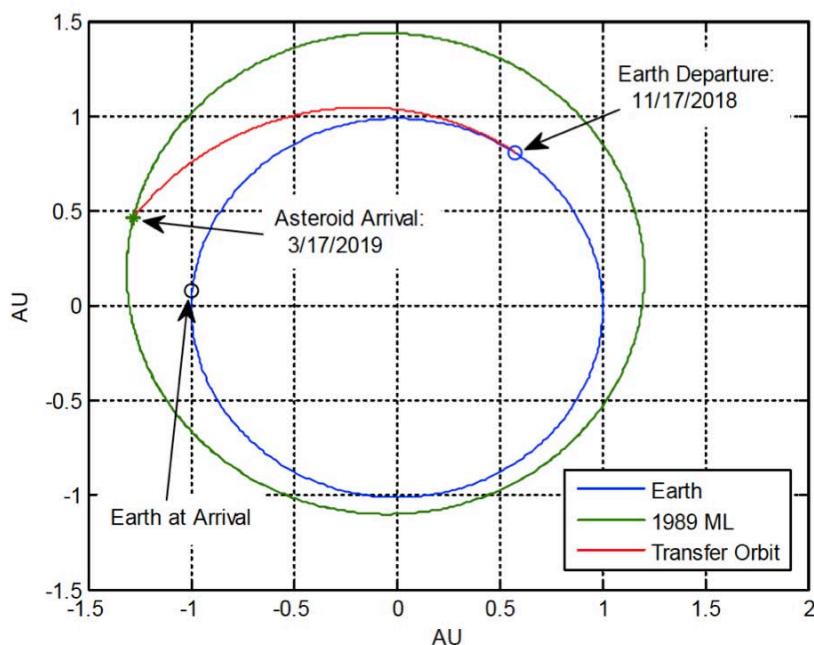


Figure 1.10: A HAIV flight validation mission trajectory. A HAIV flight validation mission concept that doesn't employ an actual nuclear explosive payload will be developed for Task 3 of Phase II.

been established that focuses on bringing together the people, processes, facilities and tools to allow a most efficient operation.

Each Lab brings in experienced discipline engineers who dedicate their time during the study dates to work with the customer team to address the major engineering aspects of defining the particular instrument or mission concept. The permanently-assigned Lab Leads and Systems Engineers direct the study using time-tested processes to assure continuous progress toward the customers' study objectives. Each discipline workstation is populated with the same engineering development software tools that the engineer would use in follow-on system design, producing useful post-study products. Lab facility equipment and arrangement allows an integrated design development and information flow that supports collaboration between all participants (local and remote) and keeps everyone abreast of the status of concept development. This allows immediate identification and resolution of design challenges, which is the key factor that permits rapid convergence toward a viable concept. A typical IDC study is performed in a single 5-day week.

IDC products are routinely used in proposals, reports and publications, and have sufficient engineering content to be a significant part of the GSFC and Agency decision-making and program/project development process. Since its inception in 1997, the IDC has conducted over 500 studies, and has contributed to the development of almost all GSFC-developed flight instruments and missions since then.

In support of Task 1 and Task 3, the MDL will conduct a comprehensive conceptual design and evaluation of the two-body HAIV system architecture. This consists of several pre-study activities intended to identify and gather all preliminary information needed to conduct the study, followed by a 5-day study in the MDL involving a full complement of discipline engineers as well as members of the proposal team. Including a day of post-study activities to produce the study products, the entire effort will involve approximately 22 GSFC engineers for a total of 7 days.

Products for Task 4 include PowerPoint summaries from each of the discipline engineers, detailing the portion of the system architecture associated with their particular discipline, how it meets the system requirements, and how it fits into the overall system architecture. Included with the summaries are any supporting information developed, such as spreadsheets, graphs, CAD drawings and other visual products, as well as all applicable and useful reference material.



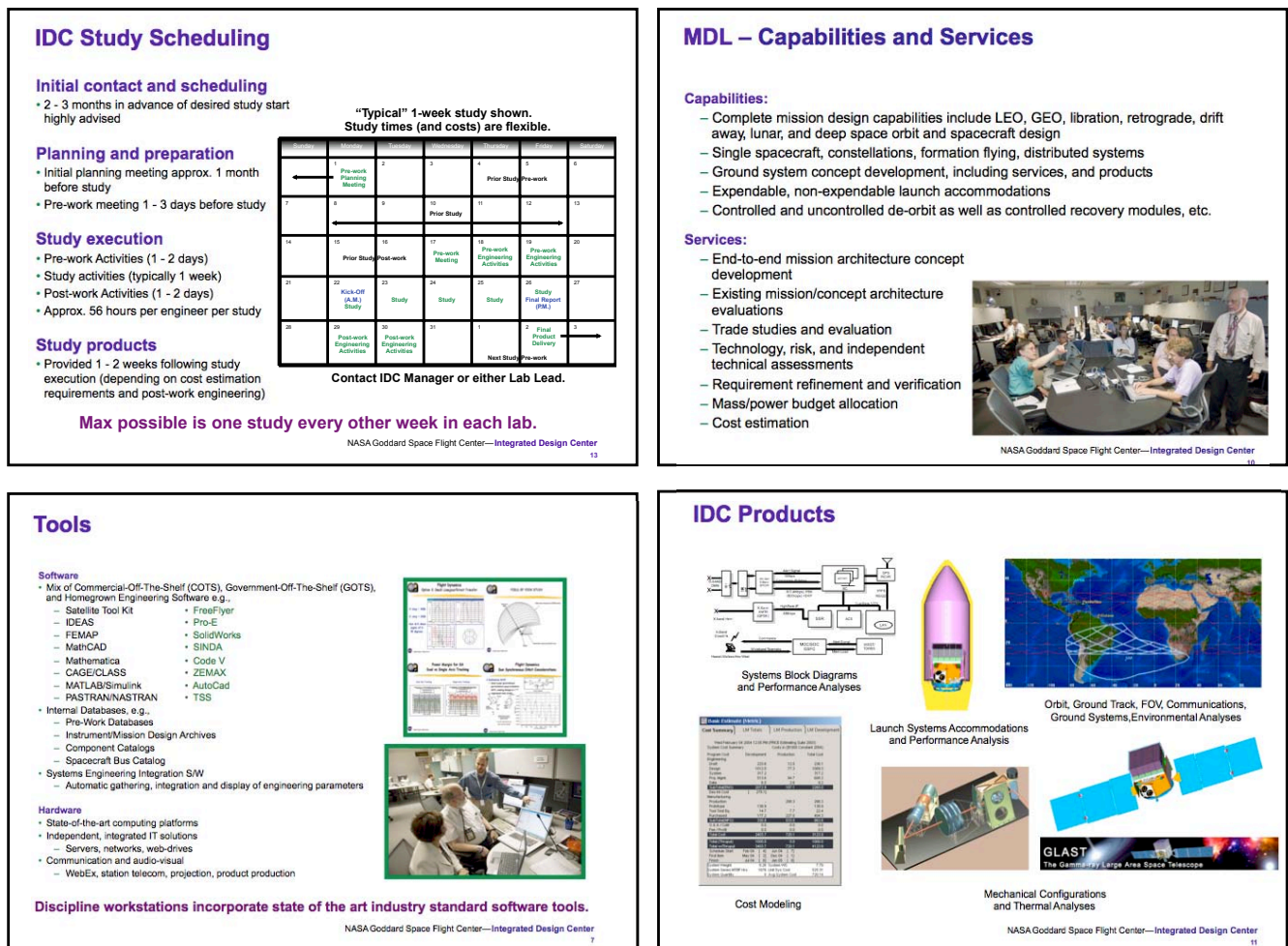


Figure 1.11: GSFC's IDC (Integrated Design Center) study scheduling, capabilities, tools, and products.

### 1.3.5 Phase II Deliverables

The key deliverables to NASA OCT are:

- Baseline HAIV system architecture and mission design (evaluated/refined by the IDC of NASA GSFC)
- Development and design of a near-term PDT flight validation mission concept (evaluated/refined by the IDC of NASA GSFC)
- Identification of key enabling technologies for the HAIV system
- 10-year technology road map for NASA's NEO Impact Threat Mitigation Challenge
- Phase III program development plan.

The following will be delivered to NASA OCT during the Phase II performance period:

- Bimonthly Status Reports
- NIAC Vision and Mission Review during a one-day Site Visit Review to provide a thorough overview of technical and programmatic progress.
- Annual Key Enabling Technologies Report. A written summary of identified key enabling technologies and prepare a pathway for development of a technology roadmap.
- NIAC Symposium Participation.
- Final Technical Report.



### 1.3.6 Study Team, Work Plan, and Project Management

The study team consists of: Prof. Bong Wie (PI), Brent Barbee (Co-I at NASA GSFC), and Ph.D. graduate students (Brian Kaplinger, Matt Hawkins, Sam Wagner, George Vardaxis, Tim Winkler, Joshua Lyzhof). In particular, these graduate students will be working collaboratively for the proposed project, as follows:

- Task 1: Matt Hawkins, Joshua Lyzhof
- Task 2: Brian Kaplinger
- Task 3: Sam Wagner, George Vardaxis, Tim Winkler

The graduate research assistants, working on a robotic and human NEO exploration study project supported by NASA's Iowa Space Grant Consortium, will also be collaboratively working for the proposed Phase II study. A technical consultant from Lawrence Livermore National Laboratory will also be working in the area of nuclear explosives and hypervelocity impact dynamics.

The Asteroid Deflection Research Center (ADRC) at Iowa State University has been developing strategies and technologies for deflection or disruption of hazardous NEOs. As the first university research center in the United States dedicated to such a complex engineering problem, the ADRC was founded in 2008 to address the engineering challenges and technology development critical to NEO impact threat mitigation. For research projects funded by NASA's Iowa Space Grant Consortium and the NIAC Phase I program, the ADRC has been developing practically viable space technologies for mitigating the NEO impact threats. Currently, six graduate students and several senior undergraduate students are actively involved in the asteroid exploration and deflection research activities of the ADRC.

**Dr. Bong Wie (PI)** is the Vance Coffman Endowed Chair Professor of Aerospace Engineering. He is the founding director of the ADRC. He was principal investigator of numerous research projects from NASA, including a \$700K solar sail research project from NASA. In 2006, the AIAA presented Dr. Wie with the Mechanics and Control of Flight Award for his innovative research on advanced control of complex spacecraft such as solar sails and large space platforms. He is the author of AIAA textbook *Space Vehicle Dynamics and Control* (2nd edition, 2008). He has been actively involved in the asteroid exploration and deflection research areas during the last five years. Currently, he is the PI of a space technology study project for NEO exploration/deflection, funded by NASA's Iowa Space Grant Consortium. He was the 2011 NIAC Phase I Fellow. *The proposed Phase II project (selected) will benefit from his unique research background in spacecraft guidance, control and dynamics and his diverse research activities in space systems and mission design, astrodynamics, spaceflight mechanics and control, and NEO impact threat mitigation. He will actively participate in this project by developing and validating the proposed HAIV system concept.*

**Brent Barbee (Co-I) at NASA GSFC** will work with the PI to ensure that project objectives are being met and assist in overseeing the research team. As GSFC's technical lead for both the Near-Earth Object Human Space Flight Accessible Targets Study (NHATS) (<http://neo.jpl.nasa.gov/nhats/>) and Flight Dynamics for the upcoming OSIRIS-REx asteroid sample return mission, the Co-I is uniquely positioned to support the planetary defense research proposed herein. Accordingly, the Co-I will provide professional engineering support in the areas of guidance, navigation, and control for HAIV designs, overall spacecraft subsystem design, asteroid trajectory design, and asteroid population surveys for candidate flight validation mission targets. The Co-I will also be responsible for assisting in the preparation of engineering data products and participating in the writing of technical reports and presentations. Additionally, the Co-I has previously participated in numerous studies at GSFC's Integrated Design Center (IDC), both as a member of the customer team and as a member of the IDC's staff of discipline engineers. The Co-I will utilize this prior experience to assist the PI in properly preparing for the planned IDC study described in this research proposal. The Co-I will also serve as the Flight Dynamics discipline engineer during the design study to be conducted in the IDC. However, the IDC discipline engineer work on the part of the Co-I is covered separately under the specific funding designated for the IDC study.

A unique approach in our Phase II study is to collaborate with the IDC at GSFC. Expanding on IDC's technical evaluation of the proposed HAIV concept, our Phase II study team will continue to develop and refine the HAIV concept and its flight validation mission architecture concept.

Key milestones of the proposed Phase II study are:

- October 15-19, 2012: Five-Day IDC Study at NASA GSFC
- November 14-15, 2012: NIAC Fall Symposium
- March/April 2013: NIAC Spring Symposium
- April 15-19, 2013: Technical paper presentation at 2013 Planetary Defense Conference, Flagstaff, AZ
- August 2013: Technical paper presentation at AIAA GNC and Astrodynamics Conferences
- September 2013: Annual Key Enabling Technologies Report
- October 2013: NIAC Vision and Mission Review Meeting at Iowa State University (or NASA HQ)
- November 2013: NIAC Fall Symposium
- March/April 2014: NIAC Spring Symposium
- August 2014: Technical paper presentation at AIAA GNC and Astrodynamics Conferences
- September 2014: Final Technical Report

## 1.4 Acknowledgments

This research has been supported by the NIAC (NASA Innovative Advanced Concepts) Phase I study project of the NASA Office of the Chief Technologist. The authors would like to thank Dr. John (Jay) Falker, the NIAC Program Executive, for his support of the proposed HAIV technology research project.

## 1.5 References

- [1] *Defending Planet Earth: Near-Earth Object Surveys and Hazard Mitigation Strategies*, National Research Council, National Academy of Sciences, 2010.
- [2] *Effects of Nuclear Earth-Penetrator and Other Weapons*, National Research Council, National Academy of Sciences, 2005.
- [3] Wie, B., “Hypervelocity Nuclear Interceptors for Asteroid Disruption,” Presented at 2011 IAA Planetary Defense Conference. Also published in *Acta Astronautica*, May 2012.
- [4] Kaplinger, B., Wie, B., and Dearborn, D., “Earth-Impact Modeling and Analysis of a Near-Earth Object Fragmented and Dispersed by Nuclear Subsurface Explosions,” to appear in *Journal of Astronautical Sciences*.
- [5] Kaplinger, B. Wie, B., and Dearborn, D., “Nuclear Fragmentation/Dispersion Modeling and Simulation of Hazardous Near-Earth Objects,” Presented at 2011 IAA Planetary Defense Conference, to appear in *Acta Astronautica*.
- [6] Pitz, A., Kaplinger, B., and Wie B., “Preliminary Design of Hypervelocity Nuclear Interceptor Spacecraft for Disruption/Fragmentation of NEOs,” AAS 12-225, AAS/AIAA Space Flight Mechanics Meeting, Charleston, SC, Jan 30-Feb 2, 2012.
- [7] Vardaxis, G., Pitz, A., and Wie, B., “Conceptual Design of Planetary Defense Technology Demonstration Mission,” AAS 12-128.
- [8] Winkler, T., Wagner, S., and Wie, B., “Target Selection for a Planetary Defense Technology Demonstration Mission,” AAS 12-226.
- [9] Pitz, A., Kaplinger, B., Vardaxis, G., Winkler, T., and Wie, B., “Conceptual Design of a Hypervelocity Asteroid Intercept Vehicle (HAIV) and Its Flight Validation Mission,” GLEX-2012.06.3x12173, 2012 IAF/AIAA Global Space Exploration Conference, Washington, DC, May 22-24, 2012.

- [10] Pitz, A., Kaplinger, B., Vardaxis, G., Winkler, T., and Wie, B., “Conceptual Design of a Hypervelocity Asteroid Intercept Vehicle (HAIV) and Its Flight Validation Mission,” AIAA 2012-4873, AIAA/AAS Astrodynamics Specialist Conference, 2012.
- [11] Kaplinger, B. and Wie, B., “High-Performance Computing for Optimal Disruption of Hazardous NEOs,” AIAA 2012-4875, AIAA/AAS Astrodynamics Specialist Conference, 2012.

## Chapter 2

# Conceptual Design of a Hypervelocity Asteroid Intercept Vehicle (HAIV)

### 2.1 Introduction

Due to uncertainties in asteroid detection and tracking, warning time of an asteroid impact with the Earth can be very short. In the case of an Earth-impacting object ( $\approx 1$  km diameter) discovered without many years of warning, the necessary velocity change becomes very large and the use of high-energy nuclear explosives in space will become inevitable [1, 2, 3]. The most probable deflection/disruption mission may use a direct intercept trajectory to the target NEO resulting in relative arrival velocities of 10 to 30 km/s [1]. While there are many different nuclear deflection/disruption techniques that can be employed, the subsurface nuclear explosion is most efficient. Delivering nuclear explosives beneath the surface of a NEO proves to be challenging because the conventional penetrating nuclear explosive devices (NED) require the impact speed to be less than 300 m/s [1]. Reference 1 presents the conceptual mission requirements associated with such a mission and an innovative design of a hypervelocity nuclear interceptor system (HAIV) using current technology to execute a nuclear disruption mission with high intercept velocities. A proposed solution includes a baseline two-body interceptor configuration, thermal shielding of a follower spacecraft, impactor targeting sensors and optical instruments, thruster configurations and terminal guidance phase operations, and other secondary optional configurations. Hydrodynamic simulations are used to assess the mission and to provide thermal and structural design constraints for the follower spacecraft carrying NEDs. Expanding upon system architectures, technologies, and concepts from NASA's Deep Impact, ESA's Don Quijote (canceled), and an Interplanetary Ballistic Missile System (IPBM) [4] studied at the Iowa State Asteroid Deflection Research Center, the preliminary development and design of a HAIV will be discussed in this paper.

It is envisioned that eventually in the near future, planetary defense technology (PDT) demonstration missions will be considered seriously by an international space community in order to validate the overall effectiveness and robustness of various nuclear options and the associated space technologies. The ADRC's mission design software tools have been utilized to conduct a search of optimal asteroid targets for a PDT demonstration mission, which would validate asteroid disruption capabilities. An ideal primary objective for a flight demonstration mission is to test and validate the HAIV using a real NED to be employed as in an actual Earth-threatening situation. However, political differences may interfere with this idea in which case a small explosive device or a representative "dummy" payload could be used as an alternative payload option to verify and validate the PD technologies. Other optional missions can be accomplished such as sending an orbiter spacecraft to observe the effectiveness of the disruption mission or collect NEO composition samples and return it to Earth for analysis. Although there are optional mission objectives that can be conducted with this mission, it is imperative that the primary objective of validating the HAIV technology is to remain paramount.

## 2.2 Nuclear Disruption Mission Requirements

A practical design solution is required for the delivery of a robust and effective subsurface explosion, using available technology, through a direct intercept trajectory, to mitigate the most probable impact threat of NEOs with a short warning time. Since the warning time is short, a rendezvous mission becomes impractical due to the resulting NEO intercept velocity exceeding 10 km/s. NEDs constitute a mature technology, with well-characterized outputs and are the most mass-efficient means for storing energy with today's technology [1, 2, 3]. Nuclear deflection/disruption strategies to be employed in a last minute, direct intercept mission include standoff explosions, surface contact bursts, and subsurface explosions. For each nuclear technique, accurate timing of the nuclear explosive detonation will be required during the terminal guidance phase of hypervelocity intercept missions. Furthermore, the conventional penetrating NEDs require the impact speed to be less than 300 m/s. A nuclear disruption mission employs nuclear explosives in three different ways. A nuclear standoff explosion is a predetermined height burst and is often considered as the preferred approach among the nuclear options. A second nuclear option exploits a contact burst on the NEO's surface. The most efficient nuclear option involves a subsurface explosion. The subsurface explosion, even with a shallow burial ( $< 5$  m), delivers large energy that can totally fragment the target NEO [3]. The NED payloads are categorized into three classes as: [4] i) a 300-kg NED with a yield of about 300 kt, ii) a 1,000-kg NED with a yield of about 1 Mt, and iii) a 1,500-kg NED with a yield of about 2 Mt.

The nuclear standoff burst technique can be used for long-term warning times. The nuclear standoff scenario utilizes the short burst of energy from a nuclear explosive to heat a thin layer of a NEO's surface. As this layer accelerates away from the NEO, its main body recoils in the opposite direction, thus altering its trajectory [2]. The area of the NEO's surface that is heated by a standoff nuclear explosion depends on the distance between the asteroid and the point of detonation. Also, the depth of penetration depends on the distance between the surface and the detonation point. Thus, detonation close to the surface heats only a small area close to the explosion. At larger distances, the explosion spreads its energy over a larger area of the asteroid, increasing the angle of effect. As a result of this, the penetration depth decreases. One advantage of this technique is that it does not require stringent spacecraft maneuvers as might be required for a surface or subsurface explosion.

Numerous studies have been conducted in the past to understand the effect of a standoff nuclear explosion and its  $\Delta V$  capability. In Reference 2, the study simulated the effect of a nuclear standoff detonation on homogeneous 1 km-diameter NEOs with densities between 1.91 and 1.31 g/cm<sup>3</sup>. Approximately 40 seconds after the standoff burst, at 150 m above the NEO's surface, the NEO's speed change ranged from 2.2 to 2.4 cm/s. It was estimated that 97.5% of each NEO from all simulations remained intact, while about 2.5% of its mass was ejected at greater than escape speed by the rebound to the shock wave that passes through the body in reaction to the ejection of heated material [2]. The NEO was held by gravity only and had no tensile strength model. The study concludes that deeper neutron penetration is not dependent on NEO composition.

Another nuclear technique involves the subsurface use of nuclear explosives. The nuclear subsurface method even with a shallow burial ( $< 5$  m) delivers large energy, potentially disrupting the NEO completely [3]. The major advantage of a nuclear subsurface explosion over a surface or above-ground nuclear explosion is the effectiveness with which energy is transmitted into the NEO. The effectiveness of earth-penetrating weapons can be used to illustrate the nuclear subsurface method on a NEO.

Nuclear earth-penetrator weapons (EPWs) [5] with a depth of penetration of approximately 3 meters captures most of the advantage associated with the coupling of ground shock. According to Figure 2.1, the yield required of a nuclear weapon to destroy a deeply buried target is reduced by a factor of 15 to 25 by ground-shock coupling enhancement. The EPW is designed to detonate below the ground surface after surviving the extremely high shock and structural loading environments that result during high-speed impact and penetration. However, its impact speed is limited to approximately 300 m/s. While additional depth of penetration increases ground-shock coupling, it also increases the uncertainty of EPW survival. The ground-shock coupling factor makes the subsurface technique much more efficient than the other nuclear techniques.

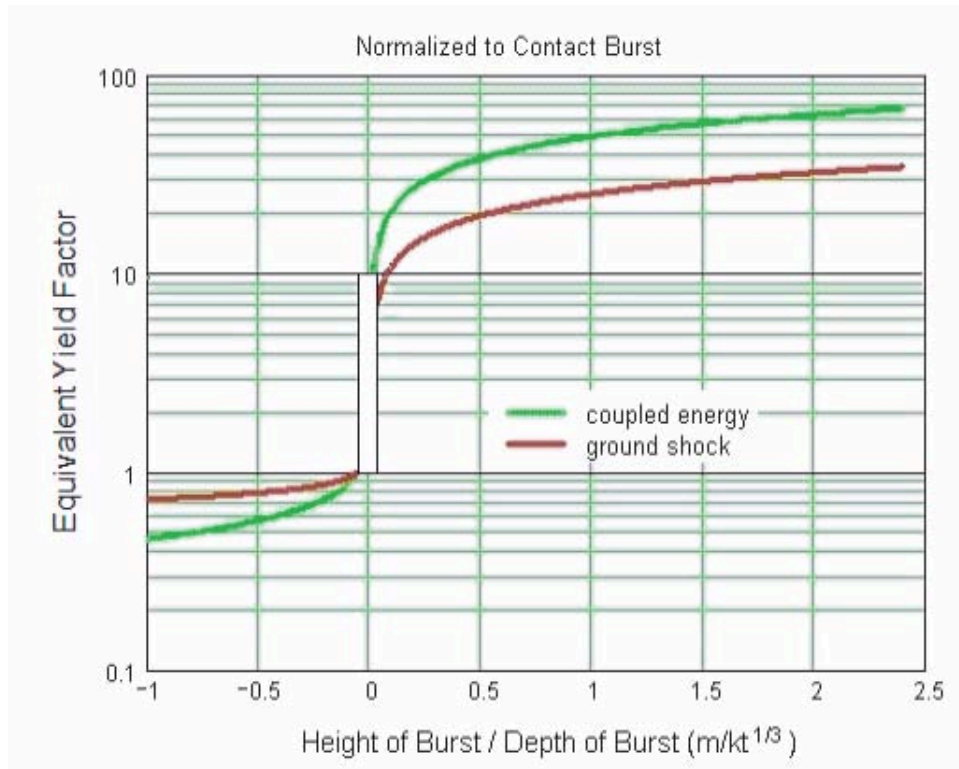


Figure 2.1: Equivalent yield factors for total coupled energy and ground-shock coupled energy normalized to a contact burst [5].

The ground-shock coupled energy of an EPW approaches 50% with increasing depth of burst (DOB), and is fully coupled at a scaled DOB of about  $(2.3)DOB/Y^{1/3}$ , where DOB is the depth of burst in meters and Y is the yield in kilotons [5]. Scaled DOB, defined as  $DOB/Y^{1/3}$ , is a normalization of the actual depth (or height) of a burst based on weapon yield to that for a 1-kt weapon. Thus, the scaled DOB and actual DOB are the same for a 1-kt EPW. For example, a 1-kt weapon buried 3 meters has a 3 scaled DOB, whereas a 300-kt weapon buried at the same depth of 3 meters couples its energy to the ground as if it were a 1-kt weapon buried at an actual depth of about 0.45 meter; that is,  $3/300^{1/3} = 3/6.67 = 0.45$ . For a generic 300-kt EPW at 3-m depth of burst (scaled DOB =  $3/(300)^{1/3} = 0.45$ ), the ground-shock-coupling factor is about 20, which is equivalent to a contact burst of about 6-Mt EPW.

Active research and development on bunker-buster technology has produced a New Generation Multiple Warhead System (NGMWS). MBDA has conducted the second test firing of a new bunker-busting warhead under a bilateral technology demonstration program involving France and the U.K. The NGMWS is designed to defeat a wide range of targets such as command and control facilities, infrastructure and underground facilities including caves, reflecting current and potential future operations [6]. The test firing was carried out using a representative missile airframe on the long rocket sled test track at Biscarrosse testing facility. The live precursor charge was detonated just in front of the massive concrete target and the inert follow-through bomb penetrated through and exited the rear face of the target, demonstrating a penetration capability significantly in excess of any warhead currently produced by MBDA [6]. The trial was also designed to assess the robustness of the compact ruggedized electronic in-line fuze that will incorporate embedded smart fuzing algorithms. This trial builds upon the successful first trial conducted at the Biscarrosse test range on the 18th May 2010, where the novel concepts underpinning the NGMWS design were successfully demonstrated [6].

Fundamental principles of Keplerian orbital dynamics can be effectively used for examining the effects of the nuclear subsurface explosion under various physical modeling uncertainties [3]. In [3], the study considers such a nuclear subsurface explosion with a shallow burial of approximately 5 m for different models of NEOs.

Sourcing energies equivalent to 900 and 300 kt are used to simulate realistic subsurface explosions [7]. In the simulations, the energy source region expands creating a shock that propagates through the body resulting in fragmentation and dispersal. While the material representations used have been tested in a terrestrial environment, there are low-density objects, like Mathilde, where crater evidence suggests a very porous regolith with efficient shock dissipation [3, 7]. Shock propagation may be less efficient in porous material, generally reducing the net impulse from a given amount of energy coupled into the surface.

A common concern for such a powerful nuclear option is the risk that the nuclear disruption mission could result in fragmentation of the NEO, which could substantially increase the damage upon its Earth impact. For short warning time missions, the impact mass can be reduced to 0.2% of the initial mass of the NEO, if the intercept disruption occurs nearly perpendicular to the NEO's orbital flight direction [3,7,8]. Such a sideways push is known to be optimal when a target NEO is in the last orbit before the impact [7]. The mass of Earth-impacting fragments can be further reduced by increasing the intercept-to-impact time or by increasing the nuclear yield. However, disruption/fragmentation is a feasible strategy only if it can be shown that the hazard is truly diminished. Additional research has been recommended, particularly including experiments on real comets and asteroids, to prove that nuclear disruption can be a valid method [2].

## **2.3 State-of-the-Art Interceptor Technology**

Current technology and spacecraft concepts from previous NEO missions provide a starting point for the preliminary design of a baseline HAIV. After the success of previous fly-by missions to comets such as Stardust, NASA developed the Deep Impact mission to achieve a hypervelocity intercept of a comet, retrieve information on the impact event, and obtain several high resolution images of the comet's interior. The Deep Impact mission employed two spacecraft to study the characteristics of the comet Tempel 1. ESA's Don Quijote mission concept also required two spacecraft to study the effects of a hypervelocity kinetic impactor hitting an asteroid. Unfortunately, the mission was canceled due to mission uncertainty and cost. ADRC's IPBM concept takes a versatile payload option approach to be used for a variety of deflection/disruption missions. These various system architectures are exploited for the preliminary design of a baseline HAIV.

### **2.3.1 NASA's Deep Impact Mission**

The Deep Impact mission spacecraft consisted of a flyby scientific observing spacecraft and an impactor spacecraft [9]. The flyby and impactor spacecraft were held together to form one spacecraft until the beginning of the terminal guidance phase. During the terminal phase operation, the flyby spacecraft was separated from the impactor to observe the impact event. The flyby spacecraft is equipped with two scientific instruments that serve two main purposes. In the initial stages of the mission, the instruments are used to guide the impactor and the flyby spacecraft towards the target comet, Tempel 1. The two instruments on the flyby spacecraft are the High Resolution Instrument (HRI) and the Medium Resolution Instrument (MRI). To protect these important instruments from the debris in the comet tail and the impact ejecta, the flyby spacecraft rotates and is protected by a Whipple Shield [9]. A Whipple shield is composed of a thin outer bumper that is placed on the outer walls of the spacecraft. The impactor spacecraft of the Deep Impact mission separates approximately 24 hours prior to the impact event and has a relative velocity of approximately 10.2 km/s. The 1-m diameter and 1-m long 370-kg impactor delivered approximately 19 GJ of kinetic energy to create a large crater approximately 100-m wide and 30-m deep [9]. With the help of a shield composed of spherical-shaped copper plates with a mass of 113 kg, the impactor is capable of making a significant crater in the comet for scientific observations. While the Deep Impact mission involved intercepting a comet and observing the comet's nucleus, the mission's purpose was not related to determining the effects of a kinetic impactor impacting the target body.

### 2.3.2 ESA's Don Quijote Mission Concept

The ESA's Don Quijote mission was a previously proposed mission concept with a goal to demonstrate and validate the kinetic impactor's capability of deflecting an asteroid. The first objective was to observe the momentum transfer from the impact by measuring the asteroid's characteristics and also its change in rotation and osculating orbital elements. The second objective is to carry out an Autonomous Surface Package Deployment Engineering eXperiment (ASP-DEX) and perform a mapping of the asteroid. The Don Quijote mission was designed to include two different spacecraft, an orbiter spacecraft called Sancho, and an interceptor spacecraft called Hidalgo. The 491-kg (395-kg dry mass) orbiter spacecraft, Sancho, was going to employ a reconfigured SMART-1 satellite bus. SMART-1 is a 1 cubic meter ESA satellite that orbited around the moon and took high-resolution images of the moon's surface [10]. However, changes had to be made to the communication and power systems of the SMART-1 bus to meet the mission requirements. The Sancho orbiter would be launched into space using a Vega rocket with a Star-48 upper stage. Sancho would arrive at the target NEO and observe the asteroid and its characteristics. The 1,694-kg (532-kg dry mass) Hidalgo spacecraft launches separately and has been designed to have no moving solar arrays in order to obtain the precise attitude and maneuvering requirements to impact the asteroid. Hidalgo uses advanced on-board computers and a high resolution camera to guide it to the NEO. Hidalgo intercepts the asteroid with a speed of approximately 10 km/s while Sancho deploys the ASP-DEX onto the asteroid [11]. The ASP-DEX obtains information about the asteroid's changes in trajectory, rotation, and physical characteristics.

## 2.4 Design and Analysis of a Baseline HAIV Architecture

### 2.4.1 A Baseline HAIV Mission Architecture

A baseline system concept has been developed to accommodate the technically challenging aspects of the penetrating subsurface nuclear explosion approach. A baseline HAIV consists of a leader spacecraft (kinetic impactor) and a follower spacecraft carrying an NED for the most effective disruption of a target NEO. The leader spacecraft impacts first and creates a shallow crater in the NEO. Then, the follower spacecraft enters the crater and detonates the NED. This baseline HAIV mission concept is illustrated in Figure 2.2, and the HAIV configurations are shown in Figure 2.3.

The primary HAIV carrying a 1000-kg NED payload is delivered by a Delta IV M class launch vehicle. The launch vehicle places the HAIV into a direct transfer orbit towards the target NEO. During the transfer phase, the HAIV remains as a single spacecraft by way of the leader staying attached to the follower spacecraft. The HAIV uses a bi-propellant system with a 4,400 N gimbaled engine to execute trajectory correction maneuvers (TCMs). The single spacecraft can be placed in a dormant state, periodically relaying status updates while in transit until the terminal guidance phase.

The terminal-phase guidance starts 24 hours before the impact event. Instruments located on the spacecraft detect the target NEO and the subsystems on-board the HAIV become active. Measurements are continued through optical cameras and laser radars located on the leader spacecraft and an intercept location is identified on the asteroid body. The high resolution optical cameras, provides successive images of the NEO to each flight computer where guidance and navigation algorithms are used to guide the impactor and the follower to the intercept location. The computer then uses these calculations to compute the necessary adjustments and instructs the divert and attitude control system (DACS) to execute TCMs. A 10-m boom equipped with contact fuzes and sensors is deployed from the leader spacecraft. Separation occurs between the leader spacecraft and the follower spacecraft and communication is established between the two spacecraft. As the distance between the follower spacecraft and NEO becomes smaller, the triggering system turns on, readying the fuzing mechanisms of the NED payload.

The nuclear fuzing mechanism is initiated by the contact fuzes located at the front of the 10-m deployable boom. Once the boom confirms contact the NEO's surface, it closes the electrical circuit of the contact fuze and the leader spacecraft sends a signal to the follower spacecraft to initiate the detonation sequence.



## Hypervelocity Asteroid Interceptor Vehicle Terminal Phase Operations

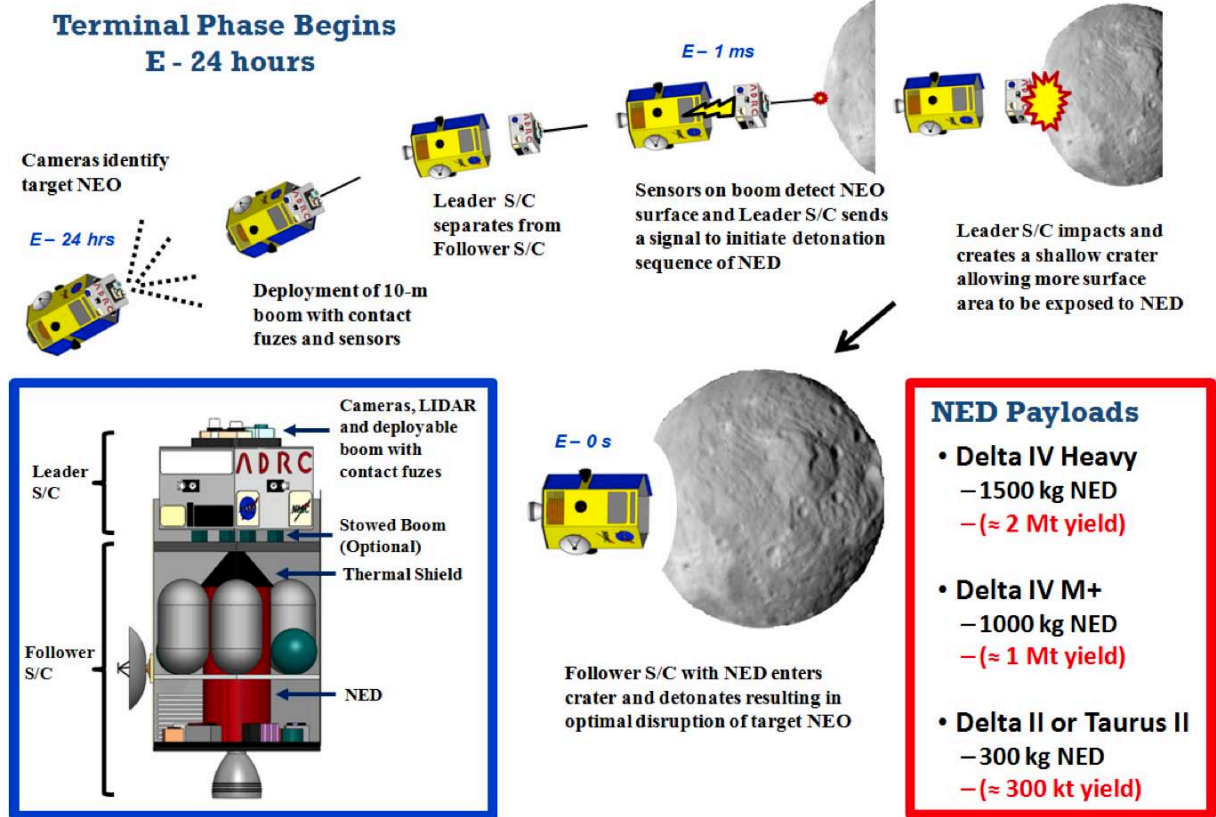


Figure 2.2: Conceptual illustration of the baseline HAIV mission architecture.

A shallow crater is then created as the leader spacecraft impacts the NEO. Hot ejecta and debris particles result as the leader spacecraft is vaporized at hypervelocity impact. The follower spacecraft is equipped with a thermally resistant, hypervelocity debris shield that protects the NED and triggering system. The shield deforms and melts as it passes through the hot plasma ejecta and the NED detonates. It is assumed that nuclear detonation sequencing requires approximately 1 millisecond of lead time. With a relative speed of 10 km/s, a 10 meter boom connected to the leader spacecraft is assumed to ensure the accuracy of the detonation timing. This timing delay is the most significant part of the disruption mission.

Partitioning options between the leader and follower spacecraft to ensure the follower spacecraft enters the crater opening confidently are discussed here. The primary option uses no connection between the two spacecraft. This configuration depends on the instruments, communication, flight computer, and guidance and tracking algorithms to carry out the terminal-phase guidance and impact.

Another option includes the use of a rigid connection between the two bodies through a deployable mast. Figure 2.4 shows an optional HAIV configuration with a deployable mast. As the mast is deployed and separation distance increases, the center of mass moves from the center towards the front of the follower spacecraft. This new configuration is still treated as a single body but achieves a two-body arrangement. Divert thrusters are pre-positioned at the expected new center of mass location to control the new system as a single body. These large divert thrusters can be gimballed to achieve the desirable thrust directions. This configuration reduces mission complexity and operations, but is limited to the length of the boom. This is proposed as an optional configuration of the primary HAIV, and it needs further study.

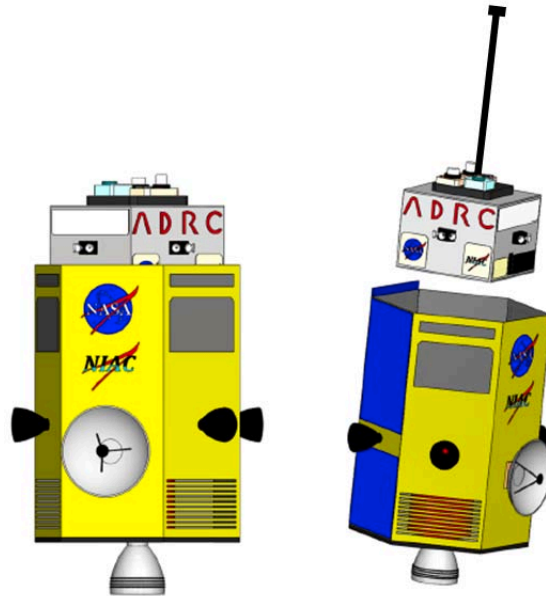


Figure 2.3: Primary two-body HAIV configuration during the terminal phase.

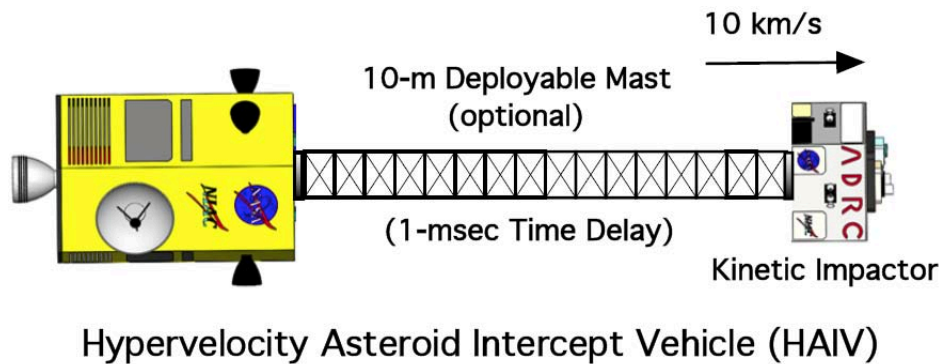


Figure 2.4: Secondary HAIV configuration by connection of a deployable boom.

## 2.4.2 Nuclear Fuzing Mechanisms

The NED triggering system is the most vital element of the HAIV. In general, a standard fuzing mechanism ensures optimum weapon effectiveness by detecting that the desired conditions for warhead detonation have been met and to provide an appropriate command signal to the firing set to initiate nuclear detonation. Fuzing generally involves devices to detect the location of the warhead with respect to the target, signal processing and logic, and an output circuit to initiate firing [13]. Without the proper selection of a reliable triggering or fuzing mechanism, there is a high risk that the mission can be unsuccessful. Current terrestrial triggering systems such as salvage fuzes, timing, contact, and radar (proximity) fuzes are employed to detonate the NEDs. These fuzes act on the instantaneous scale between 10 - 25 microseconds. This allows for absolute precision required for a hypervelocity impact nuclear disruption mission.

The salvage fuze acts as a contingency fuze which is employed as a failsafe detonation. The fuze “salvages” the bomb and explodes when all other fuzes fail [12]. The salvage fuze serves as a countermeasure to a terminal defense interceptor system and initiates after a detected collision possibility. The warhead then explodes as soon as an interceptor comes within a certain range of the warhead. Sometimes radar and contact

fuzes operate as the failsafe triggers and must function after withstanding extreme deceleration forces and delivery vehicle deformation [12]. In an asteroid direct intercept scenario, the salvage fuze comprised of several contact and radar fuzes becomes activated. The contact and radar fuzes provide one option for arming and detonating the NED.

Another option for triggering the NED is a timing fuze. The timing fuze operates by using time-to-go, estimated intercept distance, and the rate of the intercept distance. This information is provided to the triggering mechanism by the guidance, navigation, and control instruments and flight computer. The computer activates the timing fuze once the guidance parameters meet specific conditions. The timing fuze is the most appropriate as the entire deflection/disruption process will be autonomous. However, if the timing fuze proves to be inaccurate, the salvage fuzes (contact and radar fuzes) can restore the arming mechanism of the NED. A salvage fuze is always present to resume the arming of the NED in any such triggering problems.

Proper fuzing systems and operations need to be chosen. For a standoff burst disruption mission, radar acts as part of the primary fuzing system. For the subsurface or contact burst option, timing and radar fuzes may represent part of the primary detonation system, and contact fuzes are used as a failsafe detonation. The selection and sequencing of these fuzing options are chosen autonomously and are not dependent on additional hardware or configurations. Contact and radar fuzes can be located on the 10-m boom deployed from the leader spacecraft. This arrangement allows sufficient time to initiate the NED detonation sequence (1 millisecond) before impact.

### **2.4.3 Terminal Guidance Sensors/Instruments**

Optical cameras, radar altimeters, and Light Detection and Ranging (LIDAR) are used on the leader spacecraft to accurately identify and track the target NEO and initiate fuzing for the NED. The leader uses a Medium Resolution Instrument (MRI) or Wide Field of View (WFOV) Imager as used on the Deep Impact flyby spacecraft. The WFOV Imager is used to locate the target NEO at the start of the terminal phase. It is a small telescope with a diameter of 12 cm and takes images with a scale of 10 m/pixel in a spectrum of approximately 700 nm [9]. The field of view of the WFOV Imager is approximately 10 deg x 10 deg which allows to observe more stars and serves as a better navigator for the HAIV during its coasting phase [9]. As soon as possible after acquisition of the target NEO, the WFOV Imager passes information to the High Resolution Instrument (HRI) or Narrow Field of View (NFOV) Imager, which has a field of view of 2.3 deg x 2.3 deg. It is comprised of a 30-cm diameter telescope that delivers light to both an infrared spectrometer and a multispectral camera. The camera has the ability to image the NEO with a scale that is less than 2 m/pixel when the spacecraft is approximately 700 km away [9]. Table 2.1 shows the properties of each Imager. The Imagers are located on the leading front of the impactor spacecraft. These Imagers are similar to the instruments used on the Deep Impact Mission Flyby and Impactor spacecraft.

LIDAR or laser radar measures back-scattered light from a high intensity, short duration output pulse transmitted at the target NEO. It is used in the closing minutes of the terminal phase to calculate the range to the NEO. This information is shared with the fuzing device for detonation of the NED. The LIDAR requires sufficient power to operate over a range equivalent to approximately the last minutes of the terminal phase. The device design would be similar to the ones used on the NEAR and Clementine missions. The LIDAR has a mass of 20 kg and an estimated power consumption of 50 W. Radar altimeters using radio waves are used in conjunction with LIDAR. More study on these instruments is required to ensure high data rates and suitability.

### **2.4.4 Thermal Protection and Shield**

An in-house hydrodynamics code, which is being developed to accurately study the effects of nuclear disruption missions, is used to estimate the thermal and structural limits experienced by the two-body HAIV. The hydrodynamic code helps to establish a shield design and its configuration on the follower spacecraft.

Table 2.1: HAIV Imaging sensor package properties.

Parameter	NFOV Imager	WFOV Imager
Field of View (deg)	$2.3 \times 2.3$	$9.5 \times 9.5$
Angular Resolution ( $\mu\text{rad}$ )	10	40
Focal Plane Dimension (pixels)	$1024 \times 1024$	$1024 \times 1024$
Effective Aperture Size (cm)	8.5	2.1
Effective Focal Length (cm)	90	22.3
Estimated Mass (kg)	15	10
Estimated Power (W)	20	10

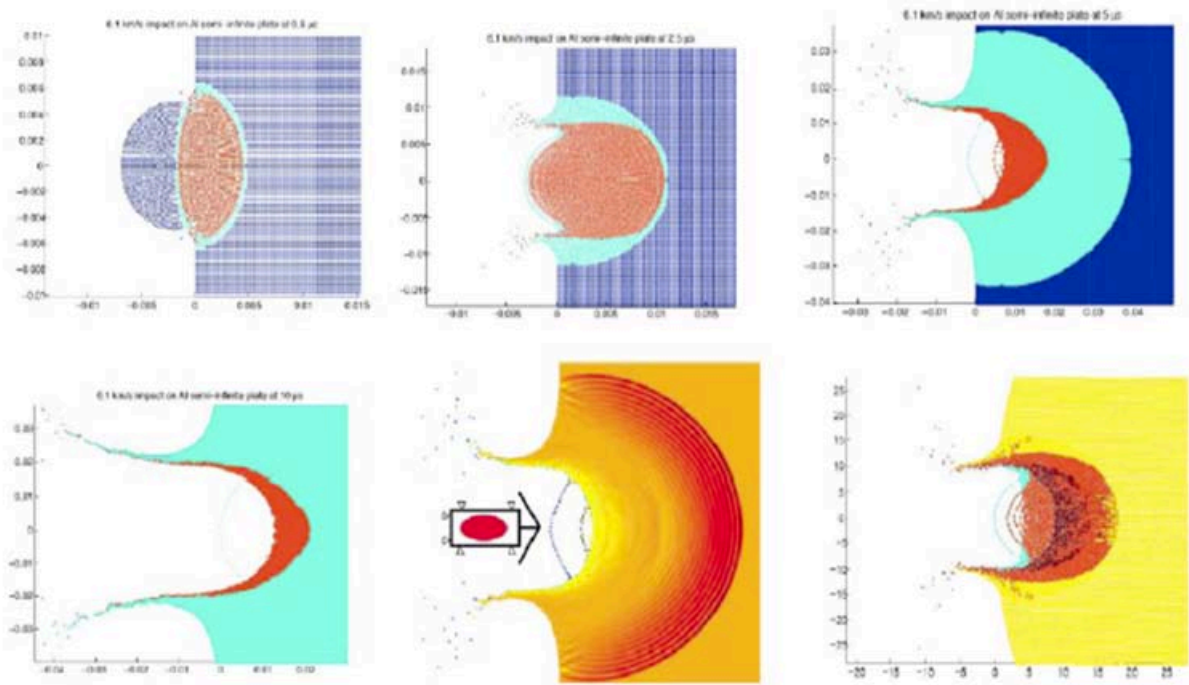
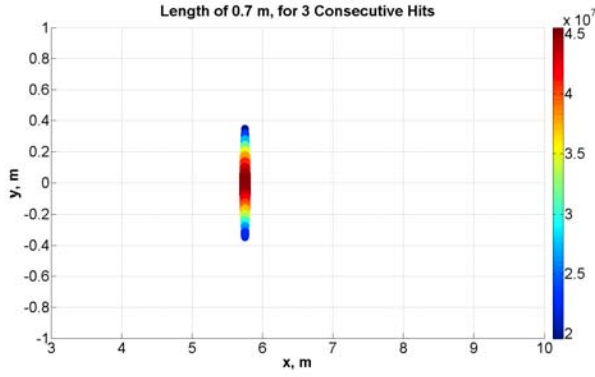


Figure 2.5: Preliminary illustrative results for the hypervelocity penetrated subsurface nuclear explosion option.

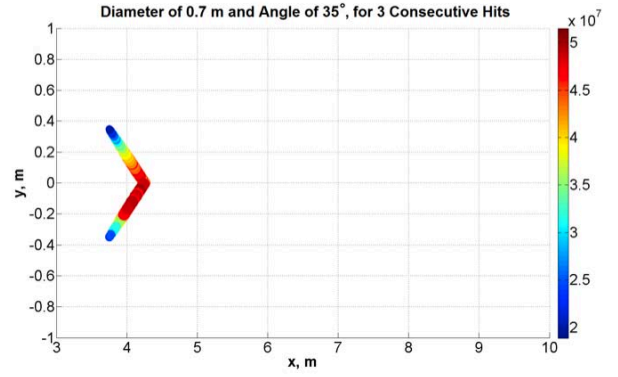
Several different geometries include a flat cylindrical plate, conical shape, spherical cap, and an EPW ogive nose cone.

Due to long turnaround times inherent to the use of any hydrocode for testing different shield designs and material properties, a single energy simulation of the impact event was ran and saved. The simulation starts with a spherical leader spacecraft impacting an asteroid modeled with strength properties of granite. The leader spacecraft traveling at approximately 10 km/s is vaporized at impact. Approximately 1 microsecond later, the follower spacecraft impacts the same location as the leader spacecraft. The energy experienced by the follower spacecraft is recorded and the simulation is saved. Figure 2.5 illustrates this process through snapshots taken from the simulation. The simulation variables are then used in a MATLAB simulation code to observe energy interactions for given shield geometries. Once the MATLAB shield test concludes specific geometries, the hydrocode simulation tests shield geometry, material properties, and shield thickness. Dissipating energy from the shield is not considered at this time but will be included in future work.

Figures 2.6-2.7 show the energy interaction for a MATLAB simulation using different geometries (thin flat plate, cone, spherical cap, and an ogive nose cone). The simulation has 36 time steps with the shield

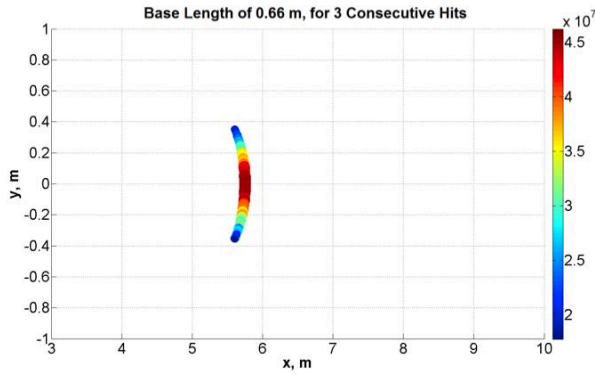


(a) A flat plate.

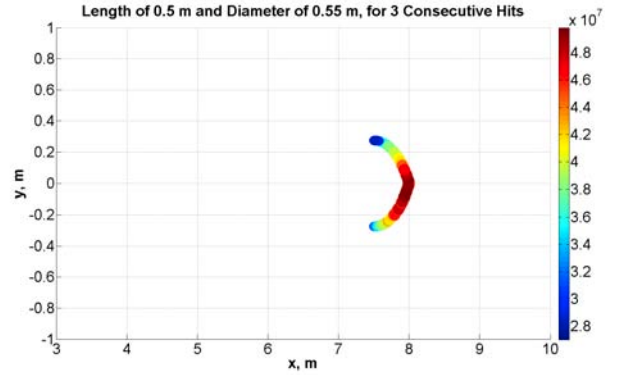


(b) A conical cone.

Figure 2.6: Estimated penetration depth of a flat plate and conical cone based on 3 consecutive hits at the same location.



(a) A spherical cap.



(b) An ogive nose cone.

Figure 2.7: Estimated penetration depth of a spherical cap and ogive nose cone based on 3 consecutive hits at the same location.

starting point at approximately 10 m from the asteroid and the ending point at a subsurface depth of 17 m. Each shield is geometrically different but the same mesh size of 5,000 points is used. The color bar legend on the right hand side of each figure shows the amount of energy encountered by the shield. It is shown that the reddest areas located on the shield confronted the highest amounts of energy (usually in the center of the shield). One study is presented using the same simple MATLAB simulation test. The simulation was stopped when a location on the shield was consecutively hit 3 times with the largest amount of energy. Figures 2.6-2.7 show the location of the shield at a subsurface depth in the asteroid and the highest amount of energy endured by the shield. From these early simulations, we can infer a shield length and geometry that can be tested in the hydrodynamics code.

Once the geometry of a shield is chosen, the mass can be estimated. A list of materials used for thermal resistant shielding in space missions are considered and listed in Table 2.2 [16]. Because of the hypervelocity impact of the HAIV, the heat of vaporization is the major concern. As the leader spacecraft of HAIV impacts, material composition on the asteroid and the materials on the follower spacecraft of HAIV act like liquid plasma, vaporizing as they both collide with the target asteroid. To make certain of the survivability of the

Table 2.2: List of materials and their properties considered for a thermal shield.

Materials	Density (kg/m <sup>3</sup> )	Energy to Melt (J/kg)	Energy to Boil (J/kg)	Energy to Vaporize (J/kg)
Aluminium	2,700	8.40e5	2.47e6	1.1e7
Beryllium	1,848	2.82e6	5.9e6	3.3e7
Cadium	8,650	1.37e5	2.39e5	8.88e5
Copper	8,960	5.3e5	1.1e6	4.73e6
Iron	7,874	7.96e5	1.33e6	6.26e6
Magnesium	1,738	9.41e5	1.39e6	5.24e6
Niobium	8,570	7.15e5	1.30e6	7.43e6
Silicon	2,330	1.2e6	2.51e6	1.28e7
Titanium	4,500	1.08e6	1.98e6	8.88e6
Tungsten	19,250	4.80e5	7.57e5	4.48e6
Vanadium	6,100	1.07e6	1.80e6	8.87e6
Zirconium	6,520	5.73e5	1.26e6	6.47e6

NED and its triggering system, a mass-efficient and thermal resistant material is needed. From Table 2.2, it can be seen that aluminum, beryllium, and silicon require very high energy to vaporize. A large variety of alloys are readily available with aluminum providing moderate temperature and good strength-to-weight ratio. Beryllium offers the highest stiffness with high temperature tolerance but its toxicity to humans requires extensive safety measures [16]. Silicon is usually mixed with other metals to provide more strength and higher thermal tolerances. Mixing it with carbon creates a great protective covering used in space mission applications such as the space shuttle. Also, titanium is a lightweight, high strength metal that can endure extreme temperatures but lacks durability. A thorough analysis of structural loads and thermal loads is undertaken through the ADRC's hydrodynamics code to find the best material properties for the thermal shield.

The hydrodynamics code developed by the ADRC is based on a meshless model used previously for asteroid impactor analysis [14]. The initial impact is generated by a spherical shell matching the mass of the leading body, resulting in a field of hot gas and ejecta through which the payload must survive. It is suggested in Reference 14 that most warhead designs will experience melting or exceed the maximum allowable structural load in this region. Therefore, a shield design is desirable to mitigate the effects of incident vaporized rock from the lead body, substantially protect the payload from micrometeorites ejected from the impact, and allow for the maximum depth of burst. Figure 2.8 shows the peak specific energy of a 0.7 m diameter cylindrical aluminum payload shield as a function of depth for three nominal thicknesses. The horizontal line represents failure of the system to adequately protect the payload, resulting in failsafe detonation.

As observed in Figure 2.8, a minimal thickness for this shield is about 10 cm. Above this value, little additional penetration is observed, given the thermal gradient in this region. A complicating factor is the acceleration of the payload. The 10 km/s initial relative speed greatly exceeds the speed of sound in the shield structure, resulting in the equivalent of a standing shock along the shield. Ahead of this shock, the payload measures only minimal interruption. Some initial acceleration due to ejecta impacts and interaction with the gas environment is measurable, but shortly thereafter the maximum structural load is reached. An example estimate of peak acceleration as a function of depth for the previously discussed shield is found in Figure 2.9. Thickness of the shield has almost no effect on the maximum depth reached before structural failure, making overly thick shields a hindrance rather than a benefit.

Since the acceleration of the payload is almost discontinuous as it approaches the impact shock, a successful fuzing system must address this by timing detonation as a result of measurable information. This will either require sensors and triggers capable of reacting to the observable impact precursors (on the order of 10-20 microseconds), or more likely will require an array of sensors placed ahead of the payload. This



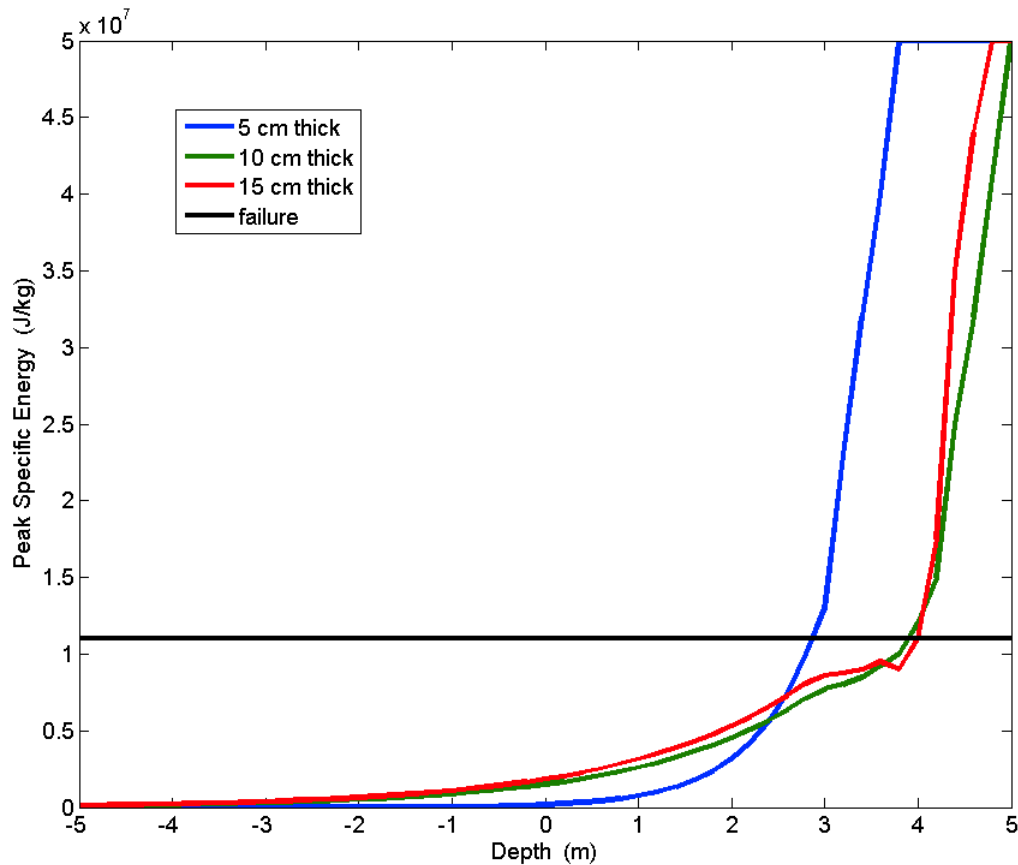


Figure 2.8: Peak payload specific energy for flat shield design.

could be accomplished either by placing sensors within the shield, or at the top of the follower spacecraft. A challenge to this approach would be that the sensors would need to survive in an environment capable of vaporizing many metals at least long enough to trigger the payload before impact.

Table 2.3 shows the results for minimum thicknesses and masses (of aluminum) of the flat, conical, spherical, and ogive nose cone discussed previously. These thicknesses are chosen to allow survival of the payload until the shield experiences structural failure. Further study found these thicknesses to depend very little on the material chosen, other than the mass of the resulting system, as the shape of the shield and the leader spacecraft tend to govern the achievable depth. Also listed in Table 2.3 is the maximum achieved depth of burst (DOB). Reduced performance can be achieved by using thinner shields, and lowering the required DOB would result in benefits for timing the detonation of the payload.

Based on this initial study, few conclusions can be drawn for the design of the payload thermal shield. First, the primary variables in achievable DOB is the shape, mass, and timing of the leader spacecraft. Additional analysis must be done to optimize this portion of the mission. Second, given a particular environment, a discontinuous shock to the payload presents challenges in determining how far to allow penetration before detonation. The payload cannot survive a direct impact at this speed, so it must be triggered using a combination of sensor and optical data at an appropriate data rate. Third, geometry of the shield seems to present a greater influence on DOB than any other variable. Adding thickness to the thermal shield in excess of the minimums presented do not result in further penetration, since both shields experience high structural loads at the maximum DOB. Finally, these results appear to be independent of the materials tested, as the limiting factor is the acceptable structural loads on the payload. However, significant mass can be saved by utilizing lighter alloys or materials for the thermal shield.

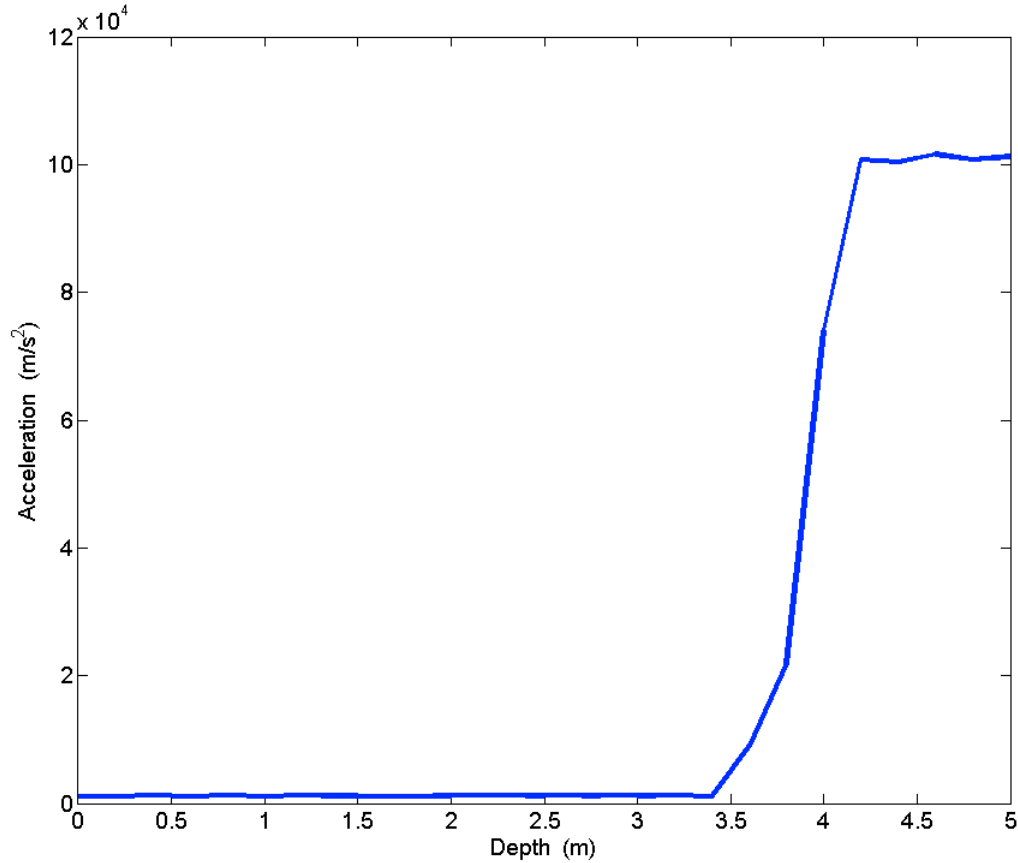


Figure 2.9: Example acceleration measurements for flat shield design.

### 2.4.5 Optional HAIIV Configuration Employing Deployable Mast

The leader and the follower can be separated and connected by deployable booms to ensure the NED payload follows the leader spacecraft safely and reliably. The boom must be sufficiently rigid to avoid oscillation motion of the two bodies. A deployable mechanism is preferable compared to a fixed structure due to volume constraints in the launch vehicle fairing. The connection mechanism can be divided into four categories, hinged, telescoping, an articulated mast system, and carbon fiber reinforced plastics (CFRP).

A hinged deployable boom consists of a hinged truss structure that is collapsible in storage and when deployed, locks into place and is held firm. ATK, the manufacturer of such trusses, reports 12.4 m and 6.2 m length trusses both with bending stiffness of  $1.5 \times 10^6 \text{ N}\cdot\text{m}^2$ , although mechanical properties are dependent on component materials [19]. Depending on the materials of the components for the system, the mass cost of such a system could be high. Most such trusses are planned to be retractable which adds a level of complexity that is unnecessary for the HAIIV application. ATK has manufactured many systems that have been tailored to specific mission requirements, and provides a favorable flight history. Another option that can also be classified as a hinged deployable boom is the folding hinged boom. ESA has been developing such systems and are much like the hinged truss. This particular option does not have the flight history as reported by ATK but mostly because it is highly tailorable to each application, making comparison difficult. The mass and mechanical properties of the hinged booms are strongly tied to the material selected. Composite materials may be lighter but more expensive and metals would be heavier but easier to manufacture.

ATK also provides a telescoping system which is also meant to be retractable. ATK reports a 5.5 m (deployed) boom with a bending strength of 72,000 N that weighs 20 kg [19]. Unfortunately, when the boom is deployed, the diameter of the next telescoping section is reduced in order to be efficiently stored. This



Table 2.3: DOB based on thickness parameter and shield geometry.

Shield	Thickness (cm)	Mass (kg)	DOB (m)
Flat Cylinder	9.4	97.7	3.8
Conical	10.1	105.0	4.1
Spherical	8.8	76.8	5.3
Ogive	10.5	116.1	4.6

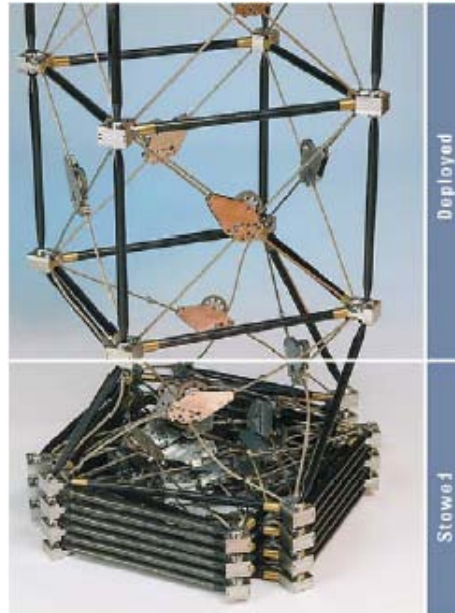


Figure 2.10: Illustrations of a deployable boom option that can be employed for the HAIV.

option has a high mass cost and is used primarily for larger spacecraft applications.

The articulated mast system is designed and manufactured by ATK and is used for deploying critical spacecraft payloads. It can be tailored for specific mission requirements and has efficient stowage volume. Its deployment capability has a high push force with or without active controls. It has lengths up to 60 m with a bending load capacity of 8,100 N·m and a bending stiffness of  $5.76 \times 10^8 \text{ N} \cdot \text{m}^2$ . The articulated mast system has had successful deployment on multiple ISS/STS missions [19]. Figure 2.4.5 shows the articulated mast system in its stored and deployed state. More research is needed to choose the boom that meets the requirements of connecting the two bodies of the HAIV.

## 2.4.6 Shock Prevention Systems

A shock prevention system may be needed to protect the NED and the triggering mechanisms from the structural shock upon impact. Hypervelocity testing is difficult and expensive making hypervelocity protection system technology premature. Nonetheless, further study of current shock prevention systems can provide a starting place for a hypervelocity nuclear interceptor application. Current shock prevention systems include airbags (automobiles and spacecraft landing systems), steel and foam energy reduction barriers, hydraulic isolators and dashpots, and foam and fiber-matrix material systems.

Airbags have been used extensively in automobiles as a safety device. It consists of a flexible shape

designed to inflate instantaneously during an automobile collision. Its purpose is to prevent occupants from striking interior objects. Airbags are also used in aerospace applications, in particular, the landing of the Mars Pathfinder exploration rover to dissipate the impact energy upon landing. The airbag configuration inflates and absorbs the impact shock when the rover is traveling less than 25 m/s. These airbags (90 kg) are rated for a maximum of 50 g deceleration for the 290 kg rover [17]. The material of the airbag and the pressure inside the airbag can be chosen depending on the kinetic energy of the object. However, airbags perform efficiently at lower speed levels and might prove to be ineffective for dissipating energy for a hypervelocity impact.

The steel and foam energy reduction barriers or soft walls are found in competitive racing. Other forms of soft walls include cello foam (mixture of polystyrene and polyethylene barriers), polyethylene energy dissipation system (stacked polyethylene cylinders), and rubber casings tied to concrete walls. Soft walls provide safer accidents in place of concrete barriers and less destructive damage to the race car on impact. The steel and foam energy reduction barriers consist of structural steel tubes and bundles of closed-cell polystyrene foam. The theory behind the design is that the barrier absorbs a small amount of the kinetic energy which is dissipated along the wall, rather than transferred back into the impacting object. Different types of density foams amounts to the energy that can be absorbed from an impact. Foam thickness, firmness, density, and porosity may affect how well the foam system can absorb shock (impact dissipation) and decelerate an object. Foams with the lowest porosity are generally better suited foams for heavier objects requiring greater energy absorption [18]. The energy dissipation comes from the distortion of the material, however the energy levels of a hypervelocity impact coincide with the vaporization of most materials. Even if the foam were to survive, the amount of energy absorption required would be so large that the volume and mass of the system would be infeasible. Hydraulic isolators, dashpots, dampers, and buffers are primarily used for shock and vibration prevention during storage and launch of aerospace and defense applications. Currently, a shock prevention system capable of handling the impact energy does not exist. Experimental efforts and testing of an integrated shock prevention system could be required for hypervelocity impacts.

## **2.4.7 Attitude Determination and Control System (ADCS)**

A baseline ADCS of the HAIV is modeled after the flight-proven system of the Deep Impact mission [21] with minor adjustments for the specific purposes of the HAIV. A baseline Divert and Attitude Control System (DACS) of the HAIV consists of 4 large divert thrusters each capable of 540 N of thrust using monomethylhydrazine (MMH) fuel and multiple smaller thrusters producing 30 N of thrust. The 4 large divert thrusters are positioned at the center of mass to provide two-directional translational control during the terminal guidance phase. The smaller thrusters are used to change and maintain the attitude of the spacecraft. The total number of thrusters and their specific locations on each spacecraft need to be further studied.

The sensors of the baseline ADCS include one Northrop Grumman Scalable Space Inertial Reference Unit (SSIRU), four Ball Aerospace's CT-633 Star Trackers, and one Imager. The SSIRU contains four Hemispherical Resonator Gyro Sensors and four accelerometers which provide a reading of angular rates and accelerations of the body in the body frame. The star trackers provide quaternions of the boresight of the instrument which then can be used to calculate attitude of the spacecraft [22]. The Imager acquires images of the impact site which are then processed for both trajectory and attitude adjustments [23]. The attitude is controlled by a set of small thrusters.

The ADCS has three operational modes, De-Tumble, Approach, and Impact. The De-Tumble mode occurs at the beginning of the terminal phase and is meant to stabilize the spacecraft's attitude. During the Approach mode, the ADCS maintains attitude while GNC executes maneuvers to impact the target NEO. During the Impact mode, ADCS gives attitude adjustments in preparations for terminal impact. Precision attitude stabilization of the two bodies, connected by deployable booms, can be a challenging control problem. In addition to the stated modes, ADCS also needs a safe mode that is required if the spacecraft is malfunctioning or experiencing unexpected errors. If this safe mode is activated, it will place the spacecraft into a low rate stabilizing spin until errors can be addressed.

Table 2.4: Peak power budget of each subsystem of the HAIV in various operational modes.

<b>Types of Mission Phase and Power Mode</b>				
	Departure	Orbit Transfer	TCMs	Terminal Phase
<b>Subsystem</b>	<b>Mode 1</b>	<b>Mode 2</b>	<b>Mode 3</b>	<b>Mode 4</b>
Propulsion	180	0	180	0
CD & H	70	70	70	70
Electrical	50	50	50	50
Communications	0	220	0	220
GNC	80	0	80	80
ADCS	75	0	75	75
Thermal	60	60	0	0
NED Payload	0	0	0	15
<b>Subtotal (W)</b>	<b>515</b>	<b>400</b>	<b>455</b>	<b>510</b>
20% Margin	103	80	91	102
<b>Total Power(W)</b>	<b>618</b>	<b>480</b>	<b>546</b>	<b>612</b>

#### 2.4.8 Power System

The peak power usage estimates for the baseline HAIV are listed in Table 2.4. Mode 1 is the initial phase of the mission and occurs immediately after spacecraft deployment from the launch vehicle fairing. During this mode, the spacecraft is performing all check-out operations and de-tumble maneuvers. Communications remain off until the attitude of the spacecraft is stabilized. Mode 2 is the main mode that the spacecraft remains in during the transfer phase and interval parts of the terminal phase. Mode 3 is used for deep space maneuvers and TCMs during the orbit transfer phase. Through these periods, the communications and thermal controls are briefly suspended to save power. Mode 4 is the final phase for both the leader and the follower spacecraft. As power for targeting, communications, and trajectory adjustments rise, the thermal control system's power is reduced. It should be noted that the power requirement for arming the NED in mode 4 is applicable for the follower spacecraft. As the operations of the HAIV are refined for each specific disruption technique, more accurate peak power estimates can be achieved.

During the orbit transfer phase, solar cells along with secondary batteries can be used. For the maximum peak power required during transfer, a minimum area of 3.3 m<sup>2</sup> is needed. A 7.4 m<sup>2</sup> Emcore In-GaP/InGaAs/Ge triple-junction solar cell panel with greater than 30% cell efficiency is mounted on one entire face of the spacecraft. It is intended that this face will be in nearly direct sunlight throughout the duration of the mission. Two adjacent faces also have solar cells. These three arrays will produce sufficient power for recharging secondary batteries after peak operations. Secondary rechargeable batteries will be necessary to power the spacecraft during peak and non-peak power operations. Research in this area is still needed to ensure the optimal product for the operations. Since secondary batteries are rechargeable, the mass of these batteries is much smaller. The follower spacecraft can use 2 Lithium-ion rechargeable batteries, each with a mass of 6 kg and capable of 300 W-h with an approximate time to recharge of 40 minutes [16]. Similar batteries have been used on the Mars Spirit and Opportunity Rovers.

Since the terminal phase requires a sufficient amount of power for at least 24 hours, the leader and follower spacecraft use primary batteries. Silver-cadmium and Nickel type batteries have a high mass cost due to their low-energy densities for the required 24-hr period. Although Silver Zinc has had a long flight history, the mass cost of such a battery is still higher than that of a Lithium type battery [16]. A Lithium type battery has a very high energy density such that for an intensive power period of 24 hours, the Lithium type batteries have an estimated mass of 17 - 43 kg [16].

Table 2.5: Mass breakdown for a baseline primary HAIV using Delta IV M+ launch vehicle class.

Vehicle	Description	Mass (kg)
Leader/Impactor	Dry Mass	285
	MMH Propellant	30
	<b>Wet Mass</b>	<b>315</b>
Follower	Dry Mass	1,170
	NED Payload	1,000
	Thermal Shield	135
	Deployable Boom (Optional)	55
	<b>Total Dry Mass</b>	<b>2,170</b>
	N <sub>2</sub> O <sub>4</sub> Propellant	775
	<b>Wet Mass</b>	<b>2,945</b>
Total Spacecraft	Dry Mass	2,455
	Wet Mass at Launch	3,260
	Mass at NEO	2,710
	Mass Margin (30%)	978
	<b>Total Mass w/ Margin</b>	<b>4,238</b>

#### 2.4.9 Mass Budget Summary

Table 2.5 shows the mass breakdown of a baseline primary HAIV carrying a 1000-kg NED payload. The leader spacecraft has a wet mass of 315 kg and the ability to provide a total  $\Delta V$  of 270 m/s which is similar to what the impactor spacecraft used in the Deep Impact mission during its terminal phase. The follower spacecraft has a dry mass of 1,170 kg carrying an NED payload of 1,000 kg. Depending on the material selected, the thermal shield and the optional deployable booms are estimated at an average of 135 kg and 55 kg, respectively, which correspond to previous space missions (Deep Impact Mission and Space Shuttle). The follower spacecraft also has the propellant necessary to execute trajectory correction maneuvers ( $\Delta V$  of 550 m/s) during the transfer orbit and adjustment maneuvers ( $\Delta V$  of 270 m/s) during the terminal phase. The mass of the HAIV upon arrival at the target NEO is estimated at 2,710 kg. A mass margin of 30% is used to account for uncertainties, thus making the total wet mass at launch approximately 4,238 kg.

Figure 2.11 illustrates the HAIV in a Delta IV M+ fairing. Without using an upper stage or orbital transfer vehicle, the Delta IV M+ has the capability to deliver the HAIV in a direct C3 trajectory towards the target NEO [24]. The propellant system on the HAIV uses a bi-propellant feed system of dinitrogen tetroxide (N<sub>2</sub>O<sub>4</sub>) coupled with MMH attitude thrusters. The N<sub>2</sub>O<sub>4</sub> propellant system has a restartable engine capable of producing 4,400 N of thrust at a specific impulse of 326 seconds, making it favorable for executing TCMs. The MMH attitude thrusters are used for attitude adjustments and terminal adjustment maneuvers. The leader and follower spacecraft are equipped with small MMH attitude thrusters.

The proposed HAIV, as shown in Figure 2.11, takes the form of a box-shaped impactor spacecraft equipped with thrusters and targeting instruments. It connects to a hexagon-shaped follower spacecraft equipped with 4 divert thrusters, a high-gain antenna, a thermally resistant shield, and an NED. The HAIV has a total length of approximately 6.7 m and a circular base of 4 m. The follower spacecraft incorporates a shelf that holds the leader spacecraft and the optional stowed booms. The leader spacecraft separates from the follower spacecraft by pyrotechnic attachments.

The HAIV is configured by using unscaled dimensions of commercial off-the-shelf components and materials such as ATK's fuel tanks, bi-propellant engine, optical instruments, etc. These dimensions and mass properties accurately reflect a preliminary configuration of an innovative HAIV. Through these dimensions and mass properties, the center of mass (CM) can be calculated. The reference coordinate system lies at the top center of the engine with the  $y$ -axis going through the length of the spacecraft, the  $z$ -axis pointing away

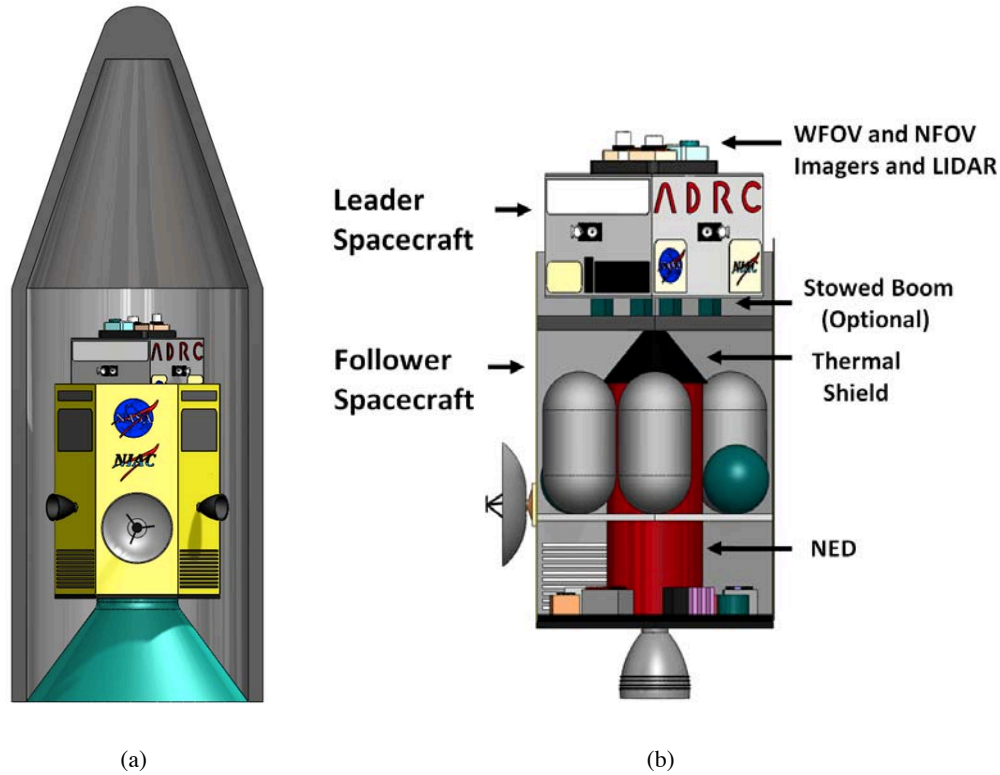


Figure 2.11: A baseline two-body HAIV configured for launch.

from the HGA, and the  $x$ -axis orthogonal to both. Assuming the CM of each component is its centroid, the CM of the HAIV at launch is located at (0, 2.15, -0.013) m. After separation between the two bodies, the follower spacecraft takes on a new CM at (0, 1.8, -0.018) m. The divert thrusters are pre-positioned at this new  $y_{cm}$  component as depicted in Figure 2.11. If the optional configuration of the HAIV with a rigid boom connection between the two bodies is chosen, the CM moves along the  $y$  direction towards the top front of the follower spacecraft. A 10-m rigid boom connecting the two bodies yields a new CM at (0, 3.45, -0.016) m. However, a 16.5-m boom could be used producing a  $y_{cm}$  of 4.22 m but is not advised as the length of the follower spacecraft is 4.3 m. The leader and boom shelf is located at 3.6 m and serves as a conservative location to not allow the CM to go beyond. By constraining the CM to the boom shelf or below, a 10-m rigid boom can be used.

Other secondary concept options of the HAIV exist depending on  $\Delta V$  demand, mission budget, and NEO characteristics. NED payloads and fuel tanks can be interchanged easily with slight modification to the HAIV and to accommodate different launch vehicles. A Delta II class launch vehicle in conjunction with an upper stage can be used to launch a smaller HAIV (1,450-kg) that is capable of carrying a 300-kg NED payload. Likewise, a Delta IV Heavy launch vehicle class can deliver a scaled up version of the HAIV (3,770-kg) capable to carry a 1,500-kg NED payload. This design process is explained in a detailed flow chart and is used to consider all feasible planetary defense technology demonstration missions.

## 2.5 Conclusion

When the warning time of an Earth-impacting asteroid is short, the use of nuclear explosives may become necessary to optimally disrupt the target NEO. Requirements of a nuclear disruption mission prove to be

challenging due to direct intercept speeds, nuclear disruption technique, impact speed limit of state-of-the-art NED fuzing mechanisms, and structural and thermal loads acting on the spacecraft. A concept of blending a hypervelocity kinetic impactor with a subsurface nuclear explosion has been proposed for optimal penetration, fragmentation, and dispersion of the target NEO. A baseline hypervelocity asteroid interceptor system consists of a kinetic-impact leader spacecraft and a follower spacecraft carrying a 1,000 kg-NED. A preliminary development of an HAIV, including thermal shielding simulations, selection of fuzes and optical instruments, terminal guidance operations, and other secondary configurations have been discussed in this paper. A more detailed spacecraft subsystem design is needed to prove spacecraft feasibility and durability. Additional hydrodynamic simulations include unique hypervelocity impact shields, calculation of the optimal separation distance between the two-body system, and possible illustration of the terminal phase for each nuclear disruption technique.

## 2.6 References

- [1] B. Wie, "Hypervelocity Nuclear Interceptors for Asteroid Deflection or Disruption," *IAA 2011 Planetary Defense Conference*, Bucharest, Romania, 9-12 May 2011. Also published in *Acta Astronautica*, May 2012.
- [2] *Defending Planet Earth: Near-Earth Object Surveys and Hazard Mitigation Strategies: Final Report*, National Research Council, 2010. [nap.edu/catalog/12842.html](http://nap.edu/catalog/12842.html)
- [3] B. Wie, and D. Dearborn, "Earth-Impact Modeling and Analysis of a Near-Earth Object Fragmented and Dispersed by Nuclear Subsurface Explosions," AAS 10-137, AAS/AIAA Space Flight Mechanics Meeting, 2010.
- [4] S. Wagner, A. Pitz, D. Zimmerman, and B. Wie, "Interplanetary Ballistic Missile (IPBM) System Architecture Design for Near-Earth Object Threat Mitigation," *2009 International Astronautical Congress*, Daejeon, Korea, 2009.
- [5] *Effects of Nuclear Earth-Penetrator and Other Weapons*, National Research Council, 2005. [nap.edu/catalog/12842.html](http://nap.edu/catalog/12842.html)
- [6] C. Hoyle, "MBDA reveals work on 'Hardbut' bunker-buster", *FLIGHT*, London, UK, October 14, 2010.
- [7] B. Kaplinger, B. Wie, D. Dearborn, "Preliminary Results for High-Fidelity Modeling and Simulation of Orbital Dispersion of Asteroids Disrupted by Nuclear Explosives," AIAA-2010-7982, AIAA Guidance, Navigation, and Control Conference, 2010.
- [8] A. Pitz, C. Teubert, B. Wie, "Earth-Impact Probability Computation of Disrupted Asteroid Fragments Using GAMT/STK/CODES," AAS-2011-408, AAS/AIAA Astrodynamics Specialist Conference Girdwood, AK, 2011.
- [9] D. Kubitschek, "Impactor Spacecraft Encounter Sequence Design for the Deep Impact Mission," Deep Space Systems, 2008.
- [10] "ESA - NEO Don Quijote Concept," European Space Agency, 2005. [esa.int/esa.html](http://esa.int/esa.html)
- [11] I. Carnelli, A. Galvex, F. Ongaro, "Industrial Design of the Don Quijote Mission," *57th International Astronautical Congress*, 2006.
- [12] C. Hansen, "Part V: Arming and Fuzing: Techniques and Equipment," 1995. [cryptome.org/nuke\\_fuze.htm](http://cryptome.org/nuke_fuze.htm)
- [13] "Nuclear Weapon Design," Federation of American Scientists, 1995. [fas.org/nuke/design.htm](http://fas.org/nuke/design.htm)
- [14] B. Kaplinger, B. Wie, and D. Dearborn, "Nuclear Fragmentation/Dispersion Modeling and Simulation of Hazardous Near-Earth Objects," IAA Planetary Defense Conference, Bucharest, Romania, May 9-12, 2011.
- [15] V. G. Chistov et al., "Nuclear Explosive Deep Penetration Method into Asteroid," Central Institute of Physics and Technology, Russia, 1997. [csc.ac.ru/news/1997\\_1/ae31.pdf](http://csc.ac.ru/news/1997_1/ae31.pdf)

- [16] J. French and M. Griffin, *Space Vehicle Design*, AIAA, 2004.
- [17] “Mars Pathfinder and Mars Rover Airbag Systems,” ILC Dover, 2011. [ilcdover.com/Mars-Pathfinder-Exploration-Rover-MER/](http://ilcdover.com/Mars-Pathfinder-Exploration-Rover-MER/)
- [18] “Information on Flexible Polyurethane Foam,” Polyurethane Foam Association, INTOUCH, Vol. 5, 1996.
- [19] “Deployable Structures,” ATK, 2011. [atk.com/capabilities/deployable\\_structures.asp](http://atk.com/capabilities/deployable_structures.asp)
- [20] L. Herbeck et al., “Development and Test of Deployable Ultralightweight CFRP-Booms for a Solar Sail,” European Conference on Spacecraft Structures, Materials and Mechanical Testing, 2000.
- [21] M. Hughes, C. Schira, “Deep Impact Attitude Estimator Design and Flight Performance,” *Advances in Aeronautical Sciences*, Published for the American Astronautical Society by Univelt, 2006.
- [22] “Space Inertial Reference Units,” Northrop Grumman, 2011. [northropgrumman.com/solutions/siru/](http://northropgrumman.com/solutions/siru/)
- [23] D. Kubitschek et al., “Autonomous Navigation for the Deep Impact Mission Encounter with Comet Tempel 1,” Deep Impact Mission: Looking Beneath the Surface of a Cometary Nucleus, 2005.
- [24] G. Vardaxis et al., “Conceptual Design and Analysis of Planetary Defense Technology Demonstration Mission,” AAS 12-128, AAS/AIAA Space Flight Mechanics Meeting, 2012.

## Chapter 3

# Modeling and Simulation of Hypervelocity Kinetic Impact and Nuclear Explosions

### 3.1 Introduction

The threat of a hazardous asteroid impacting the Earth is a subject that has garnered much attention over the past couple of decades. One of the issues that remain unresolved is the engineering of systems capable of mitigating these threats. While the most likely near-term threat is that of a low-altitude airburst, the expected energy of an event such as Tunguska would be devastating in a highly populated area. Additionally, though the population of catastrophic impactors has been well surveyed, it is estimated that thousands of bodies over 140 m in diameter remain undiscovered [1]. Therefore, it is unknown whether a proposed flight system could reach a majority of orbits for these types of objects within a reasonable timeframe, while controlling mission parameters such as the relative arrival (intercept) velocity. A study by the National Research Council suggests that nuclear explosive devices may be the only option for late warning cases [2]. It has been shown that disruption of a small body can be a viable late-term mitigation method for a variety of orbits with as little as 10 days of lead time between intercept and the predicted impact date [3,4]. This effect has so far been studied with a small set of possible break-up behaviors of the target asteroid. The current project extends this exploration to asymmetric 3D targets, in an effort to better characterize the orbits for which this approach may yield satisfactory results.

The problem to be solved is that of a disrupted NEO dispersing along the orbit as a result of a standoff, contact, or subsurface nuclear explosion mission. Initial simulations in [3,5,7,8] used a spherical axisymmetric NEO model, with the key limitations being the size of the target and a lack of a range of source energy input. With a new computational approach to the hydrodynamic simulations, we efficiently compute results for a 3D model of general characteristics. This will allow the current model to address much larger targets with increased resolution and a faster turnaround time, so the influence of more parameters can be investigated. A nonlinear orbit solver is presented that calculates an impacting trajectory given boundaries of a  $(a, e, i)$  sampling space. This approach increases our understanding of what components of the interplanetary environment affect the likelihood of a NEO being on a collision path with the Earth. Dispersion along these orbits is computed including particle self-gravitational effects and collisions [6] to determine mission effectiveness for a variety of possible cases.

A major bottleneck in determining appropriate mitigation methods for NEOs has been a lack of experimental data on the efficacy of each approach, forcing a reliance on simulations to determine mission effectiveness. As we move from the concept stage into true mission planning for effective NEO threat mitigation, we must depart from simulation of a few sample cases and instead use actual mission parameters to integrate modeling and simulation into the mission design cycle. This chapter presents the development of simulation tools designed to be implemented as part of the mission design procedure for nuclear fragmentation and dispersion of a NEO. New high-throughput neighbor-finding methods are suggested for the particle represen-



tation of disrupted NEOs. This approach becomes more effective using the GPU (graphic processing unit) accelerated computational technology of the current simulation toolkit. In contrast to the Weibull distribution used to seed implicit flaws in brittle materials [3,5], the current simulation set develops a tensor relationship for material characteristics and orientation. This allows for more realistic size and shape generation for NEO fragments by treating damage as a local quantity (cracks) rather than a distributed state variable. GPU acceleration of this model is up to 200x faster on a single workstation, continuing a trend of increasing computational complexity while also increasing efficiency. This approach allows us to compute a range of values rather than monolithic single simulations, and is incredibly critical for the orbital dispersion analysis. Sensitivity to the orbital parameters is a true unknown, since large impacting NEOs have yet to be observed, so computation for a range of these values is a necessity.

Previous work [3,4,5,6] showed that a large amount of data can be processed using GPU simulation. Initial work was focused mostly on prediction of relative impacting mass, but disruption at different times along a given orbit can have a large effect on the resulting shape of debris. The proposed approach looks at the fragmentation model to better address how uncertainty in the NEO breakup affects orbital prediction, particularly in the case of variable time-to-impact. This allows for a more clear set of objectives for mission design. Another new result is the availability of representative 3D fragment distributions for non-spherical bodies. This will improve the trajectory of the desired hypervelocity intercept mission by allowing full degrees of freedom in choosing the approach asymptote.

## 3.2 Simulation Model

This section presents the equations of motion and target model used in the fragmentation and dispersion simulations. For initial simulation work, two primary reference targets are used, to emphasize the differences between material compositions. Both were 100 meters in diameter, but had different bulk densities and material strength properties. The first target is a rubble-pile asteroid, with a bulk density of  $1.91 \text{ g/cm}^3$ . This is a likely target for demonstrating the behavior of more porous material. The second target is a single granite boulder with a bulk density of  $2.63 \text{ g/cm}^3$ . A linear model for material strength is used in this target with a yield strength of 14.6 MPa and a shear modulus of 35 MPa, resulting in a more granulated fragmentation and slower dispersion velocities. Real asteroid targets are expected to fall within these two extremes, with variances for composition, distribution of mass, and orientation. A Smoothed Particle Hydrodynamics (SPH) model [5] is used for the asteroid fragmentation simulation under 3 initial conditions: a subsurface explosion of 100 kt buried at a 5 m depth, a surface blast of 100 kt surrounded by a 1 m thick aluminum impactor, and a standoff blast at 10 m above the surface. We assumed an isotropic Weibull distribution of implicit flaws in the NEO material and conducted Monte Carlo simulation to establish a mean response of the target NEO to the fragmentation process for the initial model.

### 3.2.1 HAIV System Targets

Initial demonstration of the two body HAIV concept used spherical spacecraft dummy payloads to hit an inhomogeneous target with a diameter of 54 m. This method was directly compared to a single explosion on contact with the surface. The current asymmetric target consists of a contact binary system with a rubble pile exterior. With binary systems comprising about 16% of the known NEA population [9], an impactor mission faces an approximately 1 in 6 chance that the target it approaches will be a binary system. This is a characteristic that will be unable to be predicted ahead of time without radar observation, in the case of systems with close secondaries. It has been suggested that many irregularly shaped asteroids with unusual spin states could be contact binary (or multiple) systems. These types of systems would exhibit some of the same characteristics as monolithic rocks and as rubble piles [10]. Further, those asteroids identified as rubble piles could have large solid components beneath their regolith.

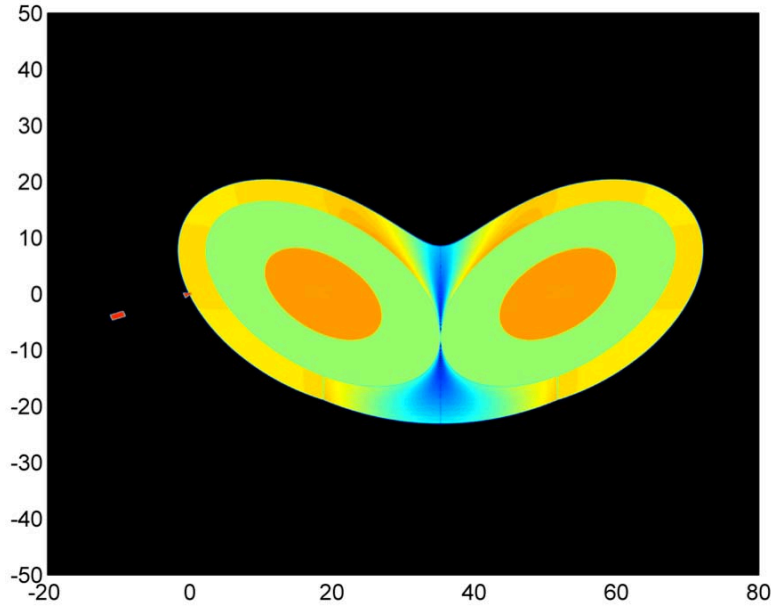


Figure 3.1: Asymmetric target asteroid model for 3D penetrated explosion simulation.

The two cores of the model system are elliptical, with major and minor axes of 50 and 30 meters, respectively. These cores are given material properties similar to granite using a linear elastic-plastic strength model, and are canted by 45 degrees relative to the horizontal. There is a vertical line of symmetry, so the cores are mirror images of one another. A rubble regolith extends 2 meters in depth vertically above each core, and is packed along lines of constant potential around the body, resulting in a maximum regolith depth of 14 meters. These properties result in exterior dimensions of the target being approximately 76 x 42 meters, as shown in Figure 3.1. The inner half of each core has an initial bulk density of  $2630 \text{ kg/m}^3$ , while the outer portion of the core is more porous material with an average bulk density of  $1910 \text{ kg/m}^3$ . Both sections use values for yield strength between 7-203 MPa and shear modulus between 8-22 MPa.

The initial impactor of the two-body spacecraft is an aluminum wedge 1 m in base diameter and 1.5 m in length. The nuclear payload follows, depositing 70 kilotons of energy upon reaching the initial impact site of the lead body. Most of this energy is absorbed in the crater region formed by the initial impact, though deeper absorption is allowed due to the fact that much of the material in this region has already been vaporized and superheated into a plasma state. The resulting shock wave has a peak compression of more than 2 times the initial density, and quickly overtakes the initial shock of the lead body impact, which is much weaker. This shock compresses much of one core far beyond the fracture strength of even the worst case material, rebounding off of the nearer side. This asymmetric behavior dissipates some energy due to interactions with the rebounding shock front. In the center area of deeper regolith, the seeding process naturally results in a much more porous material, absorbing energy from the shock. Upon reaching the second core at the far side, some large chunks escape the disruption process in some cases (even with lower material strengths).

In addition to the equations of motion used for the previous simulation version [3], an extra dimension was added. This was to investigate the potential for sources of errors in 2D cylindrical Smoothed Particle Hydrodynamics (SPH) codes, rather than an axisymmetric model. Other than an increase to the complexity of neighbor-finding calculations (as discussed later), no significant increase in code complexity was required. This is due to the fact that the SPH model equations are originally a 3D component/tensor formulation. Resulting coherent masses from the fragmentation process were propagated through a model of solar system dynamics until the predetermined date of impact. Masses remaining on impact trajectories undergo a simulation of reentry into Earth's atmosphere, resulting in final tallies of mass missing the Earth, fragments on capture trajectories, airburst events, and impacts of reduced-mass fragments.

### 3.2.2 Hydrodynamic Equations

For the purposes of the present simulation study, a meshless hydrodynamics model was desired. This approach would eliminate the need for storing and updating a grid, simplify calculations for large deformations, and allow for contiguous memory access to local field properties. The SPH formulation [11,12] was chosen to satisfy the first two goals, while the latter will be discussed with regards to the GPU implementation. The core idea of SPH is to approximate a field property  $f(x)$  by using a mollifier  $W$  (also known as an approximate identity) with compact support, as follows:

$$\langle f(x) \rangle = \int_{\Omega} f(s)W(x-s)ds, \quad W \in C_0^1(\mathbb{R}^n), \quad \Omega = \text{supp}(W) \quad (1)$$

where the brackets indicate the SPH approximation [12], allowing the field variables to be computed as a sum over the nearest neighbor particles representing the flow. In the present formulation,  $W$  is taken as the cubic spline kernel [11,12], with a variable isotropic domain of support with radius  $h$ . Changing  $h$  in space and time allows for the simulation to respond to changes in flow conditions with a change in local resolution [11,12]. A mass  $m$  is assigned to each particle representative in the model, as well as initial position and velocity components ( $x^\beta$  and  $v^\beta$ ) in each  $\beta$  direction. Material properties such as density,  $\rho$ , and specific energy,  $e$ , complete the state description. Similar to the above integral relationship, derivatives and integrals of field functions can be approximated, resulting in the following set of equations involving the kernel derivative (a scalar valued function of vector position  $\mathbf{x}$ ) [11-13]:

$$\frac{Dx_i^\alpha}{Dt} = v_i^\alpha \quad (2)$$

$$\frac{D\rho_i}{Dt} = \sum_{j=1}^N m_j (v_i^\beta - v_j^\beta) \frac{\partial W(\mathbf{x}_j - \mathbf{x}_i)}{\partial x^\beta} \quad (3)$$

$$\frac{Dv_i^\alpha}{Dt} = - \sum_{j=1}^N m_j \left( \frac{\sigma_i^{\alpha\beta}}{\rho_i^2} + \frac{\sigma_j^{\alpha\beta}}{\rho_j^2} + \Pi_{ij} \right) \frac{\partial W(\mathbf{x}_j - \mathbf{x}_i)}{\partial x^\beta} + F_i^\alpha \quad (4)$$

$$\frac{De}{Dt} = \frac{1}{2} \sum_{j=1}^N m_j \left( \frac{P_i}{\rho_i^2} + \frac{P_j}{\rho_j^2} + \Pi_{ij} \right) (v_i^\beta - v_j^\beta) \frac{\partial W(\mathbf{x}_j - \mathbf{x}_i)}{\partial x^\beta} + \frac{1}{\rho_i} S_i^{\alpha\beta} \epsilon_i^{\alpha\beta} + H_i \quad (5)$$

where repeated indices in a product indicate implied summation over all possible values,  $\sigma^{\alpha\beta}$  is the stress tensor,  $P$  is the pressure,  $S^{\alpha\beta}$  is the deviatoric (traceless) stress tensor,  $\epsilon^{\alpha\beta}$  is the local strain rate tensor,  $F$  represents external forces, and  $H$  represents energy sources.  $\Pi_{ij}$  represents the Monaghan numerical viscosity [12,14] used to resolve shocks, accommodate heating along the shock, and resist unphysical material penetration. The material strength model for the solid target uses an elastic-perfectly plastic description of strength [11-13], where the hydrodynamic stress is determined as

$$\sigma_i^{\alpha\beta} = -P_i \delta^{\alpha\beta} + (1 - \eta) S_i^{\alpha\beta}, \quad \eta \in [0, 1] \quad (6)$$

where  $\eta$  is a material damage indicator, to be discussed later. It should be noted that fully damaged material ( $\eta = 1$ ) is relieved of all stress due to deformation and behaves as a cohesionless fluid [13,15]. The rubble-pile target is treated in this manner by default. In this elastic-plastic model, the components of the deviatoric stress tensor  $S^{\alpha\beta}$  evolve using the following equation based on Hooke's law [11,16]:

$$\frac{DS_i^{\alpha\beta}}{Dt} = 2G_s \left( \epsilon_i^{\alpha\beta} - 3\delta_i^{\alpha\beta} \epsilon_i^{\gamma\gamma} \right) + S_i^{\alpha\gamma} R_i^{\beta\gamma} + R_i^{\alpha\gamma} S_i^{\gamma\beta} \quad (7)$$

where  $R^{\alpha\beta}$  is the local rotation rate tensor,  $G_s$  is the shear modulus, and the SPH approximation for these terms is given by

Table 3.1: Parameters for Tillotson equation of state in core material.

Parameter	Numerical Value	Units
$a_t$	0.5	
$b_t$	1.5	
$A_t$	7.1E10	Pa
$B_t$	7.5E10	Pa
$\alpha_t$	5	
$\beta_t$	5	
$E_0$	4.87E8	J/kg
$E_{iv}$	4.72E6	J/kg
$E_{cv}$	1.82E7	J/kg

$$\epsilon_i^{\alpha\beta} = \frac{1}{2} \sum_{j=1}^N \frac{m_j}{\rho_j} \left[ (v_j^\alpha - v_i^\alpha) \frac{\partial W(\mathbf{x}_j - \mathbf{x}_i)}{\partial x^\beta} + (v_j^\beta - v_i^\beta) \frac{\partial W(\mathbf{x}_j - \mathbf{x}_i)}{\partial x^\alpha} \right] \quad (8)$$

$$R_i^{\alpha\beta} = \frac{1}{2} \sum_{j=1}^N \frac{m_j}{\rho_j} \left[ (v_j^\alpha - v_i^\alpha) \frac{\partial W(\mathbf{x}_j - \mathbf{x}_i)}{\partial x^\beta} - (v_j^\beta - v_i^\beta) \frac{\partial W(\mathbf{x}_j - \mathbf{x}_i)}{\partial x^\alpha} \right] \quad (9)$$

To complete this system, we use the following equations governing the change of support radius  $h$  [11,12], and the fracture damage ratio  $\eta$  [13]. The latter is limited in accordance with the number of material flaws activated in the structure as

$$\frac{Dh_i}{Dt} = -\frac{1}{n} \frac{h_i}{\rho_i} \frac{D\rho_i}{Dt}, \quad \frac{D}{Dt} \eta^{1/3} = \frac{c_g}{r_s} \quad (10)$$

where  $c_g$  is the crack growth rate, here assumed to be 0.4 times the local sound speed [13], and  $r_s$  is the radius of the subvolume subject to tensile strain. In the present model, the latter term is estimated by interpolation based on the strain rate tensor of neighbor particles. An equation of state remains to complete the mechanical system. We use the Tillotson equation of state [17] in the solid asteroid and in the aluminum penetrator used to deliver the surface explosive, with the parameters listed in Table 3.1. This is modified to include porosity, and an irreversible crush strength, for the “rubble pile” target [15,18]. We assume a power law distribution for number of implicit flaws in a volume of material with respect to local tensile strain (a Weibull distribution), and assign flaws with specific activation thresholds to each SPH particle [13]. The maximum damage allowed to accumulate in a volume is described by

$$\eta_i^{\max} = \left( \frac{n_i}{n_i^{\text{tot}}} \right)^{1/3}, \quad \epsilon_i = \frac{\sigma_i^t}{(1 - \eta_i)E} \quad (11)$$

where  $n_i$  is the number of active flaws ( $\epsilon > \epsilon^{\text{act}}$ ) and  $n_i^{\text{tot}}$  is the total number of flaws assigned to a particle, which can vary widely, but is always at least one. Equation (11) also gives the relationship for the local scalar strain, as a function of the maximum tensile stress  $\sigma^t$ , the local damage, and the Young’s modulus  $E$ .

### 3.2.3 Tensor Damage Model

In the initial SPH model for comparison, the behavior of the core material under high stress is governed by the activation of implicit flaws. These flaws are seeded in the representation particles using a Weibull distribution with a coefficient of around 4.2E23 and an exponent between 6.2-9.5. Using a range of distribution exponents and strength properties allows us to examine the behavior of the core material with varying brittleness and

material cohesion. This turns out to be very important for this contact binary system, as strong core material absorbs energy from the disruption shock and can result in large remaining chunks of material. Smoothing lengths are chosen to allow for resolution of between 1 cm and 5 cm, which results in a hydrodynamic system of between 800,000 and 6,000,000 nodes. This system is scaled to be an ideal size for the GPU simulation programs developed at the Iowa State Asteroid Deflection Research Center (ADRC), maximizing both computational efficiency and simulation turnaround time.

For this comparison, a damage model using a tensor variable was implemented. The details are the same as those used in the Spheral code, developed by Mike Owen at the Lawrence Livermore National Laboratory. The variable tracked for material stress is the deviatoric stress tensor,  $S^{\alpha\beta}$ , which is advanced using a modification of Hooke's law [11,16]:

$$\frac{DS_i^{\alpha\beta}}{Dt} = 2G_s \left( \epsilon_i^{\alpha\beta} - 3\delta_i^{\alpha\beta} \epsilon_i^{\gamma\gamma} \right) + S_i^{\alpha\gamma} R_i^{\beta\gamma} + R_i^{\alpha\gamma} S_i^{\gamma\beta} \quad (12)$$

where  $R^{\alpha\beta}$  is the local rotation rate tensor,  $\epsilon^{\alpha\beta}$  is the local strain rate tensor,  $G_s$  is the shear modulus, and the SPH approximation for these terms is given by

$$\epsilon_i^{\alpha\beta} = \frac{1}{2} \sum_{j=1}^N \frac{m_j}{\rho_j} \left[ (v_j^\alpha - v_i^\alpha) \frac{\partial W(\mathbf{x}_j - \mathbf{x}_i)}{\partial x^\beta} + (v_j^\beta - v_i^\beta) \frac{\partial W(\mathbf{x}_j - \mathbf{x}_i)}{\partial x^\alpha} \right] \quad (13)$$

$$R_i^{\alpha\beta} = \frac{1}{2} \sum_{j=1}^N \frac{m_j}{\rho_j} \left[ (v_j^\alpha - v_i^\alpha) \frac{\partial W(\mathbf{x}_j - \mathbf{x}_i)}{\partial x^\beta} - (v_j^\beta - v_i^\beta) \frac{\partial W(\mathbf{x}_j - \mathbf{x}_i)}{\partial x^\alpha} \right] \quad (14)$$

We use a tensor damage variable defined per node  $D^{\alpha\beta}$  in order to support directionality in the damage evolution. Cracks are allowed to open up in response to strain aligned perpendicularly to that direction, and there is substantially reduced crack growth in orthogonal directions to the strain. The tensor strain,  $\sigma^{\alpha\beta}$  used is the “pseudo plastic strain” of SolidSpheral, due to Mike Owen, which evolves in time as

$$\frac{D\sigma_i^{\alpha\beta}}{Dt} = \frac{1}{G_s} \frac{DS_i^{\alpha\beta}}{Dt} \quad (15)$$

This is decomposed into a set of eigenvalues,  $\sigma^\nu$ , and eigenvectors,  $\Lambda^{\alpha\nu}$ , from which the directional scalar damage,  $\Delta^\nu$  is the magnitude of the  $\nu$ -th column of  $D^{\alpha\gamma} \Lambda^{\gamma\beta}$ . The maximum damage allowed to accumulate in a volume, similar to the formulation in [3, 5] but allowing for directionality, is:

$$D^{\max} = \max \left( \frac{n_i}{n_i^{\text{tot}}}, \Delta_i^\nu \right) \quad (16)$$

where  $n_i$  is the number of active flaws ( $\epsilon > \epsilon^{\text{act}}$ ) and  $n_i^{\text{tot}}$  is the total number of flaws assigned to a particle, which can vary widely, but is always at least one. These directional damages can then be time evolved using representative scalar evolution laws [3,13].

### 3.2.4 Neighbor Finding Implementation

One of the key limitations of past simulation approaches is that most proposed neighbor-finding methods for interpolation rely on complex logic and lists not suitable for efficient GPU implementation. Therefore, the addition of the third dimension makes this problem far more complex. A new approach for efficiently computing unions and intersections of integer sets on the GPU is proposed, allowing for neighbor-finding as an update process from previously computed relative relationships. Based on a standard Sort-and-Sweep approach in computer graphics [19], the power of this approach lies in how it scales with increased number of SPH interpolants. In addition to scaling superlinearly (compared to quadratic brute force calculations),

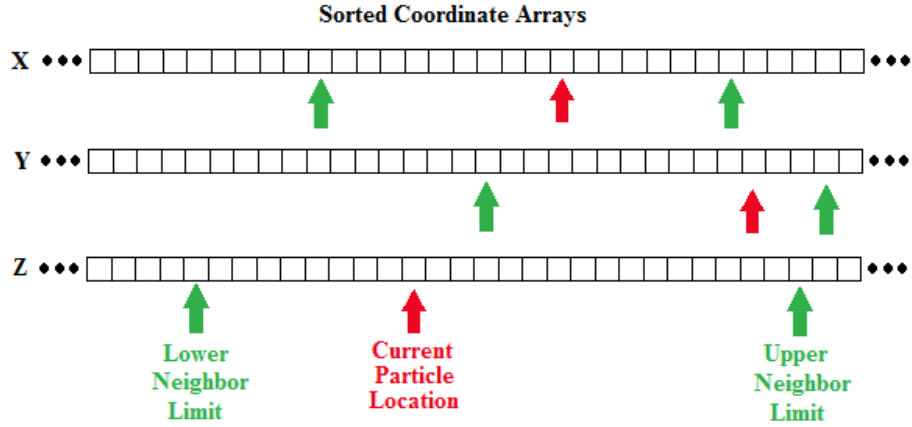


Figure 3.2: Description of sorted neighbor kernel process.

the present approach uses the Thrust library to sort the position components of the particles in parallel. This eliminates a series of memory transfers with the host and keeps all data on the GPUs.

A subsequent group of GPU kernels establish pointers to the limits on the sorted array for which candidate neighbor particles may belong. This reduces the neighbor finding to an integer union calculation, which can be conducted as a logical (true/false) operation. Comparing the position of the sorted particle IDs with the limits allows for a simple yes/no decision on whether a proposed neighbor could be within the support of the interpolation function. Figure 3.2 gives a depiction of this process for each computing thread. Figure 3.3 shows the improvements of the present model over in-place neighbor calculations (also on the GPU). While dimensionality affects the speed-up, there are still substantial gains made over past implementations.

### 3.3 Disruption Mission Profiles

This section outlines the initial conditions for three method of NEO deflection using nuclear explosive devices. For the initial demonstration cases, a 100 m diameter target asteroid is modeled with an energy source of 100 kt. The newer, asymmetric, model uses an energy source equivalent to 70 kilotons. Thermal emission is omitted from the subsurface and surface explosions due to absorption by surrounding material in the time scale of interest.

#### 3.3.1 Subsurface Explosion Setup

For this simulation, the explosive is modeled as a cylindrical energy source buried at a depth of 5 meters. As shown for the solid target in Figure 3.4, the blast wave compresses the NEO, reducing it to fragments, and disperses it primarily along the axis of the explosion. The resulting fragment distribution for a case like this has a peak between 20-70 m/s, with a tail of high-speed ejecta like that shown in Figure 3.4.

#### 3.3.2 Surface Penetrator Model

Two main models for an explosion at the surface are used. One is a static explosion, which results in vastly different systems depending on the composition of the body. For a solid target, cratering and pitting is expected rather than disruption. Even dispersed rubble-pile asteroids have a far lower mean fragment velocity than a similar subsurface system. The second model, shown here, includes an aluminum penetrator impacting the surface at 6.1 km/s. The explosion thermal energy turns the high-mass impactor into a plasma, which burrows into the surface as it releases its energy. Slower dispersion velocity is observed than the subsurface case, but this approach is extremely beneficial from an engineering standpoint, as there is strong coupling between

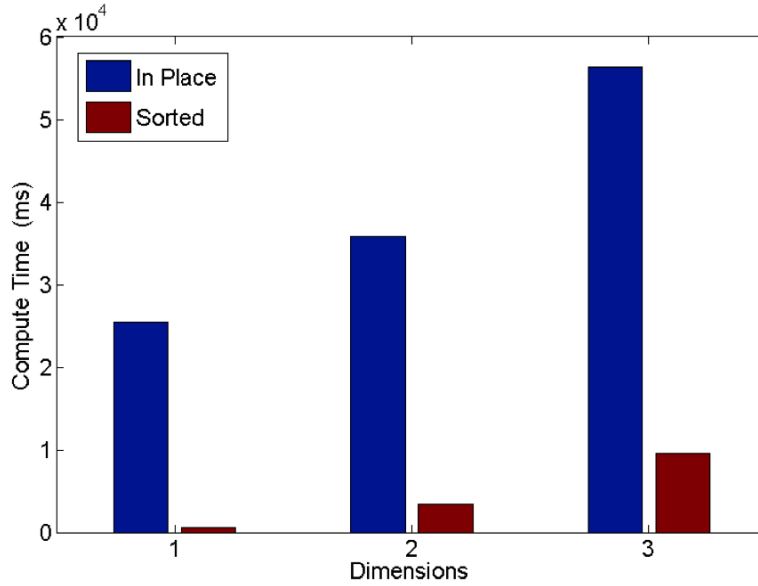


Figure 3.3: Neighbor search cost.

time-to-impact and a reduction in mission fuel cost [20]. The benefit to this method relative to a subsurface explosion is that it does not require a rendezvous, and therefore there are available launch windows for this type of mission right up until immediately before the impact date.

### 3.3.3 Standoff Energy Deposition

For a standoff blast, additional physics must be considered. An energy deposition strategy is required that does not directly compute X-ray and neutron scattering in the target. For this, a ray-tracing algorithm is used with radial energy deposition at the surface as shown in Figure 3.5 for neutrons. This is derived from a Monte Carlo scattering result from TART, a DOE neutron deposition code, in NEO analog materials [21]. A 10% neutron yield is assumed for these simulations, and a maximum deposition depth of 1.5 m to compare to deposition predicted for chondritic materials [22]. The overall deposition region (shown as the logarithm of deposited energy) is also shown in Figure 3.5. A modified SPH node representation is created that resembles an ablative modeling grid used in high-energy deposition physics. This distribution is shown in Figure 3.6, and has a minimum smoothing scale of 0.1 cm with a maximum local change rate of 10% up to 0.2 m resolution. Also in Figure 3.6, the resulting ablation provides an effect similar to that of a rocket, but also disrupts the rubble-pile target completely.

### 3.3.4 HAIV Concept

The HAIV target contains granite boulders at the elliptical cores with a bulk density of  $2.63 \text{ g/cm}^3$ . A linear model for material strength is used in this target with a yield strength of 14.6 MPa and a shear modulus of 35 MPa, resulting in a more granulated fragmentation and slower dispersion velocities. Real asteroid targets are expected to fall within the two extremes discussed earlier, with variances for composition, distribution of mass, and orientation.

A slice of the nominal three-dimensional target was shown in Figure 3.1. As an increase in computational burden, it performs moderately less efficiently than the two dimensional model. The overall velocity statistics, which are the governing variables behind successful disruption, are similar to those for the cylindrical case. The histogram for radial dispersion velocities of the fractured particles can be seen in Figure 3.7. There is a

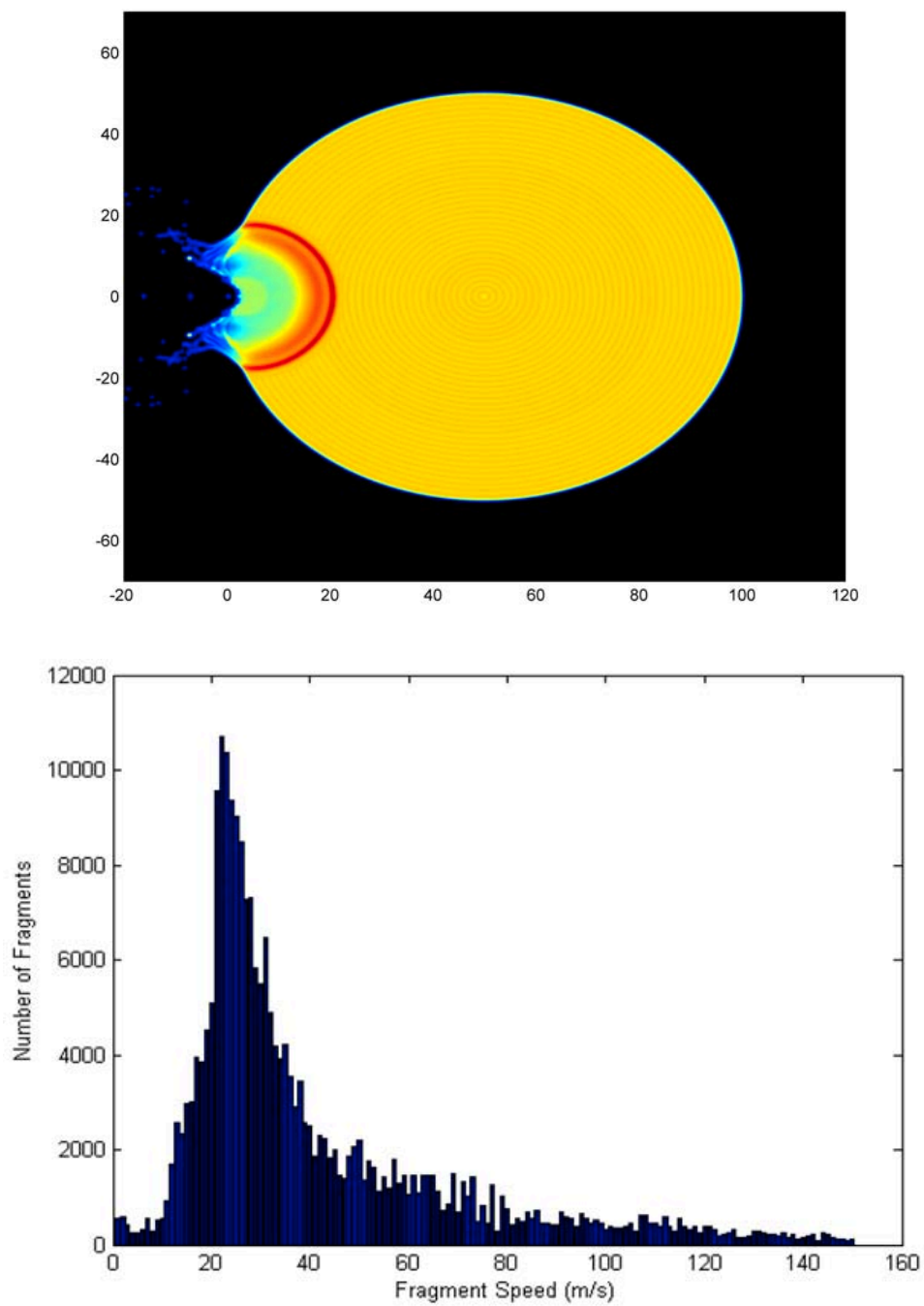


Figure 3.4: Subsurface explosion and resulting fragment velocities.



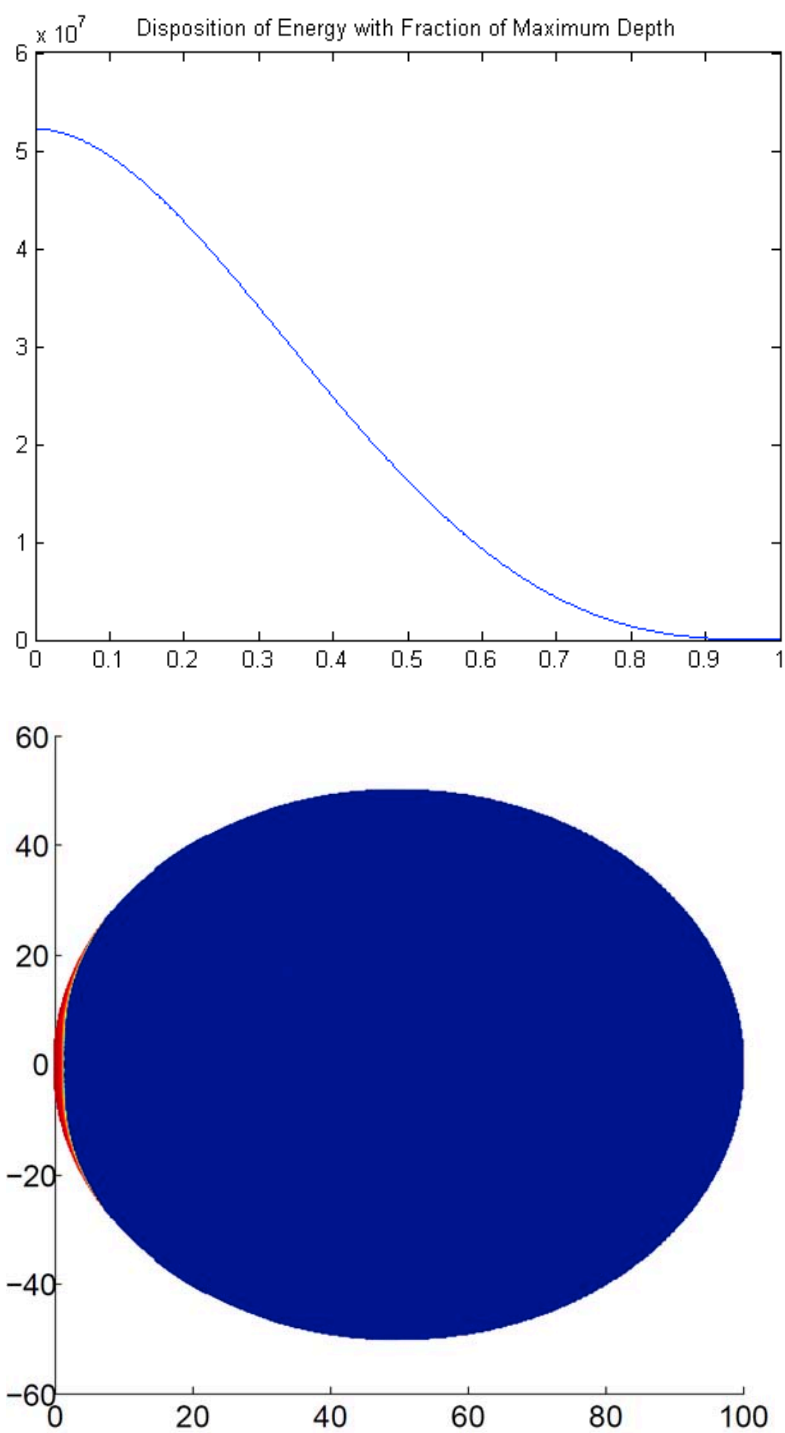


Figure 3.5: Radial energy disposition and total deposition region.

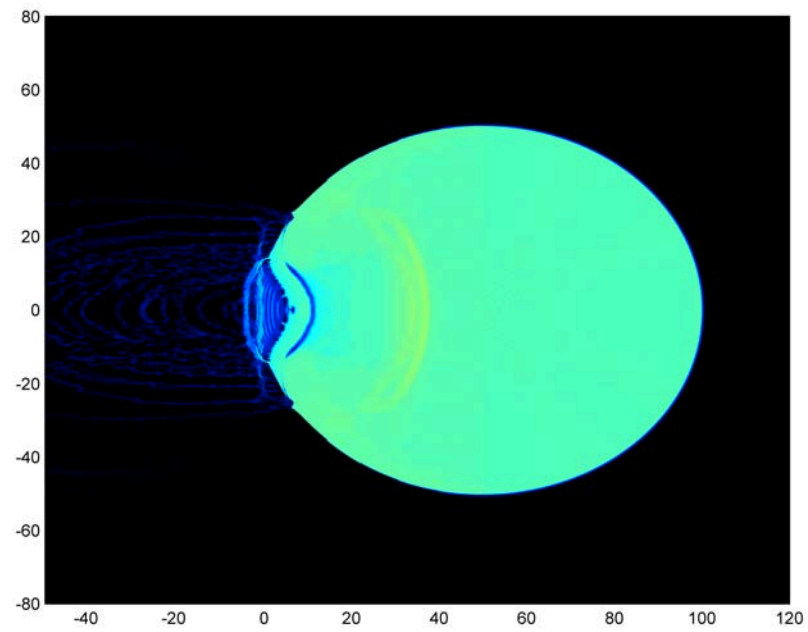
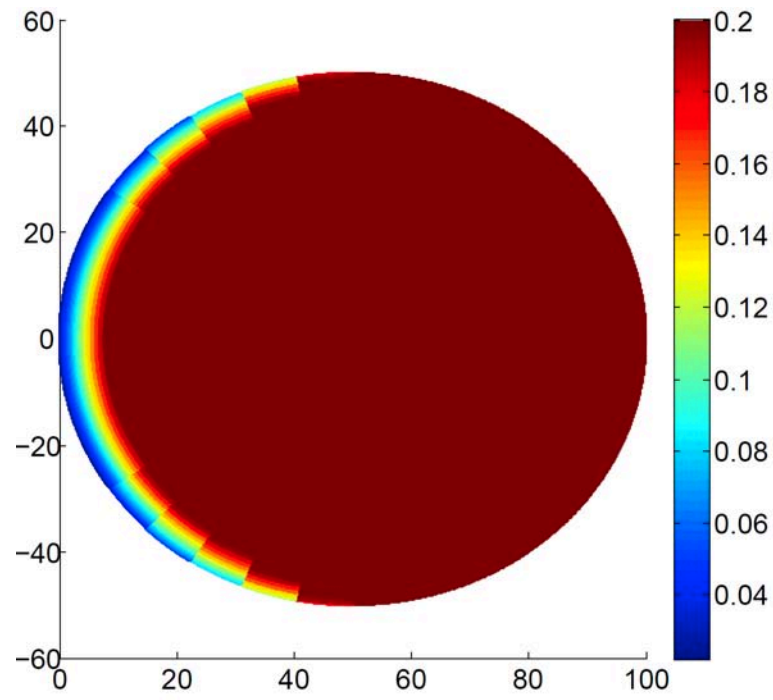


Figure 3.6: SPH nodes and resulting ablation for standoff model.

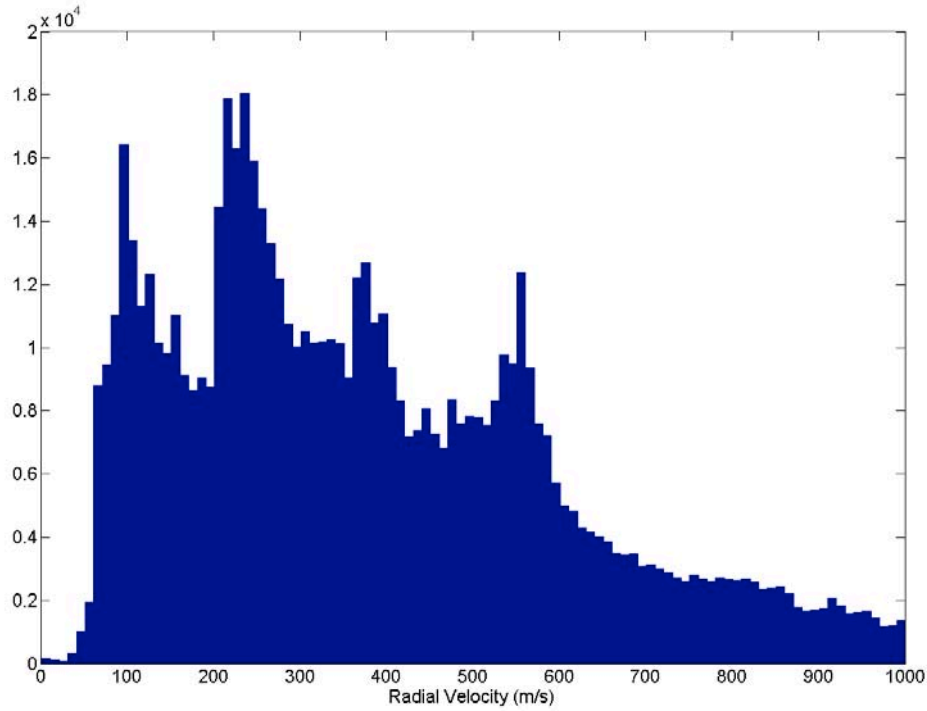


Figure 3.7: Radial dispersion velocity histogram for HAIV concept.

mean dispersion velocity for the HAIV case of almost 350 m/s.

The travel of the explosive shock can be seen in Figure 3.8. This process dissipates some energy due to interactions with the rebounding shock front. In the center area of deeper regolith, the seeding process naturally results in a much more porous material, absorbing energy from the shock. The new damage model allows for better tracking of crack propagation, such as that shown in Figure 3.9. Upon reaching the second core at the far side, some large chunks escape the disruption process in some cases (even with lower material strengths). A final hydrodynamic state can be seen in Figure 3.10.

There remains a high risk for this target of single largest chunks on the order of tens of meters. However, this material is highly stressed due to velocity gradients, and may be ripped apart in further time. The large velocity gradients and the location of the slowest debris can be observed in Figure 3.11. Further, these large chunks are still imparted substantial velocities from the blast 10-20 m/s, and have sufficient energy to disperse from the nominal impacting trajectory over tens of days.

Slower dispersion velocity is observed for the contact burst, as shown in Figure 3.12. The mean dispersion velocity is only 150 m/s, which is 2x less effective than the baseline HAIV. In terms of kinetic energy, the HAIV concept is superior by almost a factor of 10. It is clear that this HAIV approach is also extremely beneficial from an engineering standpoint, as there is strong coupling between time-to-impact and a reduction in mission fuel cost [20]. The benefit to this method relative to a subsurface explosion is that it does not require a rendezvous, and therefore there are available launch windows for this type of mission right up until immediately before the impact date.

### 3.4 Orbit Propagation

This section describes the identification of nominal orbits for a fixed impact time. Given a desired lead time, the optimal approach vector is computed using a differential step update, described in the following subsections. The cost parameter is the impacting percentage of the original target mass.

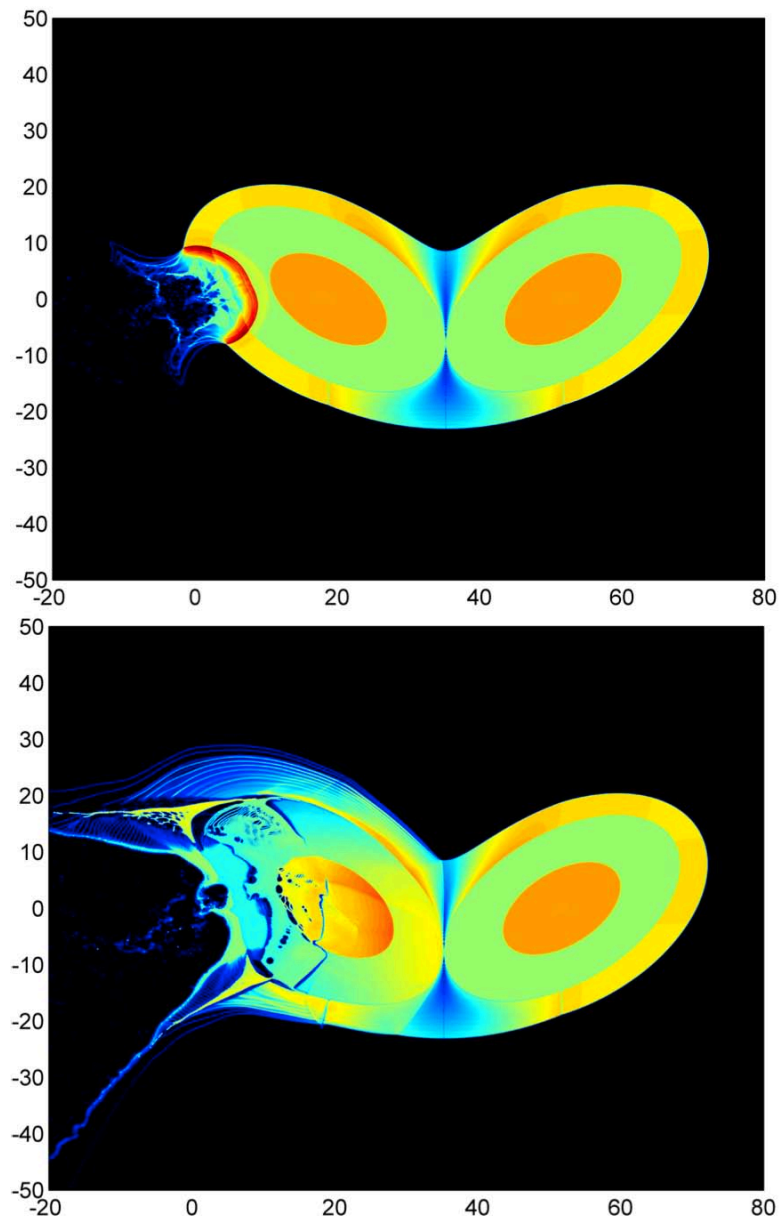


Figure 3.8: Asymmetric shock behavior.

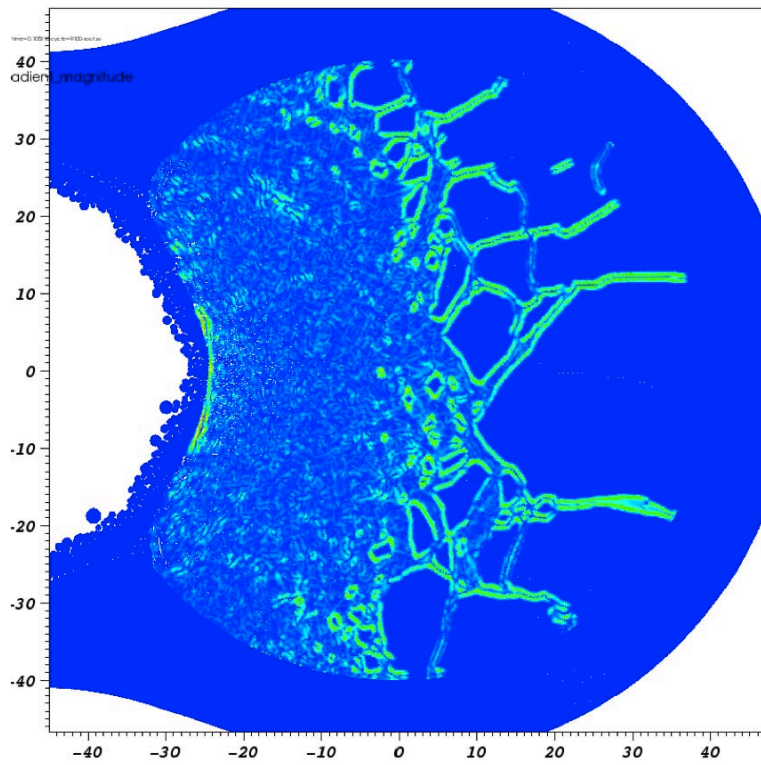


Figure 3.9: Example damage localization for tensor fracture model.

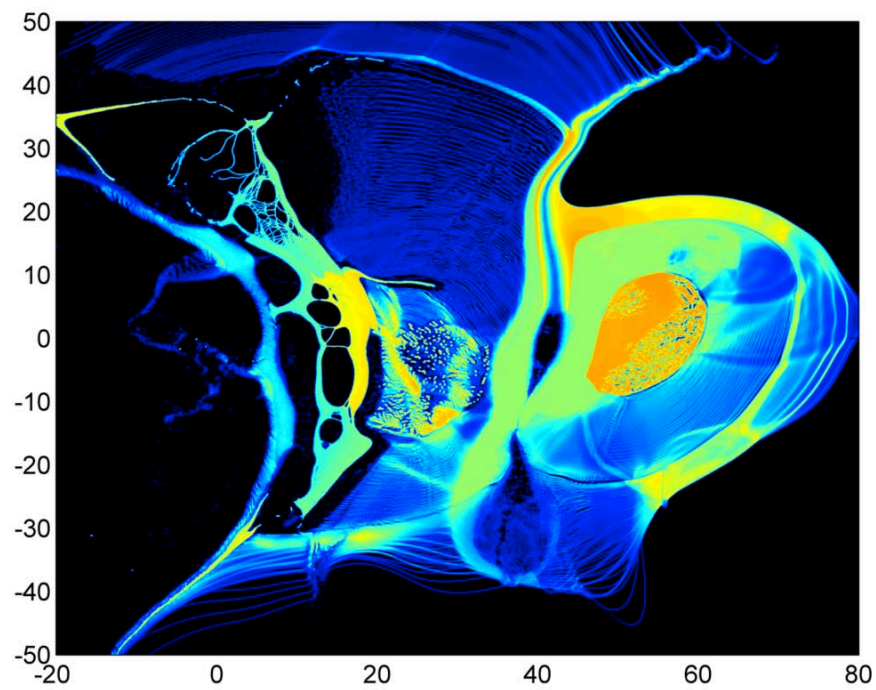


Figure 3.10: Final disruption of NEO target.

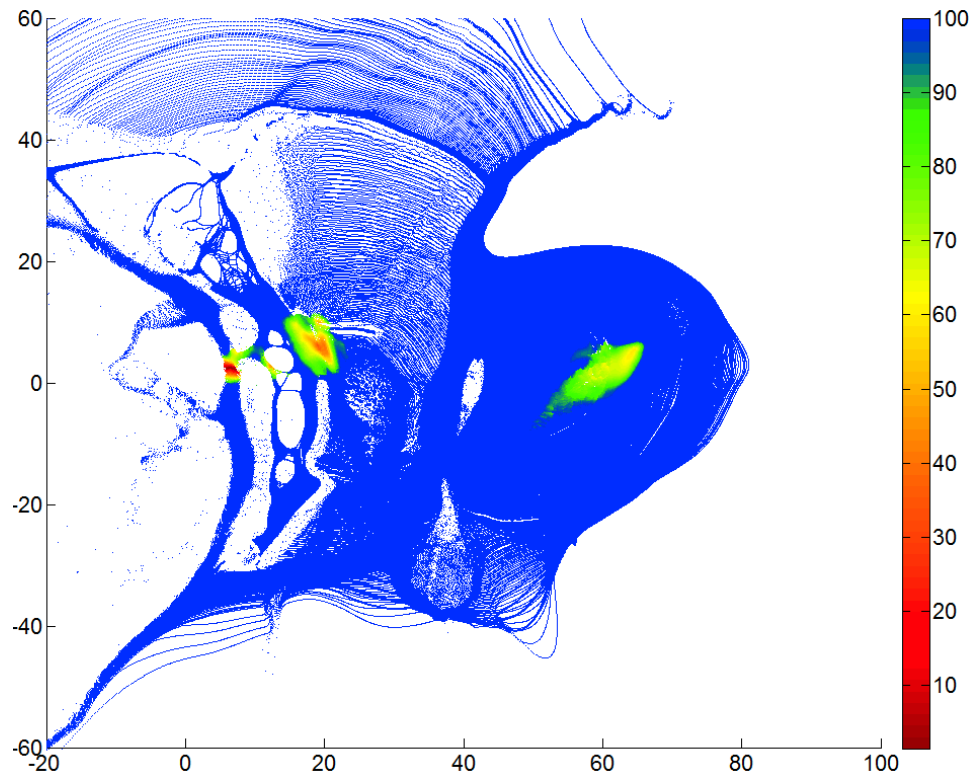


Figure 3.11: Location of slowest moving debris.

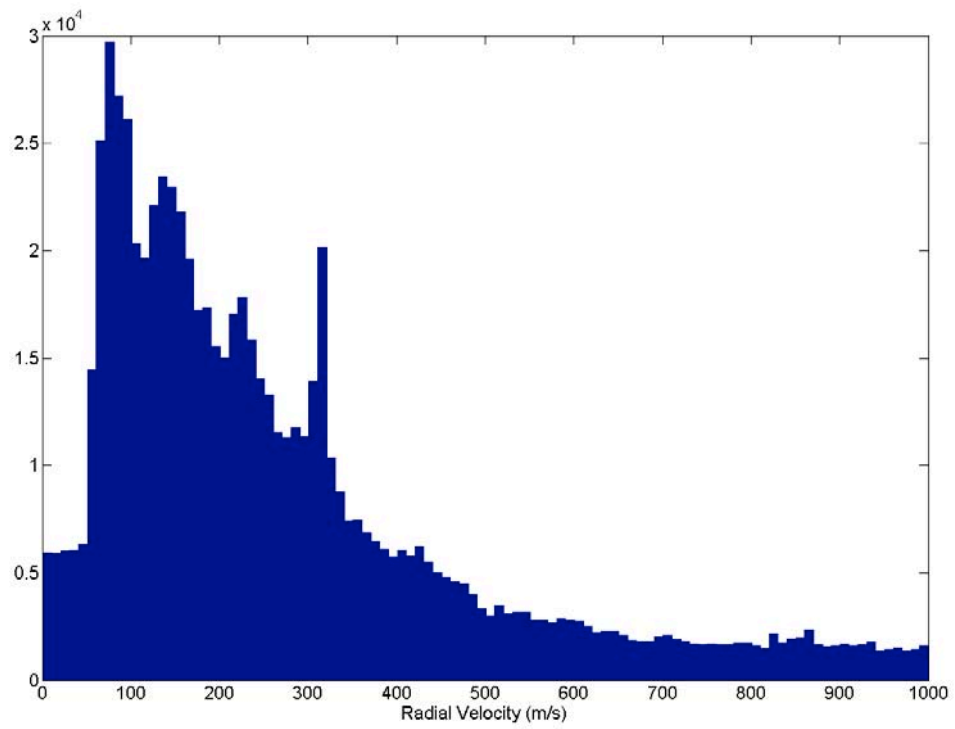


Figure 3.12: Radial dispersion velocity histogram for contact burst.

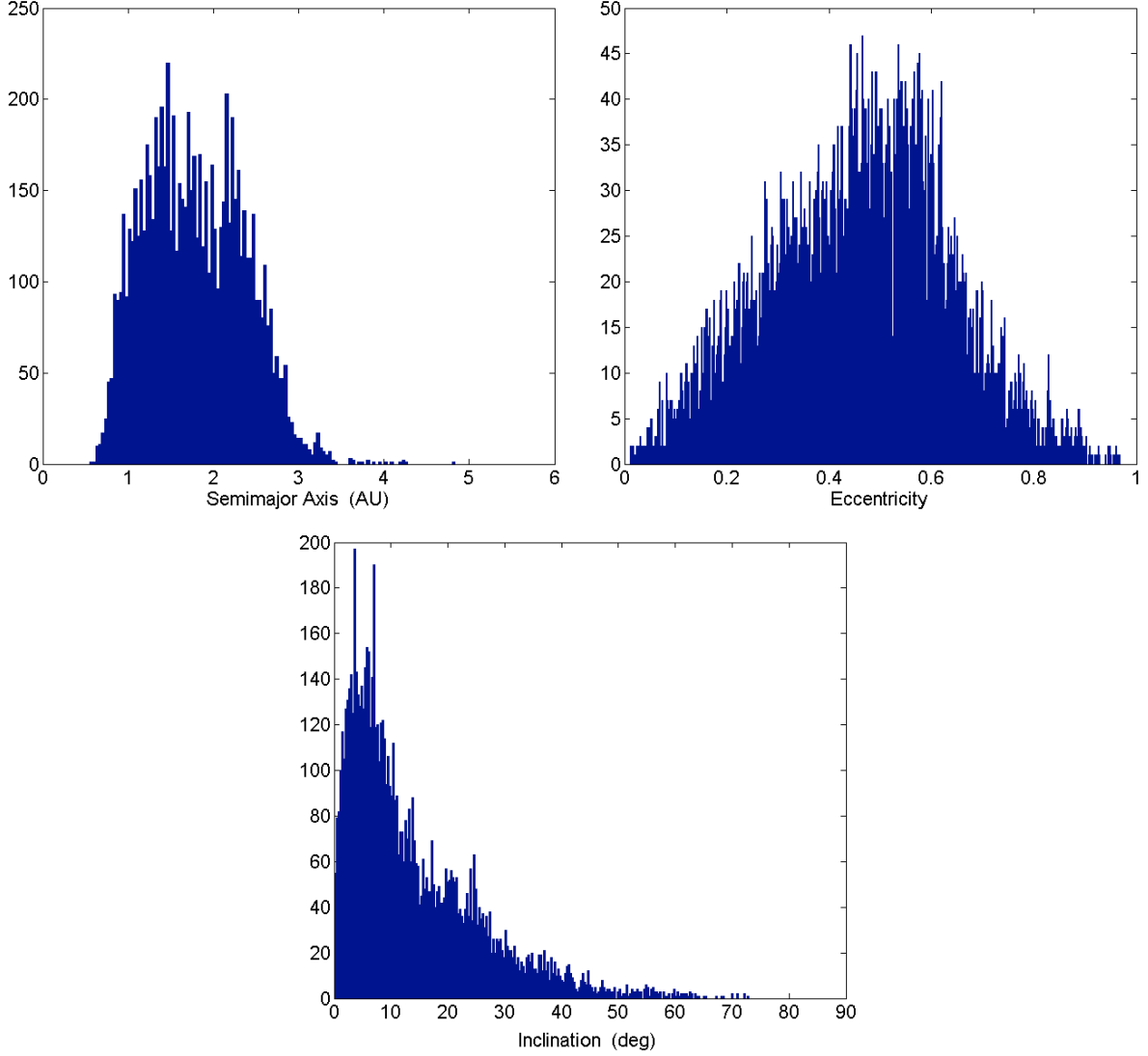


Figure 3.13: Histograms of known NEO population.

### 3.4.1 Impacting Orbit Solver

The orbital parameters for the nominal trajectory are sampled from a  $(a, e, i)$  space that represents the distribution of known NEOs, as shown in Figure 3.13. This is done using inverse transform sampling, in which a random number is mapped to the integral of the cumulative density function for each of these three parameters. Given  $a, e, i$ , and the impact date, we have all of the information needed to pin down an impacting orbit. If we assume that the orbit passes through the center of the Earth, then we have  $x_E, y_E$ , and  $z_E$ , which are the Cartesian coordinates for the Earth's center of mass at that epoch, which coincide with a point on the desired orbit.

Given  $a, e$ , and  $r = \sqrt{x_E^2 + y_E^2 + z_E^2}$ , the specific angular momentum is calculated as  $h = \sqrt{\mu a(1 - e^2)}$  [24,25]. Then, the true anomaly,  $\theta$  and velocity magnitude,  $v$ , are calculated using the orbit equation and the vis-viva equation, as

$$r = \frac{h^2}{\mu} \frac{1}{1 + e \cos \theta}; \quad \frac{v^2}{2} - \frac{\mu}{r} = -\frac{\mu}{2a} \quad (17)$$

We can also calculate the radial velocity,  $v_r$ , as

$$v_r = \frac{\mu}{h} e \sin \theta \quad (18)$$

which gives us all the needed scalars to solve the following set of nonlinear equations for the velocity components  $v_x$ ,  $v_y$ , and  $v_z$ , resulting in the desired state vector:

$$f_1(v_x, v_y, v_z) = 0 = xv_y - yv_x - h \cos i \quad (19a)$$

$$f_2(v_x, v_y, v_z) = 0 = xv_x + yv_y + zv_z - rv_r \quad (19b)$$

$$f_3(v_x, v_y, v_z) = 0 = \sqrt{v_x^2 + v_y^2 + v_z^2} - v \quad (19c)$$

### 3.4.2 Fragmented System Estimation

Statistics representing the fragmented system are collected and stored as cumulative density functions for the needed variables, similar to those shown in Figure 3.14. A representative fragment system of 10,000 to 100,000 fragments is created from these statistics using inverse transform sampling. The debris cloud is given global coordinates in a Local-Vertical-Local-Horizontal (LVLH) reference frame about the center of mass, as shown in Figure 3.15. Since the hydrodynamic model is axisymmetric, and has a definite direction of maximum momentum along the axis of symmetry, a desired deflection direction must be chosen. These are then integrated to predict an ephemeris for a 48 hour period surrounding the nominal time of impact. Since the LVLH reference frame is computationally beneficial for self-gravity and collision modeling among fragments [6], we use the nonlinear relative equations of motion for this frame to govern fragment trajectories [6,8,25,24]:

$$\ddot{x}_i = 2\dot{\theta} \left( \dot{y}_i - \frac{\dot{r}_c}{r_c} y_i \right) + \dot{\theta}^2 x_i + \frac{\mu}{r_c^2} - \frac{\mu}{r_d^3} (r_c + x_i) + \frac{\mu_E}{r_{Ei}^3} (x_E - x_i) + F_i^x \quad (20)$$

$$\ddot{y}_i = -2\dot{\theta} \left( \dot{x}_i + \frac{\dot{r}_c}{r_c} x_i \right) + \dot{\theta}^2 y_i - \frac{\mu}{r_d^3} + \frac{\mu_E}{r_{Ei}^3} (y_E - y_i) + F_i^y \quad (21)$$

$$\ddot{z}_i = -\frac{\mu}{r_d^3} z_i + \frac{\mu_E}{r_{Ei}^3} (z_E - z_i) + F_i^z \quad (22)$$

where  $x$ ,  $y$ ,  $z$ ,  $r_c$ , and  $\theta$  are defined as shown in Figure 3.15,  $r_d$  is the length of the relative coordinate vector,  $\mu$  and  $\mu_E$  are gravitational parameters for the sun and the Earth,  $r_{Ei}$  is the distance from each fragment to Earth, and  $(F^x, F^y, F^z)$  are the combined acceleration components due to 3rd body gravitational terms (solar system major body model [8]), self gravity, and collision corrections. The threading structure for computing the values for self gravity terms is described in [6], while collisions are predicted using a Sort-and-Search algorithm [19], resulting in post-collision changes to position and velocity of fragments. An elastic spherical collision model is assumed for the fragments, with a coefficient of restitution of 0.5.

### 3.4.3 Uncertainty Analysis

In order to test the response of orbital dispersion with respect to uncertain initial fragment positions and velocities, a Gaussian noise is added to the mapping around the nominal center of mass. A standard deviation of 10% is assumed, resulting in deviations from the hydrodynamic simulations up to  $\pm 30\%$ . For a given orbit, 1000 random perturbations are integrated to impact, resulting in an average system behavior and a standard deviation representative of the uncertainty due to the initial conditions.

This procedure is completed for a database of 906 orbits chosen to impact at a fixed date. The orbital parameters for the nominal trajectory are sampled from a  $(a, e, i)$  space that represents the distribution of known NEOs, as shown in Figure 3.13. For each chosen deflection direction, the Monte Carlo procedure described above results in a characteristic behavior of a disrupted NEO on the range of orbits tested.



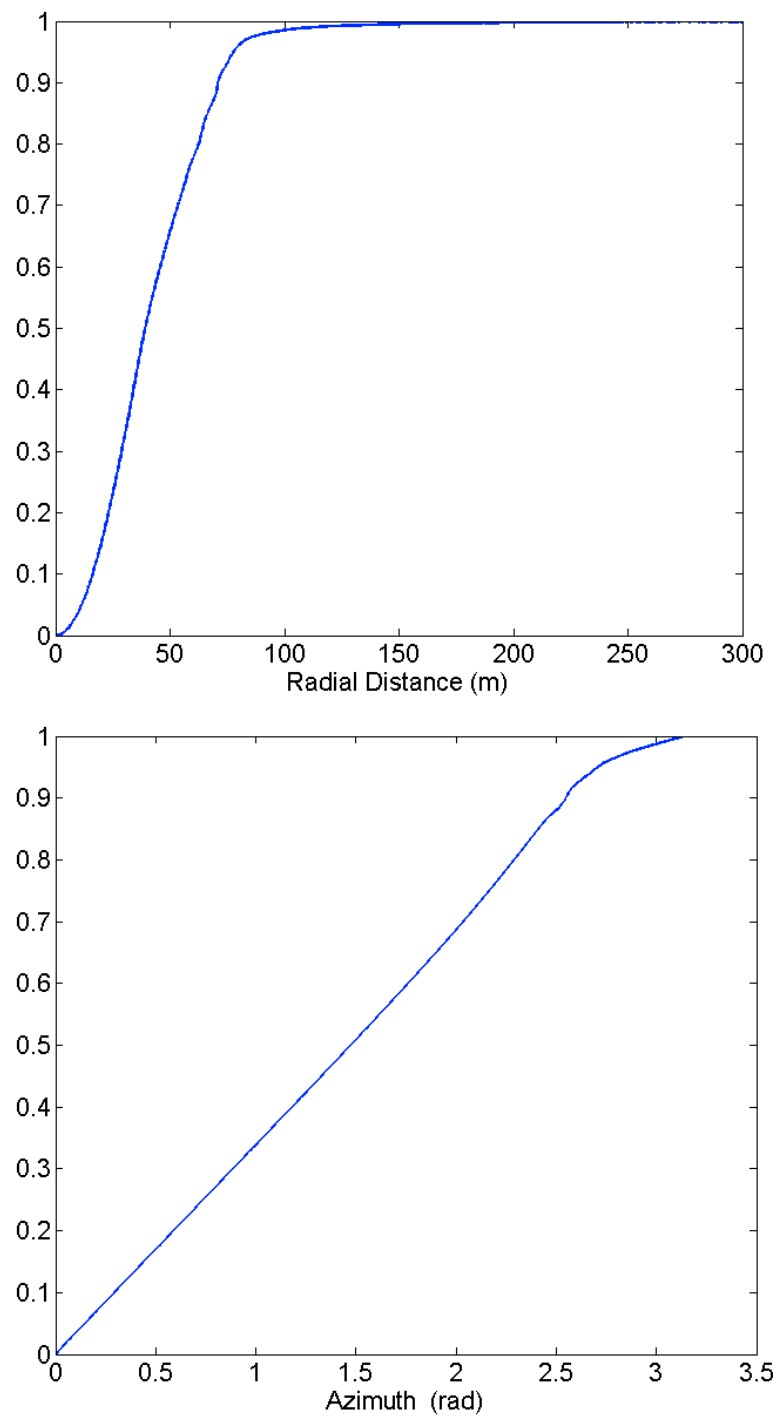


Figure 3.14: Cumulative density functions for disrupted asteroid.

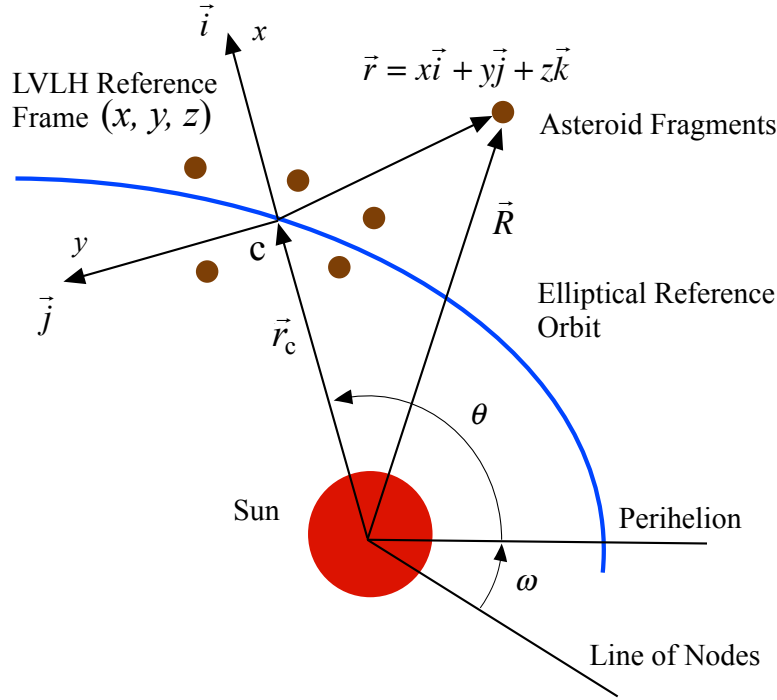


Figure 3.15: Rotating local-vertical-local-horizontal (LVLH) frame.

Given a fixed lead time in which to allow the fragmented target to disperse along its orbit, or even a minimal desired lead time, we have a point (or set) at which a desired intercept is achieved. It is clear, however, that not all approach vectors are equal. From a mission design perspective, the approach asymptote affects the transfer orbit, and therefore the cost (or even feasibility) of the mission [20]. For the present study, bounds on the approach asymptote from a mission perspective are not considered. Rather, the direction in which the approach occurs is a deciding factor in the behavior of the fragmenting body. Past work has shown that there is a clear bias towards dispersion along this vector for most of the tested hydrodynamic simulations [3].

A simple differential optimization routine is applied to this vector for each of the sampled impacting orbits. There are two degrees of freedoms for each of these problems. The optimal pointing direction will be something of interest in short warning scenarios, since a drastic difference in the dispersion patterns can occur. For some of the orbits, a grid search of the approach asymptotes was done to quantify the range of impacting mass ratios.

### 3.5 Computational Approach

This section address the computational approach used to solve the disruption problem. Each state variable update for a fragment is conducted in parallel at each time step. A variety of hardware was available for this project, with a substantial difference in performance. This allowed us to get reasonable estimates on the computational cost of this simulation. Performance can vary based on the type of arrays used, and the number of threads dedicated to each GPU calculation. These factors are determined by the CUDA Compute Capability (CUDA CC), which is a property of the GPU [23]. These cost estimates are used to determine hardware performance on the various systems. A summary of the hardware used is shown in Table 3.2 (Note: all CPUs are Intel brand, and all GPUs are NVIDIA brand).

Each thread on the GPU calculates the state variable change for one fragment, with the GPU kernel limited to one time step. This is necessary because the positions of the planets and other gravitating bodies

Table 3.2: Hardware description for benchmark comparisons

System	Machine 1	Machine 2	Machine 3	Machine 4	Machine 5
CPU	1x Core2 Q6600	1x Core2 Q6600	1x Xeon X5550	2x Xeon E5520	2x Xeon X5650
CPU Cores	4	4	4	8	12
CPU TPEAK	9.6 GFLOPs	9.6 GFLOPs	12.8 GFLOPs	21.36 GFLOPs	32.04 GFLOPs
GPU	1x 8800GTS	1x GTX470	1x GTX480	4x Tesla c1060	4x Tesla c2050
GPU Cores	112	448	480	960	1792
GPU TPEAK	84 GFLOPs	324 GFLOPs	385 GFLOPs	336 GFLOPs	2060 GFLOPs
CUDA CC	CC 1.0	CC 2.0	CC 2.0	CC 1.3	CC 2.0

must be calculated and transferred to the GPU at each time step. Additionally, the positions of fragments at each integration substep are shared among multiple GPUs and CPU threads. For this reason, the present hydrodynamics model is predominantly bandwidth-limited for small data sets. While grid information is not retained, one of the disadvantages of the SPH hydrocode is that neighboring particles must be calculated at each time step. Our approach in this model is to create a bounding volume for each SPH particle and perform the same Sort and Sweep in parallel as used to detect collisions in the orbital model [19]. We retain the information for neighbors connected by material strength, as well as carrying neighbor information through the correction step of the integrator. This results in a 28% performance improvement over recalculating neighbors at both the prediction and correction steps, while allowing for a variable time step based on the Courant condition [11,12]:

$$\delta t = \min_i \frac{h_i}{c_i} \quad (23)$$

where  $c$  is the local sound speed. While the reduction operation to determine the new time step can be done in parallel, all GPU threads must have position information for all particles to determine neighbors. This requirement could be eliminated through clever domain decomposition, but there is a tradeoff between associating a mesh to the model and taking advantage of contiguous memory sections of particles. Load balancing would also require additional communication between GPUs, which has an impact on performance, as PCI-E bandwidth is one of the limiting factors in GPU acceleration [23].

Our memory model for this simulation includes a shared host memory, distributed device memory for each GPU, and data transfers between them handled through explicit array transfer. Each block of compute threads on the GPU takes the data it needs from the global device memory when the kernel reaches its block, as shown in Figure 3.16. This is an important factor, because the varying compute capabilities have different limitations on this block memory, changing the number of threads that may be used in the calculation. Constants are transferred to all GPU memories implicitly using a pointer to the host constant value. While modern dedicated compute GPUs have a high amount of onboard memory, it usually is far less than system memory. Though it may seem advantageous to calculate parameters for every time step before the start of the simulation, the arrays resulting from this approach are quite large. Each model of GPU has a limited number of memory registers available to each computing block of threads [23]. Therefore, the use of several large arrays can actually slow down the simulation in some cases, by lowering the number of threads below the maximum allowed by the architecture. This is addressed in the present code by utilizing asynchronous data transfers and kernel launches to split the work into streams. This allows the CPU to calculate new parameters needed for the next time step while the GPU is updating the current step.

### 3.6 Results

In order to address the effectiveness of different fragmentation methods, we compare the mass remaining on impacting trajectories (including the uncertainty from the Monte Carlo process) against other methods for

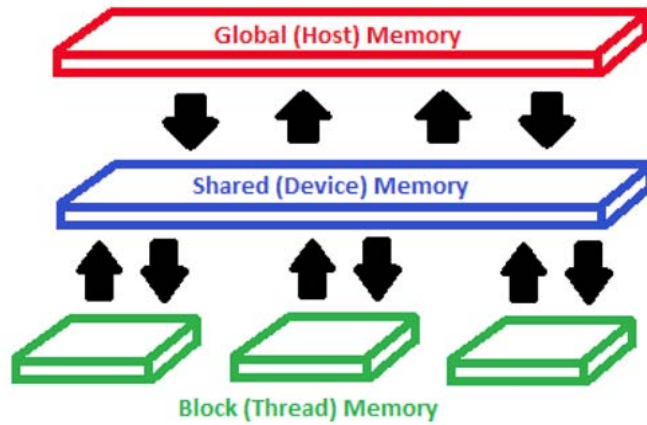


Figure 3.16: Qualitative GPU memory model.

each orbit. For example, Figure 3.17 shows the relative impacting mass for the surface penetrator in both the solid and the rubble-pile targets. On average across the orbits tested, the impacting mass was 10% higher for the solid target compared to the rubble target for deflections in the radial direction. Estimates like this will eventually allow for tabular look-up of performance for various methods without direct computation. It was also found that impacting mass for the solid target was 20% higher than the rubble target in the transverse direction.

No strong correlation was found for the semimajor axis or eccentricity of the NEO orbit with only 15 days of lead time. However, deflections on orbits with high inclination were more effective, as shown in Figure 3.18 for the subsurface case. Ejecta velocities for the dynamic surface burst (at 6.1 km/s) were within the 10% assumed noise range compared to a static buried explosive, as shown in Figure 3.19. Thus, an emphasis might be placed on hypervelocity intercept and guidance technology rather than a rendezvous mission. One possible interceptor design includes an aluminum impactor followed by an explosive. With both interceptors impacting at 6.1 km/s, the resulting ejecta speed is on average 25% higher than the single surface blast, with a standard deviation of 5.3%. Figure 3.20 shows the relative velocities for these cases, which results in 20% lower impacting mass on most orbits tested for the 54 m initial spherical target due to the proposed HAIV concept.

### 3.6.1 Computational Optimization

A single computational node was used to determine optimal distribution of MPI and OpenMP processes across the current worker topology being considered. This system has 2 sockets populated with Intel Xeon X5650 six-core CPUs at 2.66 Ghz. Intel HyperThreading technology is enabled, resulting in 24 logical processors visible to the operating system. Additionally, the default level of OpenMP threading is 24. There are 4 NVIDIA Tesla C2050 GPU cards, each connected on a dedicated PCI-E x16 bus. System RAM is 32 GB, while each GPU has 3 GB GDDR5 for a total GPU work unit of 12 GB (11.2 GB with ECC enabled). Fourteen multiprocessors on each card result in 448 shader cores each, limited to a maximum kernel launch of 1024 threads per thread block. This new “Fermi” GPU architecture has a theoretical peak performance of 515 Mflops in double precision, representing a game-changing leap forward in GPU double precision computing, as shown by real-world results [6].

While grid information does not need to be stored for this model, the drawback is that neighboring particles need to be determined at each time step. Since the integration scheme is a second order predictor-corrector scheme, particle information is needed at both steps. The first change made to the standard scheme was to retain the neighbor ID information for the corrector step. Only the kernel and kernel derivative values at the new neighbor predicted position need to be computed. This reduced time-to-solution by 30.2% compared to

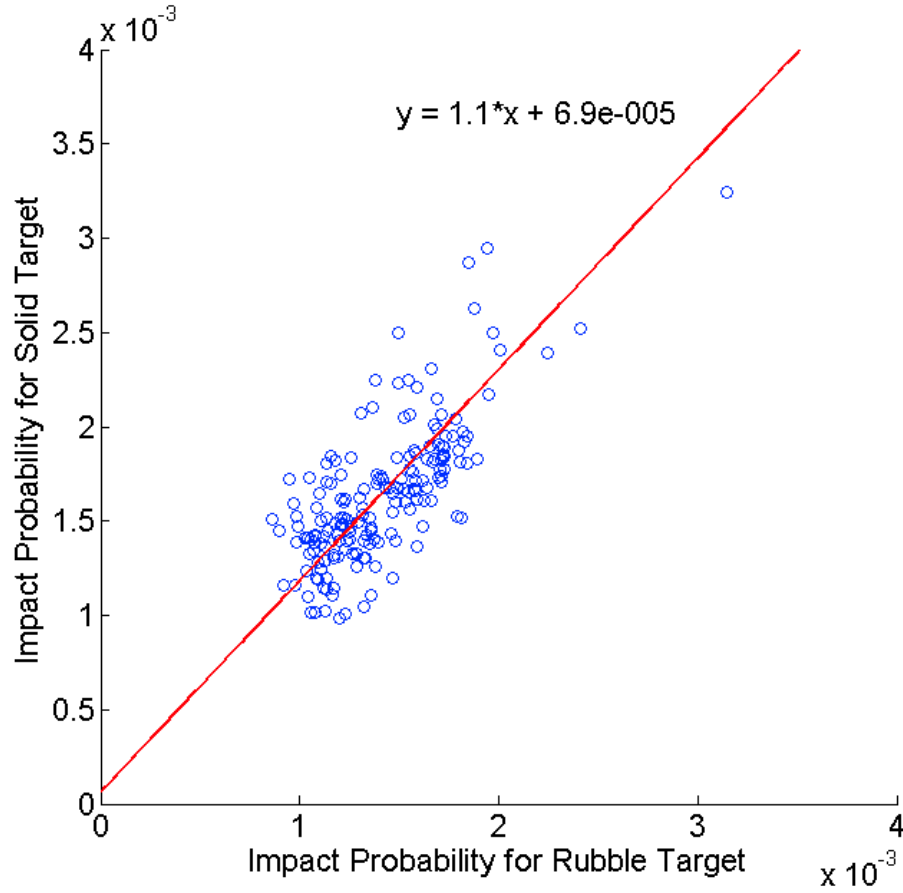


Figure 3.17: Relative performance for surface impactor.

a two-stage neighbor finding algorithm. Results for both cases were compared, and while ending state values could be slightly different the distribution remained the same, and the method conserved energy slightly better through the end of the simulation. A possible beneficial side effect of this approach is the reduction of importance of neighbor changes in a prediction step, which might help damp out numerical instabilities and allow for larger time step changes. This is something to be tested in the future. Also, while brute force computation of neighbor particles was the original approach, a Sort-and-Sweep method reduced this time by 36% for the present target model. This method scales as  $N \log N$  rather than  $N^2$  [19].

Neighbor information arrays were stored in a column-major format by particle, allowing stride 1 access to the ID number, kernel value, and kernel derivative values for each neighbor of a particle. Additionally, loop unrolling and inlining for simple functions were implemented, and optimization flags were passed in the build step. For the GPU model, utilizing asynchronous kernel launches to continue computation without synchronization resulted in an 8% performance increase. The theoretical load on each process should be equal, since each has the same number of particles for which a state update needs to be computed. However, in areas of quickly changing density (for example the expanding shock wave), the number of average neighbors for a particle goes up dramatically. This is controlled in 2 ways to aid load balancing. First, the ID assignment scheme works outward in a radial manner, while making sure that mirroring particles on opposite sides of the primary axis are adjacent in memory. Second, the evolution of  $h$  strives to keep the number of neighboring particles near the starting value, resulting in an equal computational burden. For the GPU model, a load factor was developed, dividing the minimum time to complete a section between synchronizations by the maximum time. Sampling this load factor allows one to better understand the efficiency of the code section. At a time of 1.2 ms, an example chosen because of the high energy of this point of the simulation, a vertical distribution of

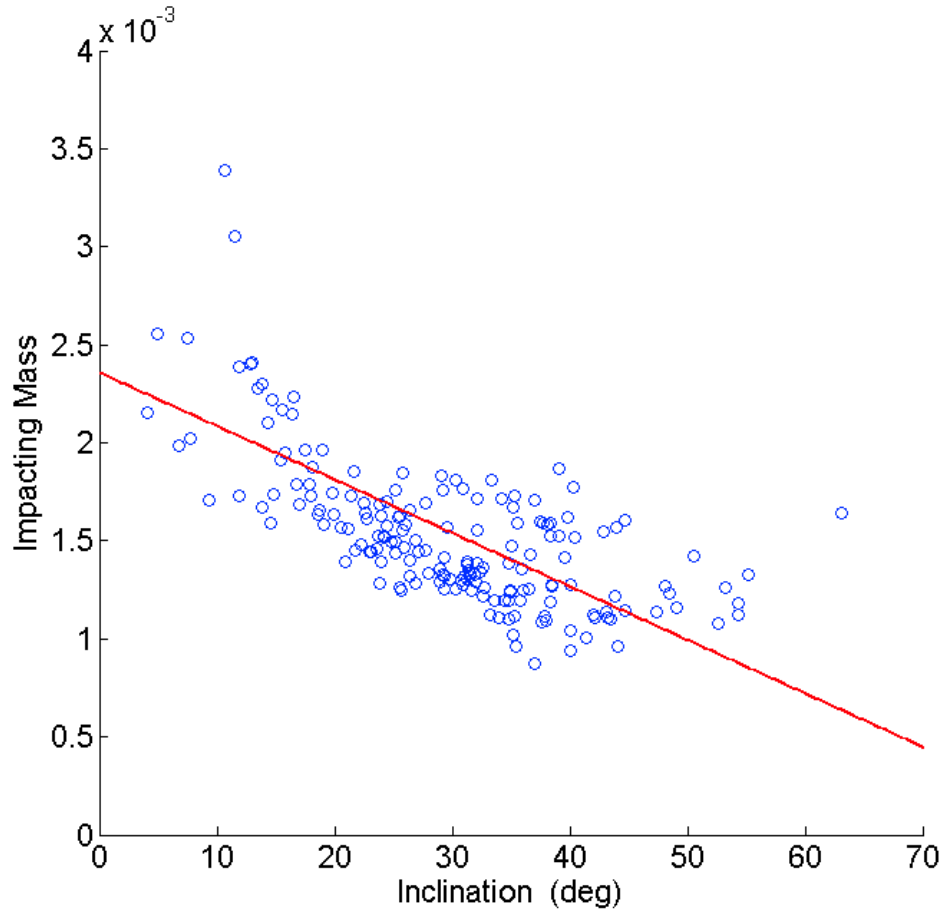


Figure 3.18: Impacting mass for subsurface explosion on orbits with varying inclination.

particle IDs resulted in a load factor efficiency of around 0.68. The present method has improved this portion to a median of 0.87.

### 3.6.2 Optimal Mission Results

The present simulation package has the advantage of being able to handle millions of decoupled optimization problems in parallel to one another. Thus, the generation of data outpaces the capability for displaying it in the present work. However, sample results are shown for a nominal impacting trajectory with a lead time of 15 days. Figure 3.22 shows the cost function contours for approach asymptotes of a sample mission. This impacting trajectory has a semimajor axis of 0.968, an eccentricity of 0.0242, and an inclination of 7.309 degrees.

It is clear for this case that, not only do local optimal solutions exist, but that there are specific conditions which should be avoided. However, this was not the case for all of the virtual impacting trajectories. This fact was especially true for orbits of high eccentricity ( $> 20$  degrees), which had many local minimums, and a wider range of effective dispersion options. Deeper cost function wells existed for these cases, though the geometry was more complicated than the lower inclination case, as shown. The contours are colored according to the base 10 logarithm of the resulting impact probability, showing a range of orders of magnitude. No clear result for the optimal direction for all cases was established. In the sample case, the conditions to be avoided were a perturbation normal to the plane of the orbit. The optimal directions in this case are near parallel to the velocity direction. The vectors forming the solutions of the tested orbits were uniformly distributed, which may be indicative of the lower lead time mission.

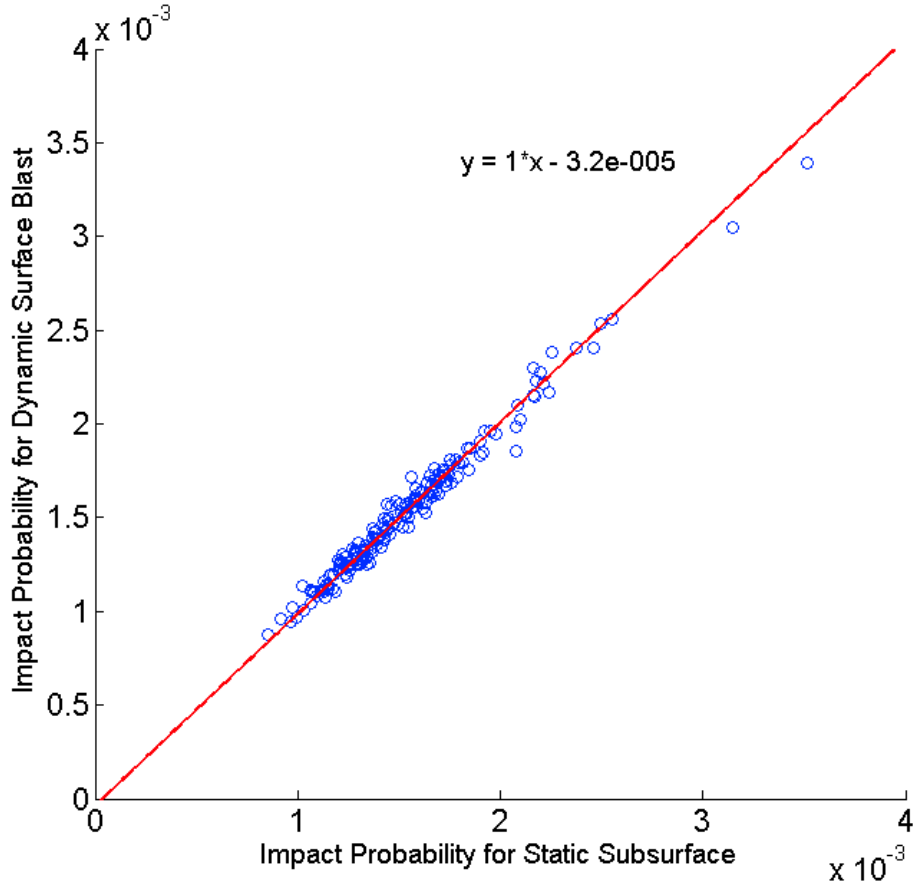


Figure 3.19: Impacting mass comparison for subsurface and dynamic surface cases.

As discussed in [20], some approach asymptotes are critical for interception with a single launch. Therefore, future work should address the coupled problem of mission feasibility and mission effectiveness. This will likely place stricter limits on the available lead times and the payload mass deliverable to the target.

### 3.6.3 Performance

Pure MPI scalability for up to 12 processes was tested on the present hardware, resulting in near linear scaling and a total parallel speedup of 8.9 for MPI. Including OpenMP in a Hybrid parallel scheme, a total parallel speedup of 11.9 is achieved, showing near perfect expected scalability across a single node as shown in Figure 3.21. Thus, each additional planned node might add almost 12x speedup for host computation, minus internode communication overhead. As shown in Figure 3.21, when the binding option is passed to the Hydra process manager to set 1-2 MPI processes per socket, and an OpenMP thread level of 6 is set, the best performing speedup for the system is obtained. This corresponds to a value of 11.2 for 12 computational threads and 11.9 for 24 computational threads. Performance improvement using  $\geq 12$  threads is predominantly dependent on the HyperThreading hardware implementation. This is shown to only have an improvement over 12 threads when the shared thread level is 4, 6, 8, or 12. However, good performance with 12 threads among these hybrid schemes was limited to an OpenMP level of 6 and 12. While the default OpenMP maximum thread level for this system is 24, benefits from this technology are implementation dependent, so the preferred setup for future system programming is 1 MPI process per socket with an OpenMP threading level of 6 unless improvement from additional MPI processes can be demonstrated.

GPU acceleration performance for this method is a substantial improvement over a larger CPU-only clus-

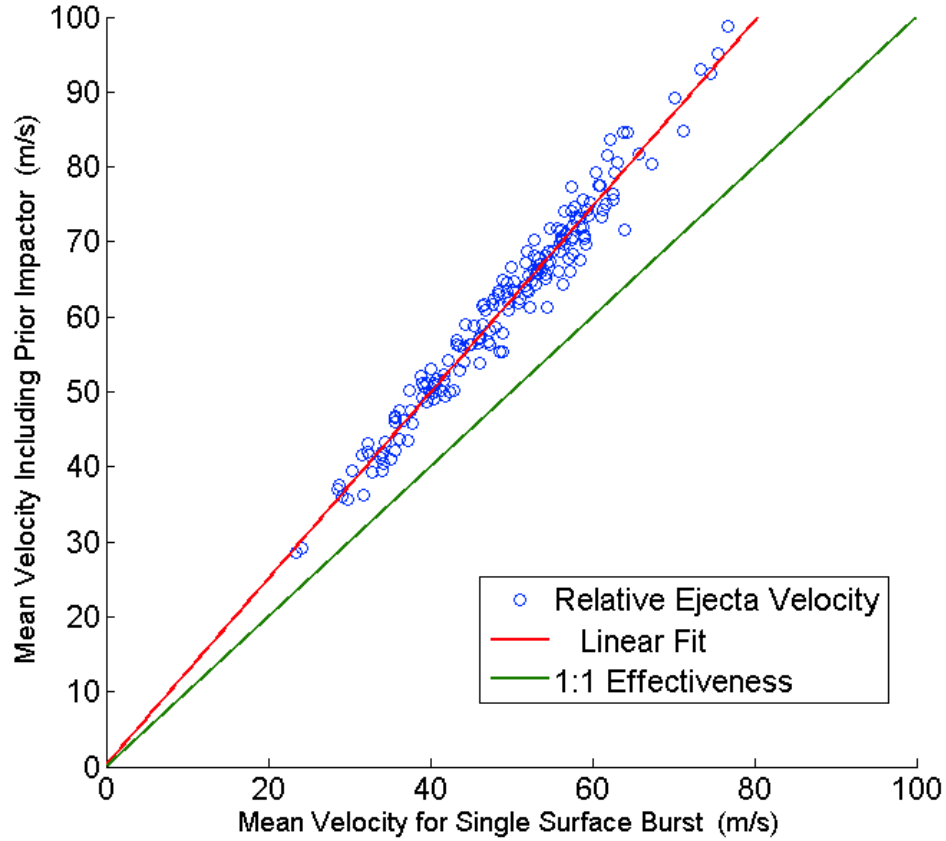


Figure 3.20: Mean ejecta velocity for single and double impactor cases.

ter. Since the threading structure of the GPU is limited to SIMD kernel launches of multiple threads on a multiprocessor, serial performance for comparison is measured on the host CPU. Figure 3.21 shows the relationship between the number of GPUs used in the state update process and the parallel speedup. At least 1 MPI thread is needed per GPU. In fact, using the currently supported CUDA Fortran toolkit (version 4.0), binding between CPU thread and GPU control requires that additional threading use a shared memory approach such as OpenMP. In a previous test, GPU speedup for this architecture ranges from 50x to 120x for a 50 m diameter target problem. Since the GPU approach works well for data-parallel problems, one would expect that increasing the scale of the problem would yield better performance. In fact, using the current solid target standoff model (3.1M particles) maximum speedup on a single node is increased to 357.9x, as shown in Figure 3.21. Since the neighbor search problem is substantially increased, the parallel structure of the GPU is far preferred to the hybrid CPU programming model.

### 3.7 Conclusion

The present SPH hydrocode suggests that a dynamic model of a hypervelocity surface burst yields results similar in spatial and temporal distribution at Earth impact to a static subsurface explosion. This gives additional launch windows for mission design, limits the fuel needed for a rendezvous burn, and avoids the need to bury the explosive payload. Additionally, the dynamic model should better predict system behavior when addressing high velocity penetrator architectures. The primary mechanism for this improvement is to use impactor momentum to couple energy into the surface material. Since impact at over 6 km/s is not survivable by



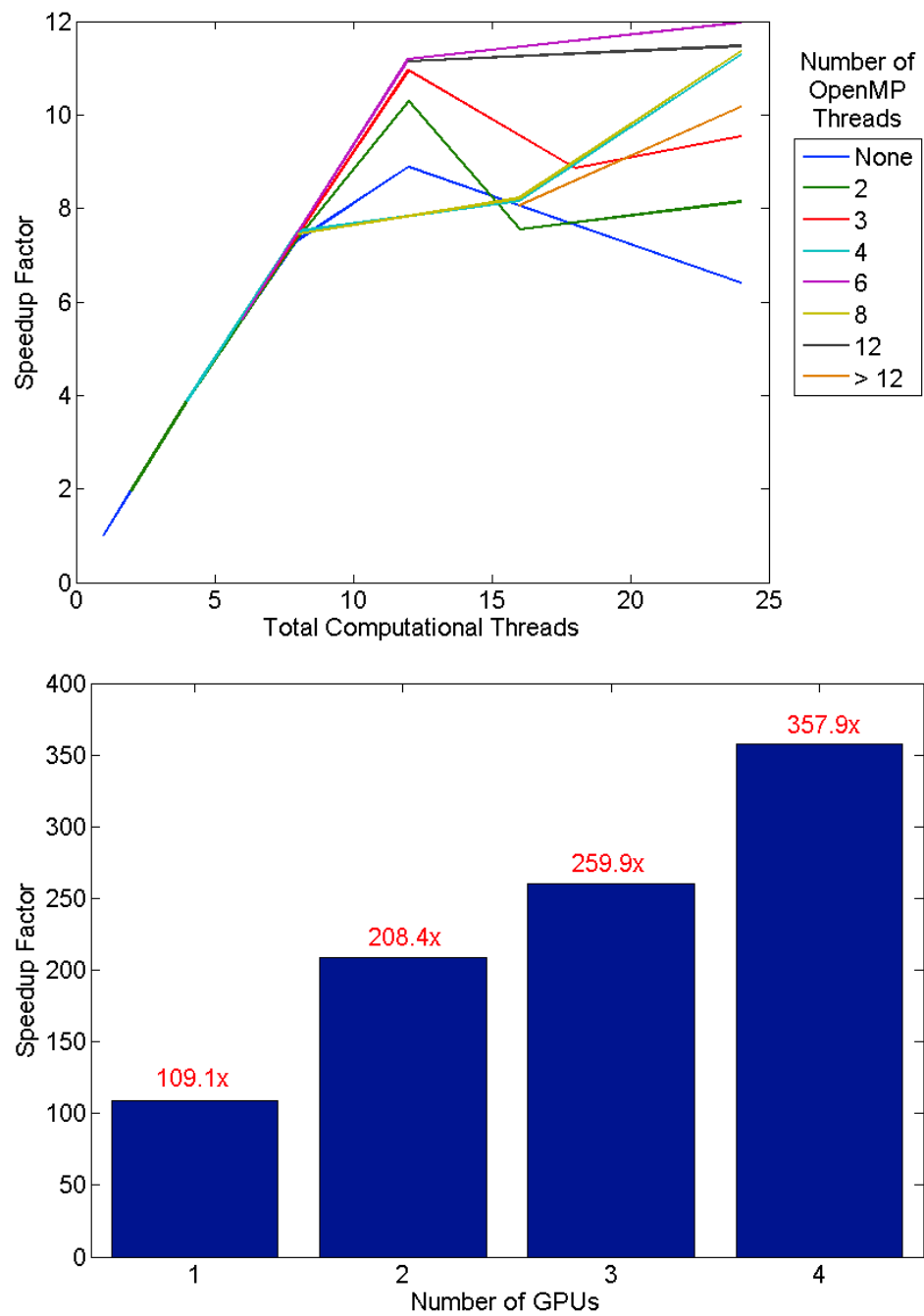


Figure 3.21: Comparison of single-node performance on CPU and GPU.

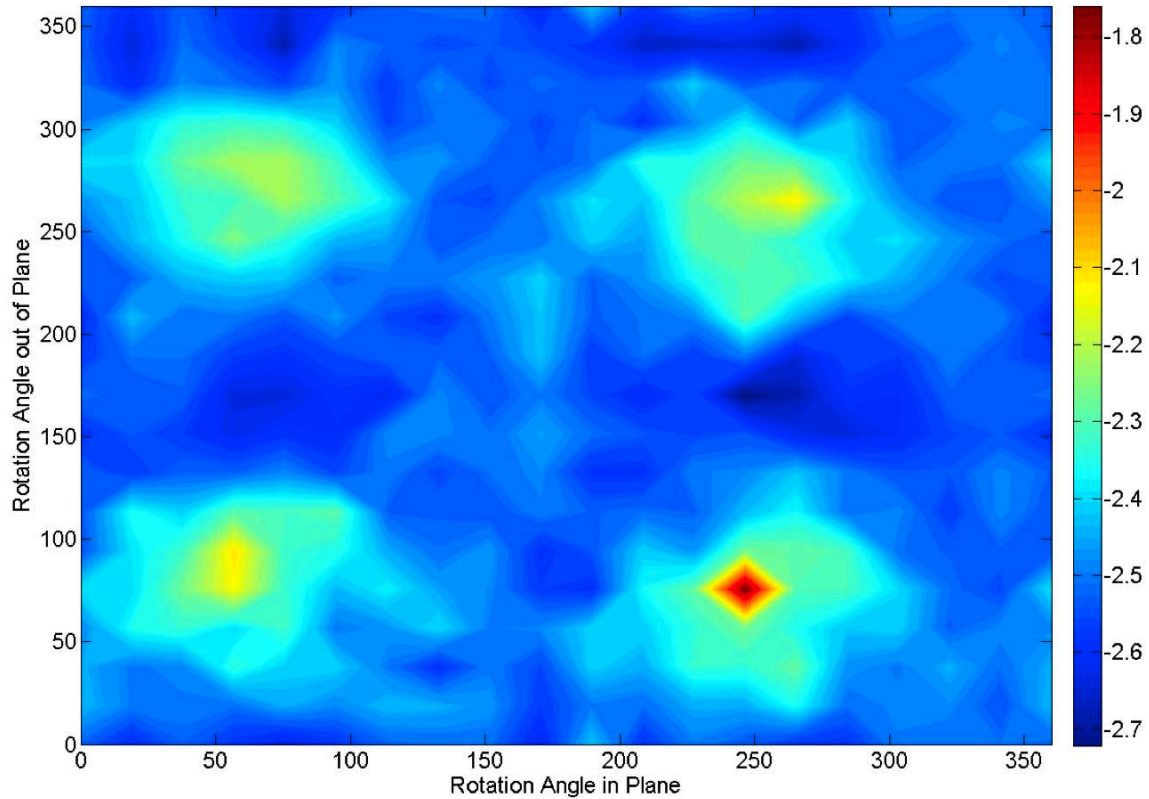


Figure 3.22: Cost function contours for sample mission approach asymptotes.

current explosive system technology, this naive approach is not a viable option. However, the proposed HAIV concept offers similar promise. This might give an option for realistically determining the limits of such a system for asteroid deflection missions. NEO orbital parameters such as semimajor axis and eccentricity were not found to be important for these time scale, but it was found that inclination was important in determining effectiveness of any given method.

All methods of disruption using a 100 kt nuclear energy source were quite effective for 100 m diameter targets for 15 days lead time, regardless of the orbit considered. This models of a hypervelocity impact fragmentation of a NEO was extended and applied to a 3D inhomogeneous asteroid model with randomly generated sections and generic material parameters. It is clear from the discrepancy in dispersion speed for the 76 m asymmetric target that the proposed HAIV concept is successful in reducing the mass remaining on impacting trajectories over a simple contact burst. Future work should consider larger bodies, a range of source energies, and lead times specific to the available mission time for a given orbit.

New HPC technology utilizing GPU acceleration has resulted in orders of magnitude improvement in computational ability. Speedup of the GPU accelerated model compared to serial execution for the both target models has been demonstrated. While the 330,000 particles of the penetrator target are limited mostly by communication bandwidth, the 3.1 million particles in the standoff model are limited by computational speed and memory bandwidth for the threads on the GPU. A substantial speedup improvement, from 53x to 358x, is observed. New high-throughput neighbor-finding methods were suggested, using the GPU acceleration technology of the current simulation toolkit. The current simulation set develops a tensor relationship for material characteristics and orientation. This allows for more realistic size and shape generation for NEO fragments by treating damage as a local quantity (cracks) rather than a distributed state variable. GPU acceleration of the 3D model is up to 200x on a single workstation, continuing a trend of increasing computational complexity while also increasing efficiency. This approach allows us to compute a range of values rather than monolithic

single simulations, and is incredibly important for the orbital analysis. Sensitivity to the orbital parameters is a true unknown, since large impacting NEOs have yet to be observed, so computation for a range of these values is a necessity.

This shows single node computational performance on the same order as a moderate cluster. The ability to run multiple cases to address statistical system behavior results in simulation being integrated into overall mission design. Mission effectiveness can be estimated in advance of a need for mission design, allowing new architectures and interchangeable components for a universal deflection plan. This paper outlined the development of software and hardware tools to aid the planning of NEO deflection mission design, and the current project strives to identify key technologies for effective implementation. This technology provides a useful reduction in time-to-solution comparable to 30 similar CPU-only nodes (which would cost \$4,000 each) in a \$14,000 form factor, showing a 8.6x improvement in cost-adjusted performance. Since a large amount of data can be processed using GPU simulation, this work confirms that disruption at different times along a given orbit can have a large effect on the resulting shape of debris. This allows for a more clear set of objectives for mission design. Another new result is the availability of representative 3D fragment distributions. This will improve the trajectory of the desired hypervelocity intercept mission by allowing full degrees of freedom in choosing the approach asymptote.

### 3.8 References

- [1] Boslough, M., "Airburst Warning and Response," IAA-PDC-2166721, *2nd IAA Planetary Defense Conference*, Bucharest, Romania, May 9-12, 2011.
- [2] *Defending Planet Earth: Near-Earth Object Surveys and Hazard Mitigation Strategies*, Committee to Review Near-Earth Object Surveys and Hazard Mitigation Strategies, National Research Council, 2010.
- [3] Kaplinger, B.D., and Wie, B., "Comparison of Fragmentation/Dispersion Models for Asteroid Nuclear Disruption Mission Design," AAS-11-403, *AAS/AIAA Astrodynamics Specialist Conference*, Girdwood, AK, July 31- August 4, 2011.
- [4] Kaplinger, B., and Wie, B., "Parameter Variation In Near-Earth Object Disruption Simulations Using GPU Acceleration," AAS-11-267, *21st AAS/AIAA Spaceflight Mechanics Meeting*, New Orleans, LA, Feb. 13-17, 2011.
- [5] Kaplinger, B., Wie, B., and Dearborn, D., "Nuclear Fragmentation/Dispersion Modeling and Simulation of Hazardous Near-Earth Objects," IAA-PDC-2138266, *2nd IAA Planetary Defense Conference*, Bucharest, Romania, May 9-12, 2011.
- [6] Kaplinger, B., and Wie, B., "Optimized GPU Simulation of a Disrupted Near-Earth Object Including Self-Gravity," AAS-11-266, *21st AAS/AIAA Spaceflight Mechanics Meeting*, New Orleans, LA, February 13-17, 2011.
- [7] Wie, B. and Dearborn, D., "Earth-Impact Modeling and Analysis of a Near-Earth Object Fragmented and Dispersed by Nuclear Subsurface Explosions," AAS 10-137, *20th AAS/AIAA Space Flight Mechanics Meeting*, San Diego, CA, February 15-17, 2010.
- [8] Kaplinger, B.D., Wie, B., and Dearborn, D., "Preliminary Results for High-Fidelity Modeling and Simulation of Orbital Dispersion of Asteroids Disrupted by Nuclear Explosives," AIAA-2010-7982, *AIAA/AAS Astrodynamics Specialists Conference*, Toronto, Ontario, Canada, August 2-5, 2010.
- [9] Margot, J.L., Nolan, M.C., Benner, L.A.M., Ostro, S.J., Jurgens, R.F., Giorgini, J.D., Slade, M.A., Campbell, D.B., "Binary Asteroids in the Near-Earth Object Population," *Science*, 296, 2002.
- [10] Michel, P., "Physical Properties of Near-Earth Objects that Inform Mitigation," *2nd IAA Planetary Defense Conference*, Bucharest, Romania, May 9-12, 2011.
- [11] Monaghan, J.J., "Smoothed Particle Hydrodynamics," *Rep. on Prog. in Physics*, Vol. 68, July 2005, pp. 1703-1759.

- [12] Liu, G.R., and Liu, M.B., *Smoothed Particle Hydrodynamics: A Meshfree Particle Method*, World Scientific Publishing, Singapore, 2003.
- [13] Benz, W., and Asphaug, E., "Simulations of Brittle Solids using Smooth Particle Hydrodynamics," *Computer Physics Communications*, Vol. 87, 1995, pp. 253-265.
- [14] Hiermaier, S., Konke, D., Stilp, A.J., and Thoma, K., "Computational Simulation of the Hypervelocity Impact of Al-Spheres on Thin Plates of Different Materials," *Intl. Journal of Impact Engineering*, Vol. 20, 1997, pp. 363-374.
- [15] Jutzi, M., Benz, W., and Michel, P., "Numerical Simulations of Impacts Involving Porous Bodies I. Implementing Sub-Resolution Porosity in a 3D SPH Hydrocode," *Icarus*, Vol. 198, 2008, pp. 242-255.
- [16] Randles, P.W., and Libersky, L.D., "Smoothed Particle Hydrodynamics: Some Recent Improvements and Applications," *Computer Methods in Applied Mechanics and Engineering*, Vol. 139, 1996, pp. 375-408.
- [17] Tillotson, J.H., "Metallic Equations of State for Hypervelocity Impact," General Atomic Technical Report GA-3216, 1962.
- [18] Schuster, S.H., and Isenberg, J., "Equations of State for Geologic Materials," Defense Nuclear Agency Technical Report DNA-2925Z, 1972.
- [19] LeGrand, S., "Broad-Phase Collision Detection with CUDA," *GPU Gems 3*, ed. H. Nguyen, Addison-Wesley, 2007.
- [20] Wagner, S., and Wie, B., "Analysis and Design of Fictive Post-2029 Apophis Intercept Mission for Nuclear Disruption," AIAA-2010-8375, *AIAA/AAS Astrodynamics Specialists Conference*, Toronto, Ontario, Canada, August 2-5, 2010.
- [21] Miles, A.R., "Asteroid Deflection via Standoff Nuclear Explosions," *Asteroid Deflection Research Symposium*, Arlington, VA, October 23-24, 2008.
- [22] Plesko, C.S., Weaver, R.P., and Huebner, W.F., "Energy Deposition in Hazard Mitigation by Nuclear Burst: Sensitivity to Energy Source Characteristics, Geometry, and Target Composition," Paper 2588, *42nd Lunar and Planetary Science Conference*, March 7-11, 2011.
- [23] Kirk, D.B. and Hwu, W.W., *Programming Massively Parallel Processors*, Morgan Kaufmann, Burlington, 2010.
- [24] Curtis, H.D., *Orbital Mechanics for Engineering Students*, Elsevier Aerospace Engineering Series, Oxford, UK, 2006.
- [25] Vallado, D.A., *Fundamentals of Astrodynamics and Applications*, Third Edition, Microcosm Press, Hawthorne, CA, 2007.

## Chapter 4

# Terminal Intercept Guidance and Control

### 4.1 Introduction

On July 4, 2005, NASA's Deep Impact mission successfully delivered an autonomous impactor to comet Tempel 1 [1]. This mission demonstrated the technical feasibility of hitting a 5-km object in space with a hypervelocity intercept speed of 10 km/s. The planetary defense community can more confidently include kinetic impact as a potential mission option to deflect or disrupt threatening near-Earth objects.

Terminal-phase guidance laws are one of the essential ingredients in a successful intercept mission. A variety of guidance laws can be employed for asteroid intercept, from classical proportional navigation to predictive laws to optimally derived laws. Different laws can be used based on performance requirements, type of spacecraft engines, and available navigational data.

This chapter begins with a description of the mathematical models, followed by a description of several guidance laws. Simulation results are shown for some of the guidance laws. Finally, a high-fidelity spacecraft simulator, GMV's CLEON computer program [2,3], is described, and simulation results of certain guidance laws with realistic spacecraft characteristics are presented in this chapter.

### 4.2 Mathematical Modeling

The target asteroid is modeled as a point mass in a standard heliocentric Keplerian orbit, described by

$$\dot{\mathbf{r}}_T = \mathbf{v}_T \quad (1a)$$

$$\dot{\mathbf{v}}_T = \mathbf{g}_T \quad (1b)$$

where  $\mathbf{r}_T$  and  $\mathbf{v}_T$  are the position and the velocity vectors of the target and  $\mathbf{g}_T$  is the gravitational acceleration due to the sun, expressed as

$$\mathbf{g}_T = -\frac{\mu_{\odot} \mathbf{r}_T}{r_T^3} \quad (2)$$

where  $\mu_{\odot}$  is the solar gravitational parameter. Similarly, the motion of the spacecraft is described by

$$\dot{\mathbf{r}}_S = \mathbf{v}_S \quad (3a)$$

$$\dot{\mathbf{v}}_S = \mathbf{g}_S + \mathbf{a} \quad (3b)$$

where  $\mathbf{r}_S$  and  $\mathbf{v}_S$  are the position and the velocity vectors of the spacecraft and  $\mathbf{g}_S$  is the gravitational acceleration due to the sun, and  $\mathbf{a}$  is the control acceleration provided by control thrusters.

For some guidance problems the gravitational acceleration can be considered constant or negligible, but for asteroid terminal guidance missions, the gravitational acceleration must be considered a nonlinear function of position. There are some other disturbing accelerations that act on the spacecraft, such as radiation pressure

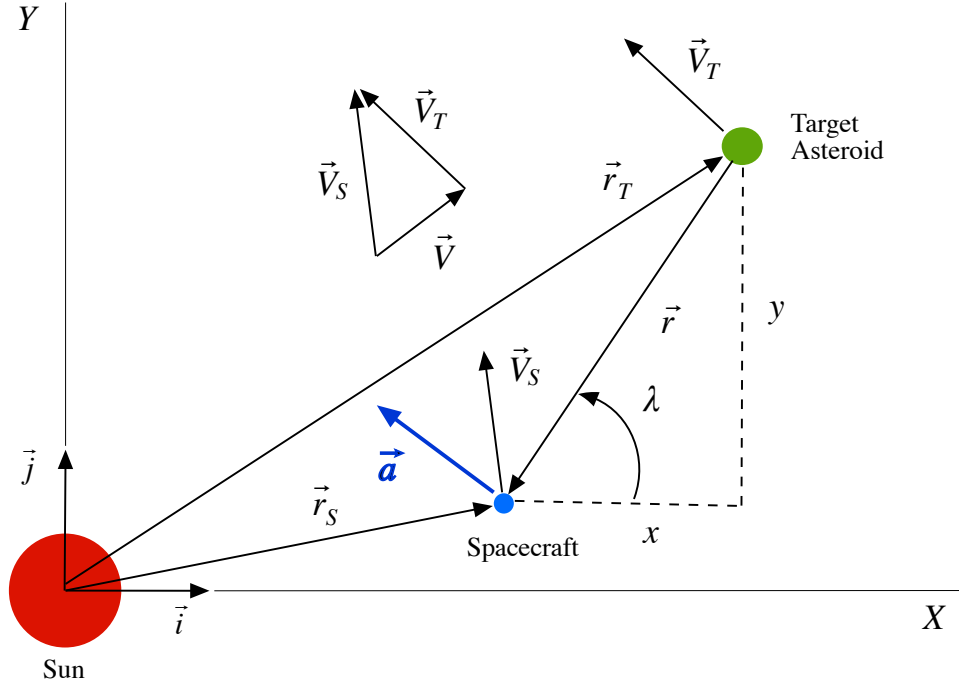


Figure 4.1: Coordinate system definition.

and the gravitational acceleration due to the asteroid. However, intercept and rendezvous missions to small asteroids can neglect these.

The equation of motion of the spacecraft with respect to the target becomes

$$\ddot{\mathbf{r}} = \mathbf{g} + \mathbf{a} \quad (4)$$

where  $\mathbf{r}$  is the position vector of the spacecraft with respect to the target defined as

$$\mathbf{r} = \mathbf{r}_S - \mathbf{r}_T \quad (5)$$

and  $\mathbf{g}$  represents the apparent gravitational accelerations acting on the target defined as

$$\begin{aligned} \mathbf{g} &= -\frac{\mu_{\odot}}{r_S^3} \mathbf{r}_S + \frac{\mu_{\odot}}{r_T^3} \mathbf{r}_T \\ &= -\frac{\mu_{\odot}}{|\mathbf{r}_T + \mathbf{r}|^3} (\mathbf{r}_T + \mathbf{r}) + \frac{\mu_{\odot}}{r_T^3} \mathbf{r}_T \\ &\cong -\frac{\mu_{\odot}}{r_T^3} \mathbf{r} + \frac{3\mu_{\odot}}{r_T^5} \mathbf{r}_T (\mathbf{r}_T \cdot \mathbf{r}) \quad \text{for } r \ll r_T \end{aligned} \quad (6)$$

From Figure 4.1, it can be seen that

$$\lambda = \tan^{-1} \frac{y}{x} \quad (7)$$

where  $\lambda$  is the line-of-sight (LOS) angle and  $(x, y)$  are the components of the relative position vector along the inertial  $(X, Y)$  coordinates. Differentiating this with respect to time gives

$$\dot{\lambda} = \frac{x\dot{y} - y\dot{x}}{r^2} \quad (8)$$

where  $\dot{\lambda}$  is the LOS rate and  $r = \sqrt{x^2 + y^2}$ . The rate of change of the distance between the target and the spacecraft is the closing velocity, found by differentiating  $r$  with respect to time as

$$V_c = -\dot{r} = \frac{-(x\dot{y} + y\dot{x})}{r} \quad (9)$$

## 4.3 Classical Feedback Guidance Laws

### 4.3.1 PN-based Feedback Guidance Laws

#### Classical Proportional Navigation (PN) Guidance

The guidance law considered first is the so-called proportional navigation (PN) guidance. The PN guidance attempts to drive the LOS rate to zero by applying accelerations perpendicular to the LOS direction. The PN guidance law is expressed as

$$a = nV_c\dot{\lambda} \quad (10)$$

where  $a$  is the acceleration command and  $n$  is the effective navigation ratio, a designer-tunable parameter. The navigation ratio is typically chosen between 3 and 5 [4]. Its theoretical optimal value, which will be derived and discussed in a later section, is 3. Larger values are chosen to provide more robustness against disturbances and errors. This can be seen by inspecting Eq. (10). Inaccurate estimates of the closing velocity or the LOS rate are equivalent to changing the navigation ratio and using accurate closing velocity and LOS rate information. Large navigation ratios will command unnecessarily large accelerations, while small navigation ratios risk commanding too little acceleration and missing the target. Thus a larger navigation ratio ensures that measurement errors will not make the accelerations too small to achieve impact.

Because the acceleration commands are always perpendicular to the LOS, the PN law gives a scalar value. The PN guidance acceleration command is then expressed in the inertial reference frame as

$$\mathbf{a} = nV_c\dot{\lambda} \begin{bmatrix} -\sin \lambda \\ \cos \lambda \end{bmatrix} \quad (11)$$

The PN guidance law for steering the interceptor is also called constant-bearing guidance, as it steers the interceptor in such a way that the LOS does not rotate. An interceptor using PN guidance, on a perfect collision course, will maintain a constant bearing (i.e.  $\dot{\lambda}$  is zero). When the interceptor is not on a collision course, the trajectory is not truly constant-bearing for  $n < \infty$ . As the effective navigation ratio becomes very large, the LOS rate approaches zero faster, at the expense of more commanded acceleration.

The PN guidance law does not require the target or interceptor velocities to be constant, nor does it require the external accelerations to be zero. For small deviations from constant velocity and small external accelerations, the PN guidance law will still achieve intercept in a feedback fashion. For the asteroid intercept scenario, the velocities are approximately constant, and the external acceleration is due almost entirely to the sun, and can be accounted for as described below.

#### Augmented PN Guidance

The basic PN guidance law can overcome target accelerations in a feedback fashion. As can be seen from the equations for LOS rate and closing velocity, Eqs. (8) and (9), the PN guidance law uses only the position and velocity of the target, and is unable to take into account target accelerations (if they exist). A guidance law which incorporates terms to account for the target's acceleration should be able to perform better than the basic PN guidance law. Since the primary target accelerations are from the sun's gravity, the target's future accelerations are known. An augmented proportional navigation guidance (APNG) law will now be discussed. As with PNG, an easily tractable derivation will be given first, and optimality will be considered in a later section.

From Figure 4.1, with a small-angle approximation, we obtain

$$r \cong x \Rightarrow \lambda = \tan^{-1} \frac{y}{x} \cong \frac{y}{r} \quad (12)$$

where  $y$  is the spacecraft-target distance perpendicular to the reference line ( $X$ -axis). Define the mission time-to-go as

$$t_{go} = t_f - t \quad (13)$$

For a successful intercept mission, the separation at the end of the flight is zero, or  $r(t_f) = 0$ . Integrating Eq. (9) gives

$$r = V_c(t_f - t) = V_c t_{go} \quad (14)$$

Substituting Eq. (14) into Eq. (12) gives

$$\lambda \cong \frac{y}{V_c t_{go}} \quad (15)$$

Differentiating this expression gives

$$\dot{\lambda} \cong \frac{y + \dot{y}t_{go}}{V_c t_{go}^2} \quad (16)$$

Using this expression in the PNG law, we obtain

$$a = nV_c \dot{\lambda} \cong \frac{n(y + \dot{y}t_{go})}{t_{go}^2} \quad (17)$$

For PN guidance, we define the Zero-Effort-Miss (ZEM) distance as the separation between the target and the interceptor at the end of the flight, absent any further control accelerations. With no accelerations, the interceptor and target will continue on straight-line trajectories. The components of the ZEM can thus be given as

$$ZEM_x = x + \dot{x}t_{go} \quad (18a)$$

$$ZEM_y = y + \dot{y}t_{go} \quad (18b)$$

The  $ZEM$  is a simplified prediction of future target-interceptor separation. PN guidance commands are always applied perpendicular to the LOS, therefore only the component of the  $ZEM$  that is perpendicular to the LOS can be accounted for in the augmented guidance law. From trigonometry, we have

$$ZEM_{\perp} = -ZEM_x \sin \lambda + ZEM_y \cos \lambda \quad (19)$$

The PNG law, Eq. (10), is now rewritten as

$$a = n \frac{ZEM_{\perp}}{t_{go}^2} \quad (20)$$

A constant acceleration can be added to the  $ZEM$  term. The linearized  $ZEM$  equation becomes

$$ZEM_{\perp} = y + \dot{y}t_{go} + \frac{1}{2}a_T t_{go}^2 \quad (21)$$

where  $a_T$  is the apparent target acceleration as seen by the spacecraft. Substituting this into Eq. (19), and using Eq. (17), gives

$$a = n \frac{y + \dot{y}t_{go}^2 + 0.5a_T t_{go}^2}{t_{go}^2} = nV_c \dot{\lambda} + \frac{n}{2}a_T \quad (22)$$

In general, for the asteroid terminal intercept scenario, the sun's gravity is the primary disturbing force that needs to be accounted for. The above augmented proportional navigation guidance law can easily incorporate the effect of gravity. The APNG law issues commands perpendicular to the LOS. Thus the acceleration term needed is the relative solar acceleration perpendicular to the LOS. The components of the gravity term for the target and the spacecraft are

$$g_{T_x} = \frac{-\mu_{\odot} r_{T_x}}{r_T^3} \quad (23a)$$

$$g_{T_y} = \frac{-\mu_{\odot} r_{T_y}}{r_T^3} \quad (23b)$$

$$g_{S_x} = \frac{-\mu_{\odot} r_{S_x}}{r_S^3} \quad (23c)$$

$$g_{S_y} = \frac{-\mu_{\odot} r_{S_y}}{r_S^3} \quad (23d)$$



The components perpendicular to the LOS are

$$g_{T\perp} = -g_{T_x} \sin \lambda + g_{T_y} \cos \lambda \quad (24a)$$

$$g_{S\perp} = -g_{S_x} \sin \lambda + g_{S_y} \cos \lambda \quad (24b)$$

The target's apparent acceleration perpendicular to the LOS, as seen by the spacecraft, is

$$g_{\perp} = g_{t\perp} - g_{S\perp} \quad (25)$$

Substituting this equation into the APNG law, Eq. (22), gives

$$a = nV_c \dot{\lambda} + \frac{n}{2} g_{\perp} \quad (26)$$

In the inertial reference frame, the APNG law is expressed as

$$\mathbf{a} = nV_c \dot{\lambda} \begin{bmatrix} -\sin \lambda \\ \cos \lambda \end{bmatrix} + \frac{n}{2} g_{\perp} \begin{bmatrix} -\sin \lambda \\ \cos \lambda \end{bmatrix} \quad (27)$$

### Pulsed Guidance

For simple asteroid intercept, the terminal velocity is not specified, and is assumed to be the closing velocity for PNG and APNG. The PNG and APNG laws assume that continuously variable thrust is available. For thrusters with no throttling ability, a different approach to guidance laws is needed. Two approaches to formulating guidance laws for fixed-thrust-level guidance laws are PN-based guidance laws and predictive guidance laws.

The PNG law continuously generates acceleration commands to achieve intercept. Due to its feedback nature, PNG will continue to generate guidance commands until intercept is achieved. A special case of PNG occurs when the interceptor is on a direct collision course. When this is true, the guidance commands will be zero. When using PNG logic, then, an acceleration command of zero means that the interceptor is instantaneously on a direct collision course. This fact can be exploited to use PNG logic for constant-thrust engines.

Pulsed PNG (PPNG) logic computes the required acceleration commands from PNG, but applies them in continuous-thrust pulses. PPNG will “overshoot” the amount of correction specified by PNG, until the PNG command is zero. At that point, the interceptor is instantaneously on a collision course, and the engines are turned off. If there were no external accelerations or disturbances, the interceptor would continue on an interception course. Because of the acceleration due to the sun, this will not be the case, and a further engine firing will be required later as the interceptor “drifts” further and further from the straight-line collision path.

Two approaches to determining when to fire engines are threshold methods and timed methods. Both methods will be described, as well as advantages and disadvantages associated with each.

The threshold method can employ the so-called Schmitt trigger or other pulse-modulation scheme [5]. Using a Schmitt trigger, acceleration commands are calculated by the PN guidance law as before. The trigger commands the divert thrusters to turn on once the commanded acceleration exceeds a certain magnitude, chosen by the designer, and off when the commanded acceleration reaches a designer-chosen cutoff. With traditional PN guidance the LOS rate must reach zero for a successful intercept. Therefore the second cutoff is typically selected as zero. The trigger control logic for pulsed proportional navigation guidance (PPNG) is shown in Figure 4.2. The Schmitt trigger can also be used for augmented PN guidance, giving an augmented pulsed proportional navigation guidance (APPNG).

The timed method is similar to the threshold method in that the PNG commands are still calculated, and applied with constant thrust. As the name suggests, the difference is that the timed method uses predetermined firing times to turn on the thrusters. The designer must choose the firing schedule. Typically at least three firings are required. An early firing, near or at the beginning of the terminal mission phase, is used to overcome

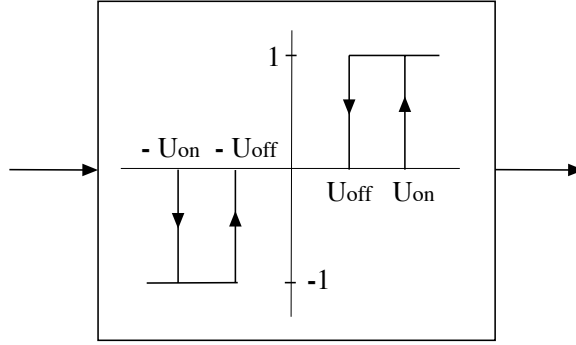


Figure 4.2: Schmitt trigger on-off logic.

most of the orbit injection errors. The final firing comes shortly before impact, with enough lead time to allow the thrust command to complete (e.g. the commanded acceleration reaches zero), but close enough to impact that only minimal further errors accumulate. Additional intermediate firings provide robustness. As with the Schmitt trigger, the timed method turns off thrusters when the commanded thrust level is zero.

The advantage of these methods is the ability to use constant-thrust engines. The Schmitt trigger has the same feedback advantages as PNG, in that it will issue commands when the spacecraft is not on an intercept course. A disadvantage of the Schmitt trigger is that the designer must select the magnitude to turn on the thrusters. Too small a magnitude risks excessive on-off cycles (chatter) for the engines, while too large a magnitude risks missing the target by failing to issue commands at all. An advantage of the timed method is that the total number of on-off cycles is known in advance and can be kept small. A disadvantage is that the timed method might not issue commands even when the calculated PNG commands are large.

#### 4.3.2 Predictive Feedback Guidance Laws

A different class of guidance laws, which also use on-off pulses, are the predictive guidance schemes. Two types of predictive guidance laws are Lambert guidance and time-varying state transition matrix (STM) guidance. Both types of predictive guidance laws will command a required velocity,  $\mathbf{v}_{req}$ . Subtracting the current velocity  $\mathbf{v}$  from this gives the velocity to be gained, denoted as  $\Delta\mathbf{v}$ . The simplest way to generate acceleration commands is to align the thrust vector with the  $\Delta\mathbf{v}$  vector. When the desired velocity is achieved,  $\Delta\mathbf{v}$  is zero and the engine is cut off. The velocity to be gained is expressed as

$$\Delta\mathbf{v} = \mathbf{v}_{req} - \mathbf{v} \quad (28)$$

For a given acceleration magnitude  $a$ , the direction of the thrust acceleration should be aligned with the velocity-to-be-gained vector; that is, we have

$$\mathbf{a} = \frac{\Delta\mathbf{v}}{\|\Delta\mathbf{v}\|} \quad (29)$$

#### Lambert Guidance

The well-known Lambert's Theorem for a two-point boundary value problem (TPBVP) in orbital mechanics states that "the orbital transfer time depends only upon the semimajor axis, the sum of the distances of the initial and final points of the arc from the center of force, and the length of the chord joining these points" [6]. Mathematically, Lambert's theorem is expressed as

$$t_2 - t_1 = f(r_1 + r_2, c, \bar{a}) \quad (30)$$

where  $t_2 - t_1$  is the time of flight,  $c = \|\mathbf{r}_2 - \mathbf{r}_1\|$ , and  $\bar{a}$  is the semi-major axis of the transfer orbit. The solution of Lambert's problem determines the required transfer orbit from position  $\mathbf{r}_1$  to  $\mathbf{r}_2$  in time  $t_2 - t_1$ .

The current position of the spacecraft is known, and the desired time-of-flight can be calculated. Recalling Eq. (14),  $r = V_c(t_f - t) = V_c t_{go}$ , we obtain the time-to-go as

$$t_{go} = \frac{r}{V_c} \quad (31)$$

The position of the target at the end of the flight time can be estimated by numerically integrating the target's current position and velocity over the time-to-go. Many different Lambert solvers have been developed that take the position vectors  $\mathbf{r}_1$  and  $\mathbf{r}_2$ , and the time of flight as inputs, and give parameters of the transfer orbit as output, including  $\mathbf{v}_1$  and  $\mathbf{v}_2$ , the velocity of the transfer orbit at the initial and final times. The initial velocity is the required velocity from the Lambert solver routine,  $\mathbf{v}_{Lambert}$ . The required velocity is thus

$$\mathbf{v}_{req} = \mathbf{v}_{Lambert} = \mathbf{v}_1 \quad (32)$$

Comparing with Eq. (28), we obtain

$$\Delta \mathbf{v} = \mathbf{v}_{Lambert} - \mathbf{v} \quad (33)$$

The acceleration command is then explicitly expressed as

$$\mathbf{a} = a \frac{\mathbf{v}_{Lambert} - \mathbf{v}}{\|\mathbf{v}_{Lambert} - \mathbf{v}\|} \quad (34)$$

The Lambert guidance routine requires a firing schedule to decide when to perform engine maneuvers. In principle, one Lambert guidance engine burn should suffice to achieve impact. In practice, multiple engine burns should be used to account for errors in calculating and applying velocity corrections. Similar to PPNG with timed firings, a minimum of three burns should be used.

### Time-varying State Transition Matrix (STM)

Impulsive guidance laws can also be formulated using the state transition matrix concept. In this approach, the target asteroid's orbit is considered to be a known, or reference, orbit. The interceptor's orbit is considered to be a perturbation from this reference orbit. The goal is then to issue guidance commands that will drive the position perturbation to zero.

A detailed derivation of the state-error transition matrix is not presented here, but can be found in [11]. We will use a 2-dimensional space; the results can be easily generalized to three dimensions. Define the spacecraft's state with respect to the target, expressed in orthogonal components with directions denoted with 1 and 2, as

$$\delta \mathbf{x} = [r_1 \ r_2 \ v_1 \ v_2]^T \quad (35)$$

The future state (position and velocity) of the spacecraft relative to the target can be approximated as

$$\delta \mathbf{x}(t_f) \cong \Phi \delta \mathbf{x}(t_0) \quad (36)$$

where  $\Delta t = t_f - t_0$ , and the state-error transition matrix  $\Phi$  is defined as

$$\Phi = \begin{bmatrix} 1 + \frac{3\mu\Delta t^2 r_1^2}{2r_0^5} - \frac{\mu\Delta t^2}{2r_0^3} & \frac{3\mu\Delta t^2 r_1 r_2}{2r_0^5} & \Delta t & 0 \\ \frac{3\mu\Delta t^2 r_1 r_2}{2r_0^5} & 1 + \frac{3\mu\Delta t^2 r_2^2}{2r_0^5} - \frac{\mu\Delta t^2}{2r_0^3} & 0 & \Delta t \\ \frac{3\mu\Delta t r_1^2}{r_0^5} - \frac{\mu\Delta t}{r_0^3} & \frac{3\mu\Delta t r_1 r_2}{r_0^5} & 1 + \frac{3\mu\Delta t^2 r_1^2}{2r_0^5} - \frac{\mu\Delta t^2}{2r_0^3} & \frac{3\mu\Delta t^2 r_1 r_2}{2r_0^5} \\ \frac{3\mu\Delta t r_1 r_2}{r_0^5} & \frac{3\mu\Delta t r_2^2}{r_0^5} - \frac{\mu\Delta t}{r_0^3} & \frac{3\mu\Delta t^2 r_1 r_2}{2r_0^5} & 1 + \frac{3\mu\Delta t^2 r_2^2}{2r_0^5} - \frac{\mu\Delta t^2}{2r_0^3} \end{bmatrix} \quad (37)$$

where  $r_0 = \sqrt{r_1^2 + r_2^2}$  and the subscript  $\odot$  is dropped for simplicity. Recall that the acceleration due to the sun's gravity is

$$\mathbf{g} = -\frac{\mu \mathbf{r}}{r^3}$$

The Jacobian of the gravitational force vector is often called the gravity-gradient matrix defined as

$$\mathbf{G}(t) = \frac{\partial \mathbf{g}}{\partial \mathbf{r}} = \begin{bmatrix} -\frac{\mu}{r^3} + \frac{3\mu r_1^2}{r_5^5} & \frac{3\mu r_1 r_2}{r_5^5} \\ \frac{3\mu r_1 r_2}{r_5^5} & -\frac{\mu}{r^3} + \frac{3\mu r_2^2}{r_5^5} \end{bmatrix} \quad (38)$$

The state-error transition matrix can now be partitioned as

$$\Phi = \begin{bmatrix} \Phi_1 & \Phi_2 \\ \Phi_3 & \Phi_4 \end{bmatrix} \quad (39)$$

where

$$\Phi_1 = \Phi_4 = \mathbf{I} + \frac{1}{2} \mathbf{G} \Delta t^2 = \begin{bmatrix} 1 + \frac{3\mu \Delta t^2 r_1^2}{2r_0^5} - \frac{\mu \Delta t^2}{2r_0^3} & \frac{3\mu \Delta t^2 r_1 r_2}{2r_0^5} \\ \frac{3\mu \Delta t^2 r_1 r_2}{2r_0^5} & 1 + \frac{3\mu \Delta t^2 r_2^2}{2r_0^5} - \frac{\mu \Delta t^2}{2r_0^3} \end{bmatrix} \quad (40a)$$

$$\Phi_2 = \mathbf{I} \Delta t = \begin{bmatrix} \Delta t & 0 \\ 0 & \Delta t \end{bmatrix} \quad (40b)$$

$$\Phi_3 = \mathbf{G} \Delta t = \begin{bmatrix} \frac{3\mu \Delta t r_1^2}{r_0^5} - \frac{\mu \Delta t}{r_0^3} & \frac{3\mu \Delta t r_1 r_2}{r_0^5} \\ \frac{3\mu \Delta t r_1 r_2}{r_0^5} & \frac{3\mu \Delta t r_2^2}{r_0^5} - \frac{\mu \Delta t}{r_0^3} \end{bmatrix} \quad (40c)$$

The simplest form of intercept guidance using the state transition matrix uses only the position information to generate a  $\Delta \mathbf{v}$  command. The first-order approximation for the final miss vector, absent any further acceleration commands, is found as

$$\mathbf{r}(t_f) \cong \tilde{\mathbf{r}}_{tf} = \Phi_1(t) \mathbf{r}(t) + \Phi_2(t) \mathbf{v}(t) \quad (41)$$

The second term on the right-hand side is negligible for small changes in closing velocity, giving

$$\mathbf{r}(t_f) \cong \tilde{\mathbf{r}}_{tf} = \Phi_1(t) \mathbf{r}(t) \quad (42)$$

Consider driving the final relative position to zero. For linearized dynamics, there are no external accelerations, so we have

$$\begin{aligned} 0 &= \mathbf{r}(t_f) - \frac{\mathbf{r}(t_f)}{\Delta t} \\ &\cong \mathbf{r}(t_0) + \mathbf{v}(t_0) - \frac{\mathbf{r}(t_f)}{\Delta t} \Delta t \\ &= \mathbf{r}(t_0) + \mathbf{v}(t_0) \Delta t + \mathbf{v}_{STM} \Delta t \end{aligned} \quad (43)$$

where  $\mathbf{v}_{STM}$  is seen to be the velocity to be gained to ensure impact.

For small changes in relative velocity, we have

$$\dot{\mathbf{r}}(t_f) \cong \dot{\mathbf{r}}(t_0) \quad (44a)$$

$$\Rightarrow \frac{\mathbf{r}(t_f)}{\Delta t} \cong \hat{\mathbf{r}}(t_f) \dot{\mathbf{r}}(t_0) \quad (44b)$$

The velocity change to be imparted becomes

$$\begin{aligned} \Delta \mathbf{v} &= \mathbf{v}_{STM} - \mathbf{v} \\ &= \hat{\mathbf{r}}(t_f) \dot{\mathbf{r}}(t_0) - \mathbf{v} \end{aligned} \quad (45)$$

The acceleration command vector is then expressed, similar to Lambert guidance, as

$$\mathbf{a} = a \frac{\mathbf{v}_{STM} - \mathbf{v}}{\|\mathbf{v}_{STM} - \mathbf{v}\|} \quad (46)$$

Using the gravity gradient matrix from Eq. (38), we can show that

$$\mathbf{r}(t_f) \approx \frac{\Delta t^2}{2} \mathbf{G}(t) \mathbf{r}(t) + \mathbf{r}(t) \quad (47)$$

### Predictive Impulsive Guidance

For practical implementation, we adopt the following definitions:

$$V_c(t) = \dot{r}(t) \quad (48a)$$

$$\Lambda(t) = \frac{\mathbf{r}(t)}{r(t)} \quad (48b)$$

$$\Lambda_c(t) = \frac{\tilde{\mathbf{r}}(t_f)}{\tilde{r}(t_f)} \quad (48c)$$

$$t_{go} = \Delta t \quad (48d)$$

Substituting these into the guidance law in Eq. (45) gives the predictive impulsive guidance law as

$$\Delta \mathbf{v} = V_c \Lambda - \mathbf{v} \quad (49)$$

### Kinematic Impulsive Guidance

In terms of the line-of-sight angle, we have

$$\Lambda(t) = \begin{bmatrix} \cos \lambda(t) \\ \sin \lambda(t) \end{bmatrix} \quad (50a)$$

$$\dot{\Lambda}(t) = \begin{bmatrix} -\dot{\lambda} \sin \lambda(t) \\ \dot{\lambda} \cos \lambda(t) \end{bmatrix} \quad (50b)$$

The relative position can also be approximated as

$$\mathbf{r}(t) \approx V_c t_{go} \Lambda(t) \quad (51)$$

and we obtain

$$\mathbf{r}(t_f) \approx \frac{V_c t_{go}^3}{2} \mathbf{G}(t) \Lambda(t) + \mathbf{V}_c t_{go} \Lambda(t) \quad (52)$$

The relative velocity can be approximated as a component along the LOS and a component perpendicular to the LOS, described as

$$\mathbf{v}(t) \approx V_c t_{go} \dot{\Lambda}(t) + V_c \Lambda(t) \quad (53)$$

Substituting Eq. (53) into Eq. (49) results in the kinematic impulsive guidance law of the form

$$\Delta \mathbf{v} = V_c \left( \Lambda_c - t_{go} \dot{\Lambda} - \Lambda \right) \quad (54)$$

## 4.4 Optimal Feedback Guidance Algorithms

For some applications it is desirable to specify terminal conditions on the interceptor. For intercept, the terminal position is by definition zero. The terminal velocity, though, may have direction or magnitude requirements, depending on the mission. Optimal feedback guidance laws can be used to achieve intercept, with the option of specifying the final velocity.

Three different optimal feedback guidance laws are considered for asteroid intercept and rendezvous. The various forms of proportional navigation and predictive guidance laws compute an estimated mission time-to-go based on relative position and velocity. This computed time-to-go is used as an input for the predictive laws, and is available as an output of the proportional navigation laws. In contrast, the optimal feedback guidance laws discussed in this section use a specified time-to-go as a mission parameter, and compute the acceleration commands needed to achieve intercept at this pre-determined time.

When the final impact velocity vector (both impact velocity and impact angle) is specified, the terminal velocity is constrained. This leads to the constrained-terminal-velocity guidance (CTVG) law. If the final velocity is free, the free-terminal-velocity guidance (FTVG) law results, as discussed in [9, 10]. When only the approach angle is commanded, the velocity vector component along the desired final direction is free, while the perpendicular components are constrained to be zero. A combination of FTVG along the impact direction and CTVG along the perpendicular directions allows pointing of the final velocity vector, referred to as intercept-angle-control guidance (IACG).

#### 4.4.1 Constrained-Terminal-Velocity Guidance (CTVG)

Consider an optimal control problem for minimizing the integral of the acceleration squared, formulated as

$$J = \frac{1}{2} \int_{t_0}^{t_f} \mathbf{a}^T \mathbf{a} dt \quad (55)$$

subject to  $\dot{\mathbf{r}} = \mathbf{v}$  and  $\dot{\mathbf{v}} = \mathbf{g} + \mathbf{a}$  with the following boundary conditions:

$$\mathbf{r}(t_0) = \mathbf{r}_0; \quad \mathbf{r}(t_f) = \mathbf{r}_f \quad (56a)$$

$$\mathbf{v}(t_0) = \mathbf{v}_0; \quad \mathbf{v}(t_f) = \mathbf{v}_f \quad (56b)$$

The Hamiltonian function is defined as

$$H = \frac{1}{2} \mathbf{a}^T \mathbf{a} + \mathbf{p}_r^T \mathbf{v} + \mathbf{p}_v^T (\mathbf{g} + \mathbf{a}) \quad (57)$$

where  $\mathbf{p}_r$  and  $\mathbf{p}_v$  are co-state vectors associated with the position and velocity vectors, respectively. In general, for a terminal-phase guidance problem gravity is a function of position and time; i.e., we have  $\mathbf{g} = \mathbf{g}(\mathbf{r}, t)$ . Using such a function will not allow a simple closed-form solution to the optimal control problem. For the class of terminal guidance problems considered here, the gravitational acceleration is approximately constant for the duration of the terminal phase. Therefore a constant gravitational acceleration is assumed to permit a closed-form solution. The co-state equations and control equation imply that

$$\dot{\mathbf{p}}_r = -\frac{\partial H}{\partial \mathbf{r}} = 0 \quad (58a)$$

$$\dot{\mathbf{p}}_v = -\frac{\partial H}{\partial \mathbf{v}} = -\mathbf{p}_r \quad (58b)$$

$$\frac{\partial H}{\partial \mathbf{a}} = 0 \Rightarrow \mathbf{a} = -\mathbf{p}_v \quad (58c)$$

For fixed terminal conditions, the co-states at  $t_f$  are non-zero. Define  $t_{go} = t_f - t$  as the time-to-go before arrival at the terminal state, and let  $\mathbf{p}_r(t_f)$  and  $\mathbf{p}_v(t_f)$  describe the values of  $\mathbf{p}_r$  and  $\mathbf{p}_v$  at  $t_f$ , respectively. Integrating the co-state equations yields

$$\mathbf{p}_r = \mathbf{p}_r(t_f) \quad (59a)$$

$$\mathbf{p}_v = t_{go} \mathbf{p}_r(t_f) + \mathbf{p}_v(t_f) \quad (59b)$$

Substituting Eq. (59) into Eq. (58) yields the optimal control solution as

$$\mathbf{a} = -t_{go} \mathbf{p}_r(t_f) - \mathbf{p}_v(t_f) \quad (60)$$

The states can thus be expressed as

$$\mathbf{v} = \frac{t_{go}^2}{2} \mathbf{p}_r(t_f) + t_{go} \mathbf{p}_v(t_f) - t_{go} \mathbf{g} + \mathbf{v}_f \quad (61)$$

$$\mathbf{r} = -\frac{t_{go}^3}{6} \mathbf{p}_r(t_f) - \frac{t_{go}^2}{2} \mathbf{p}_v(t_f) + \frac{t_{go}^2}{2} \mathbf{g} - t_{go} \mathbf{v}_f + \mathbf{r}_f \quad (62)$$

Combining Eq. (61) and Eq. (62) gives

$$\mathbf{p}_r(t_f) = \frac{6(\mathbf{v} + \mathbf{v}_f)}{t_{go}^2} + \frac{12(\mathbf{r} - \mathbf{r}_f)}{t_{go}^3} \quad (63a)$$

$$\mathbf{p}_v(t_f) = -\frac{2(\mathbf{v} + 2\mathbf{v}_f)}{t_{go}} - \frac{6(\mathbf{r} - \mathbf{r}_f)}{t_{go}^2} + \mathbf{g} \quad (63b)$$

Finally, the optimal feedback control law with specified  $\mathbf{r}_f$ ,  $\mathbf{v}_f$ , and  $t_{go}$ , the CTVG law, is obtained as

$$\mathbf{a} = \frac{6[\mathbf{r}_f - (\mathbf{r} + t_{go}\mathbf{v})]}{t_{go}^2} - \frac{2(\mathbf{v}_f - \mathbf{v})}{t_{go}} - \mathbf{g} \quad (64)$$

or

$$\mathbf{a} = \frac{6[\mathbf{r}_f - (\mathbf{r} + t_{go}\mathbf{v}_f)]}{t_{go}^2} + \frac{4(\mathbf{v}_f - \mathbf{v})}{t_{go}} - \mathbf{g} \quad (65)$$

#### 4.4.2 Free-Terminal-Velocity Guidance (FTVG)

For the case when the terminal velocity is free, the boundary conditions for unconstrained final velocity give  $\mathbf{p}_v(t_f) = 0$ , thus from Eq. (59),  $\mathbf{p}_v$  becomes

$$\mathbf{p}_v = t_{go}\mathbf{p}_r(t_f) \quad (66)$$

The acceleration command is then given as

$$\mathbf{a} = -\mathbf{p}_v = -t_{go}\mathbf{p}_r(t_f) \quad (67)$$

Accordingly we have

$$\mathbf{v} = \frac{t_{go}^2}{2}\mathbf{p}_r(t_f) - t_{go}\mathbf{g} + \mathbf{v}_f \quad (68a)$$

$$\mathbf{r} = -\frac{t_{go}^3}{6}\mathbf{p}_r(t_f) + \frac{t_{go}^2}{2}\mathbf{g} - t_{go}\mathbf{v}_f + \mathbf{r}_f \quad (68b)$$

Solving the above equations results in

$$\mathbf{p}_r(t_f) = -\frac{3}{t_{go}^3} \left( \mathbf{r}_f - \mathbf{r} - \mathbf{v}t_{go} - \frac{t_{go}^2}{2}\mathbf{g} \right) \quad (69)$$

The terminal velocity can be expressed in terms of time-to-go and system states after substituting Eq. (69) into Eq. (68), as

$$\mathbf{v}_f = \frac{3}{2t_{go}}(\mathbf{r}_f - \mathbf{r}) - \frac{1}{2}\mathbf{v} + \frac{1}{4}t_{go}\mathbf{g} \quad (70)$$

which is a function of time with given initial position and velocity vectors.

Finally, substituting Eq. (69) into Eq. (67), we obtain the FTVG law as

$$\mathbf{a} = \frac{3}{t_{go}^2}(\mathbf{r}_f - \mathbf{r}) - \frac{3}{t_{go}}\mathbf{v} - \frac{3}{2}\mathbf{g} \quad (71)$$

#### 4.4.3 Intercept-Angle-Control Guidance (IACG)

Both CTVG and FTVG command the final position. The terminal velocity vector can be commanded, as in CTVG, or free as in FTVG. Consider an orthogonal coordinate system with the first component ( $\mathbf{e}_1$ ) in the direction of the desired terminal velocity, and the other two components ( $\mathbf{e}_2$  and  $\mathbf{e}_3$ ) perpendicular to this direction. The acceleration vector can be expressed as

$$\mathbf{a} = a_1\mathbf{e}_1 + a_2\mathbf{e}_2 + a_3\mathbf{e}_3 \quad (72)$$

The performance index then becomes

$$J = \frac{1}{2} \int_{t_0}^{t_f} (a_1^2 + a_2^2 + a_3^2) dt \quad (73)$$

The position, velocity, and gravity vectors can also be expressed as

$$\begin{aligned} \mathbf{r} &= r_1\mathbf{e}_1 + r_2\mathbf{e}_2 + r_3\mathbf{e}_3 \\ \mathbf{v} &= v_1\mathbf{e}_1 + v_2\mathbf{e}_2 + v_3\mathbf{e}_3 \\ \mathbf{g} &= g_1\mathbf{e}_1 + g_2\mathbf{e}_2 + g_3\mathbf{e}_3 \end{aligned} \quad (74a)$$

In order to achieve impact along the  $\mathbf{e}_1$ -direction, it is required that  $v_1$  is free, and  $v_2$  and  $v_3$  are both zero.

The IACG algorithm combines the CTVG and FTVG algorithms as follows:

$$\mathbf{a} = \left( \frac{3(r_{f1} - r_1)}{t_{go}^2} - \frac{3v_1}{t_{go}} - \frac{3g_1}{2} \right) \mathbf{e}_1 + \left( \frac{3(r_{f2} - r_2)}{t_{go}^2} - \frac{3v_2}{t_{go}} - \frac{3g_2}{2} \right) \mathbf{e}_2 + \left( \frac{3(r_{f3} - r_3)}{t_{go}^2} - \frac{3v_3}{t_{go}} - \frac{3g_3}{2} \right) \mathbf{e}_3 \quad (75)$$

This algorithm can also be expressed in terms of vectors  $\mathbf{r}$ ,  $\mathbf{r}_f$ ,  $\mathbf{v}$ , and  $\mathbf{g}$ , as follows:

$$\mathbf{a} = (3\mathbf{e}_1\mathbf{e}_1^T + 6\mathbf{e}_2\mathbf{e}_2^T + 6\mathbf{e}_3\mathbf{e}_3^T) \frac{\mathbf{r}_f - \mathbf{r}}{t_{go}^2} - (3\mathbf{e}_1\mathbf{e}_1^T + 4\mathbf{e}_2\mathbf{e}_2^T + 4\mathbf{e}_3\mathbf{e}_3^T) \frac{\mathbf{v}}{t_{go}} - \left( \frac{3}{2}\mathbf{e}_1\mathbf{e}_1^T + \mathbf{e}_2\mathbf{e}_2^T + \mathbf{e}_3\mathbf{e}_3^T \right) \mathbf{g} \quad (76)$$

It is important to note that the IACG guidance law does not impose a unique direction on the final velocity. Ultimately the velocity is only constrained to be parallel to the specified direction. The final velocity direction will depend on the initial conditions. If the spacecraft is initially moving toward the target in the  $\mathbf{e}_1$  direction, that is  $(r_{f1} - r_1) v_1 > 0$ , then the intercept will be in the specified direction. Otherwise, when  $(r_{f1} - r_1) v_1 \leq 0$ , the spacecraft will intercept opposite the specified direction.

#### 4.4.4 Relationship Between PNG and Optimal Feedback Guidance

As mentioned in the previous section on PNG, the optimal value for the navigation constant is 3. To show this, first consider a two-dimensional problem with

$$\mathbf{r}_f - \mathbf{r} = [x \ y]^T \quad (77a)$$

$$-\mathbf{v} = [\dot{x} \ \dot{y}]^T \quad (77b)$$

$$\lambda = \tan^{-1} \frac{y}{x} \quad (77c)$$

where  $\lambda$  is the LOS angle as before. Define  $R = |\mathbf{r}_f - \mathbf{r}|$  as the distance from the spacecraft to the target along the LOS. The closing velocity and time-to-go are given by

$$V_c = -\dot{R} \quad (78a)$$

$$t_{go} = \frac{R}{V_c} \quad (78b)$$



The optimal FTVG algorithm thus becomes

$$\mathbf{a} = 3V_c \dot{\lambda} \begin{bmatrix} -\sin \lambda \\ \cos \lambda \end{bmatrix} - \frac{3}{2} \mathbf{g} \quad (79)$$

This is the augmented PNG logic, with an effective navigation ratio of 3.

Controlling the direction of the final velocity is equivalent to controlling the final impact angle, but not the velocity [8]. Since the PNG laws only command control perpendicular to the LOS, the velocity along the LOS is free. For the case with small LOS angles, it can be shown that IACG becomes PNG with impact angle control

$$a = 4V_c \dot{\lambda} + \frac{2V_c (\lambda - \lambda_f)}{t_{go}} - g \quad (80)$$

where  $\lambda_f$  is the desired final impact angle.

#### 4.4.5 Calculation of Time-To-Go

The basic PNG laws do not specify the time-to-go, and can estimate it based on current conditions. In contrast, the optimal feedback guidance laws are derived for a fixed flight time. The time-to-go appears in the acceleration commands. For some missions it may be desirable to specify the mission time. However, for asteroid intercept it is often not necessary to achieve impact or rendezvous at a particular time, and a difference of a few seconds or minutes is not significant to the overall mission.

Consider, for example, an interceptor that is already on a collision course with the target. Proportional navigation will not issue any commands, and intercept will occur based on the interceptor's velocity relative to the target. If one of the optimal guidance laws is used with a different time-to-go, intercept will still occur, but the spacecraft will spend unnecessary fuel either speeding up or slowing down the spacecraft along the LOS direction. It is natural to ask, then, if there is an optimal choice for time-to-go. For both the CTVG and FTVG laws, under certain conditions a local minimum for the performance index with respect to mission time is possible. This condition will be given next. A complete derivation can be found in [11].

#### CTVG

The optimal mission time-to-go for the CTVG law is given by [11]

$$t_{go} = \begin{cases} \tau & \text{if } B^2 - 4AC > 0 \text{ and } B < 0 \\ \text{no solution} & \text{otherwise} \end{cases} \quad (81)$$

where

$$\tau = \frac{-B - \sqrt{B^2 - 4AC}}{2A} \quad (82a)$$

$$A = (\mathbf{v}^T \mathbf{v} + \mathbf{v}_f^T \mathbf{v} + \mathbf{v}_f^T \mathbf{v}_f) \geq 0 \quad (82b)$$

$$B = 6 (\mathbf{r}_f - \mathbf{r})^T (\mathbf{v} + \mathbf{v}_f) \quad (82c)$$

$$C = 9 (\mathbf{r}_f - \mathbf{r})^T (\mathbf{r}_f - \mathbf{r}) \quad (82d)$$

When there is no solution, increasing values of  $t_{go}$  lead to decreasing values of the performance index.

#### FTVG

The optimal mission time-to-go for the FTVG law is [11]

$$\tau = \frac{2|\mathbf{r}_f - \mathbf{r}|}{|\mathbf{v}|} \left( \cos \theta - \sqrt{\cos^2 \theta - 3/4} \right); \quad \theta \in (-30^\circ, 30^\circ) \quad (83)$$

where  $\theta$  is the angle between the vectors  $\mathbf{v}$  and  $(\mathbf{r}_f - \mathbf{r})$ . As before, outside this range there is no finite solution, and increasing the time-to-go decreases the performance index.

There is not in general a way to derive an optimal time-to-go for IACG. Recall that IACG consists of FTVG along the final impact velocity direction, and CTVG perpendicular to this. Typically, then, there will be two different optimal times, and the true local minimum will be dependent on the particular mission geometry.

#### 4.4.6 ZEM/ZEV Feedback Guidance

In the preceding section, the optimal feedback guidance laws were discussed assuming a uniform gravitational field ( $\mathbf{g} = \text{constant}$ ). If  $\mathbf{g}$  is an explicit function of time, it is also possible to derive the optimal CTVG and FTVG algorithms.

Let the zero-effort-miss (ZEM) be the position offset at the end of the mission if no more acceleration is applied. Also let the zero-effort velocity (ZEV) be the end-of-mission velocity offset with no acceleration applied. The dynamic equations of motion with no control acceleration are

$$\begin{aligned}\dot{\mathbf{r}} &= \mathbf{v} \\ \dot{\mathbf{v}} &= \mathbf{g}(t)\end{aligned}\tag{84a}$$

These equations can be integrated to find the ZEV and ZEM as

$$\mathbf{ZEV} = \mathbf{v}_f - \left[ \mathbf{v} + \int_t^{t_f} \mathbf{g}(\tau) d\tau \right]\tag{85a}$$

$$\mathbf{ZEM} = \mathbf{r}_f - \left[ \mathbf{v}t_{go} + \int_t^{t_f} (t_f - \tau) \mathbf{g}(\tau) d\tau \right]\tag{85b}$$

With the ZEM and ZEV defined as above, the ZEM/ZEV version of the CTVG law is expressed as

$$\mathbf{a} = \frac{6}{t_{go}^2} \mathbf{ZEM} - \frac{2}{t_{go}} \mathbf{ZEV}\tag{86}$$

The FTVG law is expressed as

$$\mathbf{a} = \frac{3}{t_{go}} \mathbf{ZEM}\tag{87}$$

As was the case for the optimal laws, the ZEM/ZEV laws are optimal for a specified flight time. When a particular flight time is needed as a mission requirement, ZEM/ZEV laws can be applied using that flight time. If the exact flight time is not important, some additional analysis can be applied to find the optimal flight time. The optimal flight times found above for CTVG and FTVG, for example, can be used as a starting point for the optimal flight time.

#### 4.4.7 Estimation of the ZEM and ZEV

For the case when gravity is not constant, the ZEM and ZEV must be found somehow. There are three basic options, of varying complexity. The most complex option is simple numerical integration of the equations of motion. This method is computationally intensive, but will result in the most accurate estimates of ZEM and ZEV. The second option employs the time-varying STM. Recall that the ZEM is the difference between the desired final position and the final position in the absence of corrective maneuvers. For the asteroid intercept/rendezvous problem, this can be expressed as

$$\mathbf{ZEM}(t) = [\mathbf{r}(t_f) - \mathbf{r}_f]_{\mathbf{a}=0}\tag{88}$$

Table 4.1: Initial conditions.

	x position, km	y position, km	x velocity, km/s	y velocity, km/s
Target	$111.62 \times 10^6$	0	0	37.63
Interceptor	$111.62 \times 10^6$	$936.35 \times 10^3$	0	26.79

where  $\mathbf{r}(t_f)$  is the predicted spacecraft position at  $t = t_f$  and  $\mathbf{r}_f$  is the desired final position. Then, the ZEM estimate using the time-varying STM becomes

$$\mathbf{ZEM}_{STM}(t) \approx \delta \mathbf{r}(t_f) = \Phi_1 \delta \mathbf{r}(t) + \Phi_2 \delta \mathbf{v}(t) \quad (89)$$

Similarly, the ZEV can be estimated as

$$\mathbf{ZEV}(t) = [\mathbf{v}(t_f) - \mathbf{v}_f]_{\mathbf{a}=0} \quad (90)$$

$$\mathbf{ZEV}_{STM}(t) \approx \delta \mathbf{r}(t_f) = \Phi_3 \delta \mathbf{r}(t) + \Phi_4 \delta \mathbf{v}(t) \quad (91)$$

Finally, for cases when the gravitational force is not significant, the ZEM and ZEV can be estimated by direct linearization of the relative states. Ignoring any external accelerations, we can estimate the ZEV as the current relative velocity and the ZEM as the current relative position plus the relative velocity times time-to-go, described as

$$\mathbf{ZEM}(t) \approx \delta \mathbf{r}(t) + \delta \mathbf{v}(t) \Delta t \quad (92a)$$

$$\mathbf{ZEV}(t) \approx \delta \mathbf{v}(t) \quad (92b)$$

## 4.5 Simulation Results

The guidance laws described in this chapter were evaluated with a 4th-order Runge-Kutta numerical integration scheme. Some of simulation study results are presented in this chapter. Detailed simulation results can be found in [7–10]. The asteroid Apophis was considered as a reference target. It was assumed to be at perihelion at the beginning of the terminal phase and its diameter was assumed as 280 m. The initial conditions are given in Table 4.1. The interceptor spacecraft is ahead of the target and displaced outward radially. This scenario puts extreme demands on the GNC algorithms, starting with a 10.8 km/s closing velocity. In the absence of guidance commands, the initial conditions will result in a miss distance of 40,000 km. The baseline spacecraft is a 1000-kg interceptor spacecraft with 10-N thrusters. Thrusters are turned off for the final ten minutes of each mission scenario. For the basic simulations it is assumed that all measurements of positions in the heliocentric frame, relative positions, angles and angular rates, and the LOS are available with no errors.

### 4.5.1 Classical Feedback Guidance Laws

A kinetic impact mission to the asteroid Apophis was simulated with the various PN guidance laws, as well as the predictive and kinetic impulsive laws. Predictive guidance schemes use a pre-defined firing schedule for trajectory correction maneuvers. Earlier firing times require less  $\Delta V$  because the impactor trajectory has not deviated as far from the reference trajectory. However, measured or estimated relative states for realistic sensing equipment are less reliable when the spacecraft is further from the target. Later firing times benefit from improved measurements, but require larger corrective maneuvers to overcome position deviations. Because the guidance theory itself is linearized, the calculated corrective maneuver at any given time will, in general, not be accurate. The first maneuver in particular is not sufficient by itself for intercept, as the approximations from linearization are increasingly detrimental with increasing position and velocity deviations. Therefore

Table 4.2: Performance comparison of classical feedback guidance laws.

Guidance Laws	$\Delta v$ , m/s	ZEM, m
PN	5.6	4.2
Augmented PN	5.5	3.4
Pulsed PN	4.7	4.3
Pulsed Augmented PN	4.2	3.3
Predictive Impulsive	4.3	3.3
Kinematic Impulsive	4.3	4.8

multiple firings are required to assure successful intercept. The linearized results are more accurate on some parts of the trajectory than on others. However, there is no way to know when better firing times are, as the accuracy of the linearization changes for different orbits. Finally, the performance of the kinematic impulsive scheme degrades near the end of the mission, as the further linearization for relative position causes increased error when the interceptor approaches the target.

For the kinematic and predictive impulsive schemes, three firing times are selected. The first firing takes place with 20 hours to go, the second with 9 hours to go, and the third with 10 minutes to go. These times encompass an early firing for a large burn to put the spacecraft much closer to an intercept course, a burn approximately halfway through the terminal phase when the linearization errors are much smaller, and a final burn shortly before impact. The firing sequence was chosen based on the three-pulse adaptive scheme used by the Deep Impact mission.

Table 4.2 summarizes the  $\Delta V$  requirements and final miss distance for each guidance law. Trajectories of the spacecraft and target, LOS and LOS rate histories, and  $\Delta V$  usage are shown in Figures 4.3-4.6.

#### 4.5.2 Optimal Feedback Guidance Algorithms

Test cases using the CTVG, FTVG, and IACG algorithms were numerically simulated. Throughout the numerical simulation studies, we assumed that the system states can be measured with no error even though these feedback controllers possess good performance robustness. A generic spacecraft model from [2] is used for these three test cases. The initial mass of the spacecraft is 1905 kg and the engine exhaust velocity is assumed as 1.964 km/s ( $1/c = 5.0910^{-4}$  s/m). A 4<sup>th</sup>-order Runge-Kutta numerical integrator with an interval time of 0.1 s is used. During the last two integration steps,  $t_{go}$  is held at 0.2 s to avoid any numerical singularity problem.

Results for the FTVG and IACG algorithms are shown in Figures 4.7-4.9. The performance of the algorithms for a variety of initial and final conditions can be confirmed. Figure 4.8 shows the corresponding performance index and propellant mass used for a different mission times. The existence of a local minimum for the performance index in some cases can be seen. It should also be noted that actual fuel use does not correspond precisely to the performance index, and especially long flight times do not lead to reduced propellant usage.

#### 4.5.3 High-Fidelity Simulation Using CLEON Software

##### Overview

GMV has developed a software (SW) tool called CLEON for high-fidelity simulation of the closed-loop trajectory of the asteroid interceptor [2,3]. CLEON is a hybrid (continuous-discrete) multi-rate SW simulator implemented in Matlab/Simulink. A block diagram of the program is shown in Figure 4.10. Two different levels of realism for the optical sensors (navigation camera and star-tracker) are available, and global-performance

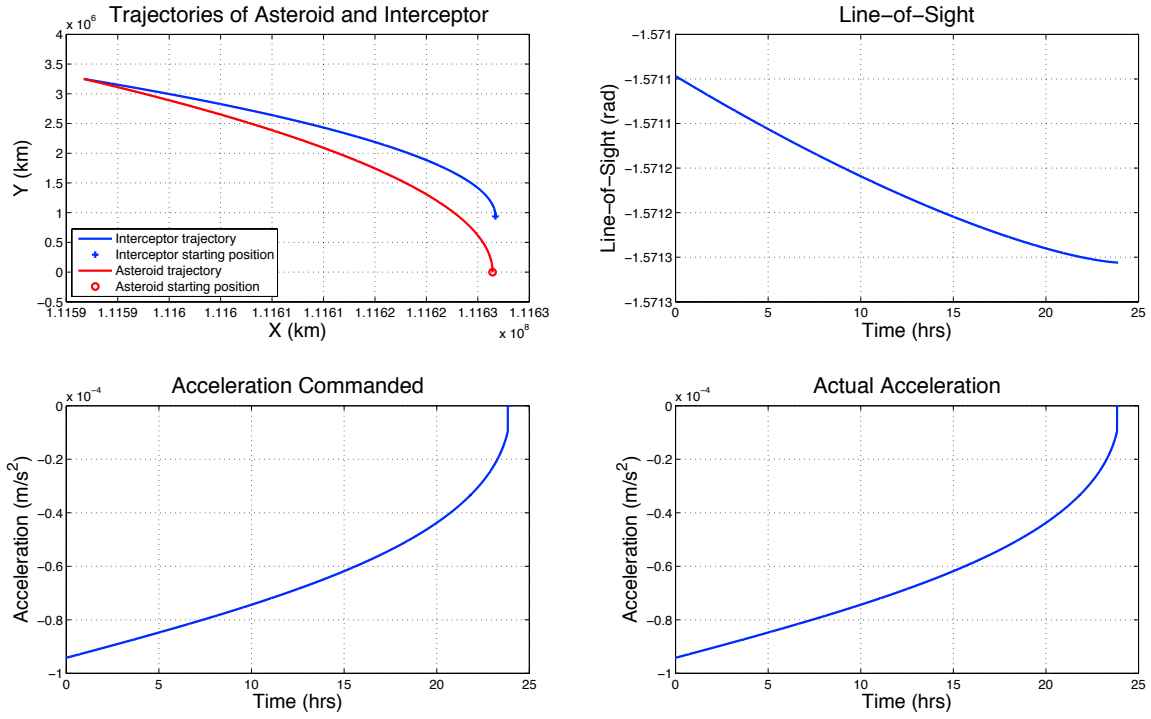


Figure 4.3: Trajectories, line-of-sight angle, commanded acceleration, and applied acceleration for PN guidance.

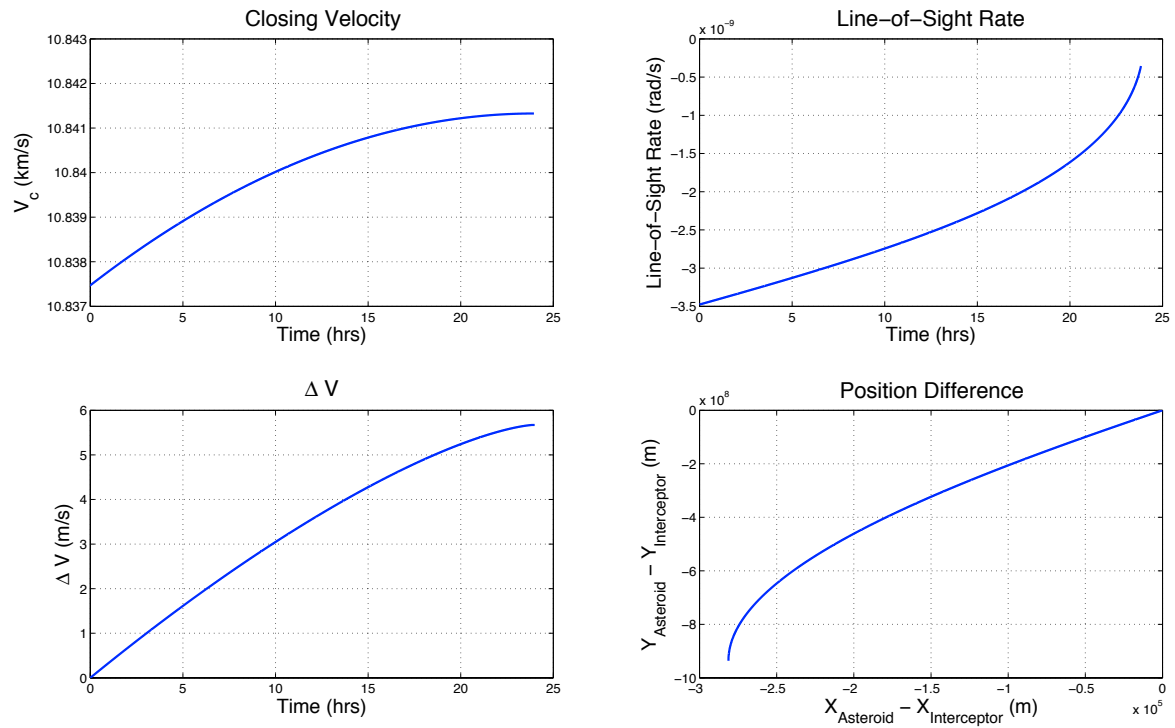


Figure 4.4: Closing velocity, line-of-sight rate,  $\Delta v$  used, and position difference for PN guidance.

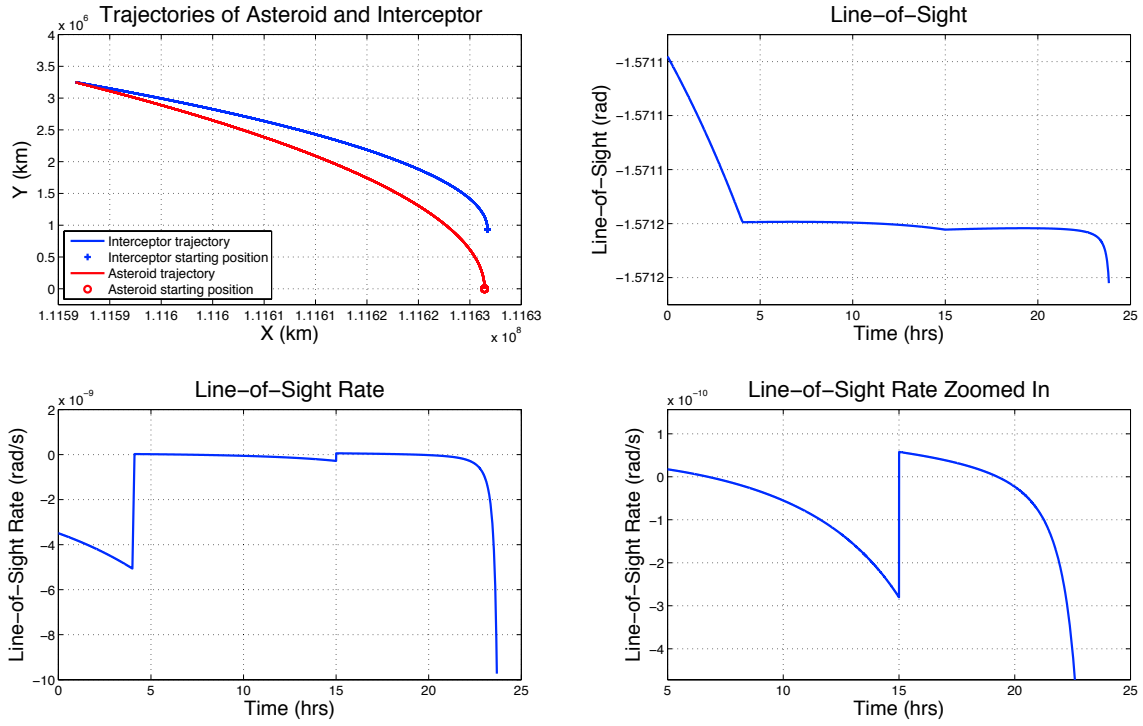


Figure 4.5: Trajectories, line-of-sight angle, line-of-sight rate, and detailed view of rate for PI guidance.

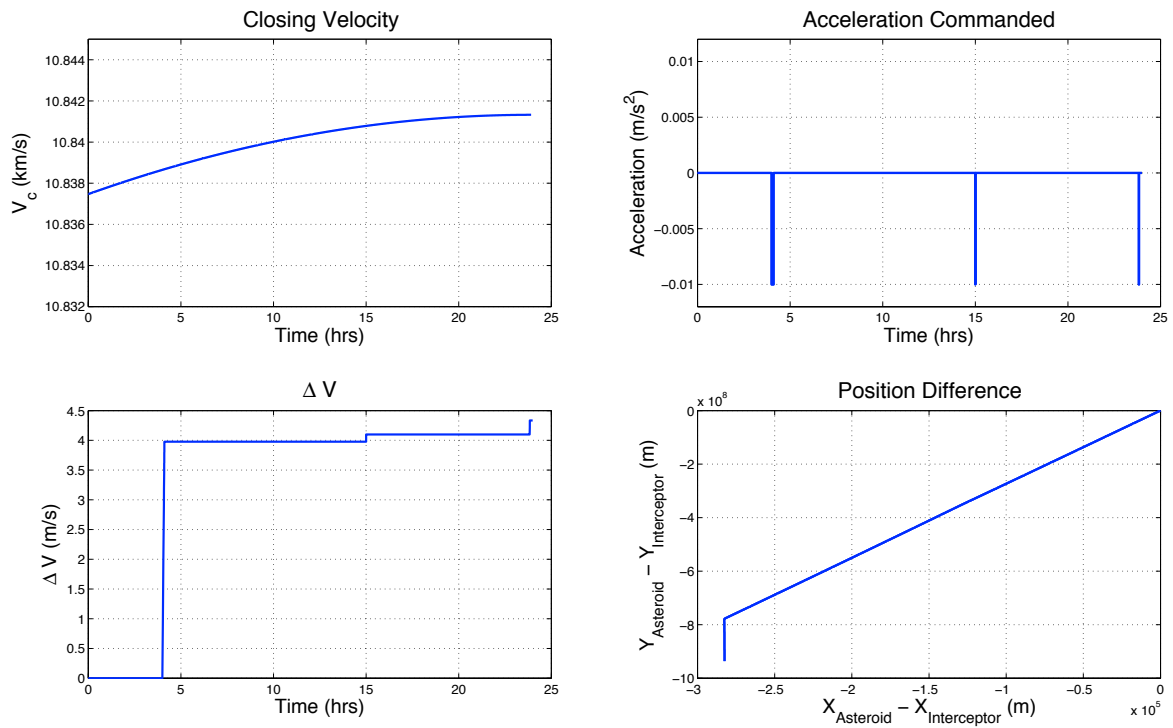
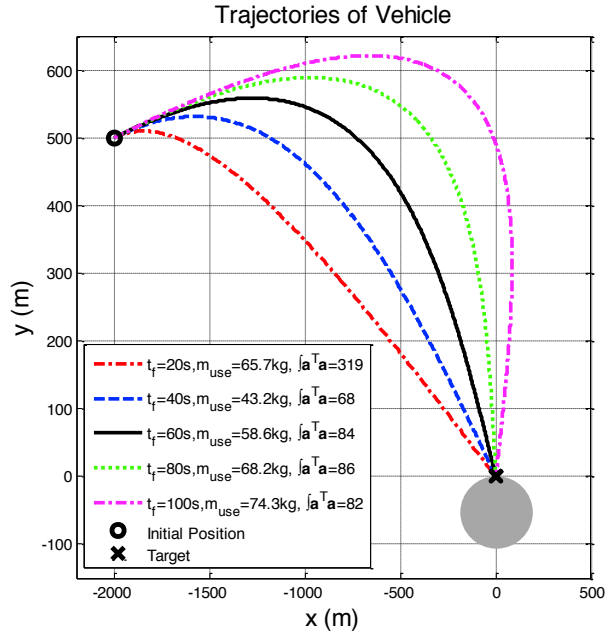
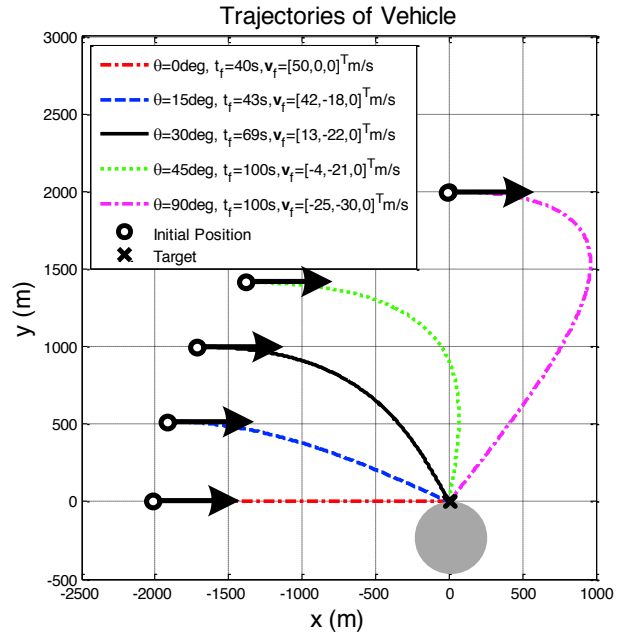


Figure 4.6: Closing velocity, commanded acceleration,  $\Delta v$  used, and position difference for PI guidance.

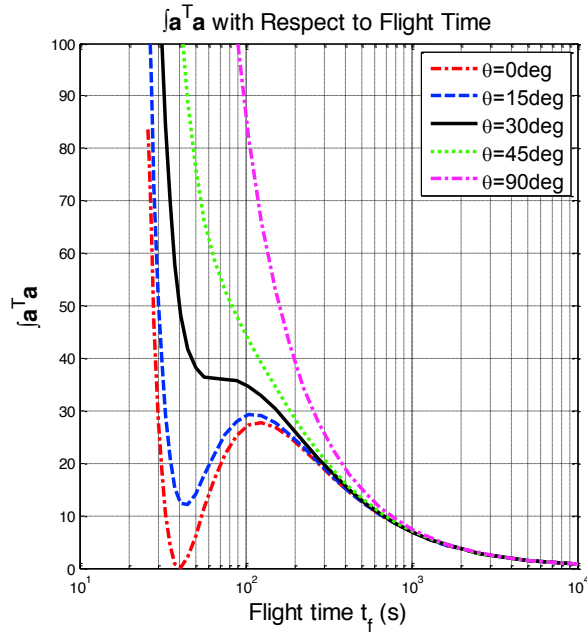


(a) Different flight times.

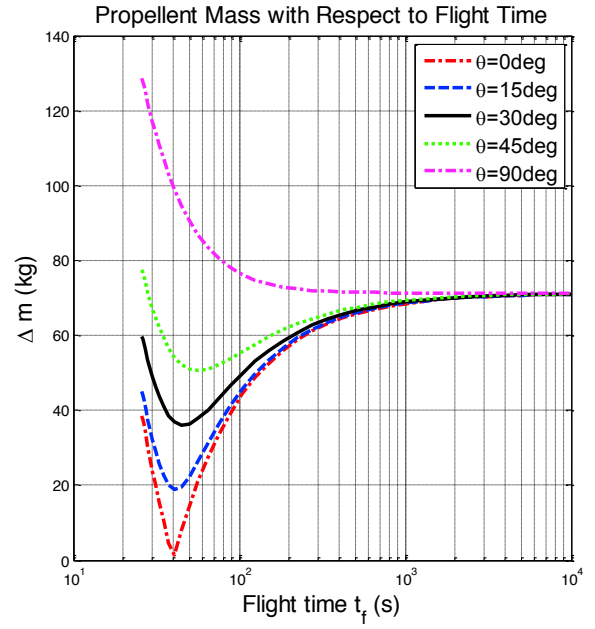


(b) Different initial positions.

Figure 4.7: FTVG guidance algorithms for asteroid intercept.

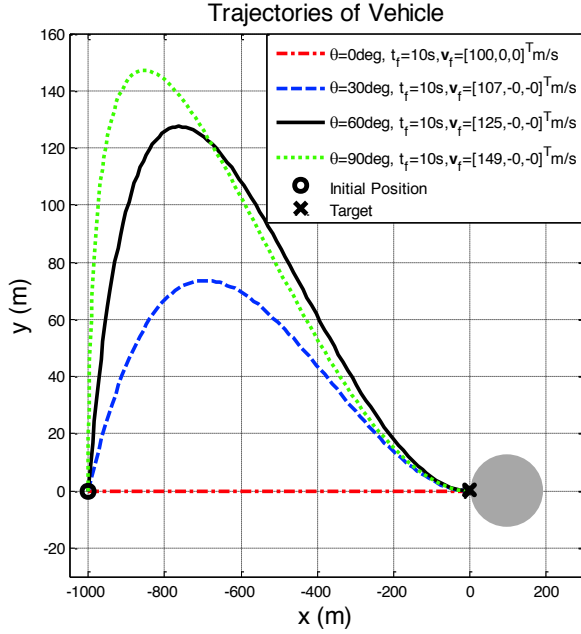


(a) Performance index.

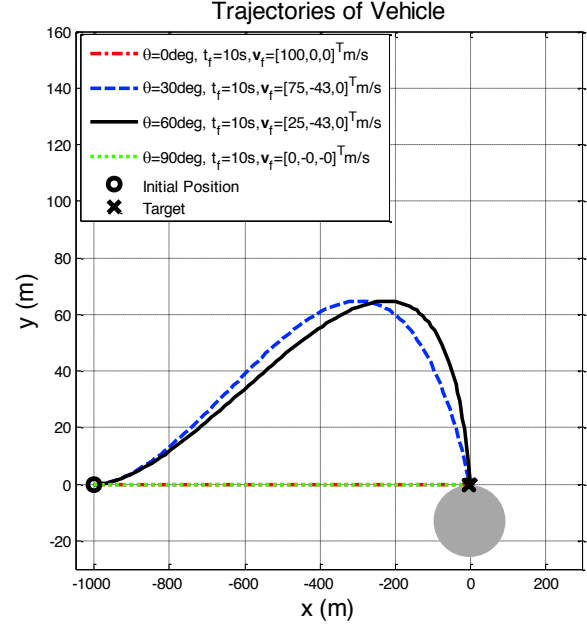


(b) Fuel usage.

Figure 4.8: Performance of the FTVG guidance algorithm.



(a) Different initial angles.



(b) Different final angles.

Figure 4.9: IACG guidance algorithms for asteroid intercept.

models are implemented for fast Monte Carlo analysis. Models are stored in a library allowing for fast changes in the simulator, for instance addition of redundant sensors or substituting an existing component by a new one.

From the Graphical User Interface (GUI), the user can edit all the configuration files and perform some simple mission analysis to help in the selection of scenario parameters. In addition, the GUI allows the user to select different spacecraft (SC) configurations. The GUI allows the selection of the type of simulation mode: Monte Carlo batch simulation with autocoding capability, or single-run that opens the simulator model. Finally, the GUI allows easy management of the simulations database and visualization of the results of any stored simulation. About the dynamics model, it is worth noting that the initial asteroid state is taken from JPL405 ephemerides and the trajectories of asteroid and SC are integrated independently in heliocentric coordinates. The accelerations acting on the SC, apart from Sun's gravitation and divert thrust, include attitude control system thrust, solar radiation pressure and asteroid gravity. CLEON includes the following models within the optical sensors for global-performance simulation of attitude (star-tracker) and LOS (navigation camera):

- The target magnitude results from the ideal magnitude with an added variation modeled as a Exponentially Correlated Random Variable (ECRV).
- The center of brightness (CoB) motion around the center of mass (CoM) can be: i) harmonic, ii) an ECRV, or iii) harmonic plus an ECRV.
- The LOS and attitude performances are computed including the following errors:
  - Mounting bias and sensor thermal drift
  - Noise equivalent angle that is function of
    - Real image: exposure time, visual magnitude of target and stars in the field of view (FOV), sky magnitude,



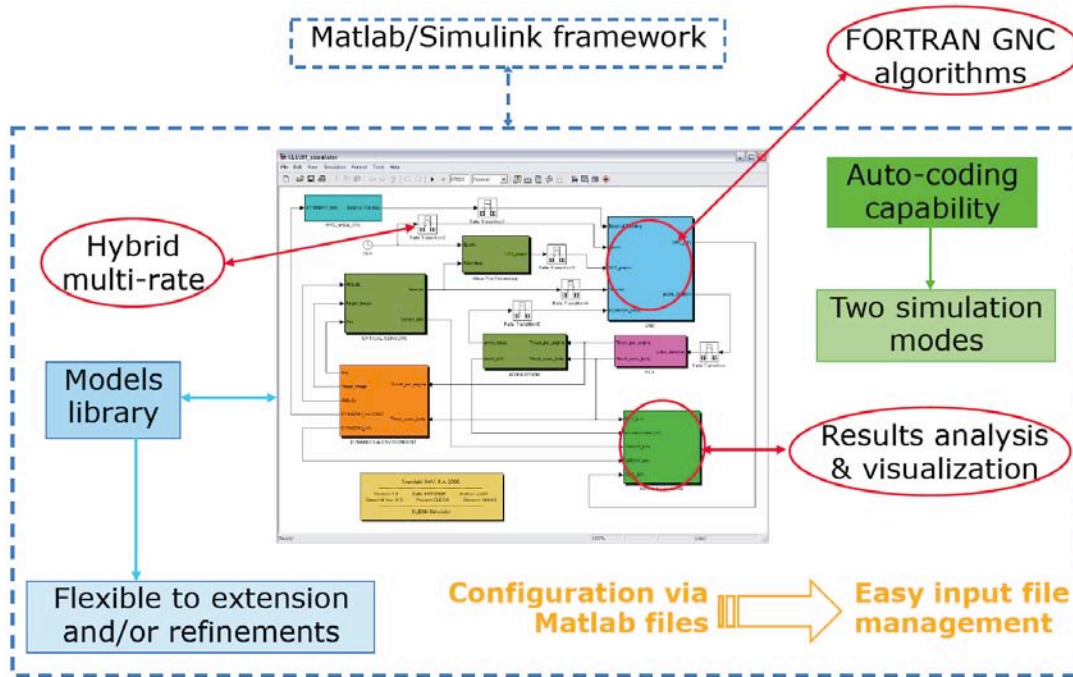


Figure 4.10: GMV's CLEON software functional illustration [2,3].

- Optics: transmittance, point spread function (PSF), stray light,
- Detector: assumed to be a CCD (pixel size, quantum efficiency, fill ratio), and
- Electronics: read-out noise, dark current
- Centroid error and other miscellaneous sources of Gaussian error
- The navigation camera includes an extended-target error model.
- The image processing performs a stacking of the navigation camera observations in order to increase the signal-to-noise ratio of the final measurement.

## Image Processing

The image processing (IP) algorithm extracts the LOS information from the images affected by real camera effects. Initially, the near-Earth object is so faint that the detected photoelectrons from the target are small compared with the image bias or noise. In order to increase the signal-to-noise ratio of the electron count coming from the target, a stacking of images is carried out prior to computing the LOS from the SC towards the target CoB. The sequence of operations of the IP algorithm is the following:

- Camera calibration to remove the bias from raw images subtracting a master dark frame. The master dark frame is computed averaging a given number of raw images taken with the same exposure time and temperature of the detector and electronics than the navigation images.
- Stacking of calibrated images to make the target detectable against a grainy background. The calibrated images are co-aligned prior to stacking. The effect of the image stacking is equivalent to a longer exposition time, but the stacking is preferred because relaxes the constraints on the ACS and prevents saturation and blooming.

- Centroiding of the pixel counts in a search-box to find the direction to the CoB. Prior to computing the centroiding, the pixels fainter than a given threshold are filtered out and, optionally, the isolated bright spots are removed.

### GNC Algorithms

Several navigation algorithms are implemented in CLEON to estimate different parameters, but they all process the same inputs coming from the optical sensors. The available GNC algorithms in CLEON are:

- For LOS navigation, i.e. to provide a smoothed LOS and LOS-rate, a digital fading memory filter proposed by Zarchan or a batch-sequential least-squares filter.
- For state navigation, i.e. to estimate the impactor state relative to the target, a sequential Kalman-Schmidt filter (or extended Kalman filter).

The suite of autonomous guidance schemes that compute the divert maneuvers include:

- Predictive guidance, which computes an impulsive maneuver at a given time that ideally cancels the ZEM with respect to the center of brightness (CoB). The gravity gradient of the sun is considered in the  $\Delta V$  computation. The configuration parameters are the times for execution of the maneuvers.
- Proportional navigation, which computes an acceleration vector proportional to the LOS-rate and the homing velocity  $V_c$ , as presented in Eq. (10). The only configuration parameter is the navigation ratio.
- Hybrid scheme, which implements mid-course predictive guidance and terminal proportional-navigation. The configuration parameters are the execution times of the impulsive maneuvers, the start time of the proportional navigation and the navigation ratio.

The control algorithm transforms the computed inertial acceleration into burning time of each thruster, considering the number and orientation of the thrusters. In predictive guidance (impulsive maneuvers), the thrusters take some cycles to complete the commanded  $\Delta V$  and the control computes the average acceleration in the next cycle using the accelerometer information. The saturation is not considered in the control algorithm but in the reaction control system model.

### CLEON Simulation Results

Monte Carlo simulations using PN guidance and PI guidance were performed for the Apophis intercept scenario. The CoB-CoM offset is assumed as half of Apophis's radius. For PI guidance, the firing schedule used in [2] is adopted. Figures 4.11 and 4.12 show the cumulative distribution functions for ZEM and  $\Delta V$ , locations of the impact points in the B-plane, and the evolution of the ZEM. The ZEM distribution shows that all of the Monte Carlo shots were within 20 meters of the CoB for PN guidance, and within 15 meters for PI guidance. The  $\Delta V$  distribution shows that all of the PN Monte Carlo shots required less than 9 m/s, with 90% requiring less than 6 m/s. For PI guidance, all of the Monte Carlo shots required less than 8 m/s, with 90% requiring less than 5 m/s. The plot of the impact points show all of the impacts clustering near the CoB. Thus, the performance as illustrated in Figures 4.11 and 4.12 is acceptable for robustly impacting a 280-m target asteroid with a CoB-CoM offset of 70 m. The impact radius evolution gives a measure of the effectiveness of the guidance law over time. PN guidance is seen to gradually and continuously decrease the expected impact radius, while PI guidance shows increasing accuracy with each maneuver.

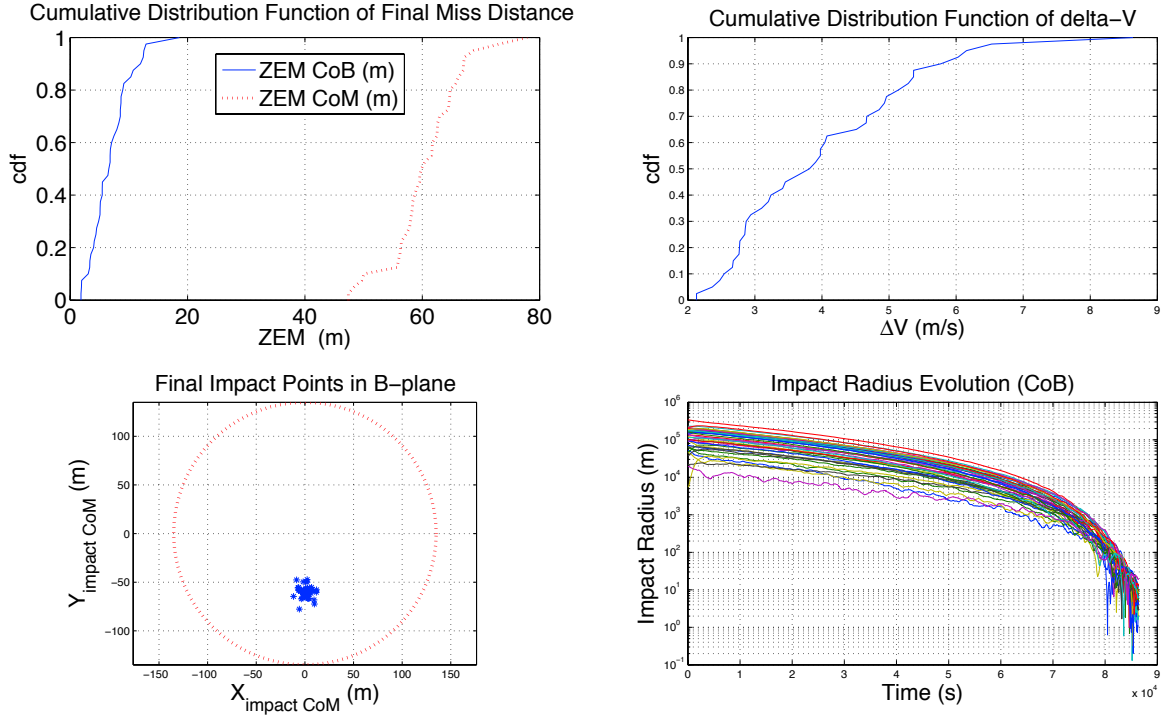


Figure 4.11: ZEM cumulative distribution function,  $\Delta v$  cumulative distribution function, impact points on target, and impact radius evolution for PN guidance.

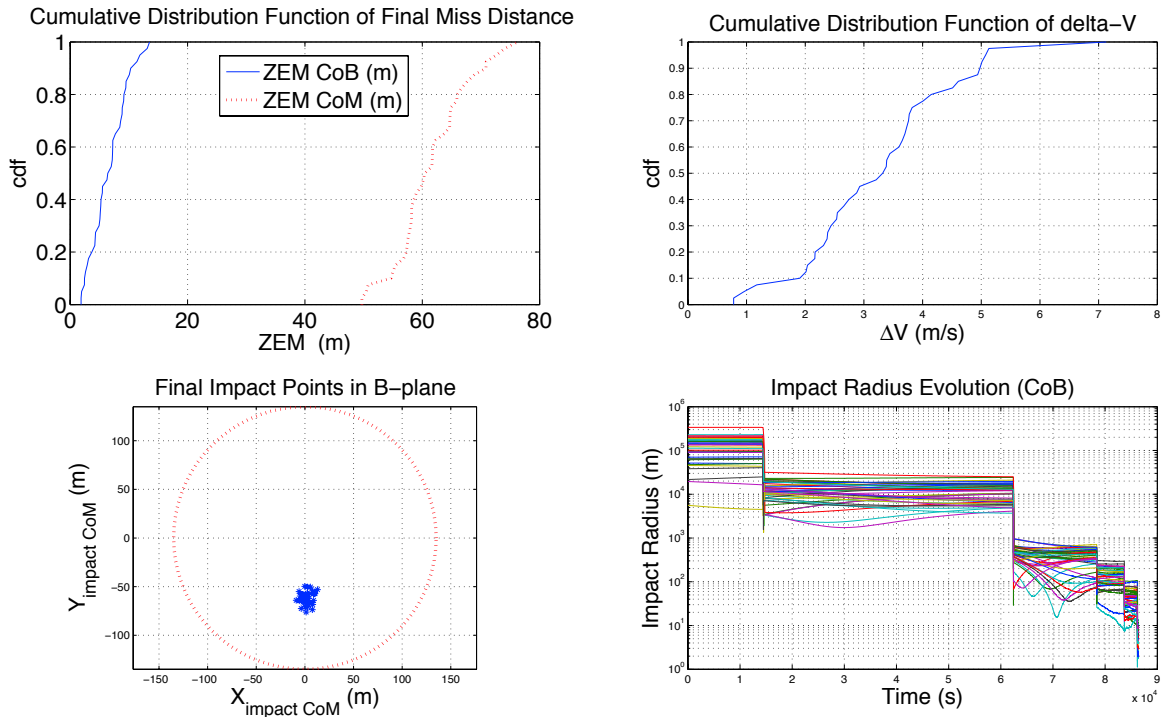


Figure 4.12: ZEM cumulative distribution function,  $\Delta v$  cumulative distribution function, impact points on target, and impact radius evolution for PI guidance

## 4.6 Conclusion

A variety of guidance algorithms, including classical PN-based guidance algorithms, more advanced predictive guidance laws, and optimal feedback guidance laws, were investigated for the terminal guidance phase of an asteroid interceptor. Simulation results showed that all of the guidance algorithms can be employed for terminal intercept missions. A high-fidelity simulator, GMV's CLEON, was also used to verify that these various algorithms can be employed to hit a 280-m target asteroid in the presence of various uncertainties (e.g., navigation error, target imaging error, attitude determination error, trajectory correction maneuver error, etc.). However, a further study for an integrated design of spacecraft hardware and terminal guidance laws should be conducted in our NIAC Phase 2 project to verify and validate the technical feasibility of hitting a target asteroid as small as 50 m with an intercept speed as high as 30 km/s.

## 4.7 References

- [1] Frauenholz, R. S., Bhat, R. S., Chesley, N., Mastrodemos, N., Owen Jr., W. M., and Ryne, M. S., "Deep Impact Navigation System Performance," *Journal of Spacecraft and Rockets*, Vol. 45, No. 1, 2008, pp. 39-56.
- [2] Gil-Fernández, J., Panzeca, R., and Corral, C., "Impacting Small Near Earth Objects," *Advances in Space Research*, Vol. 42, No. 8, October 2008, pp. 1352-1363.
- [3] Gil-Fernández, J., Cadenas-Gorgojo, R., Priet-Llaons, T., and Graziano, M., "Autonomous GNC Algorithms for Rendezvous Missions to Near-Earth Objects," AIAA 2008-7087, AIAA/AAS Astrodynamics Specialist Conference and Exhibit, Honolulu, HI, 2008.
- [4] Zarchan, P., *Tactical and Strategic Missile Guidance*, 5th Edition. Progress in Astronautics and Aeronautics, AIAA, Washington, DC, 2007.
- [5] Wie, B., *Space Vehicle Dynamics and Control*, 2nd Edition, AIAA Education Series, 2008.
- [6] Battin, R. H., *An Introduction to the Mathematics and Methods of Astrodynamics*, AIAA Education Series, 1999.
- [7] Hawkins, M., Pitz, A., Wie, B., and Gil-Fernández, J., "Terminal-Phase Guidance and Control Analysis of Asteroid Interceptors," AAS/AIAA Astrodynamics Specialist Conference, Toronto, CA, 2010.
- [8] Hawkins, M., and Wie, B., "Impact-Angle Control of Asteroid Interceptors/Penetrators," AAS/AIAA Space Flight Mechanics Winter Meeting, New Orleans, LA, 2011.
- [9] Guo, Y., Hawkins, M., and Wie, B., "Optimal Feedback Guidance Algorithms for Planetary Landing and Asteroid Intercept," AAS/AIAA Astrodynamics Specialist Conference, Girdwood, AK, 2011.
- [10] Hawkins, M., Guo, Y., and Wie, B., "Guidance Algorithms for Asteroid Intercept Missions with Precision Targeting Requirements," AAS/AIAA Astrodynamics Specialist Conference, Girdwood, AK, 2011.
- [11] Hawkins, M., Guo, Y., and Wie, B., "Spacecraft Guidance Algorithms for Asteroid Intercept and Rendezvous Missions," *International Journal of Aeronautical and Space Sciences*, Vol. 13, 2012, pp. 345-360.

## Chapter 5

# HAIV Flight Validation Mission Design

### 5.1 Introduction

Given the past occurrences of asteroids and comets colliding with the Earth, it is necessary to prepare a global plan on how to mitigate the threat of a near-Earth object (NEO) on an Earth-impacting trajectory. During the past several years, research activities at the Iowa State Asteroid Deflection Research Center (ADRC) have focused on various nuclear options, such as standoff, surface contact, and subsurface explosions [1,2,3]. The most effective approach is to use a penetrated subsurface explosion to deliver a considerable amount of energy to a small depth ( $< 5\text{m}$ ) resulting in the possible total disruption of the target NEO. Depending on the mission lead time, a timely execution of a real NEO deflection/disruption mission can be a challenging task.

When the warning time is short, the use of nuclear explosive devices (NEDs) will be the only option for generating a sufficient impulsive velocity change or to impart sufficient disruption energy to the threatening NEO. Such a last-minute intercept mission will result in a closing arrival velocity of more than 10 km/s. Because the current nuclear fusing mechanisms are limited to surviving impact speeds of less than 300 m/s, a hypervelocity asteroid intercept vehicle (HAIV) or hypervelocity nuclear interceptor spacecraft (HNIS) concept was conceived especially for penetrated subsurface explosions providing much more effective fragmentation and dispersion of the target NEO [1,2,3]. It is envisioned that eventually in the near future, planetary defense technology (PDT) demonstration missions will be considered seriously by an international space community in order to validate the overall effectiveness and robustness of various nuclear options and the associated space technologies.

### 5.2 Overview of Existing Mission Design Tools

#### 5.2.1 Integrated HAIV/OTV Design Tool

A multi-purpose, scalable configuration design of a baseline HAIV architecture is being performed at the Iowa State ADRC [6]. A baseline HAIV architecture basically consists of its bus system and its NED payload. It may consist of two separable spacecraft: a leader spacecraft (impactor) and a follower spacecraft carrying NED payload for a penetrated subsurface explosion mission [2,6]. The integrated HAIV/OTV (orbital transfer vehicle) design tool takes into account several parameters to decide the necessity of an OTV for the mission: launch vehicle, tank sizing, and fairing fit to produce a baseline mission architecture that would be suitable and applicable to a chosen target and mission. With the detailed design of the HAIV taken out of the mission design loop, there are a few less variables to deal with, but constrains the solution to work with the specific design.

The pre-mission design software tool is comprised of several functions and subroutines calculating several OTV and preliminary design variables. Using information about the masses of the HAIV bus and NED payload, mission  $\Delta V$  or C3 needed to reach the target NEO, and class of launch vehicles to be analyzed, the

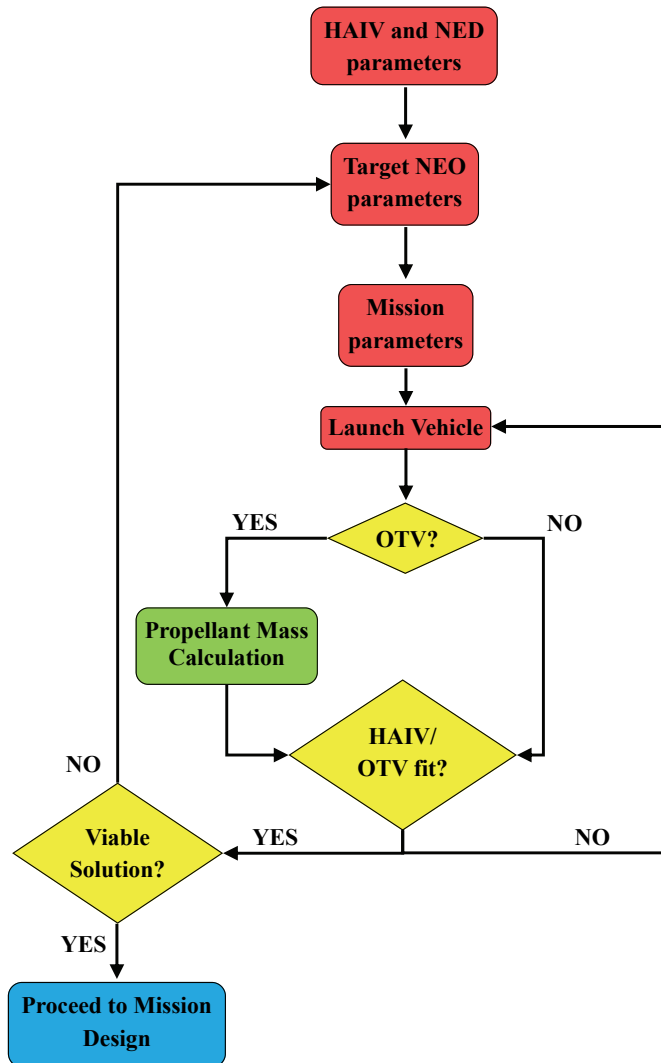


Figure 5.1: Flowchart illustration of the pre-mission design process.

algorithm begins the process of calculating the payload capacity of the launch vehicles, the propellant mass of the OTV, size of the propellant tanks, if the payload configuration will fit in the fairing, and analyzing the solution. A flowchart of the pre-mission design process is provided in Figure 5.1.

The beginning of the design algorithm takes inputs about the HAIV bus system and NED payload, then requires additional data on the target NEO and mission parameters, and launch vehicles to be considered for the mission. With the pre-prescribed design of the HAIV, consisting of an impactor and a follower with NED payload, the program will ask whether the mission is a direct C3 injection orbit or if there would be an applied  $\Delta V$  from the 185 km altitude circular parking orbit. If the indication is a C3 orbit, the program will ask for the class of launch vehicles to be analyzed for use in the mission. For the C3 orbit missions, if Delta II class launch vehicles are chosen, only the three-stage Delta II launch vehicles are considered because of their C3 payload capabilities. If a  $\Delta V$  is to be applied, it tells the program that an OTV is planned on being used for the purposes of the mission, and the program will ask for the amount of  $\Delta V$  required of the OTV.

With all the given inputs, the program looks to see if the parameters indicate the need of an OTV. If not,

the HAIV mass and dimensions are analyzed against the fairing sizes of the launch vehicles to ensure that it will fit inside the fairing and can be carried to the specified orbit. If there is a need for an OTV, the amount of  $\Delta V$  needed enables the program to calculate the mass and proportions of the bi-propellant fuel. The two common types of bi-propellant used for the OTV are liquid oxygen/liquid hydrogen (LOX/LH<sub>2</sub>) and nitrogen tetroxide/hydrazine (N<sub>2</sub>O<sub>4</sub>/Hydrazine). Based on the choice of fuel type, the mass and capability of the fuel can be calculated. From there, the HAIV plus OTV configuration is then checked against the launch vehicle fairing sizes to see if the entire payload can fit inside. If the HAIV or HAIV/OTV configuration does not fit within the specified class of launch vehicles' fairings, then a new class of launch vehicles will need to be specified for analysis. If the HAIV does fit within one of the launch vehicle fairings, then the algorithm has found a possible solution.

With a set of solutions obtained by the HAIV/OTV design algorithm, each solution has to be analyzed to ensure its viability. The user enters the design-loop at this point, deeming a solution as either acceptable or not, and potentially restarting the entire design process if necessary. If a viable design is found from the resulting set of solutions then it can be taken and used to design the corresponding mission to a specified target NEO.

### **5.2.2 An On-line Tool by The Aerospace Corporation**

The Aerospace Corporation is developing an on-line tool to aid in the design and understanding of deflection impulses necessary for guarding against objects that are on an Earth-impacting trajectory. Using several variables to characterize the target NEO (warning time, size/density, orbit parameters, etc.) and mitigation mission design parameters ( $\Delta V$  impulse vector, number of days before impact to launch, number of days before impact to deflect, etc.), users can simulate the designed mission transfer from Earth to the target NEO and deflected NEO orbit. After the applied deflection and propagation time, the Earth miss distance would be determined on the Earth B-plane in Earth radii. This on-line tool is still under development, with the hopes of incorporating several more design variables and limitations to only allow feasible mission designs based on current launch and mission capabilities [5].

### **5.2.3 NASA's Mission Design Software Tools**

Through the In-Space Propulsion Technologies Program, in the Space Science Projects Office at NASA Glenn Research Center, several optimization tools have been developed for trajectory and mission optimization, such as MALTO, COPERNICUS, OTIS, Mystic, and SNAP [6].

#### **COPERNICUS**

Originally developed by the University of Texas at Austin, under the technical direction of Johnson Space Center, Copernicus is a generalized trajectory design and optimization program that allows the user to model simple to complex missions using constraints, optimization variables, and cost functions. Copernicus can be used to model various trajectory parameters from simple impulsive maneuvers about a point mass to multiple spacecraft with multiple finite and impulse maneuvers in complex gravity fields. The models of Copernicus contain an n-body tool and as a whole is considered high fidelity.

#### **OTIS**

The Optimal Trajectories by Implicit Simulation (OTIS) program was developed by the NASA Glenn Research Center and Boeing. OTIS is named for its original implicit integration method, but includes capabilities for explicit integration and analytic propagation. Earlier versions of OTIS have been primarily been launch vehicle trajectory and analysis programs. Since then, the program has been updated for robust and accurate interplanetary mission analyses, including low-thrust trajectories. OTIS is a high fidelity optimization and

simulation program that uses SLSQP and SNOPT to solve the nonlinear programming problem associated with the solution of the implicit integration method.

## **Mystic**

Mystic, developed at the Jet Propulsion Laboratory (JPL), uses a Static/Dynamic optimal control (SDC) method to perform nonlinear optimization. The tool is an n-body tool and can analyze interplanetary missions as well as planet-centered missions in complex gravity fields. One of the strengths of Mystic is its ability to automatically find and use gravity assists, and also allows the user to plan for spacecraft operation and navigation activities. The mission input and post processing can be performed using a MATLAB based GUI.

### **5.2.4 NASA's General Mission Analysis Tool**

Developed by NASA Goddard Space Flight Center, the General Mission Analysis Tool (GMAT) is a space trajectory optimization and mission analysis system. Analysts use GMAT to design spacecraft trajectories, optimize maneuvers, visualize and communicate mission parameters, and understand mission trade space. GMAT has several features beyond those that are common to many mission analysis systems, features that are less common or unique to GMAT. Its main strength over other software choices is GMAT's versatility. Its scripting ability is easy to use and edit without knowledge of computer languages. And, the MATLAB plug-in allows an expansion of the user's ability to personalize each mission [7].

### **5.2.5 Mission Design Program Comparisons**

The trajectory and mission optimization tools developed through the In-Space Propulsion Technologies Program and GMAT are all rather high fidelity programs. One of the common denominators of all these tools are that they primarily look at the intermediate stage of a mission, the spacecraft trajectory from one target to another. The other two mission stages are more or less overlooked in comparison to the spacecraft's mission trajectory. The AMiDST does not currently possess the high-fidelity trajectory optimization of Copernicus, Otis, or Mystic, but instead focuses on the launch and terminal phase of any given NEO mission.

Looking into several launch vehicle and spacecraft configurations to complete a given mission design to a designated target NEO, the mission design software evaluates the possible combinations based upon several evaluation criteria such as space in the launch vehicle fairing, mission  $\Delta V$  requirements, and excess launch vehicle  $\Delta V$ . A staple of this mission design tool is the evaluation of estimated total mission cost, the determining factor between mission configurations in the cases where more than one launch configuration can result in a successful mission.

The terminal phase of a NEO mission currently is limited to kinetic impact perturbations to a target NEO's orbital trajectory. Using the impact angle and arrival velocities of both the spacecraft and target NEO, along with both masses, the trajectory of the perturbed asteroid is tracked in order to find how much the trajectory is altered from the previous unperturbed orbit. Depending on the chosen NEO, a mission can be designed to explore the capabilities of a kinetic impactor on a target NEO or to design a mission to deflect the target NEO from its Earth-impacting trajectory.

## **5.3 Asteroid Mission Design Software Tool (AMiDST)**

Building from the previously established Pre-Mission Design Algorithm, the AMiDST incorporates all elements of the pre-existing algorithm and expands upon them. Using a combination of MATLAB and FORTRAN codes, the AMiDST incorporates elements of launch vehicle selection mission trajectory using a Lambert-Battin solver, mission cost estimation, and high fidelity numerical integration to track perturbed NEO trajectories. Figure 5.2 shows a flow-chart illustration of the AMiDST. The design tool begins with a



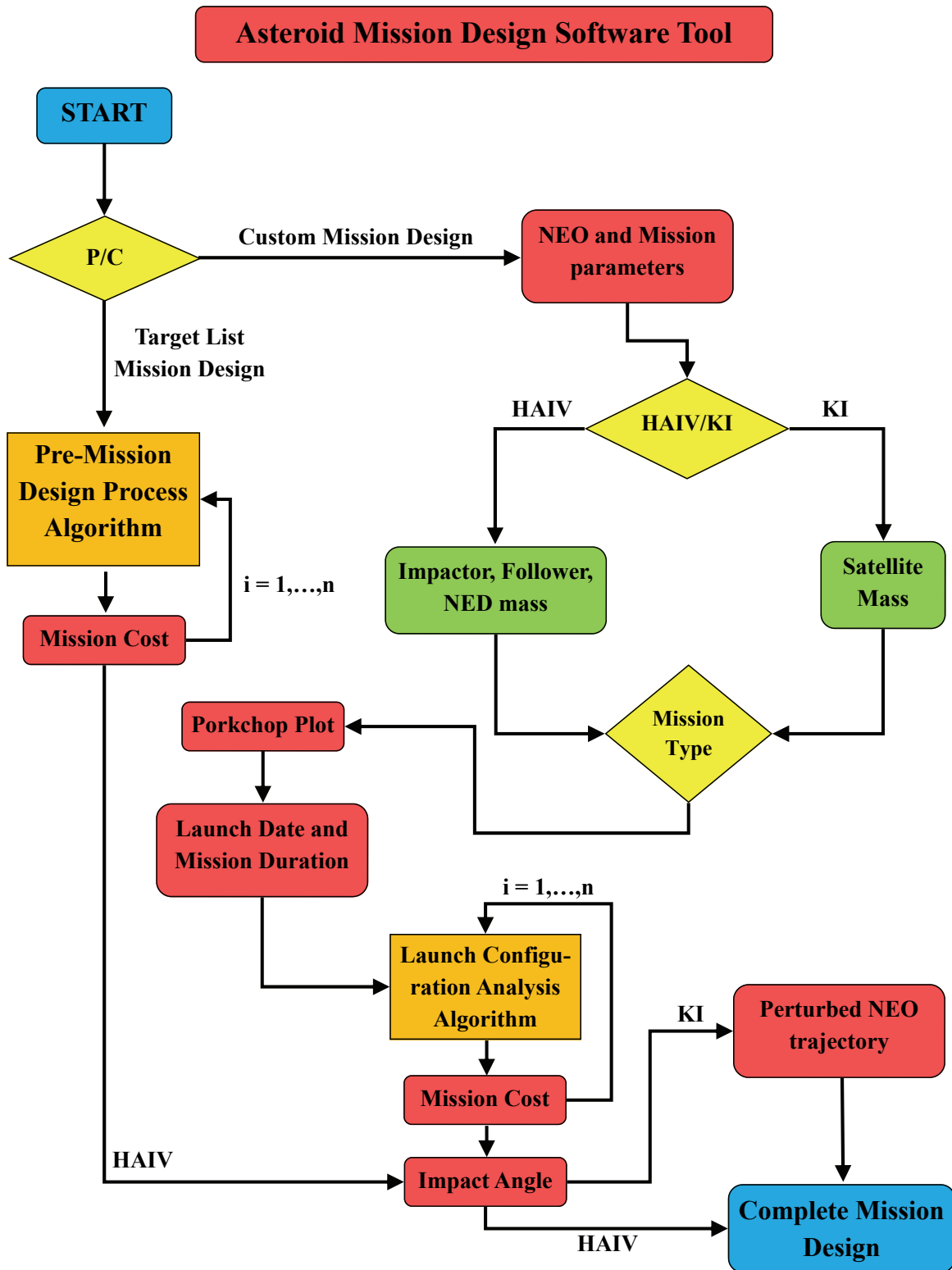


Figure 5.2: Flowchart illustration of the AMiDST.

Table 5.1: List of NEOs selected for planetary defense technology demonstration missions [8].

Target NEO	Diameter (m)	a (AU)	e	i (deg)	$\omega$ (deg)	$\Omega$ (deg)
2003 GA	300	1.28153	0.19124	3.84189	66.76837	192.93186
2006 SJ198	1200	2.08969	0.45631	2.43325	212.25852	266.89138
2009 TB3	300	1.31863	0.21926	12.22404	249.57728	22.17938
2007 FS35	620	1.92244	0.38986	0.31887	107.40624	183.00756
2003 QC	400	2.57094	0.53140	7.85444	37.43616	321.68183
2004 GY	480	1.44817	0.21804	23.43610	182.87114	50.88706
2001 SX269	280	1.88042	0.34613	4.02404	29.53738	320.17092
1998 SB15	330	1.22609	0.16126	15.62791	67.63148	67.93695
2004 KE1	240	1.29867	0.18079	2.88387	283.67731	42.77468
2011 BX10	1000	2.82541	0.64134	9.73567	348.36692	79.118387

choice between analyzing a pre-determined list of target NEOs to design a mission for or build a custom mission design for a personally selected target NEO. With the hard-coded NEO target list, the software follows the Pre-Mission Design Algorithm, described previously, to analyze all launch configurations and estimated mission costs to be used for further design and analysis. The list of NEOs, shown in Table 5.1, is taken from the targets described in [7]. These asteroids are Amor class asteroids, meaning their orbits do not cross the Earth's path, and therefore pose no threat to the planet. Due to the nonexistent threat that these asteroids possess towards Earth, the pre-determined target list option is meant more as an introduction to some of AMiDST's capabilities - a way for users to get acquainted with the software tool's capabilities before trying to design their own mission(s).

A launch date is given for each individual asteroid, leaving no need for too much user input. With the launch date determined and the target defined then the spacecraft's orbital trajectory is well-defined and no longer a concern. The AMiDST analyzes all the possible launch configurations available to complete the mission, the arrival at the target NEO, and the estimated mission costs. The outputs are then made available for the user to examine and understand the results of the NEO mission design analyses. The spacecraft used for missions to these asteroids is the ADRC's HAIV spacecraft design. The results are not limited to a single HAIV design (300-kg NED, 1000-kg NED, or 1500-kg NED), but include all three, and highlights the best mission configuration for each type.

For custom mission designs, the user begins by entering information about the target NEO of interest and the low-Earth orbit (LEO) departure radius. Then the choice is given between two types of spacecraft to be used for the mission, the HAIV concept or a Kinetic Impactor (KI)/orbiter. For HAIV spacecraft, information about the mass of the impactor, follower, and NED are obtained from the user, while in the KI/orbiter spacecraft case the total mass of the satellite is needed. In either case, the user is prompted with a decision between three mission types: a direct intercept, a direct intercept at a relative speed of 10 kilometers per second, or rendezvous. The software tool then loads the appropriate porkchop plot, showing the total required mission  $\Delta V$ , where the user can select as many design points as desired, resulting in a set of launch dates and mission durations. Given the launch date(s) and mission duration(s), the transfer orbit between Earth and the target NEO is completely determined by Lambert's Problem, allowing the possible launch configurations for the mission(s) to be analyzed along with their estimated mission cost and compared to come up with the preferred launch configuration for each given mission. The resulting mission trajectories for either the HAIV or KI/orbiter spacecraft are provided along with the arrival impact angles. Since the purpose of the HAIV design was total NEO disruption, the trajectory of the remaining asteroid fragments are not tracked, however in the case of the KI spacecraft the slightly perturbed NEO is propagated forward in time to see how much the orbit has changed from the original, before the impulse was applied.

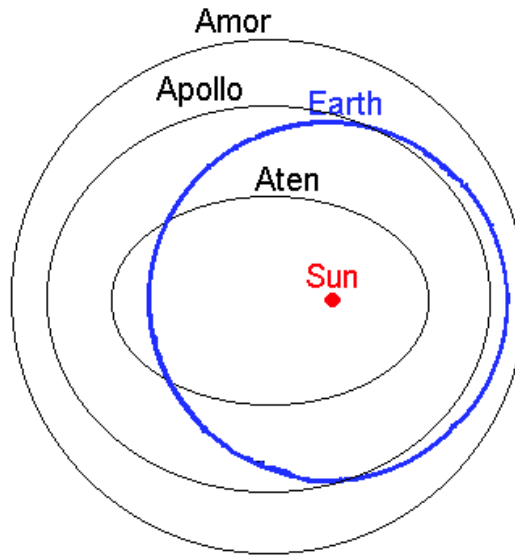


Figure 5.3: Typical Orbits of Apollo, Aten, and Apollo Asteroids.

## 5.4 Reference Target Asteroids

Near-Earth Objects are asteroids and comets with perihelion distance ( $q$ ) less than 1.3 astronomical units (AU). The vast majority of NEOs are asteroids, which are referred to as Near-Earth Asteroids (NEAs). NEAs are divided into three groups (Aten, Apollo, Amor) based on their perihelion distance ( $q$ ), aphelion distance ( $Q$ ), and semi-major axes ( $a$ ). Atens are Earth-crossing NEAs with semi-major axes smaller than Earth's ( $a < 1.0$  AU,  $Q > 0.983$  AU). Apollos are Earth-crossing NEAs with semi-major axes larger than Earth's ( $a > 1.0$  AU,  $q < 1.017$  AU). Amors are Earth-approaching NEAs with orbits exterior to Earth's but interior to Mars' ( $a > 1.0$  AU,  $1.017 < q < 1.3$  AU) [8]. Figure 5.3 shows representative orbits for the three class of asteroids in reference to Earth's orbit.

With the wide array of choices to select target NEOs from, the results presented here will mainly focus on two Apollo class asteroids, 1999 RQ36 and 2011 AG5. Both asteroids have relatively high impact probabilities with the Earth in the future, making them important objects for study.

## 5.5 Applications of the AMiDST

### 5.5.1 Target List Mission Design

Once again, the pre-determined target list option in the AMiDST is meant to be used as a guide to understanding AMiDST's capabilities and analyses. With that being said, a quick overview will be provided of the 10 Amor class asteroids used as demonstrations of AMiDST, the three size varied HAIIV spacecrafts, and the launch vehicles used for mission design feasibility. The results of these mission design studies are skipped over here, due to their lack of importance compared to the results shown later with respect to asteroids 1999 RQ36 and 2011 AG5.

From the over 3000 Amor asteroids 10 of the most suitable asteroids, as identified in [3], were selected as appropriate targets for at least one of the three HAIIV designs. The asteroids' estimated diameter, departure  $\Delta V$ , departure date, and C3 are shown in Table 5.2.

The mission design studies conducted at the ADRC considered three classes of launch vehicle: i) Delta II, ii) Delta IV, and iii) Atlas V. Due to the payload capacity and launch costs, the 300-kg NED mission will primarily look at Delta II class launch vehicles, the 1000-kg NED mission could be handled by any launch vehicle from the Delta IV and Atlas V classes, and the 1500-kg NED mission will likely need a Delta IV

Table 5.2: List of pre-determined asteroids available for study in the AMiDST [3].

Target NEO	Diameter (m)	Departure $\Delta V$ (km/s)	Departure Date	C3 (km <sup>2</sup> /s <sup>2</sup> )
2003 GA	300	3.519	12/03/2015	6.50
2006 SJ198	1200	4.595	03/17/2015	32.01
2009 TB3	300	3.600	01/27/2018	8.35
2007 FS35	620	3.473	02/04/2015	5.46
2003 QC	400	4.479	01/01/2015	29.14
2004 GY	480	4.354	06/30/2015	26.09
2001 SX269	280	3.572	05/02/2019	7.70
1998 SB15	330	3.335	05/05/2017	2.37
2004 KE1	240	4.539	02/08/2017	30.62
2011 BX10	1000	3.948	01/01/2015	16.39

Heavy launch vehicle due to the large amount of mass designated to the NED special payload. The launch vehicles will be carrying specially designed HAIV, comprised of an impactor and follower spacecraft, with the NED payload contained within the follower spacecraft. An OTV option is considered, that would accompany the HAIV on its mission, to provide extra  $\Delta V$  for trajectory correction maneuvers (TCMs) or orbital insertion, as needed.

The Delta II launch vehicles have a 98% reliability record, with capabilities to launch from either the East or West coast. The vehicles can be configured with two or three stages with up to nine strap-on graphite-epoxy motors, and two sizes of payload fairings. The versatility and the low cost of the Delta II launch vehicles makes it ideal for smaller body asteroid missions [8].

The types of Delta II launch vehicles considered are the Delta II 732X, Delta II 742X, Delta II 792X, and Delta II 792XH, where X can be 0 (no third stage), 5 (STAR-48B third stage), or 6 (STAR-37FM third stage). The major differences between the two and three stage configurations of the Delta II are the payload and orbit injection capabilities. Two-stage Delta II rockets can really only take payloads into low Earth orbits (LEOs), while the three-stage configurations have the ability to inject payloads into hyperbolic C3 orbits- Earth escape trajectories. The C3 value is defined by the energy of the orbit that the payload is placed in, expressed as

$$C3 = v_{\infty}^2 \quad (1)$$

where  $v_{\infty}$  is the hyperbolic excess speed of the spacecraft. With payload mass being such an important variable for a mission using a Delta II class launch vehicle, special attention must be paid to two-stage configurations Delta II to LEO plus OTV and the three-stage Delta II configurations to the desired C3 energy orbit, to find which configuration would be more accommodating for the HAIV/OTV design.

The Delta IV class of launch vehicles are much larger launch vehicles, capable of not only taking large payloads to LEO but directly injecting them into high C3 orbits. The variety within the Delta IV class allows for a rocket from this group to be picked for any of the NED mission configurations. The Atlas V launch vehicles are also rather powerful rockets, with comparable if not better payload capabilities to that of their equivalent Delta IV rocket counterparts, with the exception of the Delta IV Heavy launch vehicle. The currently available launch vehicles for use for either of those missions are: Delta IV Medium, Delta IV M+(4,2), Delta IV M+(5,4), Delta IV Heavy, Atlas V 401, Atlas V 431, and Atlas V 551.

## 5.6 Examples of PDT Demonstration Mission Design

For the sake of simplicity and space, only a couple of the important variables are shown for each target selected for planetary defense technology (PDT) demonstration missions. Table 5.3 shows the suggested

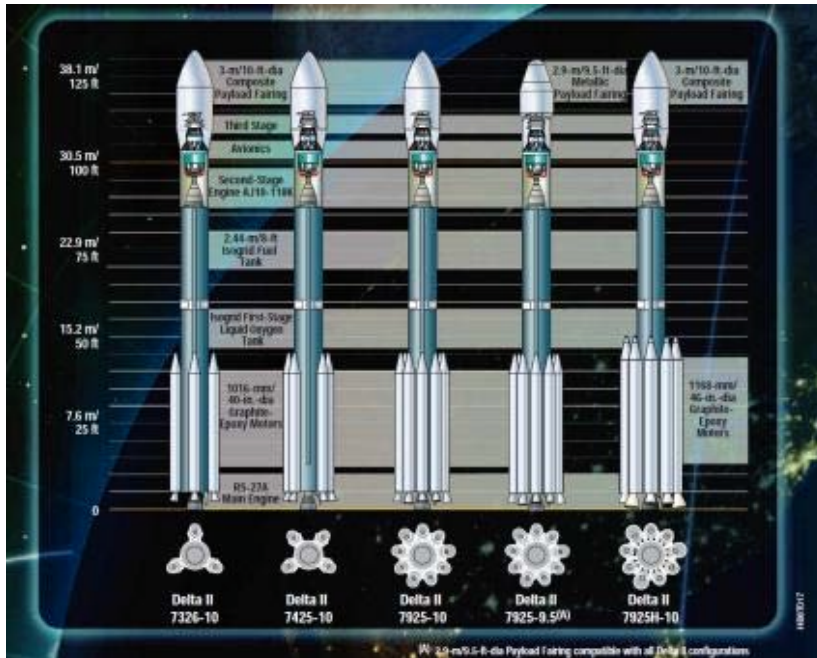


Figure 5.4: Delta II launch vehicle configurations [8].

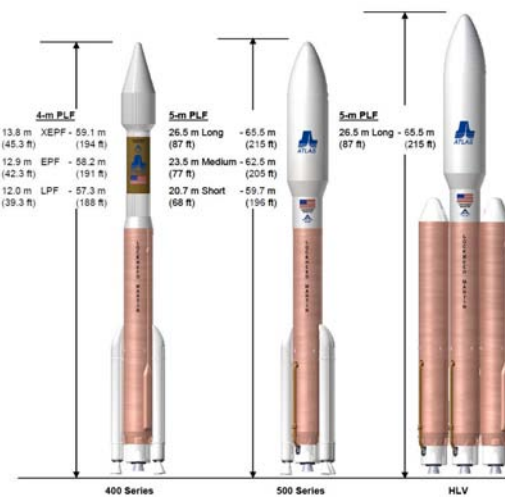
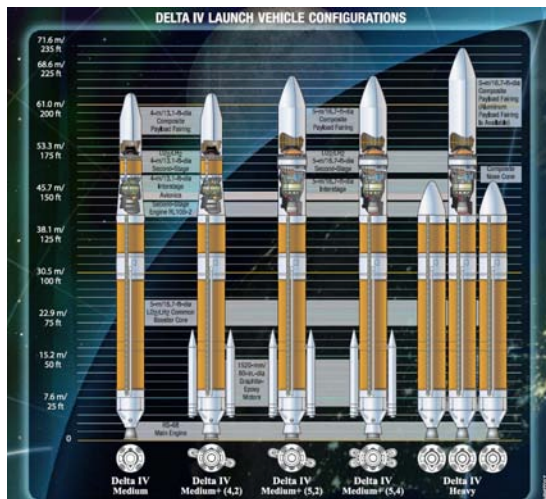


Figure 5.5: Delta IV (left) and Atlas V (right) launch vehicles [9,10].

Table 5.3: Preferred launch vehicles to be used for PDT demonstration missions and estimated mission costs for 300 kg NED/1000 kg NED/1500 kg NED HAIV spacecraft.

Target NEO	Launch Vehicle	Estimated Mission Cost (\$)
2003 GA	Delta IV Medium	762.20M
	Atlas V 431	1322.53M
	Atlas V 551	1694.24M
2006 SJ198	Atlas V 401	770.52M
	Delta IV Heavy	1495.51M
	NP	NP
2009 TB3	Delta IV Medium	762.20M
	Atlas V 431	1322.53M
	Delta IV Heavy	1797.36M
2007 FS35	Delta IV Medium	762.20M
	Atlas V 431	1322.53M
	Atlas V 551	1694.24M
2003 QC	Delta IV M+(4,2)	770.52M
	Delta IV Heavy	1495.51M
	NP	NP
2004 GY	Delta IV M+(4,2)	770.52M
	Atlas V 551	1392.39M
	NP	NP
2001 SX269	Delta IV Medium	762.20M
	Atlas V 431	1322.53M
	Atlas V 551	1694.24M
1998 SB15	Delta IV Medium	762.20M
	Atlas V 431	1322.53M
	Atlas V 551	1694.24M
2004 KE1	Delta IV M+(4,2)	770.52M
	Delta IV Heavy	1495.51M
	NP	NP
2011 BX10	Delta IV Medium	762.20M
	Atlas V 431	1322.53M
	Delta IV Heavy	1797.36M

Table 5.4: Orbital elements at Epoch 2456000.5 (March 14, 2012) of asteroid 1999 RQ36 [9].

Element	Symbol	Value	Units
Semi-Major Axis	$a$	1.126038025838632	AU
Eccentricity	$e$	.2036994928473318	
Inclination	$i$	6.035405340360255	deg
Argument of Periapse	$\omega$	66.2666863129749	deg
Longitude of the Ascending Node	$\Omega$	2.051615098784052	deg
Mean Anomaly at Epoch	$M_0$	102.8657778912915	deg

launch vehicles and estimated mission cost to deliver an HAIV spacecraft carrying a 300-kg, 1000-kg, and 1500-kg NED to the selected target asteroids. More detailed results for each of these missions can be found by running the AMiDST program and selecting the pre-determined target list for analysis. In some instances, the resulting launch vehicle and cost is listed as NP, standing for “not possible”, because given the total mass of the HAIV, target asteroid, departure date, transfer duration, and total departure  $\Delta V$  combination none of the currently existing launch vehicles can place the spacecraft into the 0-revolution direct transfer orbit necessary to meet the required criteria. That is not to say that a mission to these target asteroids is impossible, because it can clearly be seen that with a less massive spacecraft a mission can be designed for any of the given NEOs. At least one of the mission criteria would have to be altered for a successful mission, giving rise to the ability to create a custom mission to any given asteroid.

## 5.7 AMiDST Applications

To better understand what goes on in the analyses that the AMiDST performs, a mission design example is conducted and followed from start to finish here. We revisit the AMiDST flowchart shown in Figure 5.2, but this time partition the diagram into blocks to isolate the specific functions within each block. Aside from the pre-determined target list mission design path, Figure 5.6 shows the AMiDST flowchart sectioned into five main blocks: the custom mission parameter block, the spacecraft and mission type block, the trajectory block, the mission analysis block, and the perturbed orbit trajectory block. After going through each block in the context of the following example another two mission examples will be quickly run through to see the overall presence of the AMiDST.

### 5.7.1 Custom Mission Parameter Block

The first block that is encountered in the AMiDST program is the custom mission parameter block. Within this block, we introduce the desired target NEO and the preliminary mission parameters. As previously stated, there are two primary targets that we have chosen to study (1999 RQ36 and 2011 AG5), so we introduce both asteroids in this section.

#### Asteroid 1999 RQ36

Asteroid 1999 RQ36 is the target of NASA’s OSIRIS-Rex Mission. Table 5.4 shows the asteroid’s referenced orbital elements on March 14, 2012 and Figure 5.7 shows a depiction of the orbit in reference to the Solar System’s inner planets.

Based on 1999 RQ36’s orbit being so close to the Earth, and small inclination from the Earth’s orbital plane, it is a very good target for study due to its low  $\Delta V$  requirements. Astronomers have the chance to

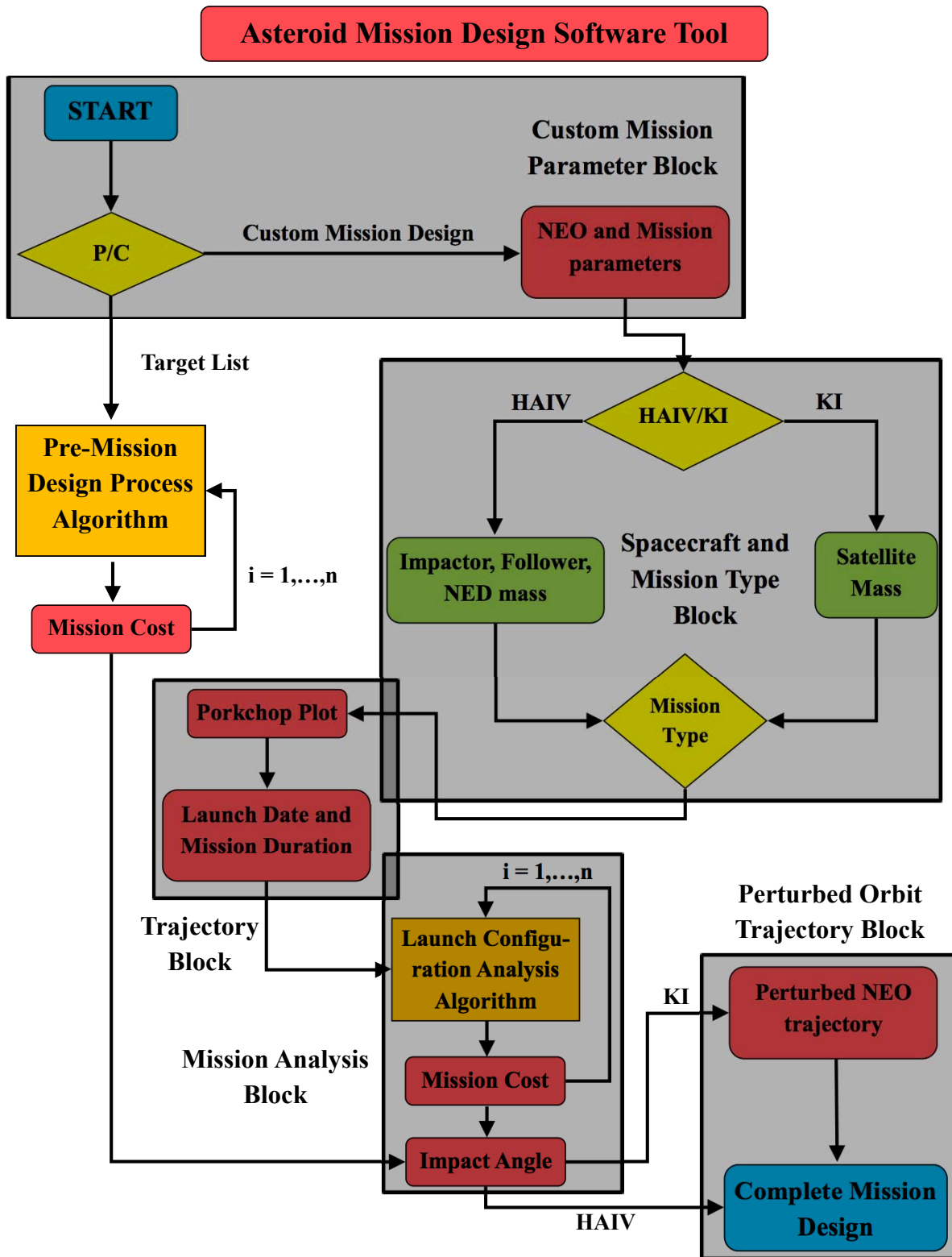


Figure 5.6: Block partition depiction of the AMiDST.



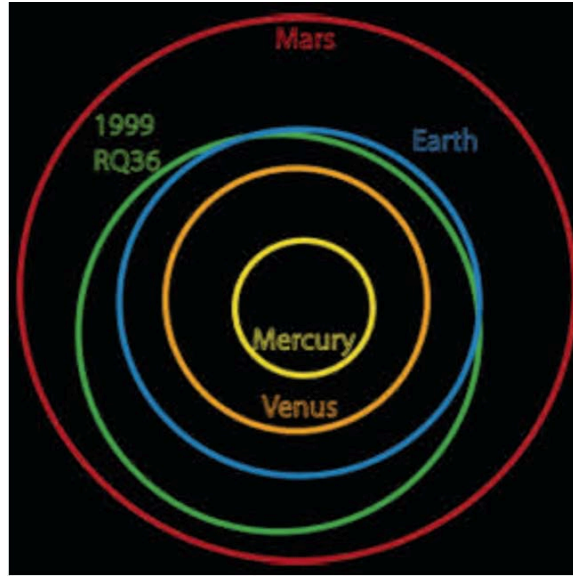


Figure 5.7: Illustration of the orbit of asteroid 1999 RQ36 in reference to the inner planets [12].

Table 5.5: Orbital elements at Epoch 2456200.5 (Sept. 20, 2012) of asteroid 2011 AG5 [9].

Element	Symbol	Value	Units
Semi-Major Axis	$a$	1.430649648860713	AU
Eccentricity	$e$	.3901259169082548	
Inclination	$i$	3.680120116707978	deg
Argument of Periapse	$\omega$	53.51980424253686	deg
Longitude of the Ascending Node	$\Omega$	135.6872472400388	deg
Mean Anomaly at Epoch	$M_0$	320.0427907507387	deg

observe the asteroid every six years, when 1999 RQ36 comes close to the Earth. By the late 2000s, 1999 RQ36 was probably one of the best-studied near-Earth asteroids that had not been visited by spacecraft.

### Asteroid 2011 AG5

Asteroid 2011 AG5 was discovered on January 8, 2011 as a part of the NASA-sponsored Catalina Sky Survey, a component of NASA's Near-Earth Object Observation Program. Based on its average albedo, 2011 AG5 has an estimated diameter of about 140 meters and a calculated impact probability of 1-in-500 with an impact velocity of 15 kilometers per second relative to Earth on February 5, 2040. For this NEO to impact the Earth in 2040, it would have to pass through a 365 km wide keyhole during a close encounter with Earth on February 3, 2023. Even with the extended observation data arc spanning back to November 8, 2010, the uncertainty in 2011 AG5's orbit allows for it to pass through a keyhole with a 1-in-500 chance. In the event that the asteroid does pass through the February 3, 2023 keyhole, 2011 AG5 will return on a 17:10 resonant return orbit (17 Earth orbits to 10 asteroid orbits about the Sun) to impact the planet on February 5, 2040. The orbital elements for 2011 AG5 are listed in Table 5.5 and the orbit diagram is shown in Figure 5.8.

More observations of 2011 AG5 are necessary to attempt to see whether the impact probability of the asteroid with Earth will decrease, especially since there is such limited observational data. Given the highly eccentric nature of the orbit, asteroid 2011 AG5 will complete one orbit in the time that it would take Earth to complete a little more than an orbit and a half of its own, therefore making observations of the asteroid a bit

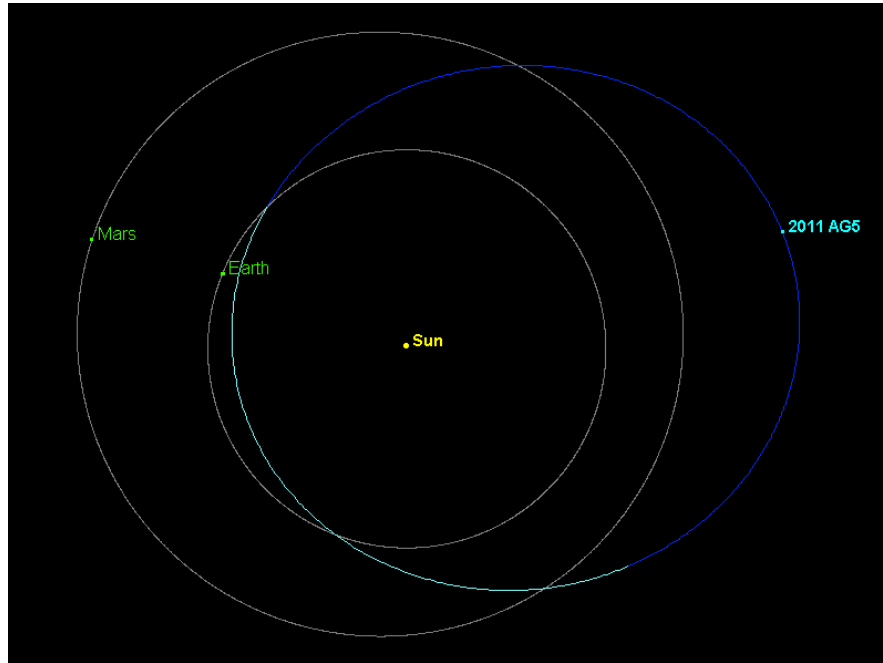


Figure 5.8: Illustration of the orbit of asteroid 2011 AG5 in reference to Earth's and Mars' orbits.

more difficult and each encounter more important to discerning orbital information. With such a small time period until 2011 AG5 may possibly impact the Earth, it is essential to be planning for the chance that action must be taken to mitigate its threat.

### 5.7.2 Spacecraft and Mission Type Block

With the targets adequately defined and selected, the AMiDST moves into the spacecraft and mission type block where the spacecraft type and mass are input, as well as the mission type: impact, impact at 10 kilometers per second, or rendezvous. The four mission studies that were conducted between the two target NEOs are listed in Table 5.6.

For each asteroid, a rendezvous and impact mission example was run using AMiDST. To highlight the remaining blocks within the AMiDST, Mission 1 from asteroid 1999 RQ36 will be used. This scenario is a pure impact mission to asteroid 1999 RQ36, using the 5720 kilogram HAIV configuration which carries a 1500-kg NED.

### 5.7.3 Trajectory Block

Due to 1999 RQ36's large mass and size, the chosen HAIV configuration is the 1500-kg NED spacecraft. In this configuration, the HAIV has a 670-kg impactor and a 3550 kg follower carrying a 1500-kg NED. With the spacecraft configuration and mission type coordinated, the AMiDST proceeds to load the appropriate contour plot for the user to pick the desired design point. The cross-hairs and black box on Figure 5.9 show the region from which the design point was chosen from.

The selected design point for this HAIV disruption mission is chosen to occur at a late launch date within the 10 year time period. The desired launch date comes out to be December 6, 2022 with a mission duration of 233 days. Given the launch date and mission duration pair, the resulting departure  $\Delta V$  from the 185-km circular low-Earth orbit is just over 4 km/s.

Table 5.6: Spacecraft and mission types for asteroids 1999 RQ36 and 2011 AG5.

Target NEO	Mission Number	Parameters	Value
<b>Asteroid 1999 RQ36</b>	Mission 1	Spacecraft Type	HAIV
		Spacecraft Mass	5720 kg
		Mission Type	Impact
	Mission 2	Spacecraft Type	Orbiter
		Spacecraft Mass	1500 kg
		Mission Type	Rendezvous
<b>Asteroid 2011 AG5</b>	Mission 1	Spacecraft Type	HAIV
		Spacecraft Mass	1843 kg
		Mission Type	Impact
	Mission 2	Spacecraft Type	Orbiter
		Spacecraft Mass	1200 kg
		Mission Type	Rendezvous

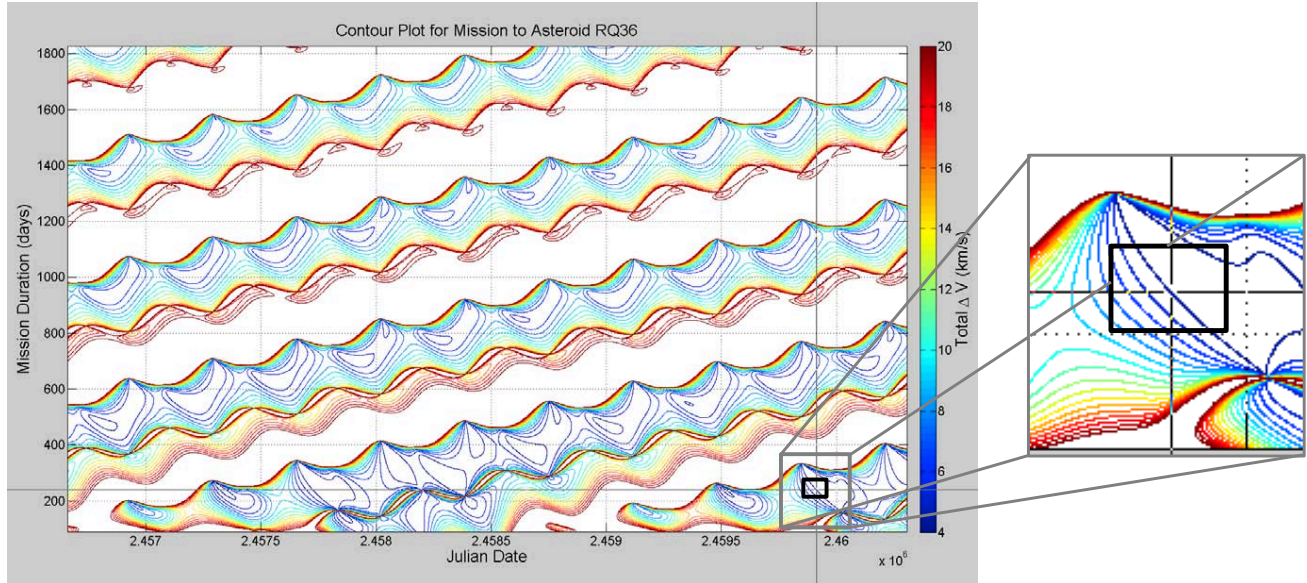


Figure 5.9: Selection of launch date and mission duration for 1999 RQ36 disruption mission.

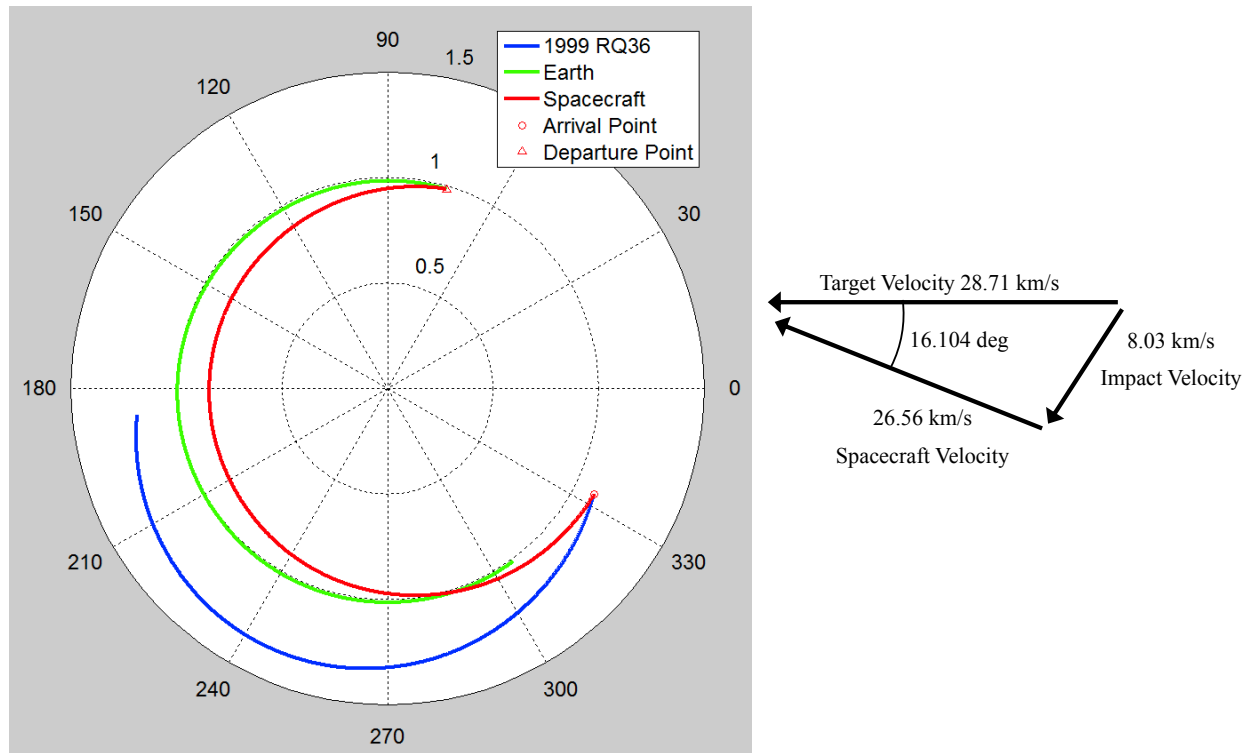


Figure 5.10: Left: Orbit diagram of transfer trajectory from Earth to 1999 RQ36. Right: Speeds and angle between spacecraft and 1999 RQ36 at impact.

#### 5.7.4 Mission Analysis Block

From these mission parameters, the spacecraft's trajectory is plotted in red along with the Earth's path (green line) and 1999 RQ36's trajectory (blue line) over the mission timespan in Figure 5.10 on the left. The HAIV would depart from Earth (red triangle) on December 6, 2022 and travel for 233 days until it would encounter the target NEO on July 27, 2023 (red circle).

On the right side of Figure 5.10, there is a depiction of the arrival conditions for the HAIV with respect to 1999 RQ36. Arriving at 1999 RQ36 on July 27, 2023 the HAIV would be traveling at about 26.5 km/s at a 16.1 degree angle to the target NEO's 28.7 km/s velocity, resulting in about an 8-km/s velocity difference, too large for a normal fusing system to survive at impact and confirming the choice of the HAIV configuration. Thanks to the large spacecraft mass and required departure  $\Delta V$ , the only launch vehicle capable of completing the given mission is the Delta IV Heavy. With such a powerful launch vehicle and massive spacecraft comes a large price tag as well, the estimated mission cost for this nuclear disruption mission is nearly \$1.8B. Table 5.7 gives all the pertinent HAIV disruption mission parameters.

#### 5.7.5 Perturbed Orbit Trajectory Block

In 1990, Congress directed NASA to find ways to increase the rate of discovery of near-Earth objects (NEOs)[14]. From those efforts, there are occasions where objects are seen to be on a potential Earth-impacting trajectory. The accurate prediction of such Earth-impacting trajectories often require high-fidelity N-body models, containing the effects of non-gravitational orbital perturbations such as solar radiation pressure. Having a highly precise asteroid orbit brings about many advantages: more specific mission planning, higher certainty of the target's location, and more accurate impact probability.

The orbital motion of an asteroid is governed by a so-called Standard Dynamical Model (SDM) of the

Table 5.7: Mission design parameters for intercept with Asteroid 1999 RQ36.

Mission Parameter	Value
Asteroid	1999 RQ36
Asteroid Mass (kg)	1.4E+11
LEO altitude (km)	185
Spacecraft Designation	HAIV
NED Mass (kg)	1500
Impactor Mass (kg)	670
Follower Mass (kg)	3550
Total HAIV Mass (kg)	5720
Departure $\Delta V$ (km/s)	4.002
C3 (km <sup>2</sup> /s <sup>2</sup> )	17.669
Launch Vehicle	Delta IV Heavy
Departure Date	December 6, 2022
Mission Duration (days)	233
Arrival Angle (deg)	16.104
Impact Velocity (km/s)	8.03
Arrival Date	July 27, 2023
Estimated Mission Cost (\$)	1797.66M

following form [14]:

$$\frac{d^2 \vec{r}}{dt^2} = -\frac{\mu}{r^3} \vec{r} + \sum_{k=1}^n \mu_k \left( \frac{\vec{r}_k - \vec{r}}{|\vec{r}_k - \vec{r}|^3} - \frac{\vec{r}_k}{r_k^3} \right) + \vec{f} \quad (2)$$

where  $\mu = GM$  is the gravitational parameter of the Sun,  $n$  is the number of perturbing bodies,  $\mu_k$  and  $\vec{r}_k$  are the gravitational parameter and heliocentric position vector of perturbing body  $k$ , respectively, and  $\vec{f}$  represents other non-conservative orbital perturbation acceleration.

Previous studies performed at the ADRC were concerned with the impact probability of potential Earth-impacting asteroids, such as 99942 Apophis. Using commercial software such as NASA's General Mission Analysis Tool (GMAT), AGI's Satellite Tool Kit (STK), and Jim Baer's Comet/asteroid Orbit Determination and Ephemeris Software (CODES), the ADRC conducted precision orbital simulation studies to compare with JPL's Sentry program [15].

Currently there are three main asteroids of interest being studied at the ADRC for high precision orbit tracking, Apophis, 1999 RQ36, and 2011 AG5. These three asteroids are of great interest because of their proximity to Earth and their relatively high impact probability. Interest in Apophis is primarily for validation of the numerical integration and orbit propagation schemes used in the N-body simulator. Using the asteroid Apophis as a reference NEO, simulations have been run from an initial epoch of August 27, 2011 until January 1, 2037 to show the capabilities of ADRC's N-body code in calculating precise, long-term orbit trajectories. Preliminary tests conducted for the period of May 23, 2029 to May 13, 2036 show the relative errors of GMAT and STK to JPL's Sentry (Horizons), as well as the error of the N-body code with respect to Sentry, as shown in Figure 5.11. The error in the radial position of Apophis between the N-body code to that of JPL's Sentry is much lower than that of both GMAT and STK. The N-body simulator used to obtain the aforementioned results uses a Runge-Kutta Fehlberg (RKF) 7(8) fixed-timestep method, including the orbital perturbations of all eight planets, Pluto, and Earth's Moon.

## Error Comparison - GMAT, STK, Nbody versus Horizons

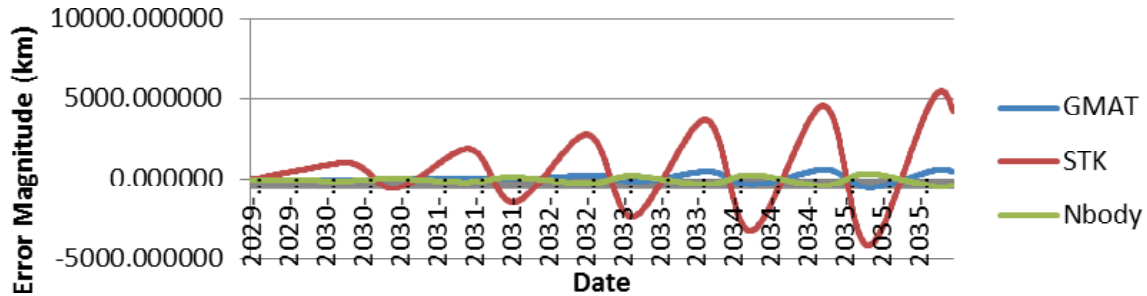


Figure 5.11: Relative error plot of GMAT, STK, and the ADRC's N-body code versus JPL's Sentry.

## 5.8 Asteroid 2011 AG5 Mission Design Examples

Now that we have successfully navigated through the workings of the AMiDST in the context of an impact mission example to 1999 RQ36, two more mission design examples are presented for asteroid 2011 AG5, a rendezvous and another impact mission.

### 5.8.1 Rendezvous Mission Design

Being such a recent discovery, asteroid 2011 AG5's orbit is still relatively unknown. Based on what is known about the asteroid's orbit however indicates that there is relatively high impact probability with the Earth, compared to other NEOs. Therefore, there is a need to better understand 2011 AG5's orbit so as to refine that impact probability. A rendezvous mission to the target NEO would be one way to accomplish this task. A spacecraft of mass 1200 kg is chosen for this case study. Together with the rendezvous mission type, a launch date and mission duration are chosen from the rendezvous contour plot for asteroid 2011 AG5, Figure 5.12. The cross-hairs and black box in the figure show the region of the grid where the design point was chosen from.

The chosen launch date and mission duration pair contains an April 29, 2028 launch date and 280 day mission transfer time. The departure date comes from one of the more feasible launch windows in the 25-year time frame. The launch window is wider than the window that opens in early 2023, and is still early enough for an adequately long mission studying the asteroid, assessing its composition, size, and threat to planet Earth. The spacecraft would arrive at 2011 AG5 in February 3, 2029, and could conduct proximity operations for a year or two before another decent launch window presents itself to launch a deflection mission if the asteroid's threat is deemed great enough to warrant action. On the left side of Figure 5.13 the transfer trajectory of the rendezvous satellite, illustrated by the red line, is depicted from Earth, whose orbit during the transfer time is shown in green, to the target NEO, portrayed by the blue line. The satellite's departure and arrival points are represented by the red triangle and circle, respectively.

The right side of Figure 5.13 shows the terminal conditions of the spacecraft's rendezvous with asteroid 2011 AG5. Since the spacecraft would be encountering the target NEO far from the Sun, the spacecraft would have more energy than the asteroid, requiring it to lose speed on approach to ensure a successful capture. The given transfer trajectory conditions create a 6.32 degree arrival angle between the target asteroid and



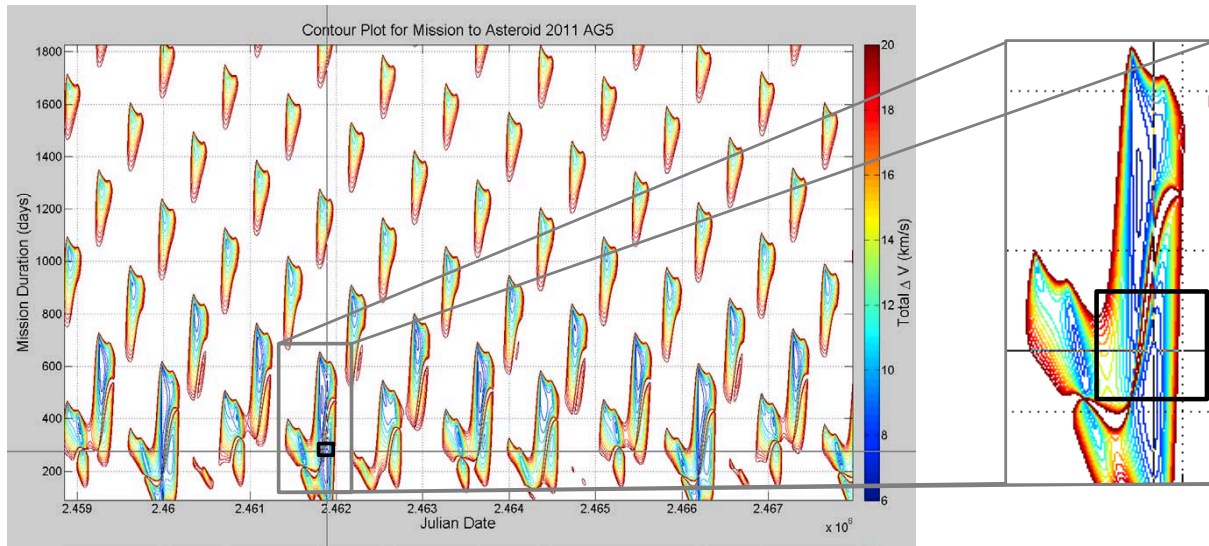


Figure 5.12: Selection of launch date and mission duration for 2011 AG5 rendezvous mission.

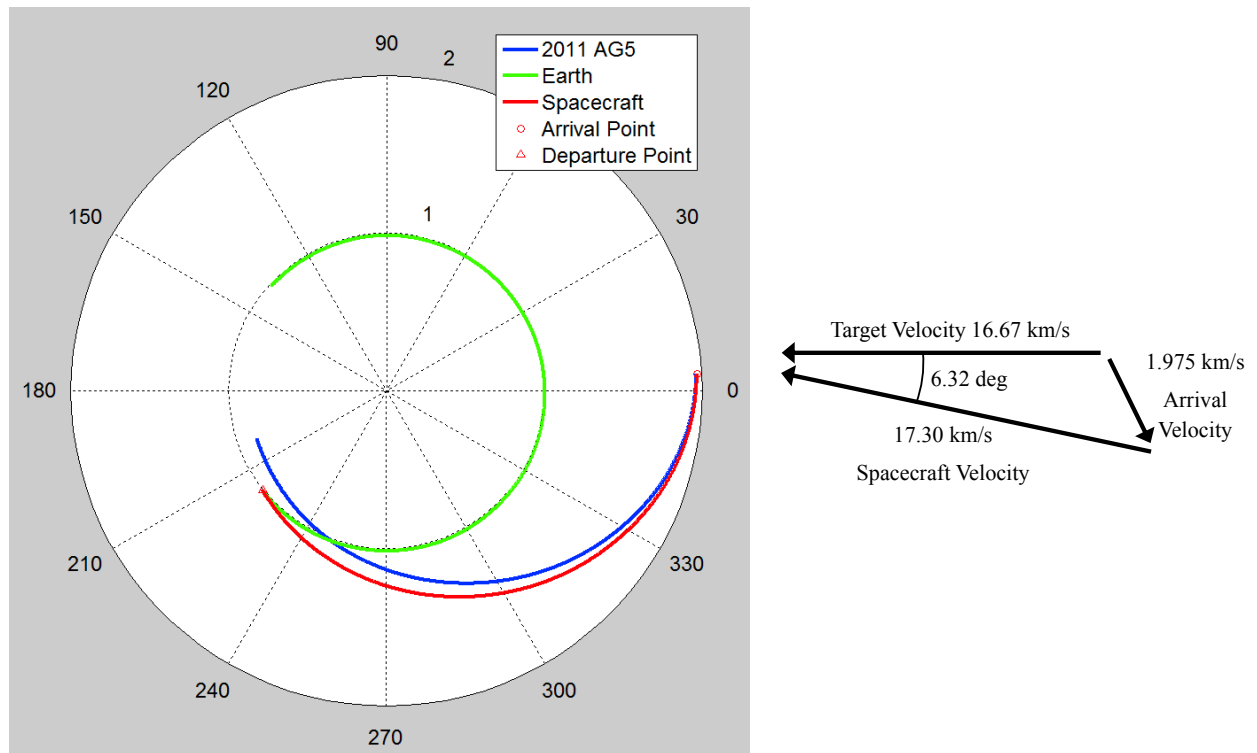


Figure 5.13: Left: Orbit diagram of transfer trajectory from Earth to 2011 AG5. Right: Speeds and angle between spacecraft and 2011 AG5 at arrival.

Table 5.8: Mission design parameters for rendezvous with Asteroid 2011 AG5.

Mission Parameter	Value
Asteroid	2011 AG5
Asteroid Mass (kg)	4.1E+9
LEO altitude (km)	185
Spacecraft Designation	Kinetic Impactor
Satellite Mass (kg)	1200
Departure $\Delta V$ (km/s)	4.668
C3 (km <sup>2</sup> /s <sup>2</sup> )	33.82
Launch Vehicle	Delta IV Medium
Departure Date	April 29, 2028
Mission Duration (days)	280
Arrival Angle (deg)	6.32
Arrival Velocity (km/s)	1.975
Arrival Date	February 3, 2029
Estimated Mission Cost (\$)	655.357M

spacecraft. At the end of the transfer trajectory the asteroid would only be moving at about 16.7 km/s, while the spacecraft would be traveling approximately 17.3 km/s, leaving the spacecraft to carry almost 2-km/s of  $\Delta V$  to be used for braking purposes.

Despite the large departure  $\Delta V$  of nearly 4.7 km/s, the spacecraft's low mass allows for a smaller launch vehicle to complete the mission design, saving the mission a considerable amount of cost. The launch vehicle deemed most appropriate for this 2011 AG5 rendezvous mission is the Delta IV Medium. As a whole, this mission comes out to be relatively cheap compared to the previous mission designs, estimated to cost a little over \$655M. A brief summary of the important mission design parameters are given in Table 5.8.

### 5.8.2 HAIV Disruption Mission Design

If asteroid 2011 AG5 were deemed a realistic threat to the survival of the planet, a deflection/disruption mission would need to be launched. An important thing to remember when selecting a launch date for a deflection/disruption mission to a target NEO is to give plenty of time for the perturbed asteroid or asteroid debris to settle into its/their new orbit(s). Again, an HAIV design is used for this particular disruption mission case study. Figure 5.14 shows the contour plot for a direct intercept mission with 2011 AG5. The cross-hairs and black box in the diagram show where the design point which is used to design the disruption mission. The current direct intercept mission case study has a departure date April 15, 2027 and a mission duration of 350 days.

With nearly a full year of transit time, the HAIV would not arrive to the target NEO until March 30, 2028, about 12 years before the estimated impact date. The orbit plot on the left of Figure 5.15 shows the impact between the HAIV and the target to occur inside the Earth's orbital radius. The spacecraft will depart from Earth on April 15, 2027, represented by the red triangle, and travel for 350 days until its encounter with asteroid 2011 AG5 on March 30, 2028, shown as the red circle. The spacecraft, asteroid, and Earth's orbits are depicted by the red, blue, and green lines, respectively.

The right side of Figure 5.15 shows the anticipated encounter between the HAIV and target NEO. Arrival at 2011 AG5 from the given trajectory will result in an impact angle of about 14.3 degrees. Such an arrival angle results in a relative velocity between the asteroid and the HAIV of over 9 km/s. High relative impact velocities, similar to the one present in this mission, are the reasons why the ADRC has been developing



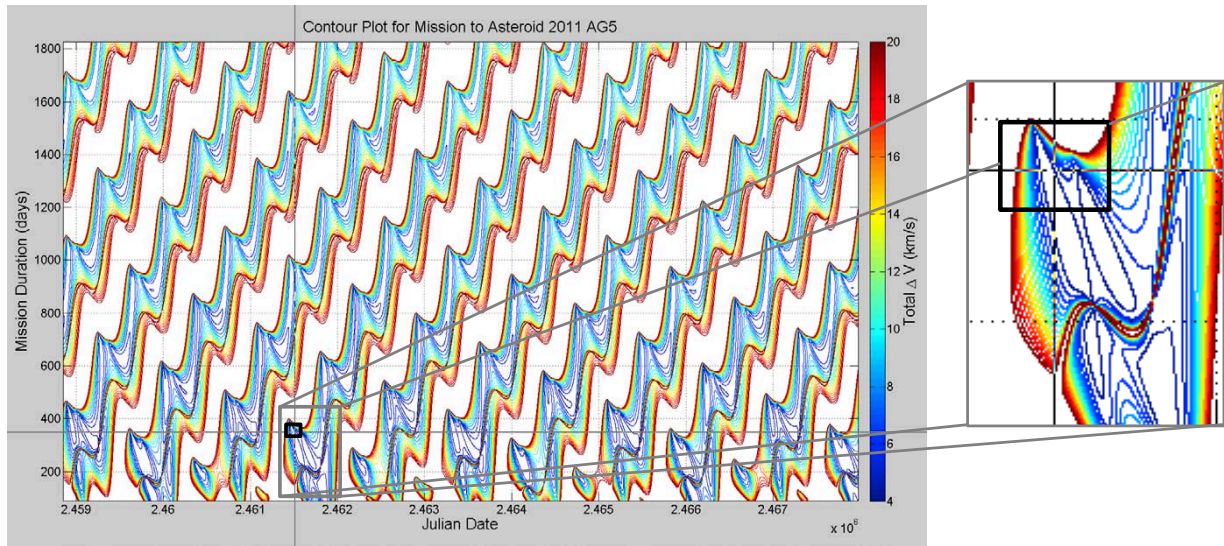


Figure 5.14: Selection of launch date and mission duration for 2011 AG5 disruption mission.

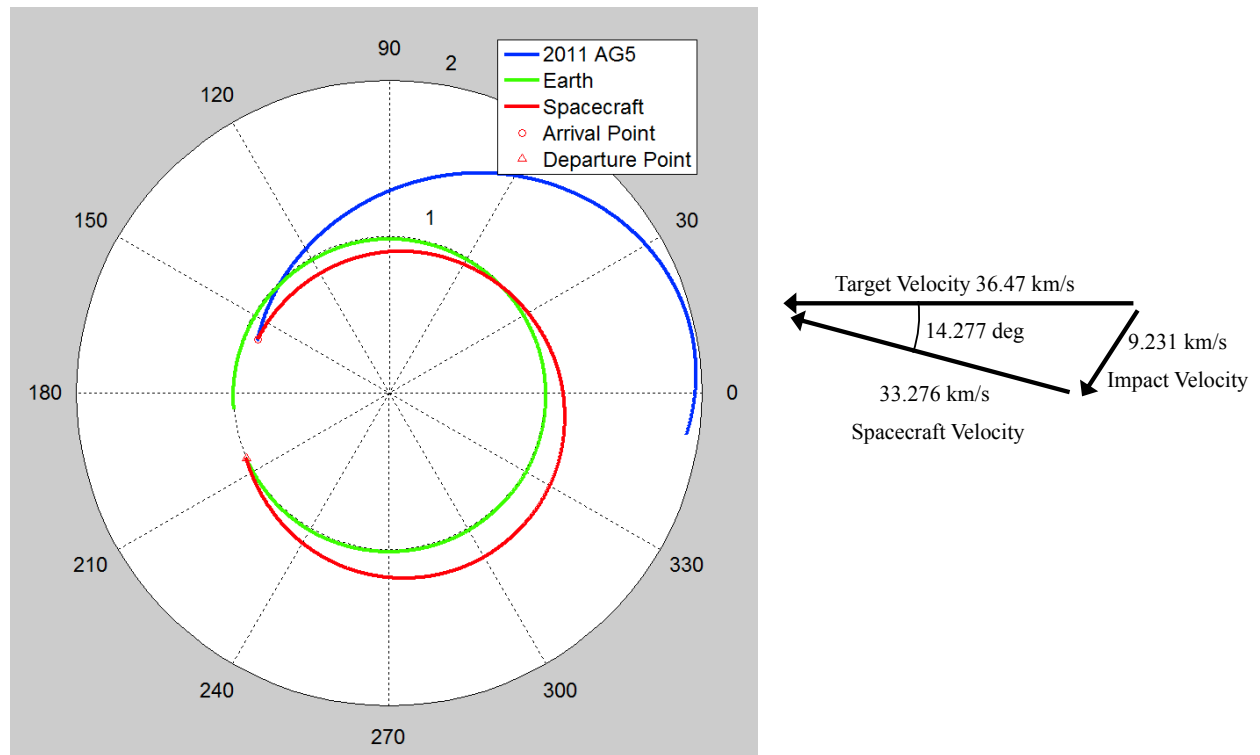


Figure 5.15: Left: Orbit diagram of transfer trajectory from Earth to 2011 AG5. Right: Speeds and angle between spacecraft and 2011 AG5 at impact.

Table 5.9: Mission design parameters for intercept with Asteroid 2011 AG5 [17].

Mission Parameter	Value
Asteroid	2011 AG5
Asteroid Mass (kg)	4.1E+9
LEO altitude (km)	185
Spacecraft Designation	HAIV
NED Mass (kg)	300
Impactor Mass (kg)	360
Follower Mass (kg)	1183
Total HAIV Mass (kg)	1843
Departure $\Delta V$ (km/s)	5.961
C3 (km <sup>2</sup> /s <sup>2</sup> )	67.709
Launch Vehicle	Atlas V 551
Departure Date	April 15, 2027
Mission Duration (days)	350
Arrival Angle (deg)	14.277
Impact Velocity (km/s)	9.231
Arrival Date	March 30, 2028
Estimated Mission Cost (\$)	860.340M

the HAIV concept. Since 2011 AG5’s mass is estimated to be smaller than that of 1999 RQ36, the 300-kg NED HAIV design was chosen for this mission. The pertinent mission parameters for this direct intercept disruption mission are given in Table 5.9. The departure  $\Delta V$  for this case study is the highest of all the case study missions at just under 6 km/s. The departure  $\Delta V$  (4.7 km/s versus 6 km/s) and spacecraft masses (1200 kg versus 1843 kg) between the two 2011 AG5 missions are pretty similar, there are large distinctions in the resulting launch configurations and mission cost. Unlike the 2011 AG5 rendezvous case where a smaller launch vehicle was preferred to the larger launch vehicles, an Atlas V 551 launch vehicle is needed to impart the required change in velocity from low-Earth orbit. Also, the estimated mission cost for this disruption mission is nearly \$1B. It is interesting to note that while there are several regions where a feasible mission can be designed, there are many more design points where there is no feasible launch configuration that will apply enough  $\Delta V$  to inject the spacecraft into the required direct transfer orbit.

## 5.9 Conclusion

In this chapter the various aspects of the Asteroid Mission Design Software Tool (AMiDST), which is being developed at the Iowa State ADRC, have been presented for preliminary mission designs of direct intercept and rendezvous of reference target NEOs, such as 1999 RQ36 and 2011 AG5, as well as the accurate tracking of asteroid Apophis in long-term, N-body gravitational simulations. This paper has shown that the AMiDST is capable of accurately simulating the orbit of a body around the Sun, taking into account gravitational perturbations of the eight planets, Pluto, and Earth’s Moon, as well as various designs for direct intercept and rendezvous missions to Earth-threatening asteroids. Despite the odds of Earth being struck by an asteroid of sufficient size to worry about deflection missions to those threatening bodies, the day may come when the Earth is truly in danger. When that day arises, software tools like the one described in this paper can provide a first-order approximation and critical knowledge that can be pivotal to the success of a real mission to a target NEO.

## 5.10 References

- [1] Vardaxis, G., et al. "Conceptual Design of Planetary Defense Technology Demonstration Mission," AAS 12-128, AAS/AIAA Space Flight Mechanics Meeting, February 2012.
- [2] Pitz, A., et al. "A Hypervelocity Nuclear Interceptor System (HAIV) for Optimal Disruption of Near-Earth Objects," AAS 12-225, AAS/AIAA Space Flight Mechanics Meeting, February 2012.
- [3] T. Winkler, et al. "Target Selection for a Planetary Defense Technology Demonstration Mission," AAS 12-226, AAS/AIAA Space Flight Mechanics Meeting, February 2012.
- [4] Vardaxis, G., Pitz, A., and Wie, B., "Conceptual Design of Planetary Defense Technology Demonstration Mission," AAS 12-128, AAS/AIAA Space Flight Mechanics Meeting, 2012.
- [5] Melamed, N., "Development of a handbook and an on-line tool on defending Earth against Potentially Hazardous Objects", *Acta Astronautica* (2012), <http://dx.doi.org/10.1016/j.actaastro.2012.02.021>.
- [6] "LTTT Suite Optimization Tools." *LTTT Suite Optimization Tools*. Ed. Timothy A. Reckart. NASA Glenn Research Center Space Science Projects Office, 23 Apr. 2012.  
< [http : //microgravity.grc.nasa.gov/SSPO/ISPTProg/LTTT/](http://microgravity.grc.nasa.gov/SSPO/ISPTProg/LTTT/) >.
- [7] GMAT Design Team, "General Mission Analysis Tool (GMAT)," < [gmatsfsc.nasa.gov/index.html](http://gmatsfsc.nasa.gov/index.html) >.
- [8] "Near-Earth Object Program." *Near-Earth Object Program*. Ed. Donald K. Yeomans. National Aeronautics and Space Administration. < [http : //neo.jpl.nasa.gov/index.html](http://neo.jpl.nasa.gov/index.html) >.
- [9] "JPL Solar System Dynamics." *JPL Solar System Dynamics*. Ed. Donald K. Yeomans. NASA Jet Propulsion Laboratory. < [http : //ssd.jpl.nasa.gov/](http://ssd.jpl.nasa.gov/) >.
- [10] "National Aeronautics and Space Administration - Marshall Space Flight Center." *NEW FRONTIERS Programs*. Ed. Anthony Goodeill. Marshall Space Flight Center.  
< [http : //discoverynewfrontiers.nasa.gov/missions/index.cfm](http://discoverynewfrontiers.nasa.gov/missions/index.cfm) >.
- [11] Agle, D. C., "JPL News – NASA Scientists Use Radar to Detect Asteroid Force," Space, Stars, Mars, Earth, Planets and More - NASA Jet Propulsion Laboratory.  
< [http : //www.jpl.nasa.gov/releases/2003/163.cfm](http://www.jpl.nasa.gov/releases/2003/163.cfm) >.
- [12] "The OSIRIS-REx Mission - An Asteroid Sample Return Mission." *The OSIRIS-REx Mission - An Asteroid Sample Return Mission*. < [http : //osiris - rex.lpl.arizona.edu/](http://osiris-rex.lpl.arizona.edu/) >.
- [13] Vallado, David A., and Wayne D. McClain. *Fundamentals of Astrodynamics and Applications*. 3rd ed., Microcosm, 2007.
- [14] Chodas, P. W. and Yeomans, D., "Orbit Determination and Estimation of Impact Probability for Near Earth Objects," AAS 09-002.
- [15] A. Pitz, et al. "Earth-Impact Probability Computation of Disrupted Asteroid Fragments Using GMAT/STK/CODES," AAS 11-408, AAS/AIAA Astrodynamics Specialist Conference, August 2011.
- [16] Wagner, S., Kaplinger, B., and Wie, B., "GPU Accelerated Genetic Algorithm for Multiple Gravity-Assist and Impulsive Delta-V Maneuvers," AIAA 2012-4592, AIAA/AAS Astrodynamics Specialists Conference, August 2012.
- [17] Vardaxis, G and Wie, B., "Asteroid Mission Design Software Tool (AMiDST) for Planetary Defense Mission Design Applications," AIAA 2012-4872, AIAA/AAS Astrodynamics Specialist Conference, August 2012.

## Chapter 6

# Target Selection for a HAIV Flight Validation Mission

### 6.1 Introduction

Although there is currently no known immediate threat of a near-Earth object (NEO) to the Earth, numerous new asteroids are being discovered each year. Some of these undiscovered NEOs could potentially pose a threat to the Earth with little to no warning. Every day there is a multitude of objects that impact the Earth. However, the majority of these impacts are from small meteors no bigger than 10 m and are of little cause for concern. Although rare, collisions with much larger objects have the potential to cause unprecedented damage. Various technologies, including nuclear explosions, kinetic impactors, and slow-pull gravity tractors for mitigating the impact threat of NEOs have been proposed and studied during the past two decades. However, there is no consensus on how to reliably deflect or disrupt hazardous NEOs in a timely manner. Furthermore, there has not been any flight demonstration mission to verify and validate key technologies that will be employed in a real mitigation mission.

This study will determine a list of optimal asteroid targets for a planetary defense technology (PDT) demonstration mission, which would validate asteroid deflection or disruption capabilities. For the purposes of this study, only asteroids listed in NASA's Near Earth Object Program database will be considered. This database also contains a list of near-Earth comets, which will not be considered in this paper. Although comets are also at risk of impacting the Earth, they add unnecessary complexity to the spacecraft design, as it must be shielded from the small, hypervelocity dust grains that form the coma. In addition, previous missions such as Deep Impact and Stardust have already flight-validated the necessary shielding and targeting capabilities for comets. As such, the asteroid targets identified in this study will allow a demonstration mission to focus on validating deflection/disruption technologies, which should prove equally effective against comets if the need should arise.

#### 6.1.1 Previous NEO Missions and Proposals

There have already been several successful exploration missions to asteroids and comets successfully accomplished by NASA, ESA, and JAXA. Two notable missions that involved NEO targeting technologies that would be involved in an asteroid defense mission were Deep Impact by NASA and Hayabusa by JAXA. The Hayabusa spacecraft contained a small lander called MINERVA which was to be guided to the surface of the asteroid Itokawa. Unfortunately the MINERVA lander drifted into space due to the low gravity. NASA's Deep Impact spacecraft on the other hand was comprised of an impactor and a flyby spacecraft. Approximately 24 hours before impact with the comet Tempel 1, the impactor was released and autonomously navigated to ensure a hypervelocity impact of 10 km/s with the 5-km target.

Table 6.1: Target selection criteria for the Don Quijote mission.

Orbit Characteristics	Preferred Range
Rendezvous $\Delta V$	$< 7$ km/s
Orbit type	Amor
MOID	large and increasing
Orbit accuracy	well determined orbits
Physical Characteristics	Preferred Range
Size	$< 800$ m
Density	$\sim 1.3$ g/cm <sup>3</sup>
Absolute magnitude	20.4 - 19.6
Shape	not irregular
Taxonomic type	C-type
Rotation period	$< 20$ hours
Binarity	not binary

Table 6.2: Properties of candidate targets considered for the Don Quijote mission.

Asteroid Characteristics	2002 AT4	1989 ML
Orbital period (yr)	2.549	1.463
e	0.447	0.137
i (deg)	1.5	4.4
$\Delta V$ (km/s)	6.58	4.46
Orbit type	Amor	Amor
MOID	large	large
Absolute magnitude	20.96	19.35
Taxonomic type	D-type	E-type
Diameter (m)	380	800
Rotational period (hr)	6	19

In recent years, ESA proposed a demonstration mission for a kinetic-impactor, based entirely on conventional spacecraft technologies, called the Don Quijote mission [1, 2]. The mission concept called for two separate spacecraft to be launched at the same time, but follow different interplanetary trajectories. Sancho, the orbiter spacecraft, would be the first to depart Earth's orbit, and rendezvous with a target asteroid approximately 500 m in diameter. Sancho would measure the position, shape, and other relevant characteristics before and after a hypervelocity impact by Hidalgo, the impactor spacecraft. After Sancho has studied the target for some months, Hidalgo approaches the target at a closing speed of about 10 km/s. Sancho then observes any changes in the asteroid after the kinetic impact to assess the effectiveness of this deflection strategy. Don Quijote was planned to launch in early 2011, and conclude in mid to late 2017. However, the mission concept was never realized due to higher than expected mission costs.

The selection process for the Don Quijote mission was based on a set of NEO characteristics defined by ESA's NEOMAP in Table 6.1[3]. Their analysis resulted in the selection of the asteroids 2002 AT4 and 1989 ML. As can be noticed in Table 6.2, 2002 AT4 is roughly half the size of 1989 ML, but requires a higher  $\Delta V$  in order to intercept. A realistic deflector spacecraft would require a versatile design capable of intercepting and deflecting or disrupting both kinds of targets on short notice.

Currently at the Asteroid Deflection Research Center (ADRC), a hypervelocity nuclear interceptor system (HNIS) concept is being investigated for a high-energy disruption/fragmentation mission. Such a mission

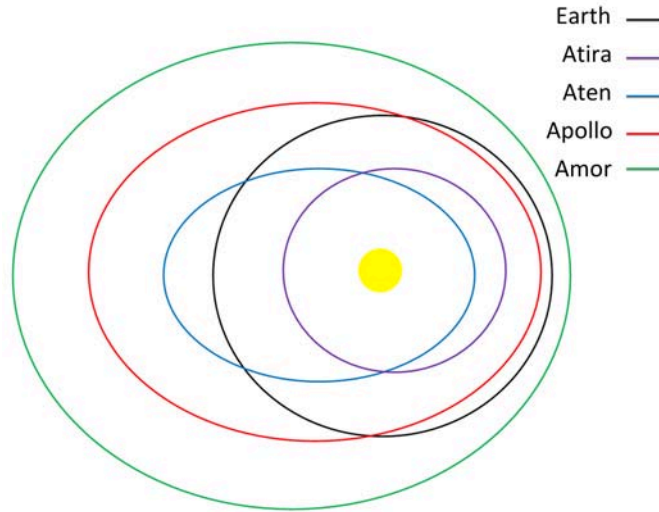


Figure 6.1: Illustration of typical orbits of Atira, Apollo, Aten and Amor asteroids.

may be necessary to mitigate the impact threat for a short warning time [4–6]. While the Don Quijote mission concept considered deflecting an asteroid with a kinetic impactor, the ADRC is focusing on a high-energy deflection/disruption demo mission by means of a standoff or contact explosion or disrupting/fragmenting the asteroid into smaller, less threatening pieces using a penetrating subsurface nuclear explosion. The latter option is accomplished by an innovative, two body penetrator design, which allows a nuclear explosive device (NED) to be detonated inside the asteroid itself to facilitate a more efficient energy transfer from the explosion [4–6]. To aid in helping the spacecraft intercept the target, an orbital transfer vehicle (OTV) is also being investigated for the purpose of providing additional  $\Delta V$  at orbit injection.

## 6.2 Optimal Target Selection Process

For the purposes of this study, only asteroids in the near-Earth asteroid (NEA) groups Apollo, Aten, and Amor were considered. Asteroids in these groups all have perihelion distances of 1.3 AU or less, and many of them also cross the Earth's orbit at some point. Asteroids in these groups are relatively close to the Earth, and have low  $\Delta V$  requirements to achieve intercept. As such, objects in these groups are the most likely candidates for an asteroid deflection/disruption demonstration mission. Apollo and Aten class asteroids are characterized by asteroids with orbits that intersect that of the Earth, which could potentially lead to lower  $\Delta V$  requirements for a mission. However, this also means that any significant perturbation in the asteroid's trajectory could cause a future Earth impact. While unlikely, a demonstration of deflection technologies could potentially an impact to occur in the future. ESA also had this in mind when they selected the asteroids 2002 AT4 and 1989 ML from the Amor group for the Don Quijote mission concept [1]. With that in mind, the Amor group shall be the focus for determining suitable candidates in this paper.

As illustrated in Figure 6.1, the Amor asteroid group is characterized by asteroids that approach the Earth, but do not actually cross its orbit. By definition the perihelion distances of these asteroids lie between 1.017 and 1.3 AU. As the entire orbit is outside that of the Earth, any disturbance in the trajectories of these asteroids is even less likely to cause them to later impact the Earth. As of 10/20/2011, there are 3084 Amor class asteroids listed in NASA's Near Earth Object Program database. This number is first reduced by only considering asteroids that are at least 100 m in diameter. This is done by only considering objects with an absolute magnitude (H value) of 22 or lower. Assuming that the asteroid's albedo falls within the presumed

Table 6.3: Target selection criteria.

Characteristic	Preferred
Orbit type	Amor
Absolute Magnitude	18 - 21
Diameter	300 – 1000 m
Total $\Delta V$	$< 5$ km/s

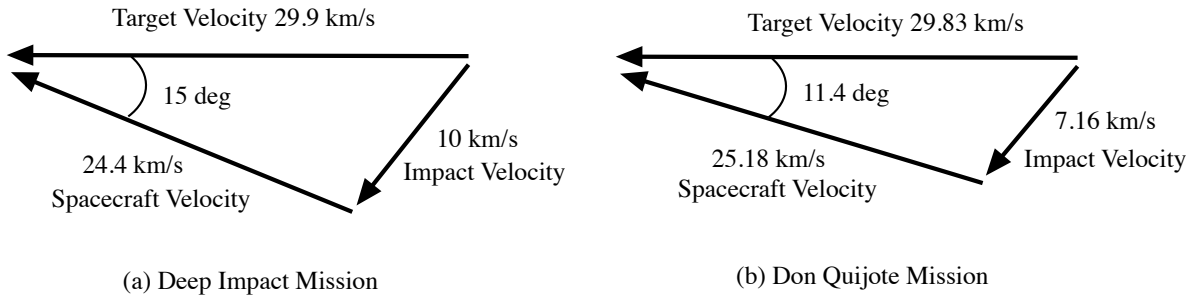


Figure 6.2: Velocity vector diagrams and impact approach angles for the Deep Impact and Don Quijote missions.

0.25 to 0.05 albedo range, this  $H$  value corresponds to an object at least 110 to 240 m in diameter. Applying this minimum size limit reduces the number of asteroids to be considered to a little more than 2200.

Table 6.3 summarizes the selection criteria used in this study. While asteroids as small as 100 m are studied, optimal candidates will have a diameter between 300 to 1000 m. This large diameter requirement is utilized due to constraints imposed by current targeting technologies, and a necessity to assess the effectiveness of nuclear fragmentation on larger, threatening objects. Should the mission successfully disrupt a larger object, it will prove equally effective on smaller sized asteroids as well. A limit on the  $\Delta V$  required for intercept is due to the limitations imposed by current launch vehicle and spacecraft capabilities. This limit also takes into account the requirement of a relative closing velocity of approximately 10 km/s. This is enforced in order to simulate a situation with a short warning time of Earth impact. The limit on total  $\Delta V$  ends up being the same upper limit for the Don Quijote mission selection process. This number was chosen due to the total  $\Delta V$  capabilities given in Table 4, which are based on maximum payload masses for each launch vehicle. These represent conservative estimates for the total payload masses, which tend toward the worst case heavier options. An additional requirement which could be used, is the impact approach angle shown in Figure 6.2. The impact approach angle is defined as the angle between the velocity vectors of the target and spacecraft at the time of impact. This is an important piece of information for a two body HNIS as the leading body must impact the asteroid ahead of the NED to successfully achieve a subsurface detonation. Furthermore, there may be cases when it is more advantageous to impact the target from a certain direction to greater facilitate the desired amount of deflection. For the purposes of this study, no constraints on the impact approach angle will be enforced

### 6.2.1 Launch Options

Based on the target criteria discussed above, ephemeris data from NASA's Horizons database was used in conjunction with programs developed at the ADRC to calculate the minimum  $\Delta V$  for missions of varying duration to each asteroid. The details of this program can be found in Ref. 7. The targets will be restricted to

Table 6.4: Estimated performance capabilities for various mission configurations.

Launch Vehicle	S/C mass (kg)	NED mass (kg)	Total $\Delta V$ (km/s)	C3 (km <sup>2</sup> /s <sup>2</sup> )
Delta II	1543	300	3.43	4.5
Atlas V	3251	1000	4.23	23
Delta IV Heavy	4220	1500	4.72	35

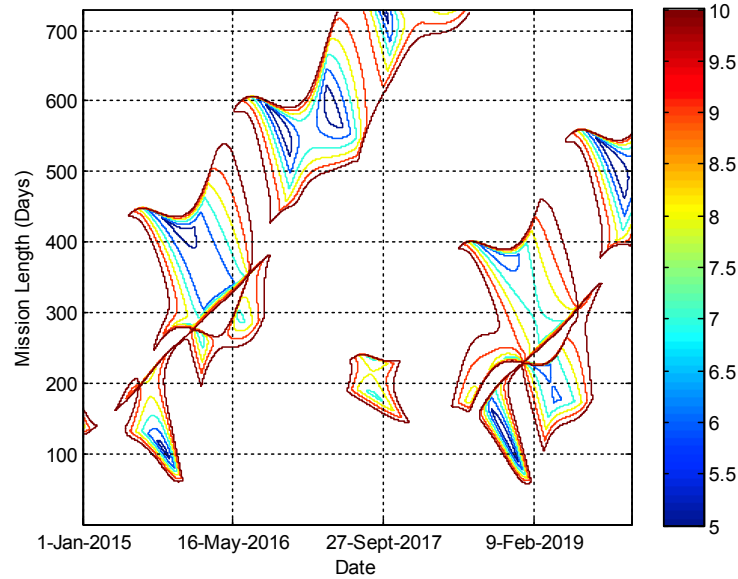


Figure 6.3: Total  $\Delta V$  (km/s) contour plot for 1989 ML.

the estimated capabilities of the spacecraft with three different launch vehicles: the Delta II 7920H, Delta IV Heavy and Atlas V 551. The estimates used in this study can be viewed in Table 6.4. These were calculated using a combination of publicly available information on each launch vehicle provided by their respective companies and the ideal rocket equation for the OTV using a bipropellant fuel of  $N_2H_4$ /hydrazine. Given the current estimates of the spacecraft mass for each of the launch configurations, the Atlas V and Delta IV Heavy do not require the use of an OTV as the third stage options can already achieve C3 values well above 20. The Delta II on the other hand, relies completely on the OTV to act as a third stage and provide  $\Delta V$  after launch. It should be noted that the Delta II will most likely be replaced by Orbital's Antares launch vehicle in the near future.

## 6.2.2 Target List

The majority of the data used to evaluate target asteroids was generated using a FORTRAN 90 program, which executed a grid search approach for potential launch dates spanning a period of twenty-five years (Jan. 1, 2015 to Jan. 1, 2040) in conjunction with various transfer durations up to a maximum of five years. Ephemeris files for 2140 Amor asteroids were automatically downloaded via a program written specifically to access NASA's Horizons system via TELNET. Using this information, each asteroid was searched using a three day time step for both the launch date and mission length. Only direct transfer orbits were considered in this program. This search was parallelized using OpenMP to utilize each core on the workstation, and required a run time of approximately 20 hours. Although data as far as 2040 was generated, only the results for the first five year time span (Jan. 1, 2015 to Jan. 1, 2020) and a maximum mission length of one year were analyzed in greater



Table 6.5: Optimal targets with corresponding minimum total  $\Delta V$ , launch date, and mission duration.

Asteroid	Launch Date	Departure $\Delta V$ (km/s)	Mission Length (days)	C3 (km <sup>2</sup> /s <sup>2</sup> )
2003 GA	12/3/2015	3.519	111	6.5
2006 SJ198	3/17/2015	4.596	337	32.01
2009 TB3	1/27/2018	3.6	97	8.35
2007 FS35	2/4/2015	3.473	272	5.47
2003 QC	1/1/2015	4.479	331	29.14
2004 GY	6/30/2015	4.354	365	26.1
2001 SX269	5/2/2019	3.572	114	7.7
1998 SB15	5/5/2017	3.335	159	2.37
2004 KE1	2/8/2017	4.539	365	30.62
1989 ML	11/17/2018	4.027	120	18.26

Table 6.6: Orbital and physical characteristics of target asteroids.

Asteroid	Semi-Major Axis (AU)	Eccentricity	Inclination (deg)	Absolute Magnitude	Diameter (m) *	Mass (kg) †
2003 GA	1.28	0.191	3.84	21.08	300	3.67E10
2006 SJ198	2.09	0.456	2.43	17.95	1200	2.35E12
2009 TB3	1.32	0.219	12.22	21.09	300	3.67E10
2007 FS35	1.92	0.390	0.32	19.56	620	3.24E11
2003 QC	2.57	0.532	7.85	20.54	400	8.71E10
2004 GY	1.45	0.218	23.44	20.11	480	1.50E11
2001 SX269	1.88	0.346	4.03	21.29	280	2.99E10
1998 SB15	1.27	0.161	15.63	20.9	330	4.89E10
2004 KE1	1.30	0.181	2.88	21.63	240	1.88E10
1989 ML	1.87	0.446	1.50	19.5	630	3.40E11

Assuming a nominal albedo of 0.07 [8]

† Assuming a sphere with a density of 2.6 g/cm<sup>3</sup> [9]

detail. As can be seen in Figure 6.3, there is no benefit to looking at mission lengths beyond that of a year for most targets in terms of  $\Delta V$ . While there are some possible mission designs at the very edge of the maximum mission length, they would not be any lower than the minimum  $\Delta V$  pockets found between 100 and 150 days. The data was then inserted into a cost function based on the hyperbolic excess velocity and the arrival burn magnitude to ensure a 10 km/s closing velocity. Ten asteroids that minimized this function were selected as optimal targets to be studied in greater detail.

The optimal asteroid targets selected in this study are listed in Table 6.5 along with their corresponding launch date,  $\Delta V$  requirements and mission length. When compared to the upper limits on the estimated launch vehicle and OTV performance in Table 6.4, it can be seen that the Delta II launch vehicle could only be used to reach the target 1998 SB15. The other targets have  $\Delta V$ s above the estimated capabilities of the Delta II configuration, and could only be reached using the Delta IV Heavy or Atlas V launch vehicles.

Some of the asteroid diameters in Table 6.6 are slightly outside the desired range of 300-1000 m. Without knowing the albedo, there is some uncertainty in either direction for these diameters. There is not too much concern for asteroids with diameters greater than 1000 m, but for those such as 2003 KE1, which has a diameter of 240 m, the targeting accuracy of the instruments may not be high enough to reasonably ensure an impact. As such, it will be left as a potential target to assess targeting capabilities of future spacecraft, but

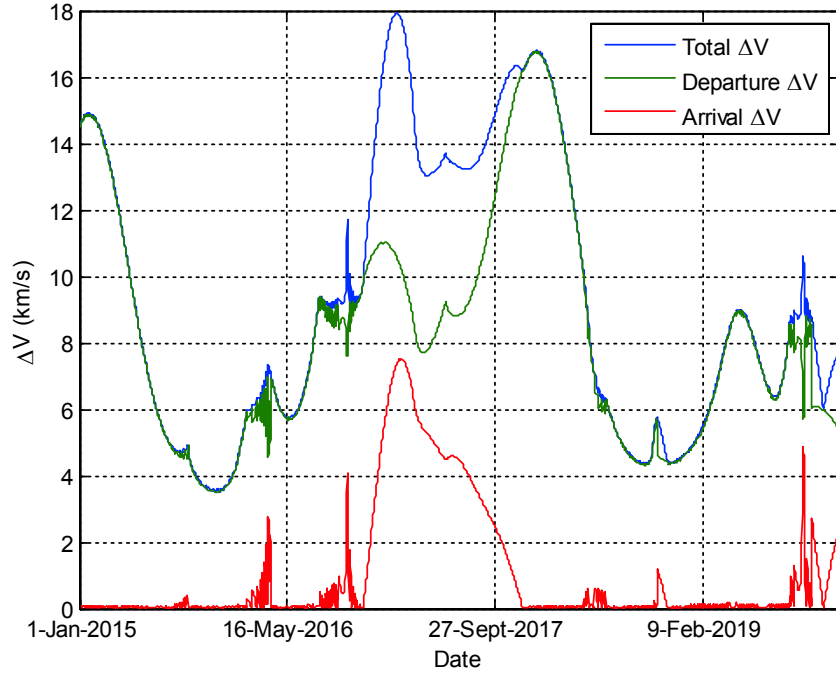


Figure 6.4: Minimum  $\Delta V$  required versus launch date for 2003 GA.

will not be seriously considered as a target for any of the mission configurations used in this study.

Once ten targets were selected, a separate analysis was conducted to verify if the optimal targets were indeed suitable for a PDT demo mission. Using the ephemeris data for the Earth and the asteroids, Lambert's problem was solved for the given time frame with a varying transfer duration. To this end, a program capable of solving this problem using either Battin's method or the universal variable method was written in MATLAB R2011b. Currently the universal variable method will always solve for the orbit that results in the shortest path between the start and end points regardless if it is prograde or retrograde. At times, this could result in total  $\Delta V$ s as high as 90-100 km/s. Battin's method, however, always kept the transfer orbit as prograde or retrograde unless specified otherwise, and has a much higher computational efficiency [7]. Therefore, Battin's method was the preferred algorithm of the two for solving Lambert's problem. Two main assumptions made were a departure from a 185 km altitude circular orbit and the arrival  $\Delta V$  is only that necessary to ensure a 10 km/s relative velocity upon impact. The program was based on the proven methods presented in Ref. 7, and was able to reproduce the  $\Delta V$  plots. For this reason, the program was assumed to be functioning properly, and producing accurate results. Figures 6.4-6.7 are select plots which were generated using this program. At times, odd oscillations or sudden, sharp spikes can be observed where normally smoother flowing curves are expected to take place. To verify these results, the  $\Delta V$  plot in Figure 6.8 was produced using the universal variables method. When the  $\Delta V$  curves are below 20 km/s, the plot is practically identical to the one produced by Battin's method (see Figure 6.4). When the total  $\Delta V$  in Figure 6.8 climbs over 20 km/s, the universal variables method reverts to a retrograde orbit, which resulted in the shortest distance between the initial and final positions. In the areas where the results are similar to Battin's method, the same unusual oscillations and sudden spikes also appear. Each plot required approximately 30 minutes of run time using Battin's method compared to the nearly 2 hours for the universal variables method.

The results given in Table 6.5 show launch dates that are scattered over the five year span. This is not completely unexpected as the launch dates shown only correspond to the minimum total  $\Delta V$  possible in the time frame. Figures 6.4-6.7 show that there do exist other potential launch dates with similar or slightly higher requirements that can still be reached with the given launch vehicles. Although not shown, almost all of the

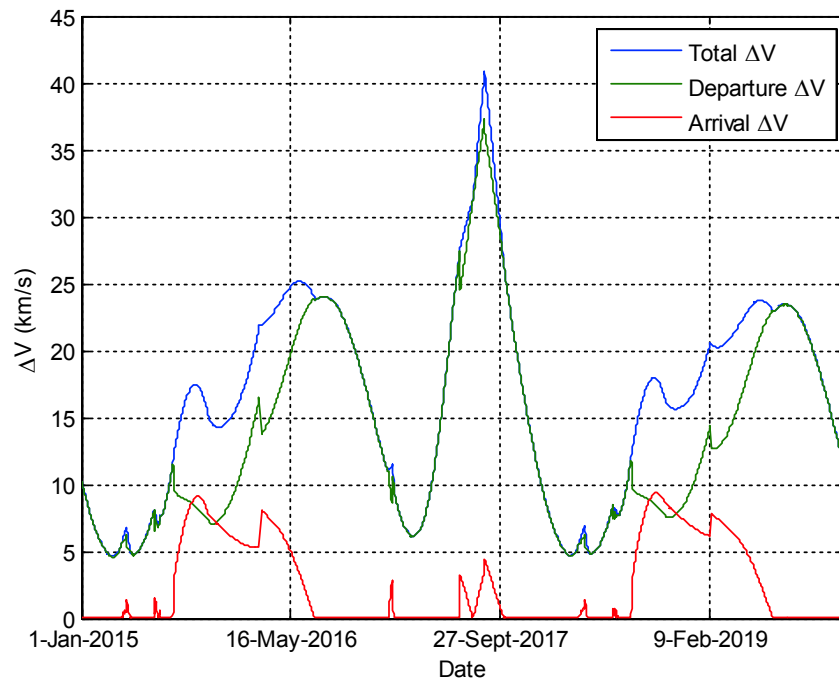


Figure 6.5: Minimum  $\Delta V$  required versus launch date for 2006 SJ198.

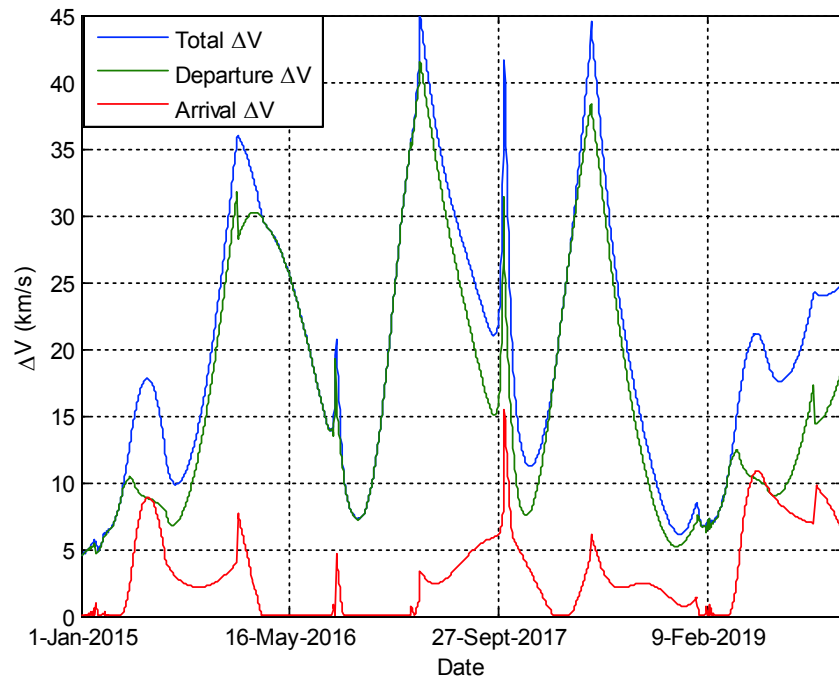


Figure 6.6: Minimum  $\Delta V$  required versus launch date for 2003 QC.

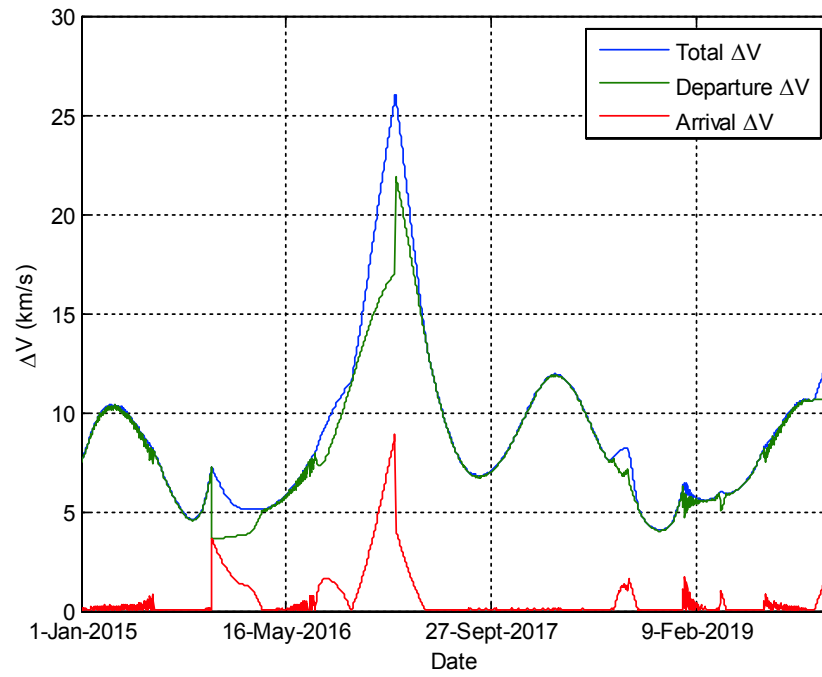


Figure 6.7: Minimum  $\Delta V$  required versus launch date for 1989 ML.

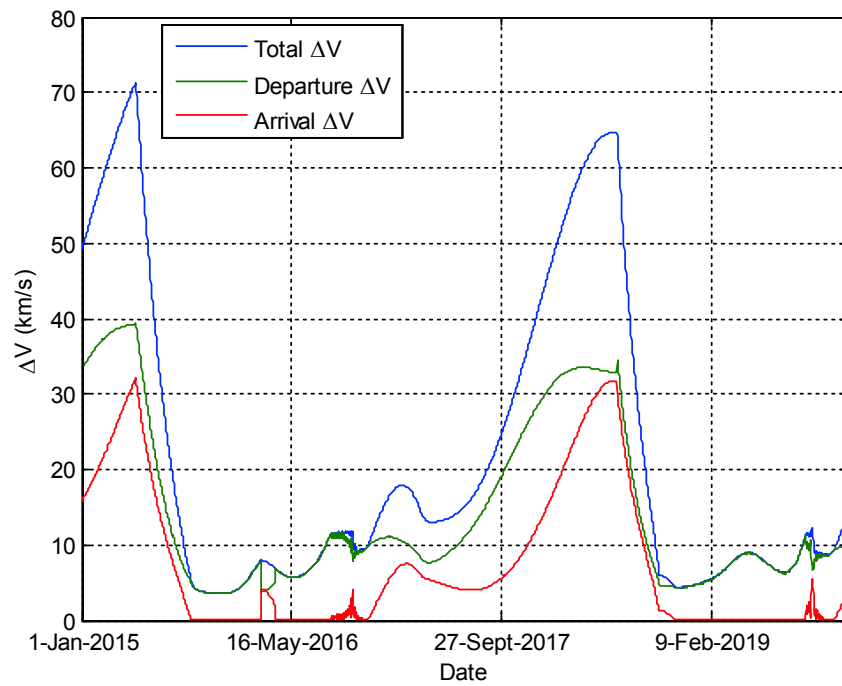


Figure 6.8: Minimum  $\Delta V$  plot for 2003 GA using the universal variables method.

Table 6.7: Early launch windows.

Asteroid	Launch Date	$\Delta V$ (km/s)	Transfer Time (days)	C3 (km <sup>2</sup> /s <sup>2</sup> )
2003 GA	12/3/2015	3.519	111	6.5
2006 SJ198	3/17/2015	4.596	337	32.01
2009 TB3	9/22/2017	3.689	202	10.37
2007 FS35	2/4/2015	3.473	272	5.47
2003 QC	1/1/2015	4.479	331	29.14
2004 GY	6/30/2015	4.354	365	26.1
2001 SX269	12/27/2015	4.952	252	40.97
1998 SB15	5/5/2017	3.335	159	2.37
2004 KE1	2/8/2017	4.539	365	30.62
1989 ML	9/29/2015	4.58	106	31.63

Table 6.8: Late launch windows.

Asteroid	Launch Date	$\Delta V$ (km/s)	Transfer Time (days)	C3 (km <sup>2</sup> /s <sup>2</sup> )
2003 GA	9/28/2018	4.333	173	25.57
2006 SJ198	3/16/2018	4.686	340	34.26
2009 TB3	1/28/2018	3.601	97	8.35
2007 FS35	10/3/2019	3.962	289	16.72
2003 QC	12/6/2018	5.293	365	49.78
2004 GY	5/23/2018	4.398	285	27.17
2001 SX269	3/5/2019	3.572	114	7.7
1998 SB15	6/22/2017	3.335	104	2.38
2004 KE1	10/29/2019	4.862	113	38.67
1989 ML	11/17/2018	4.027	120	18.26

Table 6.9: Categorization of target asteroids based on launch vehicle capabilities and target size.

<b>Launch Vehicle</b>	<b>Asteroid</b>	<b>Minimum <math>\Delta V</math> (km/s)</b>	<b>Diameter (m)</b>
<i>Early Launch Window</i>			
Delta II	1998 SB15	3.335	330
Atlas V	2007 FS35	3.473	620
	2003 GA	3.519	300
	2009 TB3	4.689	300
	1998 SB15	3.335	330
Delta IV Heavy	2006 SJ198	4.596	1200
	2007 FS35	3.473	620
	2004 GY	4.354	480
	1989 ML	4.58	630
<i>Late Launch Window</i>			
Delta II	1998 SB15	3.335	330
Atlas V	2009 TB3	3.601	300
	2007 FS35	3.962	620
	1989 ML	4.027	630
	2006 SJ198	4.686	1200
Delta IV Heavy	2007 FS35	3.962	620
	2004 GY	4.398	480
	1989 ML	4.027	630

target asteroids have at least two launch opportunities with acceptable  $\Delta V$  requirements. Table 6.7 shows the optimal launch dates for the first half of the time span. Even when the launch dates are clustered closer to one another like this, all the targets still have  $\Delta V$  requirements below 5 km/s. The majority of them actually retain the same launch date as presented previously in Table 6.5. These similar launch dates provide several convenient backup targets should a primary launch date be missed.

Should a later launch date be desired, there are viable options available for each target. As seen in Table 6.8, the total required  $\Delta V$  for the other targets is generally below 5 km/s with the exception of 2003 QC. The minimum  $\Delta V$  requirement to reach this asteroid jumps to about 5.3 km/s, and cannot be reached using any of the assumed launch configurations. For this date, the transfer time is as the maximum 365 day limit. In this particular case, extending the mission length may be beneficial and reduce the required  $\Delta V$  below 5 km/s as with the other targets.

The recommended targets for each launch vehicle configuration for both the earlier and later launch windows is given in Table 6.9. Up until this point, only the total  $\Delta V$  requirement was examined to match launch vehicles with potential targets. Now the different diameters are matched with corresponding NED sizes. There is some overlap between the categorization for asteroids with diameters that could be suited for different size NEDs meaning that either configuration could be used with the target. Should the albedo of these asteroids be known with greater certainty, a more accurate diameter can be calculated, which could then reduce the amount of overlap. It should be noted that this does not have to be strictly followed. If desired, it is entirely possible to use the larger size NEDs on targets with smaller diameters than paired with in the table or vice versa.

### 6.2.3 Target Mission Examples

In this section, preliminary mission trajectories to the targets 1998 SB15, 2006 SJ198 and 1989 ML will be studied based on the results found in the previous section. Each mission design will be assigned to differ-

Table 6.10: Orbital parameters of transfer trajectories and burn magnitudes.

Asteroid	Semi-Major Axis (AU)	Eccentricity	Inclination (deg)	Departure $\Delta V$ (km/s)	Arrival $\Delta V$ (m/s)
1998 SB15	1.1	0.271	2.10	3.34	1.3
2006 SJ198	1.4	0.294	5.76	4.60	12.2
1989 ML	1.36	0.271	3.76	4.03	8.8

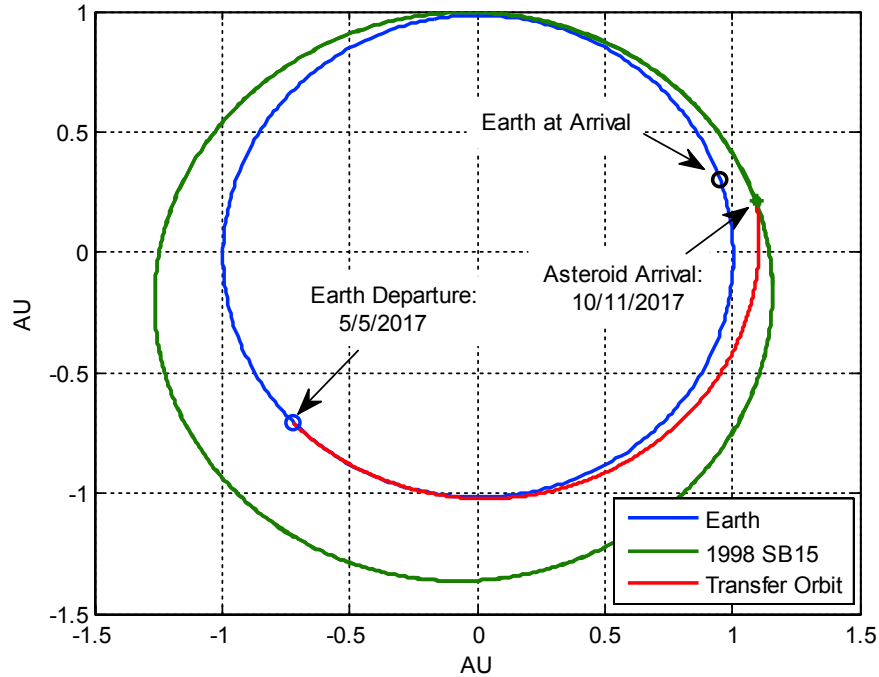


Figure 6.9: Mission trajectory to 1998 SB15 for the 5/5/2017 launch date.

ent launch configurations based on the recommendations in Table 6.9. The characteristics of each transfer trajectory is given in Table 6.10. Only direct transfer trajectories will be considered in these examples.

From Table 6.10, the departure  $\Delta V$  in every case makes up the majority of the total  $\Delta V$  required for each mission. This is due to the fact that upon arrival, the spacecraft is already traveling at approximately 10 km/s relative to the target asteroid. The largest arrival  $\Delta V$  here occurs for the 2006 SJ198 mission, but is only 12 m/s. This means that the relative velocity upon arrival is already approximately the nominal closing velocity of 10 km/s and can be disregarded.

### Delta II Mission.

The target 1998 SB15 is the only asteroid that the Delta II launch vehicle configuration can reach. This asteroid is one of the smallest selected in this study, and will most likely not require the larger size NEDs to disrupt. Its small size will also be used to test the limits of the terminal phase guidance technology. The launch date for the minimum  $\Delta V$  takes place on 5/5/2017 with a mission length of 159 days.

As can be seen in Figure 6.9, the orbit of 1998 SB15 is contained entirely within the orbits of the Earth and Mars. Unlike many asteroids whose orbits go beyond that of Mars, missions to this target do not have to wait until the close approach date as it can be reached at any point on its orbit. The trajectory depicted in

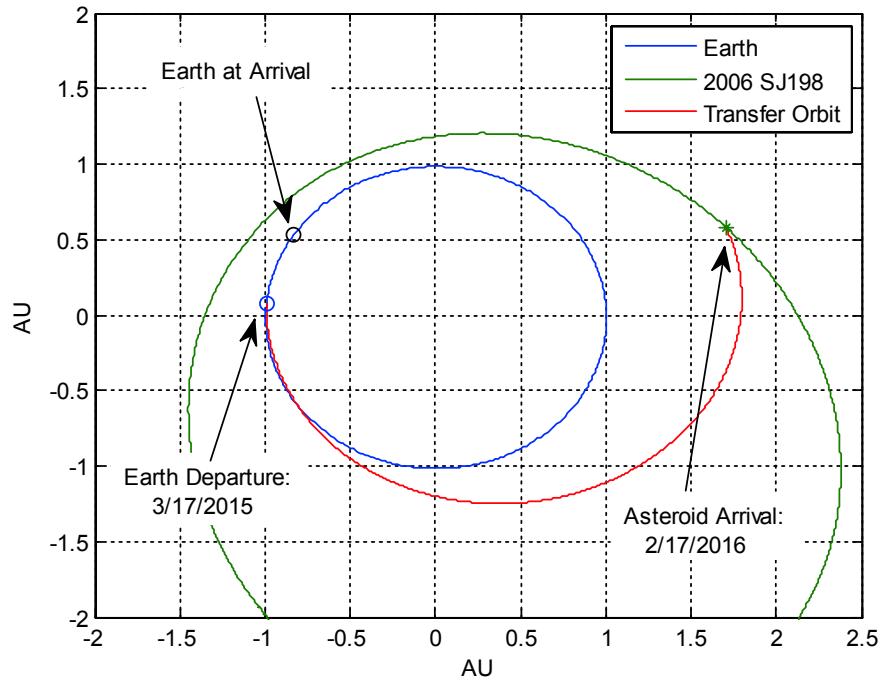


Figure 6.10: Mission trajectory to 2006 SJ198 for the 3/17/2015 launch date.

Figure 6.9 results in an impact approach angle of 19.82 degrees and a Sun-S/C-Earth angle of 44 degrees.

### Delta IV Heavy Mission

It may be desirable to explore the effects on objects larger than 2003 GA. There is also the concern of having an NED orbiting so near to the Earth should the spacecraft fail to impact. As the largest asteroid in this study, 2006 SJ198 was paired with the Delta IV Heavy launch configuration as it could carry the largest size NED. Being 4x as large as 2003 GA, the chances of failing to impact are greatly reduced. The minimum  $\Delta V$  launch date for this target takes place on 3/17/2015 with a mission length of 337 days.

The designed trajectory for this mission initially follows closely to that of the Earth, and extends out beyond Mars. Towards the arrival date, the spacecraft approaches almost from behind the target asteroid. Upon arriving at the target asteroid, the trajectory in Figure 6.10 results in an impact approach angle of 23.78 degrees and a Sun-S/C-Earth angle of 17.7 degrees.

### Atlas V Mission

The final mission design is for 1989 ML. This asteroid is also one of the largest selected in this study, and falls within the estimated capabilities of the Atlas V configuration. As with 2006 SJ198, it is significantly larger than 2003 GA, and decreases the chance of impact failure due to targeting errors. Of all the selected targets in this study, this is the only one that was also seriously considered by the ESA for the Don Quijote mission. It is also the asteroid with the most number of observations in determining its orbital elements (322 as of 1/16/2012), making its orbit the best known out of the ten targets. The impact approach and Sun-S/C-Earth angles for this mission design are 22.7 and 34.31 degrees respectively.



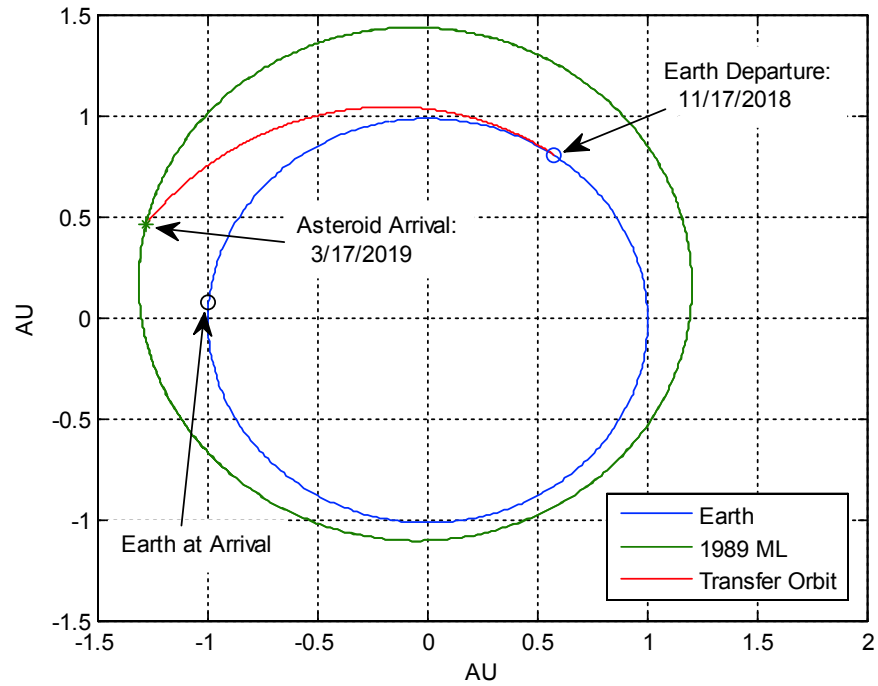


Figure 6.11: Mission trajectory to 1989 ML for the 11/17/2018 launch date.

Table 6.11: Computer Information for the Workstations Used to Run Programs.

	Fortran 90 Code	MATLAB Codes
Model	Dell T3500	Dell Precision T1600
Operating System	Windows Vista Enterprise 64 bit	Windows 7 Enterprise 64 bit
Processor	Intel(R) Xeon(R) W3520 2.67 GHz - 4 cores	Intel(R) Xeon(R) CPU E31270 @ 3.40 GHz - 4 cores
Memory	6.00 GB 1066 MHz DDR3	8.00 GB

Table 6.12: List of mission requirements.

Asteroid Types	Amor, Atira
Earliest Launch Date	1-Jan-15
Mission Completed by	1-Jan-40
Max. Earth Entry Velocity (km/s)	12
Minimum Impact Vel (km/s)	5

## 6.3 Advanced Mission Design

In this section additional advanced mission designs will be considered. For the mission analysis it is assumed that a sample return mission is required along side an impact demonstration mission. Due to the large of variables in these advanced types of missions, an exhaustive search of the Amor and interior Earth asteroids would be impractical. All mission design computations were performed using a genetic algorithm, one type of evolutionary algorithm. The types of missions considered in this section have been formulated as constrained optimization problems, which makes them ideal for evolutionary algorithms. Each mission type will first be formulated as a single-valued cost function. Several types of missions have been considered and are detailed in the following section. Detail of the development of the genetic algorithm can be found in [8].

Each mission type took approximately 3 days to run on a standard workstation. For the genetic algorithm the following parameters were used: tournament selection, double point crossover, and inversion mutation operators. The reproduction, crossover, and mutation probabilities for each mission type are 0.1, 0.9, and 0.05 respectively. The following results reflect only the mission design for each asteroid. Specific asteroid parameters such as asteroid diameter, rotational period, and brightness should be taken into account after determining all of the feasible trajectories.

### 6.3.1 Problem Formulation

All missions evaluated in this section have two basic requirements. Firstly, main spacecraft must return a sample of the asteroid to the Earth and second a hypervelocity impactor must impact the asteroid at no less than 5 km/s. A list of other mission requirement is shown in Table 6.12.

Three types of missions have been considered in this section. The first mission type, referred to as type 1 missions, consists of two separate launches, one launch is for the main spacecraft, while the other is for the impactor. Type 1 missions are the simplest type of mission to formulate, with the main spacecraft having only two mission legs, Earth departure through asteroid arrival and asteroid departure up to Earth atmospheric entry. Alternatively, the impactor has only one mission phase, Earth departure up to asteroid impact. The two other mission types require only a single launch. For the second mission type the main spacecraft has the same two phases as before, while the hypervelocity impactor performs a deep-space maneuver prior to impact. In the case of the third mission type, referred to as type 3 missions, the impactor has also have a gravity assist at Venus prior to impact. With the addition of a gravity assist the impactor is able to gain velocity during the Venus flyby, resulting in higher impact velocities and significantly lower mission costs. Table 6.13 illustrates the various elements which impact the cost function for each mission type.

The purpose of this section is to develop all the necessary pieces of the cost functions for each of the three mission types. The cost functions typically consists of all of the required mission  $\Delta V$ s, the Earth departure  $V_\infty$ , and any other required mission constraints. Depending on the mission type there are typically several possible mission  $\Delta V$ s. The main spacecraft's atmospheric entry velocity is limited to a maximum of 12 km/s, sometimes resulting in an additional  $\Delta V$  that slows the spacecraft prior to reentry. The hypervelocity impactor leg(s) also contribute to the cost function through deep-space targeting maneuvers and powered gravity assist(s). If the impactor has an arrival  $v_\infty$  of less than 5 km/s a penalty (an additional  $\Delta V$ )

Table 6.13: Break down of mission critical elements for the 3 mission types.

	Type 1 Mission		Type 2 Mission		Type 3 Mission	
	Main S/C	Impactor	Main S/C	Impactor	Main S/C	Impactor
Launch	X	X	X		X	
DSM (km/s)				X		X
Venus Powered GA						X
Asteroid Arrival $\Delta V$ (km/s)	X	X	X	X	X	X
Asteroid Departure $\Delta V$ (km/s)	X		X		X	
Earth Arrival $\Delta V$ (km/s)	X		X		X	

is added to ensure the impact velocity mission requirement is met. These penalties typically shape solutions in such a way that the impactor often arrives at a minimum velocity of 5 km/s, thus removing the need for an arrival  $\Delta V$ .

Each mission leg is calculated using solutions to Kepler’s equation and Lambert’s problem. In missions types 2 and 3 the main spacecraft and hypervelocity impactor are launched together, with the impactor performs a deep-space maneuver prior to the main spacecraft asteroid arrival. The  $\Delta V$  required by this deep-space maneuver is found in the following manner. After a Lambert solution for the main s/c has been found a burn index  $\epsilon$ , which ranges from 0 to 1, is used to define when the impactor will separate and perform the deep-space maneuver. To determine the magnitude of the deep-space maneuver, the orbit is propagate out, via a solution to Kepler’s problem, by a time  $\epsilon T_0$ , where  $T_0$  is the time of flight for the Earth departure to asteroid arrival leg of the main spacecraft. A solution to Lambert’s problem is then used to target the next phase of the impactor mission. In type 2 missions, this is the asteroid impact, while in type 3 missions the next target is the gravity assist at Venus. The magnitude of the  $\Delta V$  is simply the magnitude of the velocity differences from the Kepler and Lambert solutions. In the following section a model for the powered gravity assist, sometimes referred to as the MGA model, is discussed.

### Multiple Gravity-Assist Model

For the multiple gravity-assist model, two Lambert solutions are essentially “patched” together using the standard patched conic method. This results in a powered hyperbolic orbit for each gravity assist in which a  $\Delta V$  is allowed only at the perigee passage about the targeted planet. The  $\Delta V$  at each gravity assist is part of the final cost function. However, the  $\Delta V$  required for the gravity is usually driven to a near zero value.

For each gravity assist, the incoming and outgoing velocity vectors (in the heliocentric frame) are given from Lambert solutions. The velocities relative to the planets are then found as

$$\vec{v}_{\infty-in} = \vec{V}_{s/c-in} - \vec{V}_{\oplus} \quad (1)$$

$$\vec{v}_{\infty-out} = \vec{V}_{s/c-out} - \vec{V}_{\oplus} \quad (2)$$

From this point the goal is to determine a method to find the perigee radius that is required to patch the two solutions together. The first step is to determine the semi-major axis of the incoming and outgoing hyperbolic trajectories, as follows:

$$a_{in} = -\frac{\mu_{\oplus}}{v_{\infty-in}^2} \quad (3)$$

$$a_{out} = -\frac{\mu_{\oplus}}{v_{\infty-out}^2} \quad (4)$$

where  $\mu_{\oplus}$  is the target planet’s gravitational parameter.

The required turning angle is

$$\delta = \cos^{-1} \left( \frac{\vec{v}_{\infty-in} \cdot \vec{v}_{\infty-out}}{v_{\infty-in} \cdot v_{\infty-out}} \right) \quad (5)$$

The flyby perigee radius is equal for both legs of the hyperbolic orbit. That is, we have

$$r_p = a_{in}(1 - e_{in}) = a_{out}(1 - e_{out}) \quad (6)$$

where  $e_{in}$  and  $e_{out}$  are the incoming and outgoing orbit eccentricities. It should be noted that the orbits will be hyperbolic, so both eccentricities will be greater than 1. The turning angle  $\delta$  can also be represented as the sum of the transfer angles for the incoming and outgoing orbits.

$$\delta = \sin^{-1} \left( \frac{1}{e_{in}} \right) + \sin^{-1} \left( \frac{1}{e_{out}} \right) \quad (7)$$

Equation 6 can be then rewritten for  $e_{in}$  as

$$e_{in} = \frac{a_{out}}{a_{in}} (e_{out} - 1) + 1 \quad (8)$$

Substituting Eq. (8) into Eq. (7) gives

$$\delta = \sin^{-1} \left( \frac{1}{\frac{a_{out}}{a_{in}} (e_{out} - 1) + 1} \right) + \sin^{-1} \left( \frac{1}{e_{out}} \right) \quad (9)$$

which can be rewritten as

$$f = \left( \frac{a_{out}}{a_{in}} (e_{out} - 1) \right) \sin \left( \delta - \sin^{-1} \left( \frac{1}{e_{out}} \right) \right) - 1 = 0 \quad (10)$$

The above equation, which is now only a function of  $e_{out}$ , can be iterated upon to solve for  $e_{out}$ . A simple Newton iteration scheme works well. For this the derivative of  $f$  with respect to  $e_{out}$  must first be found.

$$\frac{df}{de_{out}} = \left( \frac{a_{out}}{a_{in}} e_{out} - \frac{a_{out}}{a_{in}} + 1 \right) \frac{\cos \left( \delta - \sin^{-1} \frac{1}{e_{out}} \right)}{e_{out}^2 \sqrt{1 - \frac{1}{e_{out}^2}}} + \frac{a_{out}}{a_{in}} \sin \left( \delta - \sin^{-1} \frac{1}{e_{out}} \right) \quad (11)$$

To start the Newton iteration an initial value for  $e_{out}$  of 1.5 works well. In a typical Newton iteration scheme a do while loop is used until  $e_{out}$  stops changing within a certain tolerance. The iteration number inside the loop should also be monitored, so the loop can be exited if convergence doesn't occur after a set number of iterations. Each new  $e_{out}$  is calculated as

$$e_{new} = e_{old} - \frac{f}{\frac{df}{de_{out}}} \quad (12)$$

When a converged  $e_{out}$  is found, the perigee radius is calculated from Eq. (6). Finally, the  $\Delta V$  that must be applied to the perigee is obtained as

$$\Delta V_{GA} = \left| \sqrt{v_{\infty-in}^2 + \frac{2\mu_{\oplus}}{r_p}} - \sqrt{v_{\infty-out}^2 + \frac{2\mu_{\oplus}}{r_p}} \right| \quad (13)$$

The flyby perigee radius and  $\Delta V$  are found directly from the spacecraft's incoming and outgoing velocities. These are found from solutions to Lambert's problem, which are a function of planetary positions and time of flight. The planetary positions are also a function of time, meaning that the decision variables for the MGA model are the time of Earth departure, time of each gravity assist, and final arrival time.

Thus, the final cost function  $C$  for the MGA portion of the problem becomes

$$C = f(\mathbf{X}) + g(\mathbf{X}) \quad (14)$$

where

$$\mathbf{X} = [T_1, T_2]^T \quad (15)$$

and  $T_i$  is the time of flight for each leg of the mission, and  $T_2$  is time of flight for the final mission leg. The penalty function,  $g(\mathbf{X})$ , will be discussed later. As shown above each element of the cost function,  $\Delta V$ s, etc., is only a function of time. This MGA cost function can then be optimized by the genetic algorithm to find optimal or near optimal solutions.

### 6.3.2 Problem Constraints

In optimization problems, constraints are often used to help shape the final solution. When implementing genetic algorithms, constraints are used, rather than hard limits, in order to keep to solution space open. If the solution space isn't sufficiently large the genetic algorithm will be unable to start, due to the random initialization process.

Common constraints for mission design problems include, perigee radius during a gravity assist, mission time/leg length constraints, and guarding against low velocity flybys. During a low-velocity flyby the spacecraft is captured by the planet, rather than gaining velocity in the heliocentric frame. Any other constraint the user wishes impose to help shape the solution can be added, as long as the constraint values are approximately the same order of magnitude at the actual cost function values. It should be noted that when using the MGA-DSM model in conjunction with a genetic algorithm all of the variables can be explicitly constrained. However, low-velocity flybys can still occur.

Often time, the MGA model results in a perigee radius that passes through the planet or too close to the planets atmosphere. In this situation a constraint-handling method is necessary to move the solution toward more feasible solutions. From Englander et al. [9], we have

$$g_i(\mathbf{X}) = -2 \log \frac{R_{pi}}{kR_{\oplus}} \quad (16)$$

where  $k$  is a multiplier used to define how close the spacecraft is allowed to flyby a target planet. For all of the examples in this section a value of 1.1 was used. The only exception was when reproducing the Galileo mission, which had an Earth close approach altitude of 300 km for the second gravity assist ( $k$  value of approximately 1.047).

The second constraint penalty method penalizes low velocity flybys. The method has also been adapted from Englander et al. [9]. Low velocity flybys are very rare, but solutions should still be protected from converging on them. The orbital energy, about the flyby planet, can be calculated as.

$$E = \frac{|\vec{v}_{\infty-in}|^2}{2} - \frac{\mu_{\oplus}}{R_{soi}} \quad (17)$$

For the flyby orbit to be hyperbolic about the planet,  $E$  must be greater than zero. However, the sphere of influence model is an approximation, so an additional 10% margin on the incoming velocity needs to be added. A simple penalty that is scaled inversely to the flyby arrival velocity scales well with. For relatively large  $v_{\infty}$  the penalty is zero or very small compared to the overall cost function value. Alternatively for very low  $v_{\infty}$  values the penalty is large enough to severely influence the final shape of the solution. The flyby orbital energy, adjusted for the 10% margin, and final constraint are calculated using the following two equations:

$$E = \frac{|0.9\vec{v}_{\infty-in}|^2}{2} - \frac{\mu_{\oplus}}{R_{soi}} \quad (18)$$

$$g_i(\mathbf{X}) = \begin{cases} 0 & E \geq 0 \\ \frac{1}{|\vec{v}_{\infty-in}|} & E < 0 \end{cases} \quad (19)$$

Time constraints are also very important for this problem because the hypervelocity impactor must impact the asteroid after the main spacecraft arrives and prior to asteroid departure. The time penalty constraints are calculated as follows.

$$g_i(\mathbf{X}) = \begin{cases} 0.1(T_{S/C-arr} - T_{impact}) & T_{impact} < T_{S/C-arr} \\ 0 & T_{S/C-arr} \leq T_{impact} \leq T_{S/C-dep} \\ 0.1(T_{impact} - T_{S/C-dep}) & T_{impact} > T_{S/C-dep} \end{cases} \quad (20)$$

With this constraint the spacecraft is penalized if the impactor arrives at the asteroid prior to the main spacecraft or if the impactor arrives after the main spacecraft has left the asteroid. This ensures that only solutions are found where the main spacecraft will be able to observe the impact and collect a sample of the impacted area/debris.

$$g(\mathbf{X}) = \sum g_i(\mathbf{X}) \quad (21)$$

With the cost function for each method finalized then next step is to develop the genetic algorithm, which will be capable of optimizing these types of advance mission design problems.

### 6.3.3 Type 1 Mission Results

For type 1 mission, a total of 6 variables are required to completely define the mission. The main spacecraft variables are launch date, time-of-flight or the Earth departure and Earth return legs and asteroid stay time. An additional 2 variables are required to define the mission for the hypervelocity impactor, the launch date and the time-of-flight for the Earth departure to asteroid impact leg.

The results from the genetic algorithm for type 1 missions are shown in Table 6.14. This table shows the 10 asteroids with the lowest cost functions. The cost functions range from 6.1 to 7.3 km/s. When compared to mission types 2 and 3 these missions have very high cost. Not just from a total  $\Delta V$  perspective, but from actual missions cost, due to the dual launch vehicle requirement. Type 1 missions serve as a baseline to compare the single launch missions (type 2 and 3). They have relatively high cost functions when compared to other mission types.

### 6.3.4 Type 2 Mission Results

A total of 6 variables are required to fully define type 2 missions. The main spacecraft requires 4 variables, departure date, Earth departure leg length, asteroid stay time, and Earth departure leg length (the same definitions as type 1 mission). Two variables are required for the hypervelocity impactor portion of the mission. The deep-space maneuver burn index and the time-of-flight from the maneuver up to the asteroid impact. The launch date ranges and mission length ranges are formulated in such a way that no portion of the mission will be at the asteroid after Jan 1st, 2040, which is the last entry for the asteroid ephemeris data.

Examination of the results in Table 6.15. While the actual required cost function values are lower than top type 1 missions, the  $\Delta V$  required for the main spacecraft and hypervelocity impactor are much higher. The solutions appear to be minimized by minimizing the departure  $v_\infty$  more than the  $\Delta V$  required after Earth departure. For type 2 missions the minimum  $\Delta V$  required by the two spacecraft is approximately 5 km/s, making these trajectories far from ideal. The hypervelocity impact speeds tend to be driven towards the minimum required 5 km/s. Relaxing the impact velocity requirements and emphasizing the Earth departure portion of the cost function may result in more feasible solutions. However solutions requiring total  $\Delta V$ 's in the 1-2 km/s range are found for the type 3 missions. It is unlikely that modifying the type 2 mission requirements will lower the required  $\Delta V$  by the 3-4 km/s required to match the type 3 mission solutions.

Table 6.14: Top 10 Asteroids for Type 1 missions.

	2012 LA	2011 MD	2003 YT70	2006 UN	2006 UB17	2007 TT24	2010 SZ3	2006 HX30	2004 KG17	1993 BD
	<b>Main Spacecraft Earth Departure</b>									
Launch Date	13-Aug-29	11-Jul-23	6-May-17	24-Dec-28	9-Nov-22	16-Nov-23	16-Oct-18	24-May-21	23-Jun-25	31-Mar-17
$v_{\infty-0}$ (km/s)	0.346	0.446	0.586	1.160	1.201	2.239	0.712	1.988	1.949	0.696
	<b>Main Spacecraft Asteroid Parameters</b>									
Time-of-Flight (days)	287.544	349.851	235.394	336.266	288.706	407.405	328.469	412.298	418.133	310.735
$\Delta V_{arr}$ (km/s)	1.647	1.083	4.791	3.898	1.404	2.177	2.127	2.755	2.822	4.845
Asteroid Stay Time (days)	262.195	26.340	219.218	212.079	95.536	345.935	52.151	172.531	151.699	209.244
$\Delta V_{dep}$ (km/s)	1.056	1.091	0.364	0.392	2.497	0.297	2.589	0.406	0.555	0.941
	<b>Main Spacecraft Earth Arrival Parameters</b>									
Time-of-Flight (days)	270.868	337.199	495.872	484.404	311.785	299.230	326.520	484.404	500.000	500.000
$\Delta V_{arr}$ (km/s)	0.000	0.000	0.191	0.118	0.000	0.000	0.000	0.010	0.034	0.217
	<b>Impactor Parameters</b>									
Launch Date	13-Mar-30	22-Jan-24	24-May-17	9-Feb-29	14-Feb-23	7-Mar-24	26-Dec-18	2-Aug-21	26-Sep-25	3-Jul-17
$v_{\infty-0}$ (km/s)	0.545	2.537	0.543	1.130	0.632	2.321	1.646	1.978	1.823	0.619
Time-of-Flight (days)	254.653	181.544	234.932	326.881	276.952	383.465	309.319	391.479	375.660	247.797
Arrival $v_{\infty}$ (km/s)	2.483	3.771	5.487	6.261	3.911	10.415	4.952	7.917	9.353	6.680
	<b>Summary</b>									
Main S/C $\Delta V$ (km/s)	2.703	2.174	5.346	4.409	3.901	2.474	4.717	3.171	3.411	6.002
Impactor $\Delta V$ (km/s)	2.517	1.229	0.000	0.000	1.089	0.000	0.048	0.000	0.000	0.000
Total Cost (km/s)	6.110	6.385	6.475	6.700	6.823	7.033	7.122	7.137	7.182	7.317

Table 6.15: Top 10 asteroids for type 2 missions.

	2008 NX	2011 MD	2004 KG17	2003 YT70	2005 GN22	2011 TP6	2010 VA140	2012 LA	2005 EZ169	2006 UN
<b>Main Spacecraft Earth Departure</b>										
Launch Date $v_{\infty-0}$ (km/s)	23-Aug-16 0.900	3-Jul-22 0.839	12-Jul-27 0.801	24-Apr-17 0.503	30-May-17 0.974	13-Feb-17 1.012	21-Dec-26 1.058	30-Aug-29 0.379	15-May-19 1.005	27-Jan-31 0.609
<b>Main Spacecraft Asteroid Parameters</b>										
Time-of-Flight (days)	336.711	328.001	352.525	254.502	352.385	290.622	340.419	267.968	333.859	291.046
$\Delta V_{arr}$ (km/s)	2.694	1.667	3.981	4.967	2.672	3.048	4.075	1.662	3.020	4.574
Asteroid Stay Time (days)	637.817	74.249	96.147	240.185	649.887	668.888	230.674	56.900	647.692	258.490
$\Delta V_{dep}$ (km/s)	0.720	0.353	0.537	0.358	0.320	0.697	0.339	0.905	0.751	0.728
<b>Main Spacecraft Earth Arrival Parameters</b>										
Time-of-Flight (days)	427.813	313.187	608.725	467.818	406.509	375.624	459.223	297.578	418.189	453.671
$\Delta V_{arr}$ (km/s)	0.000	0.000	0.207	0.192	0.000	0.000	0.143	0.000	0.000	0.183
<b>Impactor Parameters</b>										
Burn Index $\epsilon$	0.131	0.295	0.162	0.763	0.213	0.039	0.157	0.822	0.051	0.154
$\Delta V_{DSM}$ (km/s)	1.547	2.481	0.589	0.067	1.397	1.487	0.650	0.000	1.551	0.297
Time-of-Flight (days)	335.005	301.069	315.755	61.037	317.927	317.657	305.529	47.715	346.957	256.262
Arrival $v_{\infty}$ (km/s)	4.995	4.299	5.004	4.926	4.192	5.007	5.002	1.662	4.997	4.999
<b>Summary</b>										
Main S/C $\Delta V$ (km/s)	3.414	2.020	4.724	5.516	2.991	3.745	4.557	2.567	3.771	5.486
Impactor $\Delta V$ (km/s)	1.552	3.182	0.589	0.141	2.205	1.487	0.650	3.338	1.555	0.298
Total Cost (km/s)	5.866	6.041	6.115	6.161	6.170	6.244	6.265	6.284	6.331	6.392



### 6.3.5 Type 3 Mission Results

The last mission type included takes advantage of a gravity assist at Venus. The gravity-assist is used to increase the velocity of the hypervelocity impactor, resulting in higher impact speeds and lower total cost functions. By increasing the impact velocities the rest of the mission constraint is relaxed, allowing the genetic algorithm to find solutions requiring total spacecraft  $\Delta V$ 's much lower than both type 1 and 2 mission. Impact velocities range from 10.9 to 24.7 km/s for top 10 missions. This mission type requires 7 decision variables, which are the same as the type 2 with an additional time-of-flight added from the gravity-assist to impact.

As the results show from Table 6.16 show, the total cost function and required  $\Delta V$  for both the main spacecraft and the hypervelocity impactor are significantly improved over type 1 and 2 missions. The lowest cost functions range from 3.1 to 5.8 km/s. Assuming the launch vehicle and provide the necessary Earth departure  $v_\infty$  the combined total  $\Delta V$  required for the main spacecraft and hypervelocity impactor range from 1.2 to 4.23 km/s. Most of the top ten missions, by required  $\Delta V$  are type 3 mission (8 out of 10).

### 6.3.6 Advanced Mission Design Summary

Several possible mission architectures have been examined throughout this section. Multiple mission candidates have also been determined through the implementation of a genetic algorithm and searching program. The top ten missions are summarized in Table 6.17, sorted by the total combined  $\Delta V$  for the main spacecraft and hypervelocity impactor. It is assumed the launch vehicle(s) will provide the necessary  $C_3$ . By utilizing a gravity-assist at Venus mission requiring  $\Delta V$ 's as low as 1.2 km/s have been found.

## 6.4 Future Work

Future work will expand this selection process beyond the current five year time frame. Realistically, the current time frame would not provide sufficient time to develop and launch an HNIS. The ultimate goal will be to both streamline and automate the target selection process into a single integrated computer program capable of generating a target list for any NEO mission with associated physical and mission characteristics based on user-provided criteria and constraints. With the way the process is currently setup, many of the steps in the selection process are separate and require someone interpret the results before moving onto the next step. For example, once the asteroid candidates are first run through the Fortran 90 code, the outputs must be manually copied and input into the code containing the cost function. User options would include, but are not limited to, target bodies to investigate, launch vehicle, maximum mission duration, time frame, and target arrival constraints. For now the program will continue to be used to select optimal Amor class asteroids for a PDT demo mission, but could be applied to other missions as well.

Additional study of the results shown in Figures 6.4-6.7 will also be conducted. As was mentioned before, there are several locations where the  $\Delta V$  curves begin to oscillate rapidly as in Figure 6.4 or suddenly spike as in Figure 6.6. Whether these are caused by a fault in the computational method, programming, or something else entirely is currently unknown. Therefore, a further investigation of Lambert's solvers to determine the source of these oscillations and spikes is of principal interest.

## 6.5 Conclusion

A list of ten potential targets for a PDT demonstration mission to take place sometime between the years 2015 and 2020 (2040 for the more advanced sample return missions) have been examined. The launch dates given all result in close to a relative closing speed of 10 km/s without requiring any large burn upon arrival. The list encompasses asteroids ranging from the smallest desired diameter (300 m) to the largest (1000 m).

For the three given launch configurations, only the Delta II is severely restricted in terms of  $\Delta V$  requirements to the various targets. Recommendations were also made to match the listed targets with these launch



Table 6.17: Top 10 asteroids sorted by required spacecraft  $\Delta V$ .

	Mission Type	Departure $C_3$ km <sup>2</sup> /s <sup>2</sup>	Main S/C $\Delta V$ km/s	Impactor $\Delta V$ km/s	Total Required $\Delta V$ km/s
<b>2005 ER95</b>	3	7.144	1.146	0.066	1.211
<b>2006 KL103</b>	3	17.681	1.252	0.041	1.293
<b>2005 OH3</b>	3	12.650	1.641	0.132	1.773
<b>2011 MD</b>	3	1.097	1.835	0.196	2.031
<b>2002 TC70</b>	3	13.280	2.154	0.015	2.169
<b>2005 GN22</b>	3	9.231	2.144	0.031	2.175
<b>2012 LA</b>	3	1.771	2.280	0.169	2.448
<b>2011 PN1</b>	3	10.165	1.988	0.477	2.466
<b>2007 TT24</b>	1	5.013, 5.385	2.474	0.000	2.474
<b>2006 HX30</b>	1	3.951, 3.914	3.171	0.000	3.171

configurations based on the estimated size of the asteroids and the  $\Delta V$  requirements. These results would only be valid for the given five year time span. The list of targets could be altered if a mission was to take place after Jan. 1, 2020. Additional study would be required if such a mission date after 2020 is desired or if the sun phase angle requirement was to be strictly enforced.

## 6.6 References

- [1] I. Carnelli, A. Gálvez, D. Izzo, “Don Quijote: A NEO Deflection Precursor Mission,” 2006 NASA Near-Earth Object Detection and Threat Mitigation Workshop, Vail, CO, June 26-29, 2006.
- [2] J. Cano, M. Sánchez, S. Cornara, I. Carnelli, “Mission Analysis for the Don Quijote Phase-A Study,” *58<sup>th</sup> International Astronautical Congress 2007*, September 2007, pp. 24 - 28.
- [3] I. Carnelli and A. Gálvez, “ESA’s Don Quijote Mission: an Opportunity for the Investigation of an Artificial Impact Crater on an Asteroid,” Paper ISTS 2006-k-26, *25th International Symposium on Space Technology and Science*, Kanazawa, Japan, 2006.
- [4] B. Wie, “Hypervelocity Nuclear Interceptors for Asteroid Deflection or Disruption,” *Proceedings of 2<sup>nd</sup> IAA Planetary Defense Conference*, Bucharest, Romania, May 9-12, 2011.
- [5] B. Kaplinger and B. Wie, “NEO Fragmentation and Dispersion Modeling and Simulation,” *Proceedings of 2<sup>nd</sup> IAA Planetary Defense Conference*, Bucharest, Romania, May 9-12, 2011.
- [6] B. Kaplinger, and B. Wie, “Comparison of Fragmentation/Dispersion Models for Asteroid Nuclear Disruption Mission Design,” AAS 11-403, *AAS/AIAA Astrodynamics Specialist Conference*, Girdwood, AK, August 1-4, 2011.
- [7] S. Wagner and B. Wie, “Target Asteroid Selection for Human Exploration of Near Earth Objects,” AAS 10-249, *20<sup>th</sup> AAS/AIAA Space Flight Mechanics Meeting*, San Diego, CA, February 14-17, 2010.
- [8] S. Wagner, B. Kaplinger, and B. Wie, “GPU Accelerated Genetic Algorithm for Multiple Gravity-Assist and Impulsive  $\Delta V$  Maneuvers,” *AAS/AIAA Astrodynamics Specialist Conference*, Minneapolis, MN, August, 2012.
- [9] J. Englander, B. Conway, and T. Williams, “Optimal Autonomous Mission Planning Via Evolutionary Algorithms,” AAS 11-159, *21st AAS/AIAA Space Flight Mechanics Meeting*, Feb., 2011.

## Chapter 7

# Fuel-Efficient Proximity Operations Around an Irregular-Shaped Asteroid

### 7.1 Introduction

Proximity operations in the vicinity of near-Earth objects (NEOs) utilizing unmanned, robotic probes represent an emerging area of research. Scientific interest in these objects mainly focuses on what they can tell us about the evolution and diversity of our solar system. Such missions are also invaluable in the area of asteroid deflection as a probe could be sent to further investigate a potentially hazardous object. Once there, the spacecraft would fly close to the body to learn more about its physical makeup and orbit, which would help determine the most efficient deflection method.

In order to evaluate the overall performance of the guidance and control system designed for the asteroid's proximity operations, a high-fidelity dynamic model to simulate the dynamical environment must be established, where relevant perturbation forces such as a non-uniform gravitational field are taken into account. Such forces have been shown to be capable of destabilizing uncontrolled orbits, and cause the spacecraft to impact or escape the asteroid [1]. One proposed solution for closed-loop control used by the JAXA Hayabusa mission to the asteroid Itokawa was to hover above the target body [2,3]. The propellant requirements for this method, though, could lead to shorter mission durations, which would limit the scientific return.

In an effort to avoid the requirements of station-keeping, there has been much research devoted to open-loop solutions of orbits about asteroids and comets and their stability bounds [1, 4-11]. While it is possible to find orbits that remain stable for great lengths of time, Figure 7.1 shows how three different orbits with similar initial conditions about the asteroid 433 Eros can produce radically different results. The first orbit begins at a radius of 32.9 km along the inertial X-axis with a velocity equal to that of the local circular. After numerically simulating the orbit for over a week, it remains in a quasi-stable orbit around the body. The second orbit has a radius of 32.8 km also at the local circular velocity, but is shifted  $45^\circ$  from the X-axis. Here the orbit remains about the body for over a week before finally escaping. The third orbit begins at a radius of 27.85 km along the inertial Y-axis with the local circular velocity. The orbit first travels far away from the body twice before impacting. Given the sensitivity of the dynamic environment at asteroids and comets to initial conditions, it is not practical to rely entirely upon open-loop solutions to keep a spacecraft in orbit about such a body.

Several types of proximity operations will be considered: an optimal orbital transfer from a high-altitude orbit to a low-altitude orbit, fuel-efficient low-altitude orbit maintenance, and a soft landing on the asteroid surface. The orbital transfer and soft landing is accomplished using a ZEM/ZEV algorithm [12], while the low-altitude orbit maintenance utilizes simple feedback control logic augmented by disturbance-accommodating filtering [13].

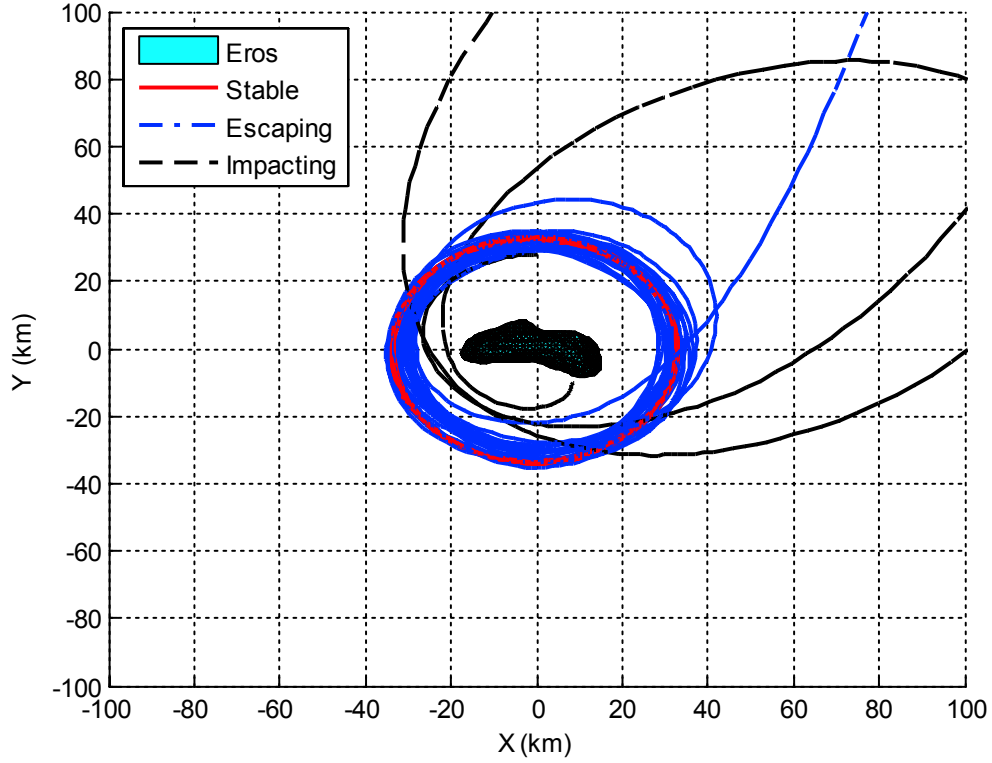


Figure 7.1: Comparisons of stable, escaping, and impacting orbits around 433 Eros. The coordinate system is an inertial frame fixed at Eros' center of mass with the positive Z-axis along the north pole spin axis. Eros is shown at initial conditions.

## 7.2 Problem Description

### 7.2.1 Coordinate Systems and Dynamic Equations

Two coordinate frames are primarily used in this study, the asteroid's body-fixed frame ( $x, y, z$ ), and the inertial frame ( $X, Y, Z$ ). Typically the body-fixed frame is used from landing, and the inertial frame is used for orbiting and orbital transfers. Both the body-fixed frame and the inertial frame have their origin at the center of mass of the asteroid. For the body-fixed frame, the  $x, y$ , and  $z$  axes align along the axes of minimum, intermediate, and maximum inertia respectively. The inertial frame shares its  $Z$ -axis with the body-fixed frame. It is assumed that the asteroid spins at a constant rate  $\omega$  about the  $z$ -axis.

The absolute acceleration of the spacecraft is described by

$$\ddot{\vec{r}} = \ddot{\vec{r}}|_B + 2\vec{\omega} \times \dot{\vec{r}}|_B + \dot{\vec{\omega}} \times \vec{r} + \vec{\omega} \times (\vec{\omega} \times \vec{r}) = \vec{g} + \vec{u} \quad (1)$$

where  $\vec{r}$  is the spacecraft position vector,  $\vec{g}$  is the gravitational acceleration,  $\vec{u}$  is the control acceleration, and  $\vec{\omega}$  is the rotation vector of the body-fixed frame (i.e., the angular velocity vector of an asteroid). With the way the coordinate systems are set up, the rotation vector has only one constant component in the positive  $z$ -direction. The spacecraft position vector can then be transformed from the body-fixed frame ( $x, y, z$ ) to the inertial frame ( $X, Y, Z$ ) as follows:

$$\begin{bmatrix} X \\ Y \\ Z \end{bmatrix} = \begin{bmatrix} \cos(\omega t) & -\sin(\omega t) & 0 \\ \sin(\omega t) & \cos(\omega t) & 0 \\ 0 & 0 & 1 \end{bmatrix} \begin{bmatrix} x \\ y \\ z \end{bmatrix} \quad (2)$$

## 7.2.2 Polyhedron Gravitation

The polyhedron gravitational model was developed by Werner and Scheeres [14], and can be advantageous when the gravitating body has a complex, irregular shape. Although computationally slower than using a spherical harmonics expansion, the model is valid anywhere around the body, whereas spherical harmonics is only valid outside of a circumscribing sphere. Here we will show the relevant equations used to simulate the gravitational attraction of a polyhedron. Note that these equations assume a constant density, and that the shape model uses triangular facets. The potential function is given as

$$U = \frac{1}{2}G\sigma \sum_{e \in \text{edges}} L_e \mathbf{r}_e^T \mathbf{E}_e \mathbf{r}_e - \frac{1}{2}G\sigma \sum_{f \in \text{facets}} \omega_f \mathbf{r}_f^T \mathbf{F}_f \mathbf{r}_f \quad (3)$$

where  $G$  is the gravitational constant,  $\sigma$  is the density,  $\mathbf{r}$  is a vector from a point in space to an edge or facet on the polyhedron,  $\mathbf{E}_e$  is a  $3 \times 3$  edge matrix,  $L_e$  is a dimensionless per-edge factor,  $\mathbf{F}_f$  is a  $3 \times 3$  facet matrix, and  $\omega_f$  is a dimensionless per-facet factor.  $\mathbf{E}_e$  and  $\mathbf{F}_f$  are given by

$$\mathbf{E}_e = \hat{\mathbf{n}}_A(\hat{\mathbf{n}}_{21}^A)^T + \hat{\mathbf{n}}_B(\hat{\mathbf{n}}_{12}^B)^T \quad (4)$$

$$\mathbf{F}_f = \hat{\mathbf{n}}_f(\hat{\mathbf{n}}_f)^T \quad (5)$$

where  $\hat{\mathbf{n}}_f$ ,  $\hat{\mathbf{n}}_A$ , and  $\hat{\mathbf{n}}_B$  are outward facing unit normal column vectors and  $\hat{\mathbf{n}}_{12}^A$  and  $\hat{\mathbf{n}}_{21}^B$  are outward facing edge unit normal column vectors. A graphical illustration of these unit vectors is shown in Figure 7.2. For a coordinate system, whose origin lies within the polyhedron, the outward facing normal vector,  $\vec{n}_f$ , and edge-normal vector on facet  $f$ ,  $\vec{n}_{ij}^f$ , can be calculated using

$$\vec{n}_f = (\vec{r}_2 - \vec{r}_1) \times (\vec{r}_3 - \vec{r}_1) = \vec{r}_1 \times \vec{r}_2 + \vec{r}_2 \times \vec{r}_3 + \vec{r}_3 \times \vec{r}_1 \quad (6)$$

$$\vec{n}_{ij}^f = (\vec{r}_j - \vec{r}_i) \times \vec{n}_f \quad (7)$$

where  $\vec{r}_{1,2,3}$  are vectors from the origin to each of the three vertices that define the triangular facet, and  $\vec{n}_f$  is the facet normal vector. Next the dimensionless factors  $L_e$  and  $\omega_f$  are given as

$$L_e = \ln \frac{r_i + r_j + e_{ij}}{r_i + r_j - e_{ij}} \quad (8)$$

$$\omega_f = 2 \arctan \frac{\vec{r}_i \cdot \vec{r}_j \times \vec{r}_k}{r_i r_j r_k + r_i(\vec{r}_j \cdot \vec{r}_k) + r_j(\vec{r}_k \cdot \vec{r}_i) + r_k(\vec{r}_i \cdot \vec{r}_j)} \quad (9)$$

where  $\vec{r}_{i,j,k}$  are vectors from the field point to one of the three vertices on the triangular facet,  $r_{i,j,k}$  is the magnitude of the vector, and  $e_{ij}$  is the length of the edge connecting  $\vec{r}_i$  and  $\vec{r}_j$ . Note that per facet, there will be one value of  $\omega_f$  and three for  $L_e$  (one for each edge). The gravitational force is then the gradient of the potential in Eq. (3) expressed as

$$\nabla U = -G\sigma \sum_{e \in \text{edges}} L_e \mathbf{E}_e \mathbf{r}_e + G\sigma \sum_{f \in \text{facets}} \omega_f \mathbf{F}_f \mathbf{r}_f \quad (10)$$

The derivation also leads to a simple method for determining whether or not a field point is outside of the polyhedron by taking the Laplacian of the potential, as follows

$$\nabla^2 U = -G\sigma \sum_{f \in \text{facets}} \omega_f \quad (11)$$

The sum of  $\omega_f$  goes to zero when the field point is located outside of the polyhedron, and  $4\pi$  inside the polyhedron. This is particularly helpful in knowing during a simulation whether or not a spacecraft remained in orbit about a body, or crashed into the surface without requiring much additional computation as  $\omega_f$  is already found at every step.

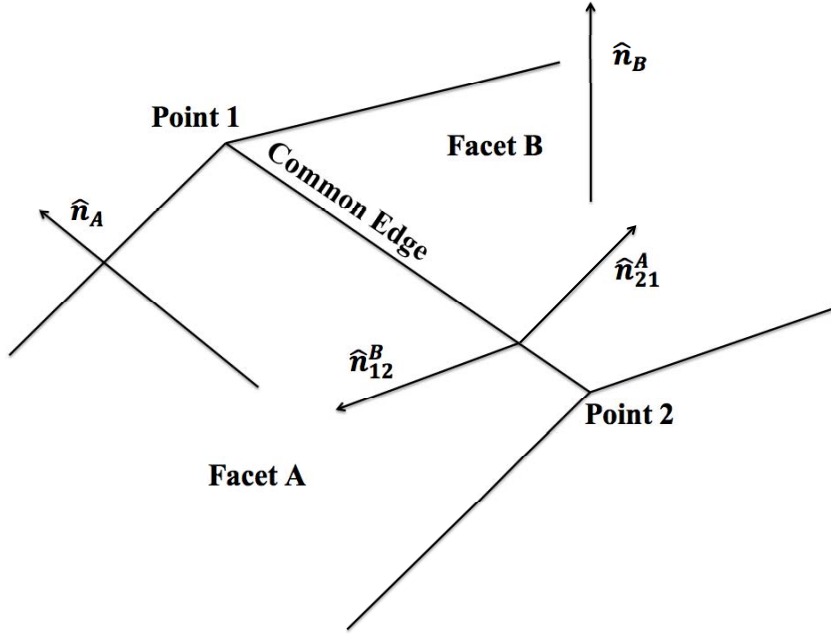


Figure 7.2: Illustration of the facet normal and edge-normal vectors.

### 7.2.3 Spherical Harmonics

A more classical approach to gravity modeling is to use spherical harmonics. Although reliable to model gravity for orbiting missions, the equations are only valid outside of a circumscribing sphere around the body. The potential function in spherical harmonics can be expressed as a double summation involving the associated Legendre polynomials,  $P_{n,m}$ , and the harmonic coefficients,  $C_{n,m}$  and  $S_{n,m}$ , as follows [25]:

$$U = \frac{\mu}{r} \sum_{n=0}^{\infty} \sum_{m=0}^n \left(\frac{R}{r}\right)^n P_{n,m}[\sin(\phi)] \{C_{n,m} \cos(m\lambda) + S_{n,m} \sin(m\lambda)\} \quad (12)$$

$$P_{n,m}[\sin(\phi)] = \frac{1}{2^n n!} (1 - \sin^2(\phi))^{m/2} \frac{d^{n+m}}{d \sin(\phi)^{n+m}} (\sin^2(\phi) - 1)^n \quad (13)$$

where  $\mu$  is the gravitational parameter,  $R$  is the reference radius of the circumscribing sphere,  $\phi$  is the latitude, and  $\lambda$  is the longitude. Figure 7.3 shows how  $\phi$  and  $\lambda$  relate to the body-fixed frame. It should be noted that all  $S_{n,0}$  equal zero, and  $C_{0,0}$  is one.

The gravitational acceleration, needed for simulation of asteroid proximity operations, can be obtained by computing the gradient of the gravitational potential

$$\vec{g} = \nabla U = \frac{\partial U}{\partial r} \hat{e}_r + \frac{1}{r} \frac{\partial U}{\partial \phi} \hat{e}_\phi + \frac{1}{r \cos(\phi)} \frac{\partial U}{\partial \lambda} \hat{e}_\lambda \quad (14)$$

where

$$\frac{\partial U}{\partial r} = -\frac{\mu}{r^2} \sum_{n=0}^{\infty} \sum_{m=0}^n \left(\frac{R}{r}\right)^n (n+1) P_{n,m}[\sin(\phi)] \{C_{n,m} \cos(m\lambda) + S_{n,m} \sin(m\lambda)\} \quad (15)$$

$$\begin{aligned} \frac{\partial U}{\partial \phi} = \frac{\mu}{r} \sum_{n=0}^{\infty} \sum_{m=0}^n \left(\frac{R}{r}\right)^n \{P_{n,m+1}[\sin(\phi)] - m \tan(\phi) P_{n,m}[\sin(\phi)]\} \{C_{n,m} \cos(m\lambda) \\ + S_{n,m} \sin(m\lambda)\} \end{aligned} \quad (16)$$

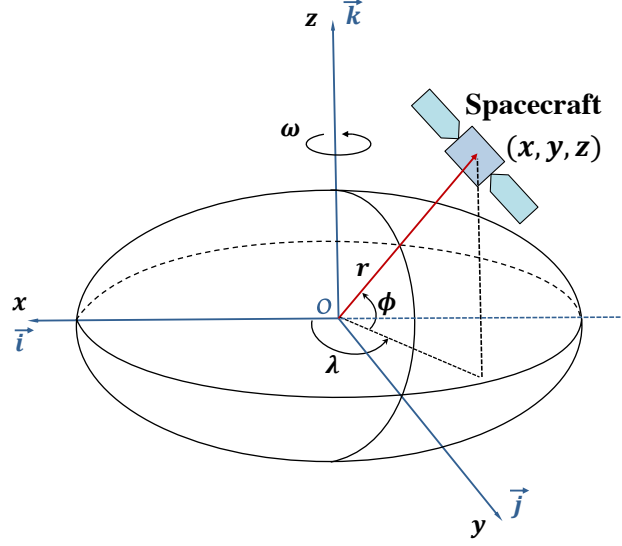


Figure 7.3: Illustration of the spherical coordinate system with respect to the body-fixed frame.

$$\frac{\partial U}{\partial \lambda} = \frac{\mu}{r} \sum_{n=0}^{\infty} \sum_{m=0}^n \left(\frac{R}{r}\right)^n m P_{n,m}[\sin(\phi)] \{S_{n,m} \cos(m\lambda) - C_{n,m} \sin m\lambda\} \quad (17)$$

The gravitational acceleration vector can then be converted from spherical coordinates to the body-fixed frame using the following transformation matrix

$$\mathbf{T} = \begin{bmatrix} \cos(\phi) \cos(\lambda) & -\sin(\phi) \cos(\lambda) & -\sin(\lambda) \\ \cos(\phi) \sin(\lambda) & -\sin(\phi) \sin(\lambda) & \cos(\lambda) \\ \sin(\phi) & \cos(\phi) & 0 \end{bmatrix} \quad (18)$$

The derivation above applies only in the case when the harmonic coefficients are not normalized. Oftentimes the coefficients will be given as normalized values on the account of the gravitational coefficients becoming very small as the degree and order get large. In some computers, this would introduce truncation errors so normalization becomes necessary to prevent inaccuracy. A common method of normalization is

$$\begin{aligned} \bar{\Pi}_{n,m} &= \sqrt{\frac{(n+m)!}{(n-m)!k(2n+1)}} \\ &k=1 \quad \text{if} \quad m=0 \\ &k=2 \quad \text{if} \quad m \neq 0 \end{aligned} \quad (19)$$

$$\bar{S}_{n,m} = \prod_{n,m} S_{n,m} \quad \bar{C}_{n,m} = \prod_{n,m} C_{n,m} \quad \bar{P}_{n,m} = \frac{P_{n,m}}{\prod_{n,m}} \quad (20)$$

It is important to remember to normalize the Legendre polynomials as well when using normalized coefficients because their product must remain the same (i.e.  $\bar{C}_{n,m} \bar{P}_{n,m} = C_{n,m} P_{n,m}$  and  $\bar{S}_{n,m} \bar{P}_{n,m} = S_{n,m} P_{n,m}$ )

## 7.3 Fuel-Efficient Orbit Control

### 7.3.1 PD Control

Proportional-derivative (PD) control is a common, simple feedback control logic. This type of control attempts to minimize the error between a measured variable and a reference value by feeding back the differ-



ence multiplied by some controller gain. To implement this control, we first express the equations of motion in state space form. As the gravitational terms are highly nonlinear, we include them as disturbances ( $\mathbf{w}$ ) and have a simple dynamical model as

$$\dot{\mathbf{x}} = \mathbf{A}\mathbf{x} + \mathbf{B}\mathbf{u} + \mathbf{w} \quad (21)$$

$$\mathbf{x} = \begin{bmatrix} X \\ Y \\ Z \\ \dot{X} \\ \dot{Y} \\ \dot{Z} \end{bmatrix}, \quad \mathbf{u} = \begin{bmatrix} u_x \\ u_y \\ u_z \end{bmatrix}, \quad \mathbf{A} = \begin{bmatrix} 0 & 0 & 0 & 1 & 0 & 0 \\ 0 & 0 & 0 & 0 & 1 & 0 \\ 0 & 0 & 0 & 0 & 0 & 1 \\ 0 & 0 & 0 & 0 & 0 & 0 \\ 0 & 0 & 0 & 0 & 0 & 0 \\ 0 & 0 & 0 & 0 & 0 & 0 \end{bmatrix}, \quad \mathbf{B} = \begin{bmatrix} 0 & 0 & 0 \\ 0 & 0 & 0 \\ 0 & 0 & 0 \\ 1 & 0 & 0 \\ 0 & 1 & 0 \\ 0 & 0 & 1 \end{bmatrix}$$

As was mentioned, PD control also requires a reference trajectory, described by

$$X_r(t) = A_x \cos(\omega_x t) \quad (22a)$$

$$Y_r(t) = A_y \sin(\omega_y t) \quad (22b)$$

$$Z_r(t) = A_z \sin(\omega_z t) \quad (22c)$$

$$\dot{X}_r(t) = -A_x \omega_x \sin(\omega_x t) \quad (22d)$$

$$\dot{Y}_r(t) = A_y \omega_y \cos(\omega_y t) \quad (22e)$$

$$\dot{Z}_r(t) = A_z \omega_z \cos(\omega_z t) \quad (22f)$$

where  $A_x$ ,  $A_y$ , and  $A_z$  are the amplitudes of the reference trajectory along the X, Y, and Z axes respectively.

For a system described by Eq. (21), with an arbitrary system matrix  $\mathbf{A}$ , the control can be expressed as

$$\mathbf{u} = -\mathbf{K}(\mathbf{x} - \mathbf{x}_r) \quad (23)$$

where  $\mathbf{K}$  is the control gain matrix to be determined, and  $\mathbf{x}_r$  is the reference state vector. One way of finding this gain matrix is using a linear quadratic regulator (LQR) method.<sup>16,17</sup> The LQR method works by selecting a  $\mathbf{K}$  that minimizes the following performance index

$$J = \frac{1}{2} \int_0^\infty (\mathbf{x}^T \mathbf{Q} \mathbf{x} + \mathbf{u}^T \mathbf{R} \mathbf{u}) dt \quad (24)$$

where  $\mathbf{Q}$  and  $\mathbf{R}$  are user-chosen weighting matrices. Once selected, the control gain matrix  $\mathbf{K}$  is obtained as

$$\mathbf{K} = \mathbf{R}^{-1} \mathbf{B}^T \mathbf{X} \quad (25)$$

where  $\mathbf{X}$  is the symmetric positive semidefinite solution of the algebraic Riccati equation (ARE)

$$\mathbf{A}^T \mathbf{X} + \mathbf{X} \mathbf{A} - \mathbf{X} \mathbf{B} \mathbf{R}^{-1} \mathbf{B}^T \mathbf{X} + \mathbf{Q} = 0 \quad (26)$$

For a unique solution of  $\mathbf{X}$  to exist, four conditions must be met:

1.  $\mathbf{Q}$  must be symmetric and positive semidefinite;
2.  $\mathbf{R}$  must be symmetric and positive definite;
3. the pair  $(\mathbf{A}, \mathbf{B})$  must be controllable (stabilizable);
4. the pair  $(\mathbf{A}, \sqrt{\mathbf{Q}}^T \sqrt{\mathbf{Q}})$  must be observable (detectable).

### 7.3.2 Disturbance-Accommodating Control

Disturbance-rejection or disturbance-accommodation control is a technique which can be used to reduce the control effort in the presence of persistent disturbances [16, 17]. It works by eliminating parts of the control acceleration, and allows the spacecraft to follow a trajectory that is closer to a natural periodic solution of the nonlinear equations of motion. As we are forcing the spacecraft to follow a particular reference orbit, the nonlinear gravitational effects can cause constant or periodic disturbances, which require a higher control magnitude to cancel out. Since these disturbances cannot be accurately modeled beforehand, we use an iterative method for designing a disturbance-accommodating controller. This method allows the spacecraft to deviate from the reference trajectory and follow one that requires less  $\Delta V$ .

When first orbiting the gravitating body with only PD control, there exist certain frequency components in the free orbit, that need to be consistently damped out via the control acceleration. These components can be found by examining an FFT (Fast Fourier Transform) plot of the control commands along each axis. Once the spectral components have been identified, we can design periodic disturbance-accommodation filters of the form

$$\ddot{\alpha}_i + \omega_{xi}^2 \alpha_i = u_x \quad (27a)$$

$$\ddot{\beta}_i + \omega_{yi}^2 \beta_i = u_y \quad (27b)$$

$$\ddot{\gamma}_i + \omega_{zi}^2 \gamma_i = u_z \quad (27c)$$

where  $\omega_{xi}$ ,  $\omega_{yi}$ , and  $\omega_{zi}$  represent the  $i$ th frequency component in each axis. For constant disturbances, the filters take the form of

$$\dot{\tau}_x = u_x \quad (28a)$$

$$\dot{\tau}_y = u_y \quad (28b)$$

$$\dot{\tau}_z = u_z \quad (28c)$$

where  $\tau_x$ ,  $\tau_y$ , and  $\tau_z$  are the filter states necessary to remove any bias in the control acceleration.

The disturbance-accommodation filter can include as many frequencies as are present in the FFT plots. The filter can then be described in state space form

$$\dot{\mathbf{x}}_d = \mathbf{A}_d \mathbf{x}_d + \mathbf{B}_d \mathbf{u} \quad (29)$$

where  $\mathbf{x}_d$  is the disturbance filter state vector. It should be noted that if a frequency or bias component is not used during the iteration, the corresponding filter state is not included in  $\mathbf{x}_d$ . The disturbance filter in Eq. (29) can then be augmented to the system in Eq. (21) as follows:

$$\begin{bmatrix} \dot{\mathbf{x}} \\ \dot{\mathbf{x}}_d \end{bmatrix} = \begin{bmatrix} \mathbf{A} & 0 \\ 0 & \mathbf{A}_d \end{bmatrix} \begin{bmatrix} \mathbf{x} \\ \mathbf{x}_d \end{bmatrix} + \begin{bmatrix} \mathbf{B} \\ \mathbf{B}_d \end{bmatrix} \mathbf{u} \quad (30)$$

The LQR method can also be applied to the augmented system in Eq. (30) to determine a control gain matrix, and the control input is then described as.

$$\mathbf{u} = -\mathbf{K} \begin{bmatrix} \mathbf{x} - \mathbf{x}_r \\ \mathbf{x}_d \end{bmatrix} \quad (31)$$

In an iterative design, spectral components are identified and added to the disturbance filter state in Eq. (29) each time the control is updated. These iterations are necessary as suppressing frequency components in the control can result in different frequency components appearing in the control. Normally these frequency components are some integer combination of the body spin rate and the orbit frequency. After several iterations, a disturbance-accommodating controller can be designed that results in a drastic reduction of  $\Delta V$ .

## 7.4 ZEM/ZEV Feedback Guidance

### 7.4.1 Generalized ZEM/ZEV Feedback Guidance Algorithm

In general, the gravitational acceleration is a function of the position and velocity of the spacecraft, as well as the attitude of the target asteroid. This will not lead to a tractable solution of the optimal control problem. If instead the gravitational acceleration is assumed to be a function of time, optimal feedback algorithms can be found. For a mission from time  $t_0$  to  $t_f$ , the optimal control acceleration is determined by minimizing the classical performance index of the form

$$J = \frac{1}{2} \int_{t_0}^{t_f} \mathbf{a}^T \mathbf{a} \, dt \quad (32)$$

subject to Equation 1 and the following given boundary conditions:

$$\mathbf{r}(t_0) = \mathbf{r}_0; \quad \mathbf{r}(t_f) = \mathbf{r}_f \quad (33a)$$

$$\mathbf{v}(t_0) = \mathbf{v}_0; \quad \mathbf{v}(t_f) = \mathbf{v}_f \quad (33b)$$

The Hamiltonian function for this problem is

$$H = \frac{1}{2} \mathbf{a}^T \mathbf{a} + \mathbf{p}_r^T \mathbf{v} + \mathbf{p}_v^T (\mathbf{g}(t) + \mathbf{a}) \quad (34)$$

where  $\mathbf{p}_r$  and  $\mathbf{p}_v$  are the co-state vectors associated with the position and velocity vectors, respectively. The co-state equations say that the optimal control solution can be expressed as a linear combination of the terminal values of the co-state vectors. Defining the time-to-go,  $t_{go}$ , as

$$t_{go} = t_f - t \quad (35)$$

the optimal acceleration command at any time  $t$  is

$$\mathbf{a} = -t_{go} \mathbf{p}_r(t_f) - \mathbf{p}_v(t_f) \quad (36)$$

By substituting the above expression into the dynamic equations to solve for  $\mathbf{p}_r(t_f)$  and  $\mathbf{p}_v(t_f)$ , the optimal control solution with the specified  $\mathbf{r}_f$ ,  $\mathbf{v}_f$ , and  $t_{go}$  is finally obtained as

$$\mathbf{a} = \frac{6[\mathbf{r}_f - (\mathbf{r} + t_{go} \mathbf{v})]}{t_{go}^2} - \frac{2(\mathbf{v}_f - \mathbf{v})}{t_{go}} + \frac{6 \int_t^{t_f} (\tau - t) \mathbf{g}(\tau) \, d\tau}{t_{go}^2} - \frac{4 \int_t^{t_f} \mathbf{g}(\tau) \, d\tau}{t_{go}} \quad (37)$$

The zero-effort-miss (ZEM) distance and zero-effort-velocity (ZEV) error denote, respectively, the differences between the desired final position and velocity and the predicted final position and velocity if not additional control is commanded after the current time. For the assumed gravitational acceleration  $\mathbf{g}(t)$ , the ZEM and ZEV have the following expressions

$$\mathbf{ZEM} = \mathbf{r}_f - \left[ \mathbf{r} + t_{go} \mathbf{v} + \int_t^{t_{go}} (t_f - \tau) \mathbf{g}(\tau) \, d\tau \right] \quad (38)$$

$$\mathbf{ZEV} = \mathbf{v}_f - \left[ \mathbf{v} + \int_t^{t_f} \mathbf{g}(\tau) \, d\tau \right] \quad (39)$$

The optimal control law, Equation 37, can be expressed as

$$\mathbf{a} = \frac{6}{t_{go}^2} \mathbf{ZEM} - \frac{2}{t_{go}} \mathbf{ZEV} \quad (40)$$

For certain missions where the terminal velocity is not specified, the optimal control law, in terms of ZEM only, can be obtained as

$$\mathbf{a} = \frac{3}{t_{go}^2} \mathbf{ZEM} \quad (41)$$

The optimal control law to regulate only the terminal velocity, which will be used for orbital transfer, in terms of ZEV only, can also be obtained as

$$\mathbf{a} = \frac{1}{t_{go}} \mathbf{ZEV} \quad (42)$$

Since the gravitational acceleration cannot be simply modeled as a function of time, the ZEM and ZEV must be found by some means. Hawkins et al. [18] describes how the ZEM and ZEV can be found by numerically integrating the dynamic equations, or can be approximated with an error state transition matrix (STM). The ZEM and ZEV are updated in real-time, accomplishing the control mission at a near-optimal level while maintaining acceptable computational complexity.

For highly nonlinear systems, predicting the future states is prone to errors. Another alternative form of the ZEM/ZEV algorithm can be adopted for this situation. Rather than predicting the effect of the nonlinear terms, the effects of these terms are directly compensated for at all times. The algorithm thus approaches feedback linearization behavior. The control algorithm, Equation 37, then simply becomes the following form suggested by Battin [19]:

$$\mathbf{a} = \frac{6 [\mathbf{r}_f - (\mathbf{r} + t_{go} \mathbf{v})]}{t_{go}^2} - \frac{2 (\mathbf{v}_f - \mathbf{v})}{t_{go}} - \mathbf{g}(\mathbf{r}) \quad (43)$$

## 7.4.2 ZEM/ZEV Guidance for Orbital Transfer

There are two implementations of ZEM/ZEV guidance to achieve orbital transfer. For proximity operations near an asteroid, it is assumed that the angular position at orbit insertion is unimportant. The longitude of the spacecraft would be relevant for spacecraft in a resonant orbit, but for this paper resonant orbits are avoided. The first orbital transfer formulation uses polar coordinates, and does not specify the angular position at orbit insertion. The second formulation uses Cartesian coordinates, and although no particular angular position is needed, one must be chosen to for the guidance law to work. For the short mission time of the orbital transfer, the asteroid can be modeled as a point mass, and differences in the gravitational force due to the point-mass model become disturbances for the control system to overcome. The two guidance schemes are described next.

### ZEM/ZEV Guidance in Polar Coordinates

The objective of the orbital transfer problem here is to transfer a spacecraft from one circular orbit to another circular orbit. The terminal constraints are that the spacecraft should be placed at a specified distance from the asteroid with corresponding circular orbital velocity. The final radial velocity is zero, and the angular position is free. Due to the nature of the constraints, polar coordinates are used. The standard dynamical models for this type of orbit raising problem are described by

$$\dot{r} = u \quad (44a)$$

$$\dot{u} = \frac{v^2}{r} - \frac{\mu}{r^2} + a_r \quad (44b)$$

$$\dot{v} = -\frac{uv}{r} + a_t \quad (44c)$$

where  $r$ ,  $u$ , and  $v$  represent the distance of the spacecraft from the center of mass of the asteroid, the radial velocity, and the transverse velocity, respectively, and  $a_r$  and  $a_t$  are the control accelerations in the radial and

transverse directions, respectively. The gravitational parameter for the asteroid is given as  $\mu$ . Recalling the harmonic expansion model, we see that  $\mu = GM$ . The required terminal states, as described above, are

$$r(t_f) = r_f \quad u(t_f) = 0 \quad v(t_f) = \sqrt{\frac{\mu}{r_f}} \quad (45)$$

The orbit raising problem is somewhat unusual in that the control requirements are different along the radial and tangential axes. In the radial direction, there are position and velocity requirements as usual. In the tangential direction, we have the rare case where only the velocity is specified. For asteroid proximity operations, the gravitational environment is highly nonlinear, so the ZEM/ZEV algorithm with direct compensation of gravitational terms, Equation 43, can be used as:

$$a_r = \frac{6}{t_{go}^2} (r_f - (r + t_{go}u)) - \frac{2}{t_{go}} (u_f - u) - \left( \frac{v^2}{r} - \frac{\mu}{r^2} \right) \quad (46a)$$

$$a_t = \frac{1}{t_{go}} (v_f - v) - \left( -\frac{uv}{r} \right) \quad (46b)$$

It is seen that the law is a combination of the ZEM/ZEV law, Equation 40, in the radial direction, and the ZEV law, Equation 42, in the tangential direction. For the orbital transfer problem between circular orbits, recall also that  $u_f = 0$ .

### ZEM/ZEV Guidance in Cartesian Coordinates

Despite being posed in such a way as to ignore the final angular position, the compensating ZEM/ZEV law suffers from the nonlinear effects of the gravitational field. Guo et al. [20] shows this for a Mars orbital transfer example, and suggests ways to overcome this. The method suggested there is to use an offline optimal solution to generate a series of waypoints to track. This is less practical for the asteroid orbit problem, as the optimal trajectory depends on both the longitude of the spacecraft, and the total angle change commanded. For the asteroid orbital transfer mission, a second method of simply finding a point on the target orbit and using ZEM/ZEV guidance in Cartesian coordinates, is suggested.

For the ZEM/ZEV orbital transfer problem in Cartesian coordinates, consider the following spacecraft dynamic equations

$$\dot{X} = V_x \quad (47a)$$

$$\dot{Y} = V_y \quad (47b)$$

$$\dot{V}_x = G(X, Y, \psi) + A_x \approx -\mu \frac{X}{(X^2 + Y^2)^{\frac{3}{2}}} + A_x \quad (47c)$$

$$\dot{V}_y = G(X, Y, \psi) + A_y \approx -\mu \frac{Y}{(X^2 + Y^2)^{\frac{3}{2}}} + A_y \quad (47d)$$

where  $(X, Y)$  and  $(V_x, V_y)$  denote the position and velocity components in the inertial frame, and  $(A_x, A_y)$  are control accelerations along the  $(X, Y)$  axes. Although the true gravitational field is represented by the harmonic expansion signified by  $G(X, Y, \psi)$ , the nonlinearities are such that it is better to use the approximate values on the right hand side of Equation 47 for numerical propagation of the orbit.

The terminal conditions for the asteroid orbital transfer problem are as follows:

$$X(t_f) = X_c \quad Y(t_f) = Y_c \quad (48)$$

$$V_x(t_f) = V_{xc} \quad V_y(t_f) = V_{yc} \quad (49)$$

The equations of motion are strongly coupled, and an analytic optimal control algorithm does not exist. The ZEM/ZEV algorithm, Equation 40, can control the terminal position and velocity at a specified final

time. These encompass all of the requirements of the orbital transfer problem, making it a good candidate for solution with ZEM/ZEV guidance. Expressed in the  $X$ - and  $Y$ -coordinates, the proposed ZEM/ZEV law becomes

$$\begin{bmatrix} A_x \\ A_y \end{bmatrix} = \frac{6}{t_{go}^2} \begin{bmatrix} ZEM_x \\ ZEM_y \end{bmatrix} - \frac{2}{t_{go}} \begin{bmatrix} ZEV_x \\ ZEV_y \end{bmatrix} \quad (50)$$

where the ZEM and ZEV are obtained by subtracting the predicted terminal states (with no further control accelerations) from the required terminal states, as follows:

$$\begin{bmatrix} ZEM_x \\ ZEM_y \end{bmatrix} = \begin{bmatrix} X_c - \tilde{X}_f \\ Y_c - \tilde{Y}_f \end{bmatrix} \quad (51a)$$

$$\begin{bmatrix} ZEV_x \\ ZEV_y \end{bmatrix} = \begin{bmatrix} V_{xc} - \tilde{V}_{xf} \\ V_{yc} - \tilde{V}_{yf} \end{bmatrix} \quad (51b)$$

### 7.4.3 ZEM/ZEV Guidance for Soft Landing on an Irregular-Shaped Asteroid

For an asteroid rendezvous or soft landing mission, the terminal velocity is by definition zero. For any practical asteroid proximity operation, the actual gravitational acceleration of the target asteroid will not be exactly known a priori, and its magnitude is often small in comparison to other accelerations and disturbances. There are several options for dealing with nonlinearities and disturbances using ZEM/ZEV logic.

The simplest way to formulate a guidance law is to outright ignore the gravitational and apparent accelerations, treating them as disturbances for the ZEM/ZEV feedback law to overcome. The ZEM/ZEV law with zero gravitational acceleration is called ZEM/ZEV-z.

The next option is to directly compensate for the Coriolis and centripetal accelerations. This law makes use of the spin rate of the asteroid without getting into the details of the gravitational field. The ZEM/ZEV law that compensates for the Coriolis and centripetal accelerations is called ZEM/ZEV-a.

Even though it is not worth invoking the modeled gravitational field, as it will inevitably differ from the true field, it is still possible to account for gravity in the ZEM/ZEV law. The generalized gravitational acceleration is the acceleration due to a point mass. This generalized gravitational acceleration can be directly compensated for. The ZEM/ZEV law that also accounts for generalized gravity is called ZEM/ZEV-g.

Finally, the usual predictive ZEM/ZEV law can be used. As with ZEM/ZEV-g, it is not necessary to consider the gravitational model. The predicted final states are found by propagating the equations of motion with point-mass gravity. The predictive ZEM/ZEV law is called ZEM/ZEV-p.

We now have the four ZEM/ZEV laws as follows:

1. ZEM/ZEV-z:

$$\mathbf{a} = \frac{6}{t_{go}^2} (\mathbf{r}_f - \mathbf{r}) + \frac{4}{t_{go}} \mathbf{v} \quad (52)$$

2. ZEM/ZEV-a:

$$\mathbf{a} = \frac{6}{t_{go}^2} (\mathbf{r}_f - \mathbf{r}) + \frac{4}{t_{go}} \mathbf{v} + 2\boldsymbol{\omega} \times \mathbf{v} + \boldsymbol{\omega} \times (\boldsymbol{\omega} \times \mathbf{r}) \quad (53)$$

3. ZEM/ZEV-g:

$$\mathbf{a} = \frac{6}{t_{go}^2} (\mathbf{r}_f - \mathbf{r}) + \frac{4}{t_{go}} \mathbf{v} + \frac{GM}{|\mathbf{r}|^3} \mathbf{r} + 2\boldsymbol{\omega} \times \mathbf{v} + \boldsymbol{\omega} \times (\boldsymbol{\omega} \times \mathbf{r}) \quad (54)$$

4. ZEM/ZEV-p:

$$\mathbf{a} = \frac{6}{t_{go}^2} (\mathbf{r}_f - \tilde{\mathbf{r}}_f) + \frac{4}{t_{go}} (\mathbf{v} - \tilde{\mathbf{v}}_f) \quad (55)$$

## 7.5 Simulation Results

The gravity models described in Section 7.2 will now be applied to the special case of 433 Eros, one of the largest near-Earth asteroids. We say special case in that the assumption of constant density in the polyhedron gravity model derivation holds true due to the measured center of mass is very close to center of mass assuming an uniform internal structure [21]. Eros is also a prime example of an asteroid with a very irregular shape with the largest dimension being more than twice as long as the smallest dimension. The asteroid was visited by the NEAR Shoemaker mission, and a high-fidelity model also exists for the spherical harmonic expansion. Because the harmonic expansion is only valid outside of the smallest bounding sphere, the polyhedron model must be used for operations near the surface. NASA provides polyhedron shape models for various numbers of facets, ranging from 1708 to 20700 [22]. Eros' density is assumed to be  $2.67 \text{ g/cm}^3$  and rotation period 5.27 hours, giving an angular velocity of  $3.31 \times 10^{-4} \text{ rad/s}$ , and the reference radius for the spherical harmonics model is 16 km.

### 7.5.1 Low-Thrust Orbital Transfer

A low-thrust (non-impulsive) orbital transfer mission from a 100-km orbit to a 35-km orbit around asteroid Eros was simulated using both the polar and the Cartesian forms of the ZEM/ZEV algorithm. The spherical harmonic expansion gravitational model was used. The orbits are prograde in the  $XY$ -plane. In general, prograde planar orbits are the least stable [1], so guidance that works for such orbits will be able to work with any other inclination. Once the spacecraft reaches the 35-km orbit, further proximity operations can begin.

The orbital transfer mission starts with the spacecraft on the positive  $X$ -axis, and the asteroid at an attitude angle of zero. The mission time is 41,234 seconds, corresponding to one half of the period of a Hohmann transfer between the two circular orbits. The exact mission time is not critical, as the true optimal solution would depend on angular positions in addition to transfer time. For such a short mission phase, a range of transfer times gives reasonable performance. The polar coordinate ZEM/ZEV algorithm does not require a final anomaly angle. For the Cartesian ZEM/ZEV algorithm, angular change is chosen as  $135^\circ$ . The Cartesian version is limited to angular changes of less than  $180^\circ$ .

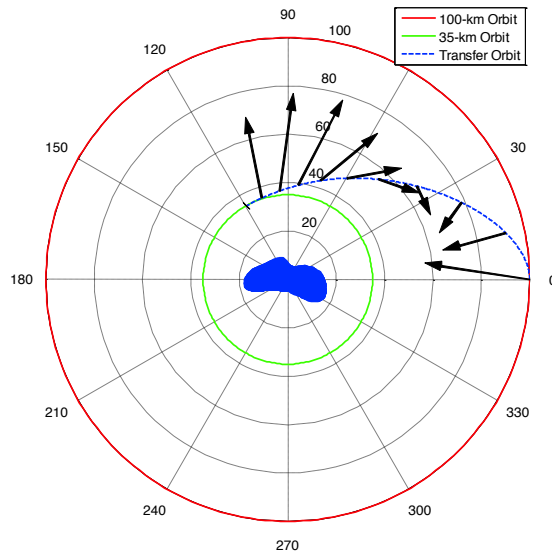
Figure 7.4 shows the transfer orbit trajectories for the two different algorithms. Also shown is the asteroid at its initial attitude. The normalized acceleration vector is shown every  $1/10^{th}$  of the total time. Both algorithms command mostly radial acceleration at the beginning. Later on the Cartesian algorithm is able to find smaller commands than the polar algorithm. Figure 7.5 shows these acceleration histories. Finally, Figure 7.6 shows the performance index histories. It is seen that the Cartesian algorithm has a lower performance index.

For a given mission time, the Cartesian algorithm is usually to be preferred. This is somewhat unexpected, as it imposes more constraints. Although not shown here, the polar algorithm is able to make transfers of greater than  $180^\circ$  and reduce the performance index. There is a practical limit to this, as for longer missions the polar algorithm will command the spacecraft to travel past the lower orbit, risking collision.

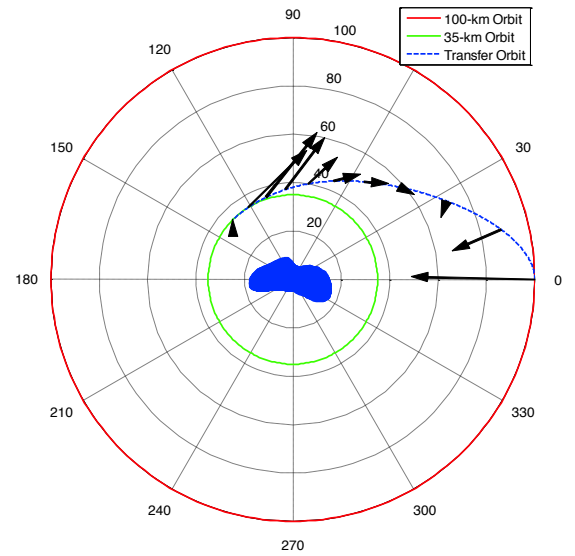
### 7.5.2 Fuel-Efficient Orbit Control

After the orbital transfer to a low 35-km altitude, two different reference circular orbits were utilized for fuel-efficient orbit maintenance: a prograde orbit in the  $XY$ -plane and a 45 deg inclined orbit. While it is unlikely that a realistic mission would follow an orbit so close to an asteroid, the irregularities in the gravity field are stronger and more noticeable the closer the spacecraft comes to the body. Being able to orbit closer to the asteroid is not without its advantages, though, as scientists can observe the object in greater detail.

We will first examine a prograde orbit in the  $XY$ -plane about the asteroid. The orbit begins at a radius of 35 km on the  $X$ -axis at the local circular velocity. The resulting orbit, control accelerations, and FFT plots are given in Figures 7.7 - 7.9. In Figure 7.8, a quick comparison between the polyhedron model and the harmonics model results show very little difference in the  $X$ - and  $Y$ -control and a slight bias difference in the  $Z$ -control. Integrating these control accelerations results in a  $\Delta V$  of 21.13 m/s per week with the polyhedron

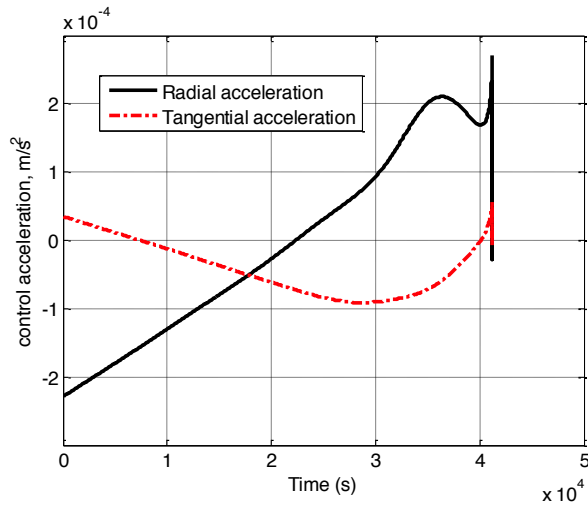


(a) Polar ZEM/ZEV

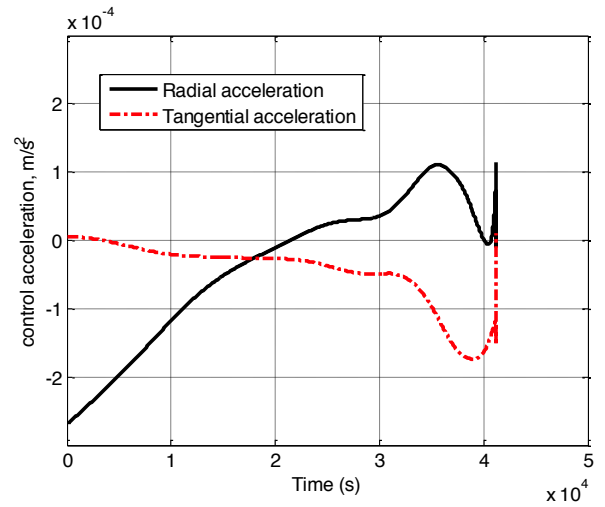


(b) Cartesian ZEM/ZEV

Figure 7.4: Transfer orbit trajectories.



(a) Polar ZEM/ZEV



(b) Cartesian ZEM/ZEV

Figure 7.5: Transfer orbit acceleration histories.



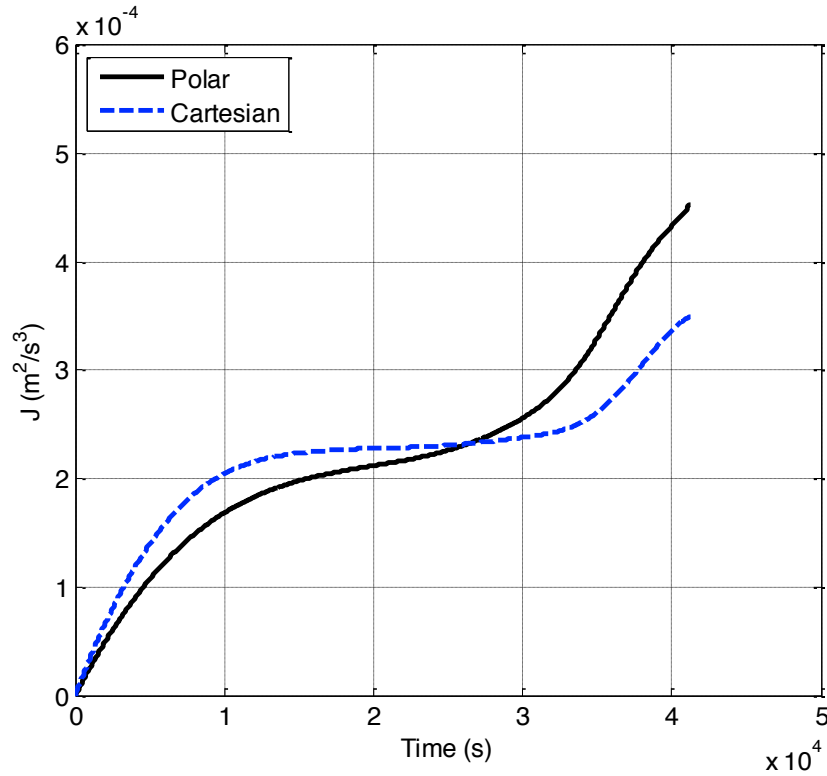


Figure 7.6: Performance index comparison.

model and 21.37 m/s with the harmonics model. Figure 7.9 contains the spectral components of the control accelerations. Both models show five noticeable peaks in the X- and Y-control and two in the Z. For the X and Y FFTs, the two highest peaks correspond to the orbit frequency and twice the asteroid rotation frequency minus three times the orbit frequency. Figures 7.10 and 7.11 show the results of adding filters of the form in Eq. (27) to each of the prominent frequency components after one iteration. After some initial transients, the control accelerations decrease to a fraction of their former magnitude, and the bias in both Z-controls was completely eliminated. Both models gave a new  $\Delta V$  requirement of slightly more than 1 m/s per week.

Next we will incline the orbit by 45 degrees to command an orbit that is not in any of the coordinate system planes. When left uncontrolled, an orbit of this type will naturally precess about the asteroid. Adding PD control will prevent this precession from happening at the expense of a  $\Delta V$  of 17.65 m/s per week for the polyhedron model and 17.59 m/s for the harmonics model. Figures 7.13-7.16 only show the results for the harmonic expansion gravity model, which were identical to those for the polyhedron model. In this case, the control accelerations along each axis exhibit the same frequency peaks in the FFT plots, though not necessarily with the same magnitude. Here the largest peak along each axis corresponds to twice the asteroid rotation frequency minus three times the orbit frequency, which is also the largest peak in the prograde case along the X- and Y- axis. Filtering these frequencies allows the spacecraft to be controlled, while also precessing as it would naturally about the asteroid as shown in Figure 7.12. After applying filters to all the frequencies present in Figure 7.14, the control accelerations go to nearly zero, and the  $\Delta V$  requirement is reduced to 0.5 m/s per week for both models.

### 7.5.3 Soft Landing on an Irregular-Shaped Asteroid

Landing site selection is one of the most important subjects for a practical asteroid landing missions. Factors such as surface conditions, communications, relative position of the Sun and the Earth, and science value

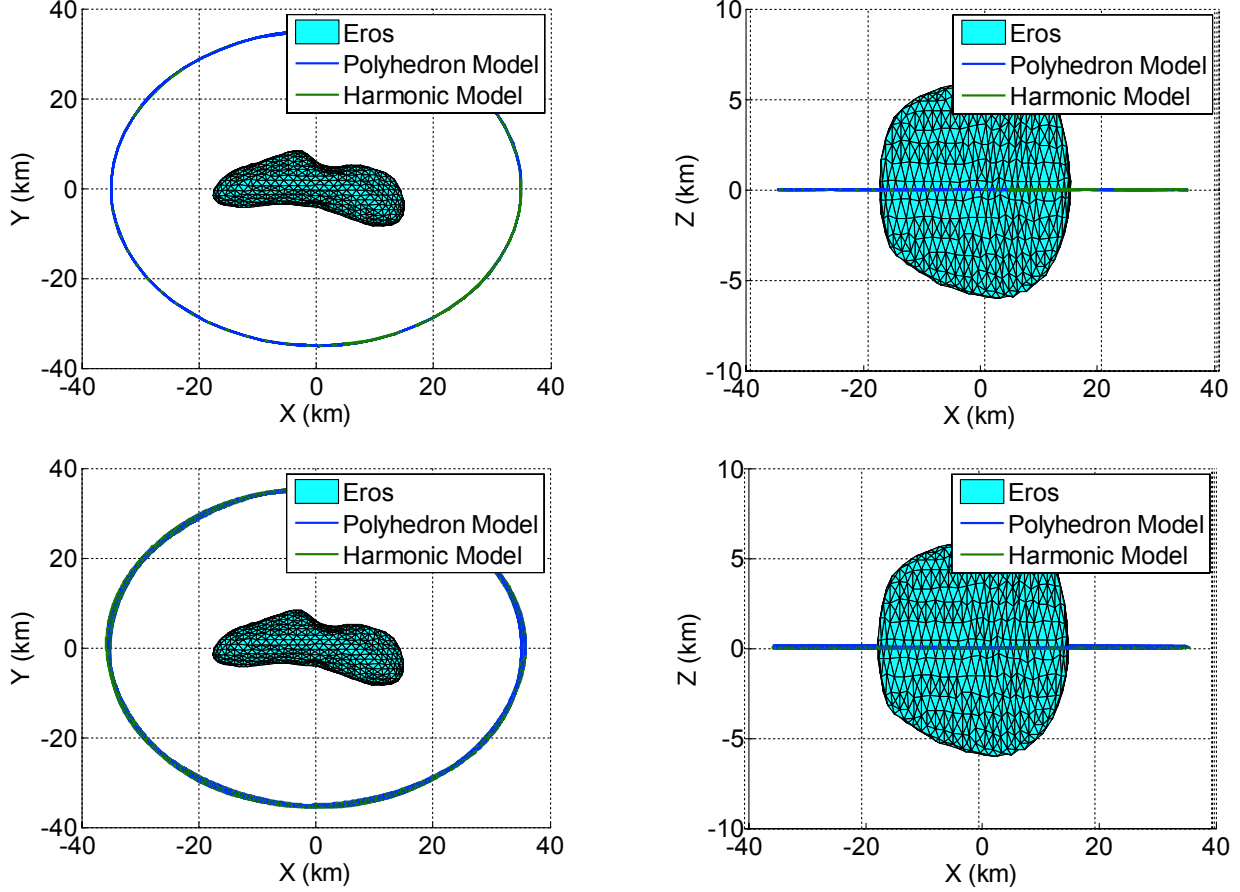


Figure 7.7: A 35-km prograde orbit in the XY-plane with PD control (top) and disturbance-accommodating control (bottom).

must all be taken into consideration. Most of these issues are not dealt with in this paper. Instead, a landing scenario from a 35-km prograde equatorial orbit to a point on Eros's equator, near the intermediate inertial axis is considered. Because the spacecraft is operating near the asteroid's surface, the polyhedron gravitational model is used for simulation.

The prograde orbit is in the inertial  $XY$ -plane, about the inertial  $Z$ -axis. At mission time  $t = 0$ , the spacecraft is at a longitude of  $-60^\circ$ , and the two frames are co-aligned. In the body frame, the initial velocity is in the positive  $x$ - and positive  $y$ -directions due to the orbital velocity. There are also components in the negative  $x$ - and  $y$ -directions due to the rotation of the body frame relative to the inertial frame. At a distance of 35 km these terms dominate, so the total body-frame initial velocity is in the negative  $x$ - and  $y$ -directions. The mission time is again selected to be 2400 s. The initial velocity is given as  $\mathbf{v}_0 = [-6.946, -4.010, 0]^T$  m/s. The initial position is  $\mathbf{r}_0 = [17.5, -30.311, 0]^T$  km. The landing site is chosen on the positive  $x$  side as  $\mathbf{r}_f = [-8.166, -7.643, 1.487]^T$  km. Landing sites on the middle or negative  $x$  side are challenging due to the kinematic accelerations. For a soft landing, the final velocity is again  $\mathbf{v}_f = 0$  m/s.

Figures 7.17 through 7.19 show the trajectories and acceleration histories for the landing mission from a prograde orbit. Figure 7.20 shows the performance index histories for the different ZEM/ZEV algorithms. The simplest algorithm clearly yields the highest performance index, while the other three are similar, with the full predictive algorithm again achieving the minimum performance index. Including an approximated gravity term does not improve performance.

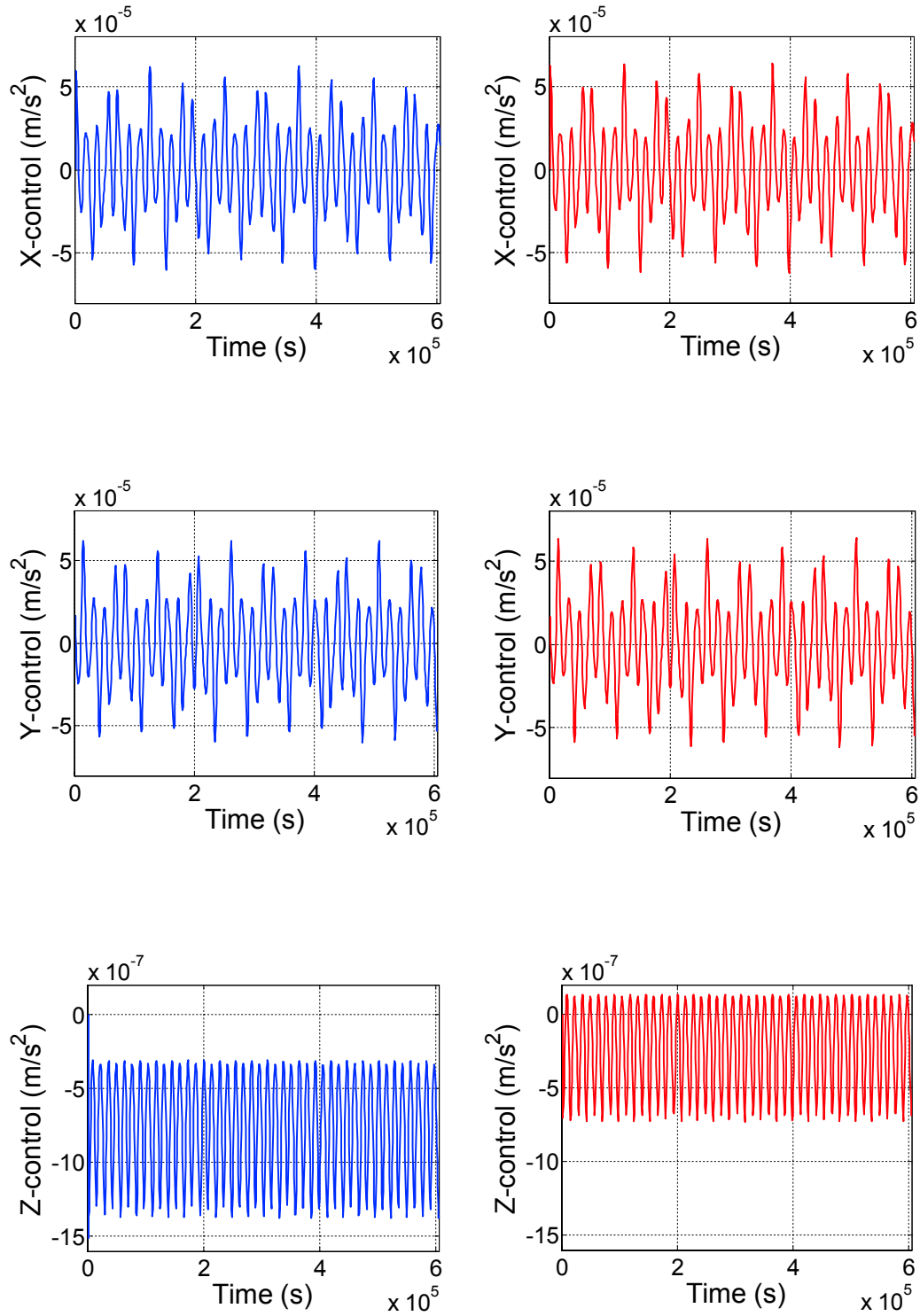


Figure 7.8: 35-km prograde orbit control acceleration histories with simple PD control. Polyhedron model on the left and the harmonics model on the right.

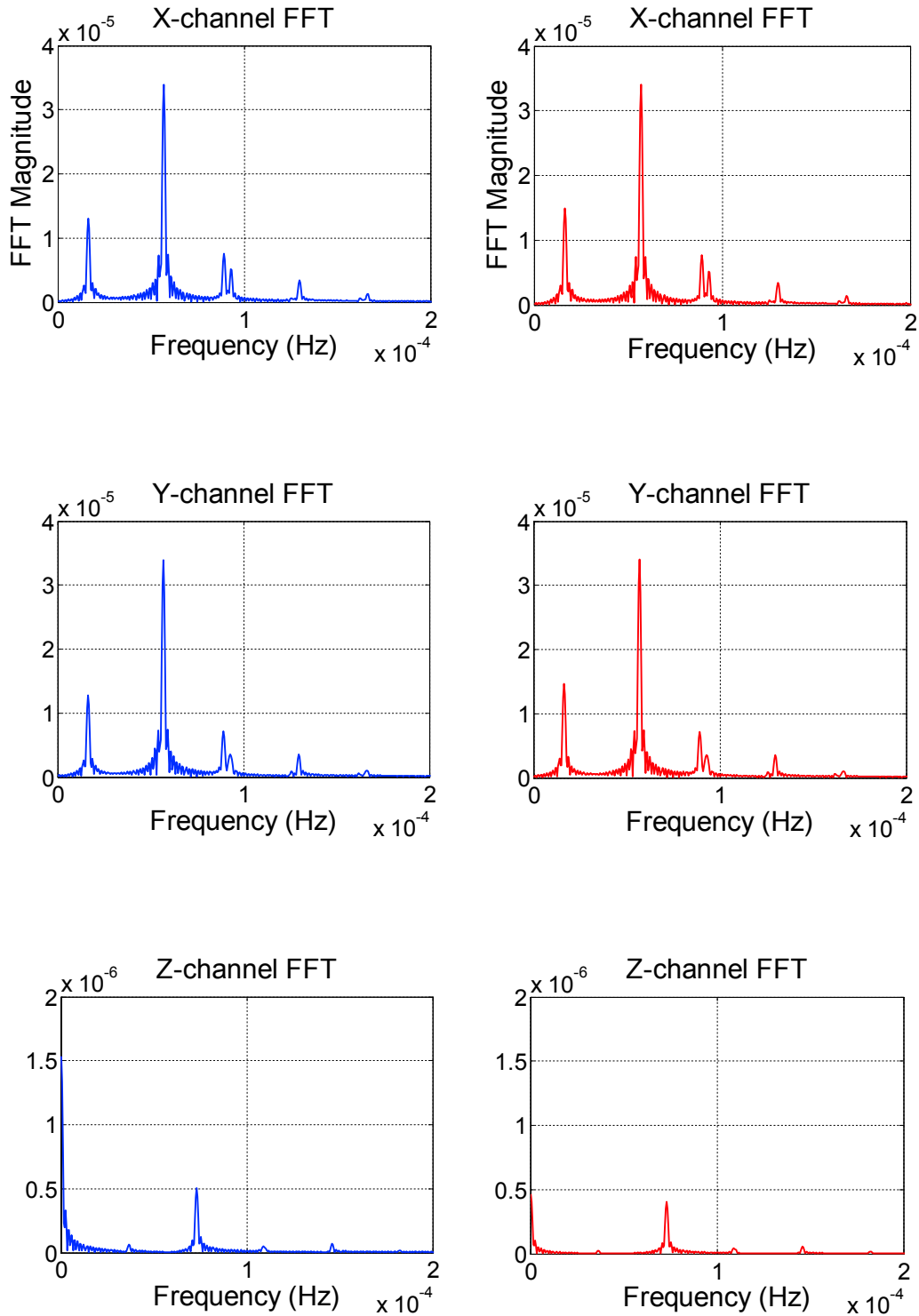


Figure 7.9: FFT plots of the PD control inputs for a 35-km prograde orbit. Polyhedron model on the left and the harmonics model on the right.

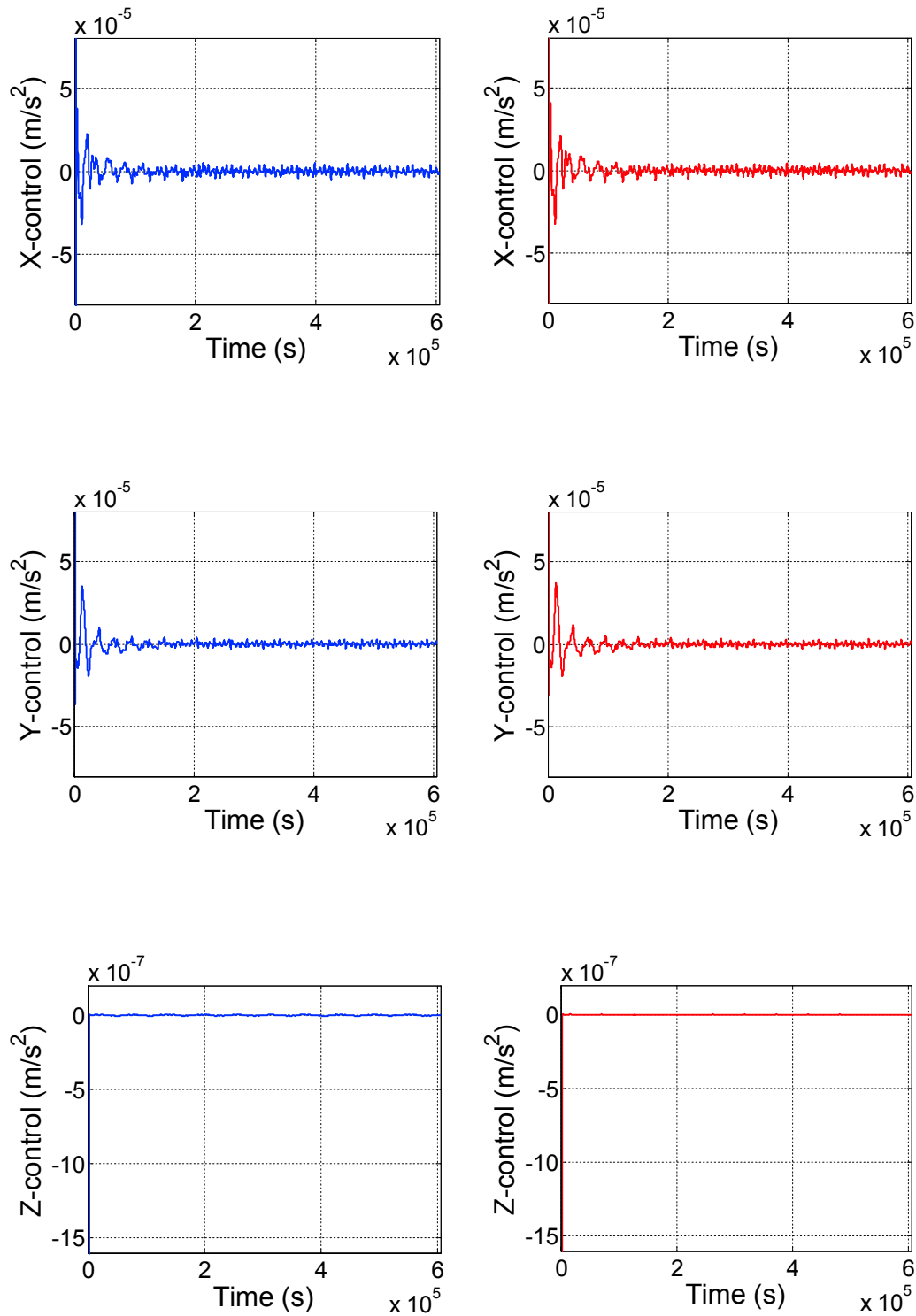


Figure 7.10: 35-km prograde orbit control acceleration histories with disturbance accommodating control. Polyhedron model on the left and the harmonics model on the right.

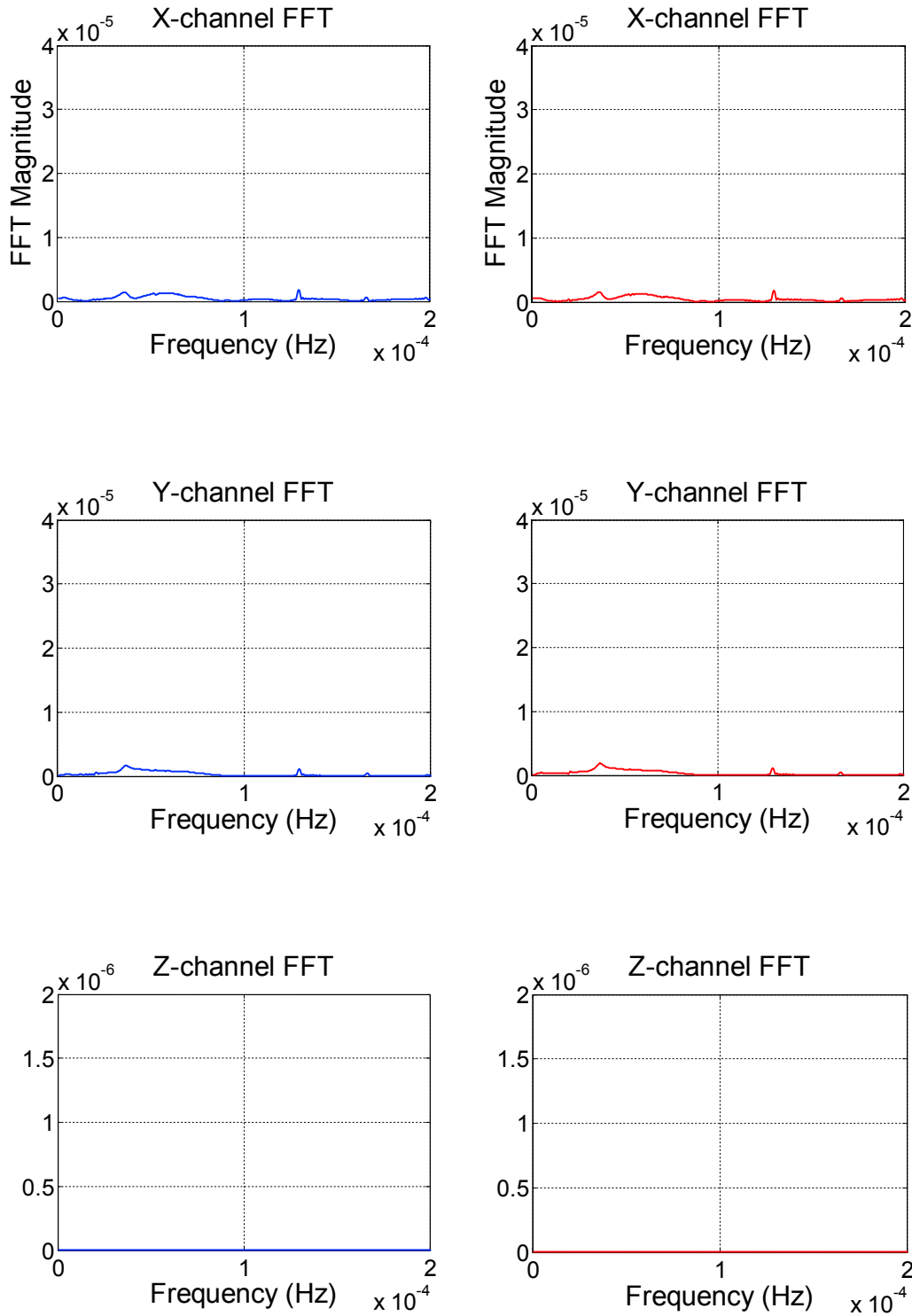


Figure 7.11: FFT plots of the disturbance accommodating control inputs for a 35-km prograde orbit. Polyhedron model on the left and the harmonics model on the right.

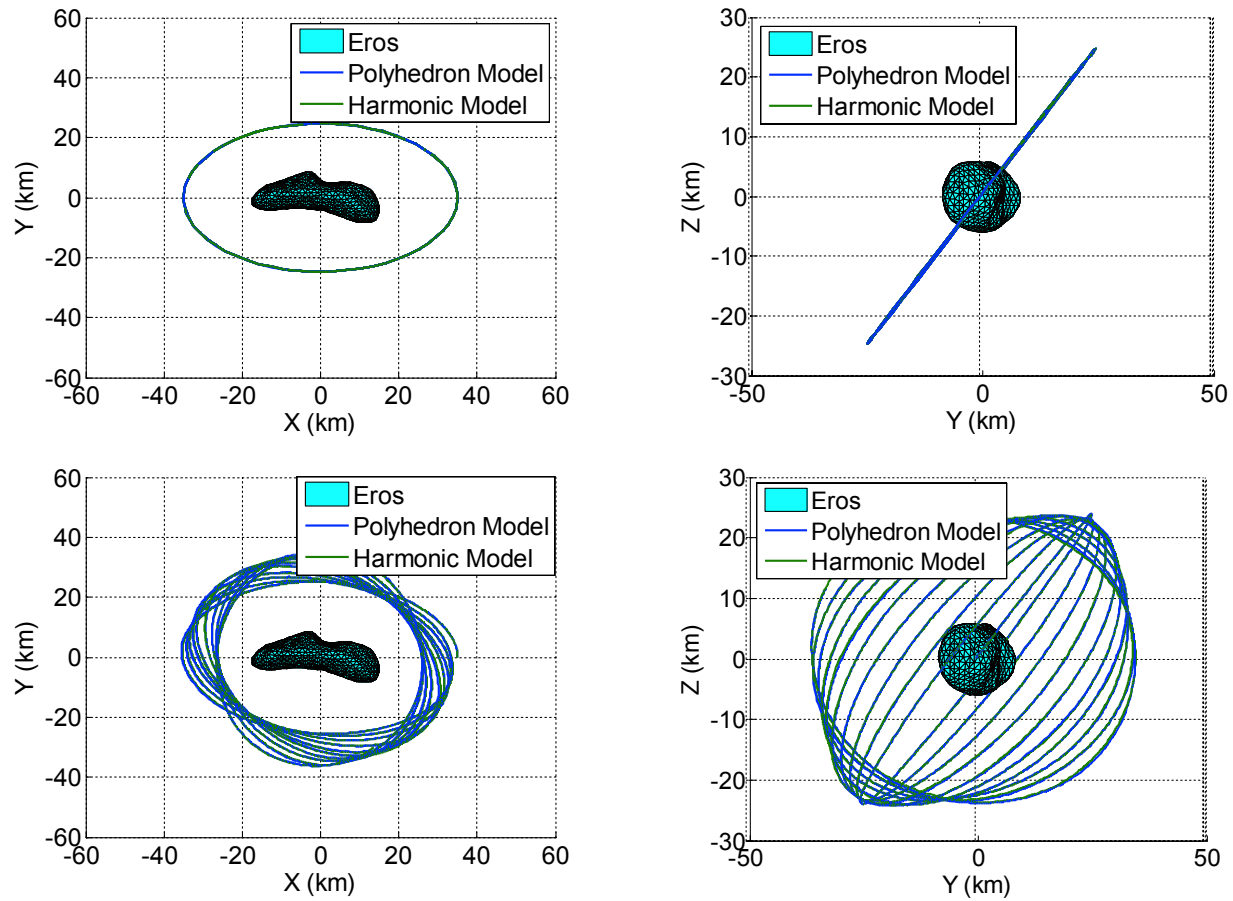


Figure 7.12: A 35-km prograde orbit in the XY-plane with PD control (top) and disturbance-accommodating control (bottom).

## 7.6 Conclusion

In this chapter, several subjects pertaining to asteroid proximity operations were investigated. First was an orbital transfer from a high-altitude orbit to a low-altitude orbit using two different ZEM/ZEV algorithms. Once in the low-altitude orbit, it was demonstrated that using simple feedback control combined with a disturbance-accommodating control filter could be implemented to ensure the spacecraft remains in a stable orbit about the body with very little control effort. One of the advantages of this control scheme over open-loop solutions is that prior knowledge of the body is not required to find the frequencies for the control filters. Finally a soft landing mission from the low-altitude orbit using four different ZEM/ZEV algorithms was examined. Numerical simulations demonstrate that the ZEM/ZEV feedback guidance scheme performs well for a realistic landing mission.

## 7.7 References

- [1] Scheeres, D. J., "Orbital Mechanics About Small Bodies," *Acta Astronautica*, Vol. 27, 2012, pp. 1-14.
- [2] Broschart, S. B. and Scheeres, D. J., "Control of Hovering Spacecraft Near Small Bodies: Application to Asteroid 25143 Itokawa," *Journal of Guidance, Control, and Dynamics*, Vol. 27, No. 2, 2005, pp. 343-354.

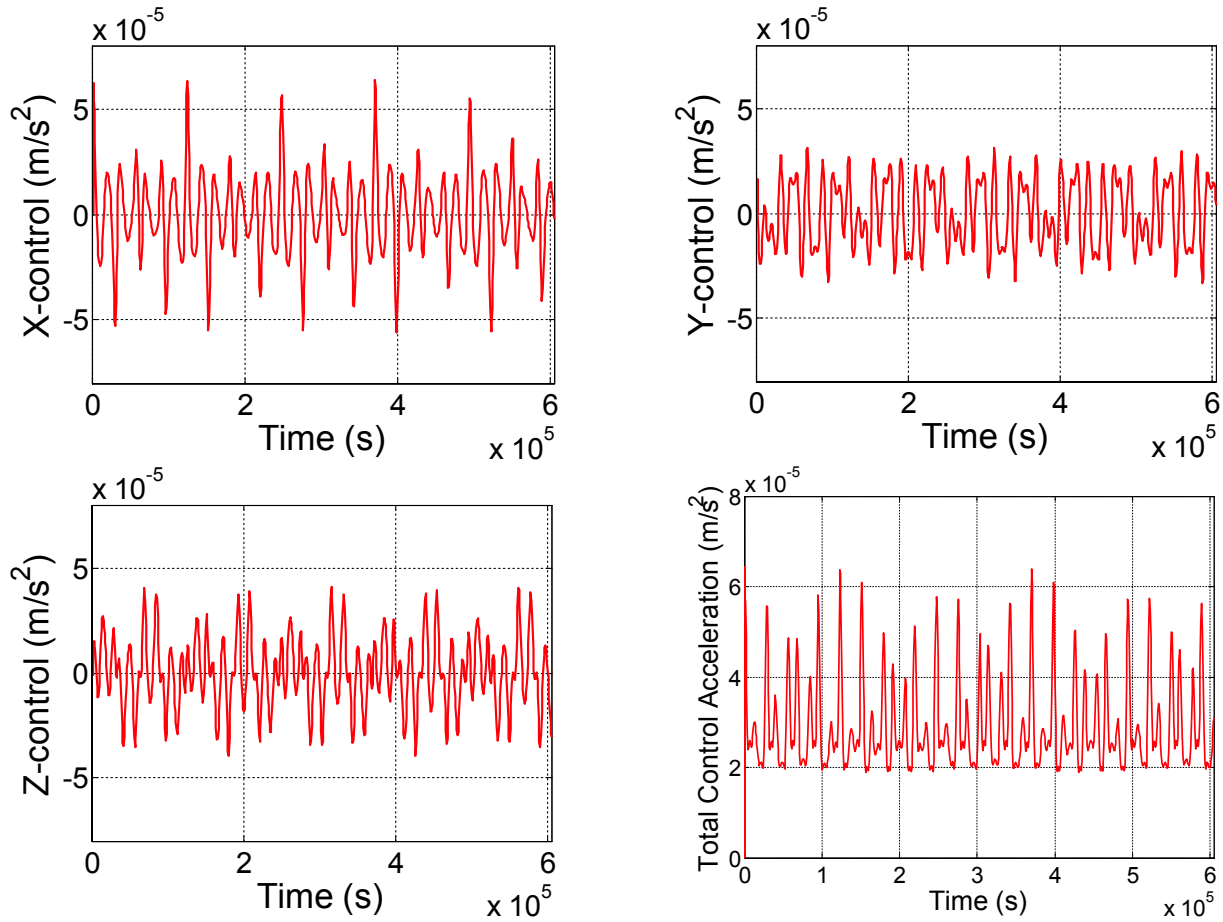


Figure 7.13: Inclined orbit control acceleration histories with PD control.

- [3] Kawaguchi, J., "Hayabusa, Summary of Guidance, Navigation and Control Achievement in its Proximity Phase," *Astrodynamics Specialist Conference*, Keystone, CO, AIAA Paper 2006-6533, Aug. 2006.
- [4] Scheeres, D. J., "Dynamics About Uniformly Rotating Tri-Axial Ellipsoids: Applications to Asteroids," *Icarus*, Vol. 110, 1994, pp. 225-238.
- [5] Scheeres, D. J., Ostro, S. J., Hudson, R. S., and Werner, R. A., "Orbits Close to Asteroid 4769 Castalia," *Icarus*, Vol. 121, 1996, pp. 67-87.
- [6] Scheeres, D. J., Williams, B. G., and Miller, J. K., "Evaluation of the Dynamic Environment of an Asteroid: Applications to 433 Eros," *Journal of Guidance, Control, and Dynamics*, Vol. 23, 2000, pp. 466-475.
- [7] Hu, W. and Scheeres, D. J., "Numerical Determination of Stability Regions for Orbital Motion in Uniformly Rotating Second Degree and Order Gravity Fields," *Planetary and Space Science*, Vol. 52, 2004, pp. 685-692.
- [8] Hu, W. and Scheeres, D. J., "Periodic Orbits in Rotating Second Degree and Order Gravity Fields," *Chinese Journal of Astronomy and Astrophysics*, Vol. 8, No. 1, 2008, pp. 108-118.
- [9] Scheeres, D. J., "Satellite Dynamics About Small Bodies: Averaged Solar Radiation Pressure Effects," *Journal of the Astronautical Sciences*, Vol. 47, No. 1, 1999, pp. 25-46.
- [10] Scheeres, D. J. and Marzari, F., "Spacecraft Dynamics in the Vicinity of a Comet," *Journal of the Astronautical Sciences*, Vol. 50, No. 1, 2002, pp. 35-52.
- [11] Scheeres, D. J., Miller, J. K., and Yeomans, D. K., "The Orbital Dynamics Environment of 433 Eros: A Case Study for Future Asteroid Missions," *InterPlanetary Network Progress Report 42-152*, 2003, pp.



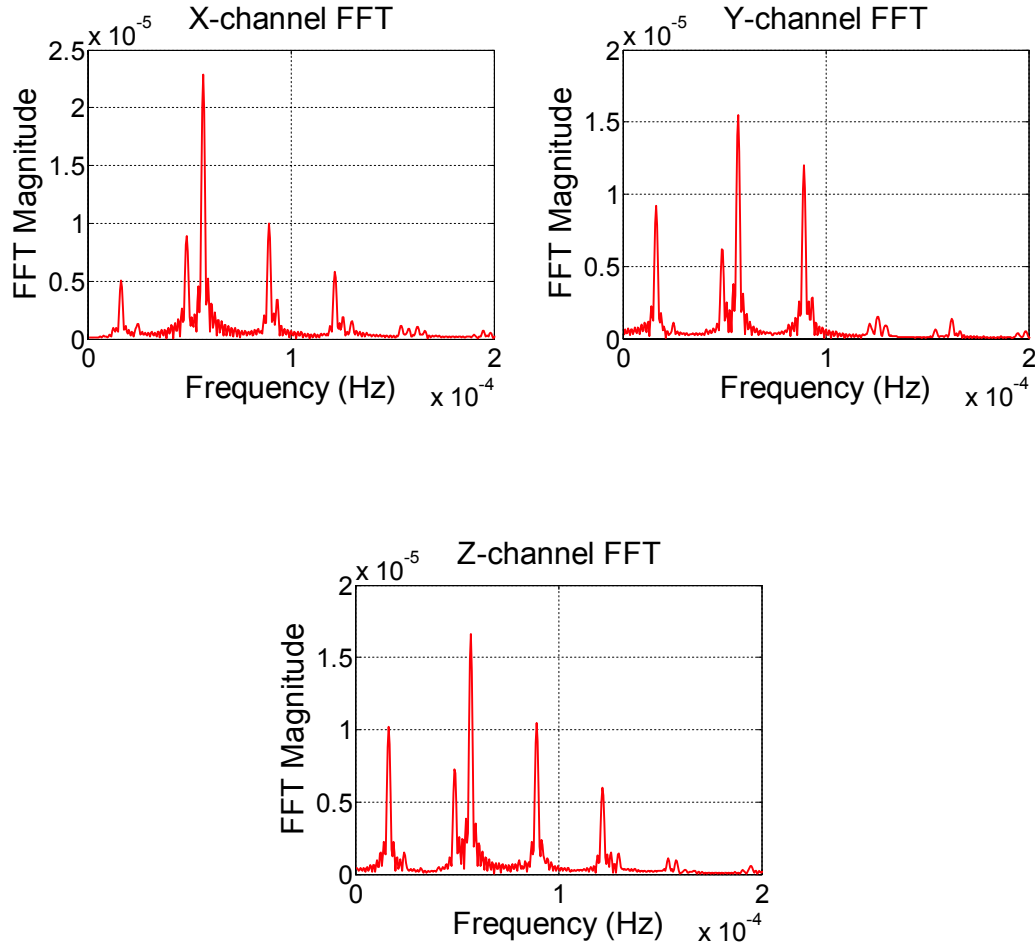


Figure 7.14: FFT plots of the PD control inputs for the inclined orbit.

1-26.

- [12] Hawkins, M., Guo, Y., and Wie, B., "ZEM/ZEV Feedback Guidance Application to Fuel-Efficient Orbital Maneuvers around an Irregular-Shaped Asteroid," AIAA-2012-5045, AIAA Guidance, Navigation, and Control Conference, 2012.
- [13] Winkler, T., Hawkins, M., Lyzhoft, J., and Wie, B., "Fuel-Efficient Feedback Control of Orbital Motion Around an Irregular-Shaped Asteroid," AIAA-2012-5044, AIAA Guidance, Navigation, and Control Conference, 2012.
- [14] Werner, R. A. and Scheeres, D. J., "Exterior Gravitation of a Polyhedron Derived and Compared with Harmonic and Mascon Gravitation Representations of Asteroid 4769 Castalia," *Celestial Mechanics and Dynamical Astronomy*, Vol. 65, 1997, pp. 313-344.
- [15] Vallado, D. A., "Fundamentals of Astrodynamics and Applications, Third Edition," Microcosm Press and Springer, 2007.
- [16] Cielaszyk, D. and Wie, B., "New Approach to Halo Orbit Determination and Control," *Journal of Guidance, Control, and Dynamics*, Vol. 19, No. 2, 1996, pp. 266-273.
- [17] Wie, B., "Space Vehicle Dynamics and Control, 2<sup>nd</sup> Edition", American Institute of Aeronautics and Astronautics, 2008
- [18] Hawkins, M., Guo, Y., and Wie, B., "Spacecraft Guidance Algorithms for Asteroid Intercept and Ren-

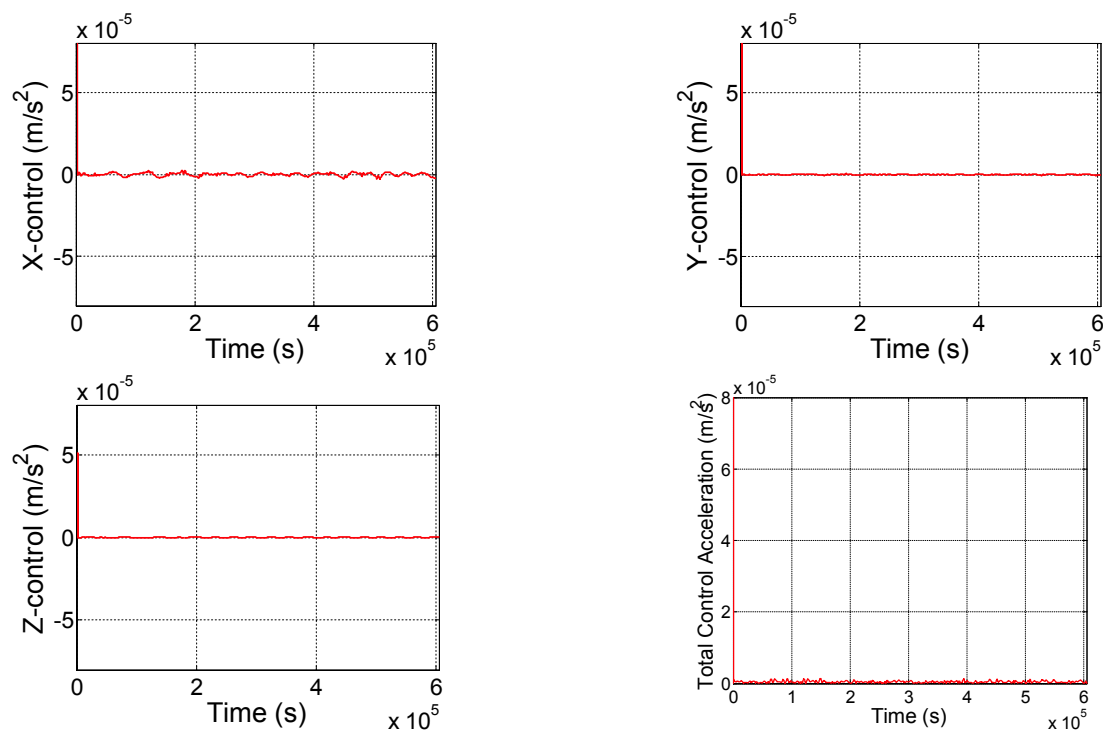


Figure 7.15: Inclined orbit control acceleration histories with disturbance-accommodating control.

- dezvous Missions: A Review,” *International Journal of Aeronautical and Space Sciences*, Vol. 13, 2012, pp. 345-360.
- [19] Battin, R. H., *An Introduction to the Mathematics and Methods of Astrodynamics*, Revised Edition, AIAA Education Series, Reston, VA, 1999.
- [20] Guo, Y., Hawkins, M., and Wie, B., “Applications of Generalized Zero-effort-miss/Zero-Effort-Velocity Feedback Guidance Algorithm,” AAS12-197, AAS/AIAA Space Flight Mechanics Meeting, 2012
- [21] Miller, J. K., et al., “Determination of Shape, Gravity, and Rotational State of Asteroid 433 Eros,” *Icarus*, Vol. 155, 2002, pp. 3-17.
- [22] “NEAR-A-5-COLLECTED-MODELS-V1.0,” URL: <http://sbn.psi.edu/pds/resource/nearbrowse.html>.

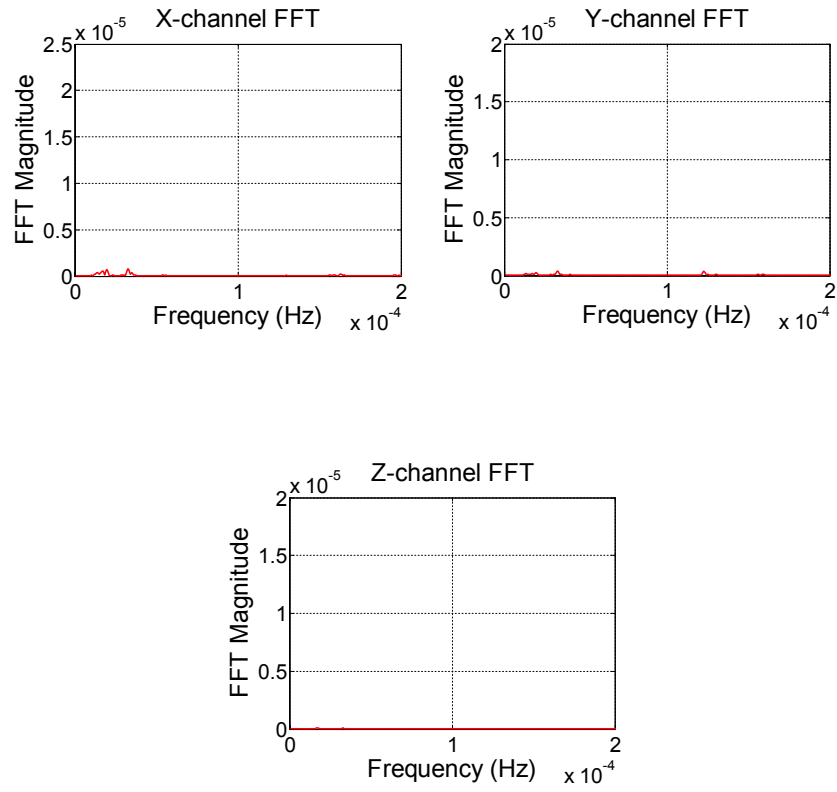


Figure 7.16: FFT plots of the disturbance-accommodating control inputs for the inclined orbits.

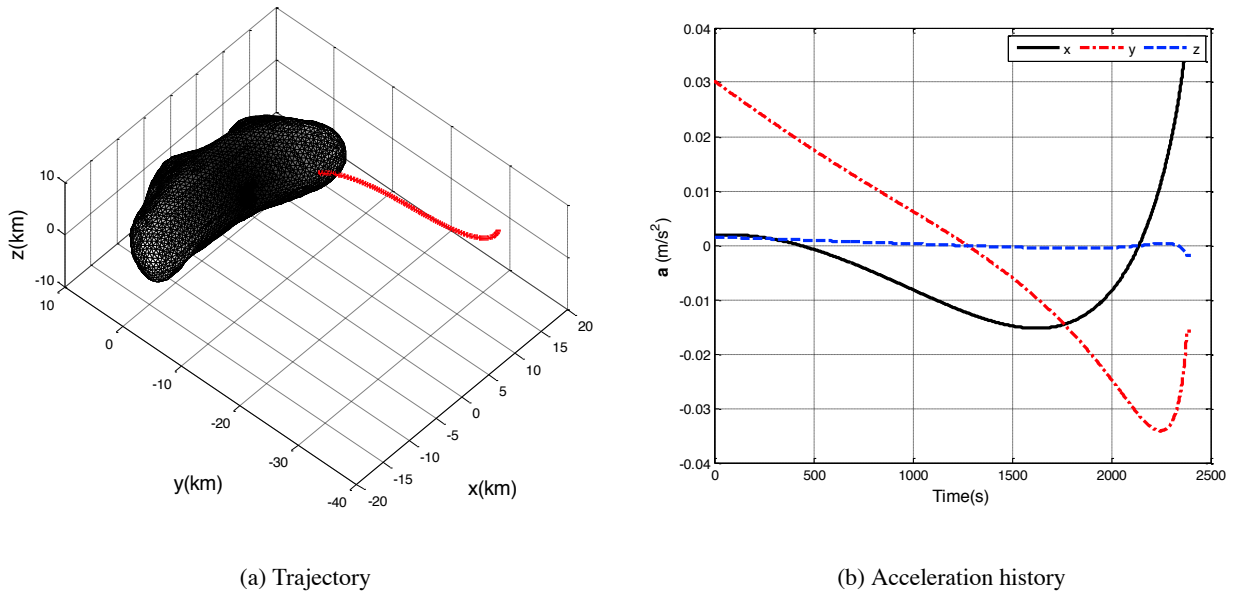
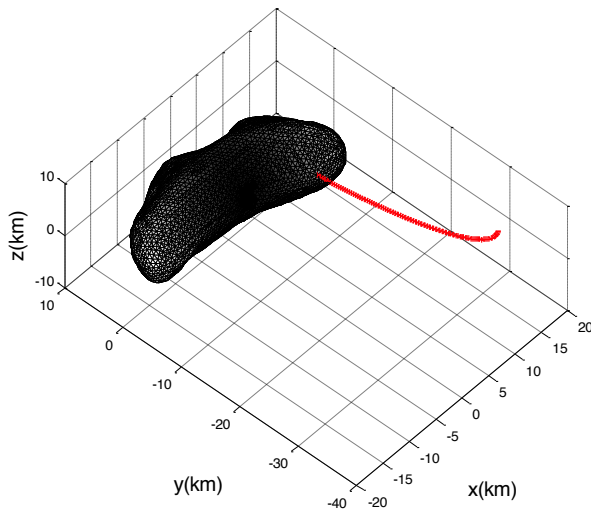
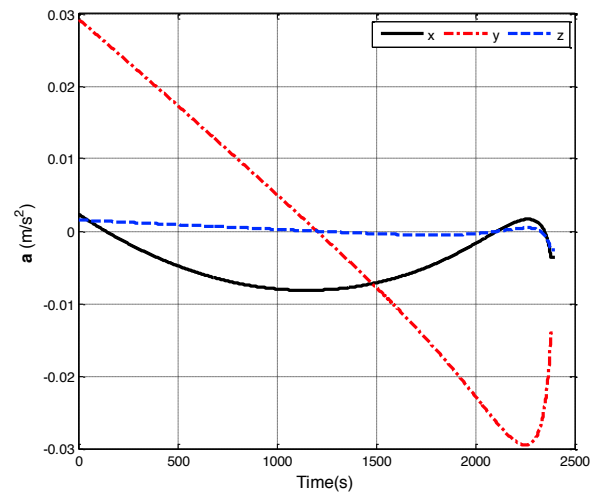


Figure 7.17: Trajectory and acceleration history, ZEM/ZEV-z.

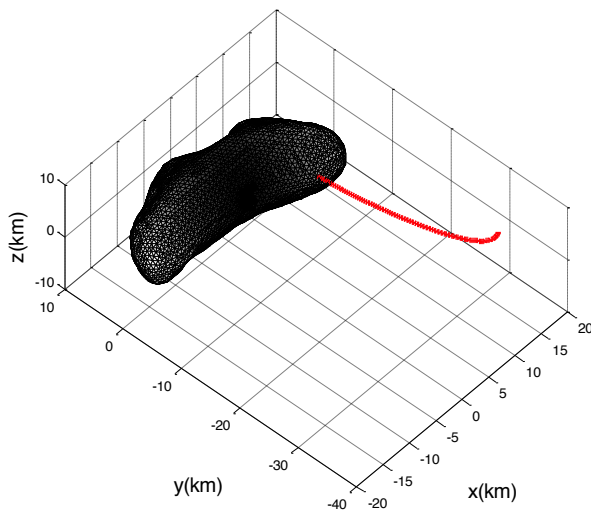


(a) Trajectory.

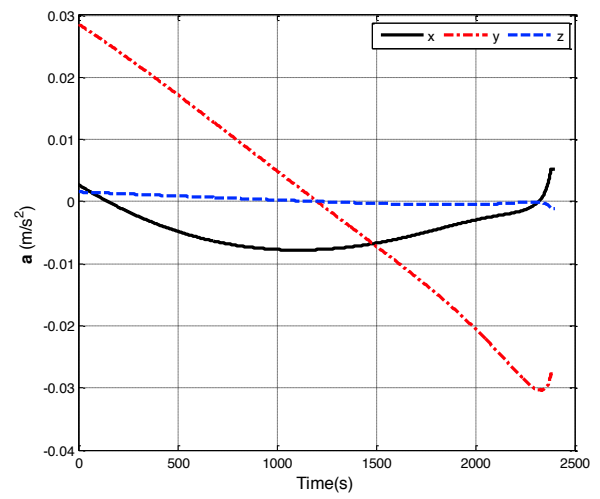


(b) Acceleration history.

Figure 7.18: Trajectory and acceleration history, ZEM/ZEV-g.



(a) Trajectory.



(b) Acceleration history.

Figure 7.19: Trajectory and acceleration history, ZEM/ZEV-p.

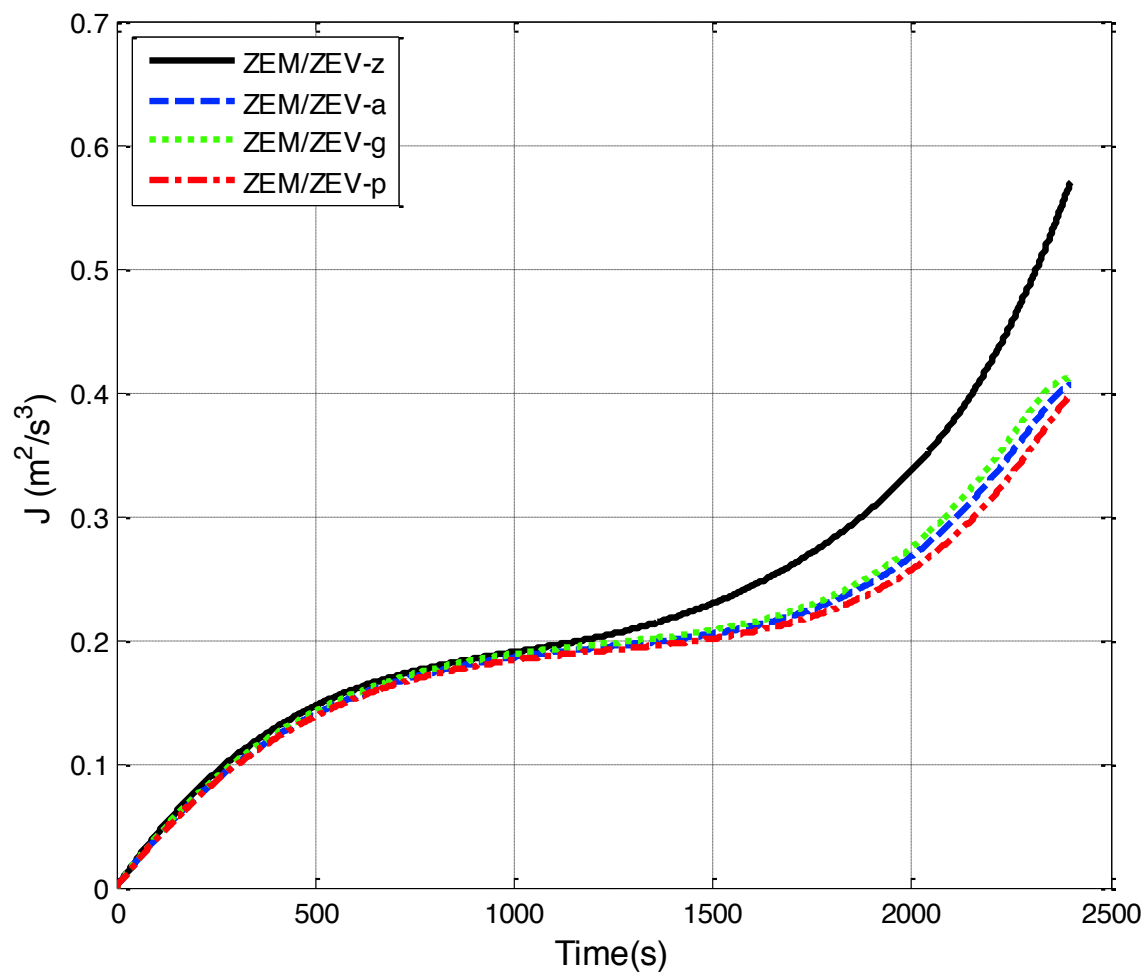


Figure 7.20: Performance index comparison.